Title

Investigating Concepts for Multilayered Thermal and Environmental Barrier Coating Systems for Porous Matrix Oxide Fiber Ceramic Composites

Author

Drtina, Thomas Joseph

Publication Date

2022

UNIVERSITY OF CALIFORNIA

Santa Barbara

Investigating Concepts for Multilayered Thermal and Environmental Barrier Coating Systems for Porous Matrix Oxide Fiber Ceramic Composites

A Dissertation submitted in partial satisfaction
of the requirements for the degree
Doctor of Philosophy
in Materials

by

Thomas Joseph Drtina

Professor Carlos G. Levi, Chair
Professor Francis W. Zok
Professor Anton Van der Ven
Professor Michael Gordon

June 2022

The dissertation of Thomas Joseph Drtina is approved.

Michael Gordon

Anton Van Der Ven

Francis W. Zok

Carlos G. Levi, Committee Chair

June 2022

Investigating Concepts for Multilayered Thermal and Environmental Barrier Coating Systems for Porous Matrix Oxide Fiber Ceramic Composites

by

Thomas Joseph Drtina

ACKNOWLEDGEMENTS

I would like to acknowledge Siemens Corporate Technology, and their collaborators for this work Stefan Lampenscherf, Niels van der Laag, and Phillip Howell, for funding this work, and providing assistance and samples for experimentation. Additional support for me was provided by the Office of Naval Research. The research made use of the MRL Shared Experimental Facilities supported by the MRSEC Program of the NSF under Award No. DMR 1720256; a member of the NSF-funded Materials Research Facilities Network (www.mrfn.org).

A huge thanks to all of my committee members, Professor Michael Gordon, Professor Anton Van der Ven, and Professor Francis W. Zok, for their patience, flexibility, and mentorship through the difficult and tumultuous times over the course of my time at UCSB. I want to thank my primary advisor, Professor Carlos G. Levi, for being an incredibly patient, hardworking, and knowledgeable mentor, who has always had the best interests of his students in mind.

This research would not be possible without the assistance and guidance of the shared instrument facility staff, past and present. Thank you to Dr. Youli Li and Miguel Zepeda for their helping with X-ray diffraction. I am incredibly grateful for Mark Cornish, Stephan Krämer, Aidan Hall, Claire Chisolm, and Ravit Silverstein for their expertise, support, and assistance in electron microscopy. Their guidance gave me the skills and knowledge to be the microscopist that I am today.

None of this would be possible without the dedicated assistance of the lab managers, Kirk Fields in the mechanical testing lab, Dano Pagenkopf and Peter Maxwell for teaching me various pieces of equipment, helping out around the lab, and even just shooting the breeze,

and especially Deryck Stave. His tireless work and countless hours helping me build and run the water vapor thermal cycling furnace, and, most importantly, running the Consarc E-beam system. Without the countless hours of toiling, heavy lifting, and sweat from Deryck, none of my coatings would have ever been grown. I learned so much about electron beams, electronics, power supplies, vacuum systems, and power and hand tools from the hours spent, and blood, sweat, and tears put into maintaining and running the Consarc.

Thank you to the members of the Levi group, past and present, for all their support, mentorship, and friendship over the last seven years. Thanks to Chandra Macauley, Kaylan Wessels, Daesung Park, Brad Lutz, Wes Jackson, Stefan Heinze, Rebecca Reitz, Colin Stewart, Najeb Abdul-Jabbar, David Poerschke, Sarah Miller, Megan Emigh, and Ravit Silverstein. Special thanks to Mayela Aldaz-Cervantes and Collin Holgate for being so wonderful and supportive of each other and myself as the three of us went through this journey together. Thank you to Mel Endsley and my intern Erin Lewis for providing me opportunity to teach and mentor, and especially for helping me stay sane in the last months of writing up this work.

I also want to acknowledge the support and friendship of other fellow students, both in Materials and other departments. Thanks specifically to Eric Yao, Emily Levin, Will Summers, Ben Callaway, Andy Ericks, Victoria Christiansen, Virginia Collier, and especially Bhavana Swaminathan for being an incredible friend and roommate. And others that are too many to name.

Thanks to my family, especially my parents Gary and Sue, for their unrelenting love and support during all these years spent halfway across the country in Santa Barbara.

I want to give a huge thank you to the ultimate frisbee community for being so friendly, supportive, and welcoming, as well as for providing me a physical outlet to get outside and enjoy Santa Barbara. And for providing me experience and connections for Santa Barbara in general. Thanks to Chandra, Siri, Trung, Kalin, Wall-E, Conrad, Mark, Pinto, Melch, Connor, Dray, Shad, Onno, Nate, Claire, Joy, Chris, Jamie, Luke, Christina, Dan, and so, so, many others for great friendship and making my time in Santa Barbara so memorable.

VITA OF THOMAS JOSEPH DRTINA

June 2022

EDUCATION

University of California Santa Barbara

Ph.D. Candidate, Materials Department, 2015-2022

Iowa State University

B.S. Materials Engineering, 2011-2015

PUBLICATIONS

1. T.J. Drtina, M. Emigh, C.G. Levi, “Morphology and growth behavior of Y_2O_3 coatings processed by electron beam–physical vapor deposition”, *In preparation*
2. T.J. Drtina, C.G. Levi, “Degradation of Nextel 720 fibers after thermal cycling in water vapor and interactions with EB-PVD coatings”, *In preparation*
3. T.J. Drtina, C.G. Levi, “Growth and performance of EB-PVD 7YSZ and $Y_4Zr_3O_{12}$ as thermal and environmental barrier coatings for oxide fiber ceramic composites”, *In preparation*
4. Q. Lin, V. Taufour, Y. Zhang, M. Wood, T. Drtina, S.L. Bud’ko, P.C. Canfield, G.J. Miller, “Oxygen trapped by rare earth tetrahedral clusters in Nd4FeOS6: Crystal structure, electronic structure, and magnetic properties,” *Journal of Solid State Chemistry*, 2015

ORAL PRESENTATIONS

1. T.J. Drtina, N. van der Laag, S. Lampenscherf, P. Howell, C.G. Levi, “EB-PVD T/EBC systems for oxide fiber ceramic composites,” *ICACC* 2020, Daytona Beach, FL, January 2020
2. T.J. Drtina, S.M. Miller, S. Lampenscherf, F.W. Zok, C.G. Levi, “EB-PVD T/EBCs for oxide fiber ceramic composites,” *MS&T* 2018, Columbus, OH, October 2018

POSTER PRESENTATIONS

1. T.J. Drtina and C.G. Levi. “Thermal/environmental barrier coatings for oxide ceramic matrix composites by electron beam – physical vapor deposition”. UCSB Winter Study Group on High Performance Materials, Santa Barbara, CA, January 2020
2. T.J. Drtina, F.W. Zok, and C.G. Levi. “Stability of environmental barrier coatings for oxide ceramic matrix composites”. UCSB Winter Study Group on High Performance Materials, Santa Barbara, CA, January 2018

RESEARCH EXPERIENCE

UCSB Microscopy and Microanalysis Facility – Student Lab Manager 2021-2022

Assumed ownership of operation, training, and maintenance, assuring smooth transition in management of microscopy facility. Provided rapid, attentive communication and in-person assistance to current users of the facility and quick turnaround training both for new users, and for advanced SEM techniques, such as low vacuum and low voltage operation. Maintained close working relationships to service staff enabling rapid service, and utilized service time to improve in-house knowledge of software and microscopy techniques. Developed expertise to independently identify and address equipment issues in a timely manner without bringing in outside service staff, thus minimizing facility interruption.

Ames Laboratory – Undergraduate Research Assistant 2012 - 2015

Helped advance the study of novel magnetic and superconductive materials. Grew novel intermetallic crystals by flux growth for analysis of electronic and magnetic properties. Used furnaces and arc-melting for sample preparation, centrifuged hot samples to recover crystals, and prepared crystal samples for analysis including XRD, electrical resistivity, and magnetic measurements. Trained new undergraduate research assistants in these laboratory procedures and test methods.

3M Corporate Research Materials Laboratory – R&D Intern Summer 2014

Advanced the development of biopolymer fibers and commercial graphics films. Blended polymer samples by twin-screw microcompounder for graphics film and fiber applications. Hot pressed extrudate into film, and evaluated material properties by DSC, DMA, tensile tests, and thermodynamic stability tests. Related material properties to mechanical performance and printability. Presented research at 3M corporate event. Trained researcher to advance the project upon my departure.

ABSTRACT

Investigating Concepts for Multilayered Thermal and Environmental Barrier Coating Systems for Porous Matrix Oxide Fiber Ceramic Composites

Thomas Joseph Drtina

Increasing the efficiency of gas turbine engines, both for aviation and commercial power generation, means higher operation temperatures and new materials capable of withstanding the increasingly extreme environments in the hot sections of these engines. Ceramic matrix composites have increased temperature capabilities, and particularly porous matrix oxide fiber ceramic composites (OFCCs) are promising materials due to their innate oxidative stability, resistance to thermal shock, cost, and ease of manufacture. However, OFCCs are not without limitations. The fibers and porous matrices have temperature limitations for microstructural stability, and the primary oxide constituents, Al_2O_3 and especially SiO_2, have issues with corrosion and volatilization in high temperature water vapor, a major constituent of combustion atmospheres. Components require thermal and environmental barrier coatings (T/EBCs) with engineered structures and properties to maximize protection. This work studied techniques for building multilayered T/EBC systems for OFCCs and tests their efficacy.

Two generations of air plasma sprayed (APS) coated OFCC coupons were supplied by Siemens Corporate Technology for durability assessment. These were compared against in-house coated OFCC coupons using electron beam-physical vapor deposition (EB-PVD) in thermocyclic testing from room temperature to 1200°C. EB-PVD coated samples performed better, with significant delamination seen in the APS coated specimens.

The porous matrices of the OFCCs, while necessary for bulk damage tolerance and fiber pullout, complicates adhesion of these barrier coatings. Precursor impregnation and pyrolysis was used to infiltrate uncoated OFCC coupons with both alumina and yttria stabilized zirconia precursor solutions to create a gradient in density to selectively strengthen the matrix region near the surface to be coated, without sacrificing bulk toughness. The gradient was characterized using Vickers microhardness indentation tests of matrix pockets in cross-section.

Further EB-PVD coating was performed on hardened, uncoated OFCCs, with additional compositions from 7wt% yttria stabilized zirconia (7YSZ) to more yttria rich compositions of $Y_4Zr_3O_{12}$ (YZO) and Y_2O_3 with better matched thermal expansion to the OFCC. The latter compositions were deposited in bilayer configurations with a thin 7YSZ interlayer to prevent diffusional interaction with the OFCC. Despite morphological irregularities observed in 7YSZ and Y_2O_3 depositions, especially at deposition temperatures above 1080°C, adherent coatings with desirable columnar microstructures were grown in all three compositions, with deposition temperatures below 1035°C.

Finally, select EB-PVD coated OFCCs were thermally cycled in flowing water vapor at 1200°C to assess durability of the coatings and amount of damage to the SiO_2 – containing fibers from water vapor ingress through the porous coating. All coatings remained adherent, fiber damage from SiO_2 volatilization was observed, especially around coating defects. Specimens with denser interlayers did mitigate some ingress, coating and OFCC surface defects still provided pathways for water vapor.

The multilayer thermal and environmental barrier coating systems for OFCCs assembled and tested in this work provides insight into creating needed effective barrier coatings for the implementation of OFCCs into hot gas components of gas turbine engines.

TABLE OF CONTENTS

LIST OF TABLES

LIST OF FIGURES

Chapter 1: Introduction

There is great demand for increasing the efficiency of gas turbine engines (GTEs), from both environmental and economic perspectives. In 2018, burning natural gas in turbines supplied about 23% of the global total energy production, and this figure is expected to rise as societies move away from coal-generated power. Additionally, 3,072 megatonnes of CO_2 were released into the atmosphere in 2018 from the burning of natural gas for electricity [1]. The aviation industry, primarily powered by GTEs, accrued $188 billion in fuel costs in 2019 and released 915 megatonnes of CO_2 into the atmosphere [2]. With the large scale of these industries, even marginal increases in turbine efficiency would save a substantial amount in operation costs and create a significantly reduced environmental impact.

The principal means of increasing GTE fuel efficiency is increasing engine operating temperatures, and a key limitation is the temperature capabilities of the structural components in the combustion gas path [3,4]. However, industry targeted temperatures are approaching the upper limit of the metallic alloys used in the hot zone components of GTEs. This has consequently motivated extensive research thrusts in developing ceramic materials for these high temperature applications. Aside from the benefit of a higher melting point, ceramic-based components bring other advantages, such as reduction in weight and less need for active component cooling. Continuous fiber-reinforced composites (CFCCs) have emerged as leading candidate ceramic materials for GTE hot zone components [5,6]. With properly engineered fiber-matrix interfaces, damage in CFCCs will occur with uncoordinated fiber failure, frictional fiber pullout, and matrix crack deflection, dramatically increasing toughness and thermal shock resistance over monolithic ceramics [7]. Significant research has been performed on SiC-based CFCCs, with success as components having reached commercialization [8] , However, SiC-based CFCC systems are not without limitations. Concerns with oxidative embrittlement at intermediate temperatures [9] and volatilization of the protective SiO_2 scale in flowing, high-pressure, high-temperature atmospheres containing water vapor [10–12]. These limitations, and to some extent cost of manufacture, have motivated the exploration of composites based on all oxide constituents, oxide fiber ceramic composites (OFCCs) [13–15].

OFCCs are often fabricated with porous matrices, providing a natural path for matrix crack deflection around the fibers and subsequent fiber pullout on failure with frictional dissipation along the matrix crack surfaces, enhancing the component toughness [14–16]. The ease of component production and low material cost have led to the commercialization of large OFCC components [8,17,18]. There is motivation to develop these materials for higher temperature, hot-zone applications, such as within the combustor [19,20], because of their relative ease of manufacture and oxidation resistance. However, these materials and components are not without limitations. OFCCs are typically based on Al_2O_3 and SiO_2 systems [21], and have similar issues to SiC-based systems regarding SiO/OH volatility and associated corrosion in high-temperature, water vapor-containing environments. While Al_2O_3 is more resistant to water vapor – induced corrosion than SiO_2, it is still of concern at the highest temperatures targeted by the GTE industry [22–24]. The issue drives the need for a protective environmental barrier coating (EBC) for OFCC components in combustion environments. EBC materials need to be resistant to water vapor themselves, as well as have good thermochemical and thermomechanical compatibility with the composite constituents [25,26].

A secondary function of the coating is as a thermal barrier (TBC). The purpose of a TBC is to protect the underlying component from thermal overload by inducing a thermal gradient from the coating surface to the composite outer boundary. TBCs are needed for OFCC systems in hot zone components due to temperature limitations of industry standard fibers, which typically are below 1200°C for long term applications [26,27]. The material property and microstructure requirements for TBCs differ from EBCs. TBCs should have low thermal conductivity and be processed with strain tolerant microstructures if they have substantial thermal expansion mismatch with the OFCC component. Coating porosity can also greatly reduce thermal conductivity. While coating porosity is beneficial for a TBC, it can be deleterious for an EBC. An ideal EBC is a dense, hermetic layer that prevents ingress of a corrosive species, typically H_2O, through the coating. A dense coating is far less strain tolerant than one with engineered porosity, and thus the coating material and composite substrate must have minimal mismatch in coefficients of thermal expansion (CTEs) to reduce mismatch stresses.

Two dominant processing techniques for barrier coatings are air plasma spray (APS) and electron beam-physical vapor deposition (EB-PVD). APS is a more economical process and amenable to novel compositions and thicker coatings, while EB-PVD coatings have more strain tolerant microstructures that are better adherent due to the higher temperature at which they are deposited, but the process is more expensive [28,29]. Conversely, the porosity in the columnar grain microstructure that gives EB-PVD coatings strain tolerance are pathways for gas ingress through the coating, limiting effectiveness as an EBC. Balancing thermal expansion mismatch, coating microstructures, and processability with coating performance are key research challenges for T/EBC systems for OFCCs.

The aim of the present investigation was to analyze the effectiveness of different T/EBC coating materials, coating techniques, and multilayer systems to understand the interplay between OFCC components and coating materials in simulated service environments. The structure of this dissertation is as follows. A literature review of relevant concepts and a background foundation is presented in **Chapter 2**. Experimental procedures, set-ups, and characterization methods and techniques are described in **Chapter 3.** The performance of APS and EB-PVD coated OFCCs in thermal cyclic testing are assessed and compared in **Chapter 4**. The limitations porous matrices bring to coating durability are addressed in **Chapter 5** with the concept of selectively strengthening matrix regions near the surface to be coated to create a layered barrier coating system. **Chapter 6** analyzes the EB-PVD growth of 7YSZ on OFCCs and bilayer configurations with lower CTE materials. Microstructures are related to their crystallographic texture and the process parameters during deposition, and challenges with EB-PVD on porous matrix OFCCs are highlighted. **Chapter 7** explores the performance of EB-PVD barrier coatings in a high temperature, water vapor-containing environment. Damage to the composite from water vapor ingress is analyzed and reactions are characterized. Finally, conclusions and future work recommendations are presented in **Chapter 8.**

Chapter 2: Background

Advancing technology in gas turbine engines (GTEs) is critical for both the power generation and aviation industries. Examples of GTEs for these applications are shown schematically in **Figure 2.1.** Engines have a compressor that increases the pressure of the incoming air. In aircraft GTEs, the main engine drives a fan that pushes much of the incoming air around the around the main compressor, called "bypass air" to provide additional thrust and improve efficiency. The compressed air is further divided, one portion going into the combustion chamber, where fuel is injected and ignited, and another redirected to the core of the engine where it goes into the engineered cooling systems for the combustor and airfoils. The hot air and combustion gas mixture then drives the high-pressure turbine, providing power to the rotating shaft that further drives the compressor. In aircraft engines, the turbine also supplies energy to the turbofan that further accelerates the bypass air [30]. For power generation GTEs, the rotating shaft powers the generator [3]; in combined cycle plants some of the exhaust gas from the GTE is used to generate steam that powers a steam turbine and a second generator. Increasing the operating temperature of the high-pressure turbine will increase thermal efficiency, reduce cooling air, and allow for more bypass air in aircraft GTEs, improving overall efficiency and reducing deleterious emissions.

Increasing GTE efficiency will inevitably require the development of components with higher temperature capability, for which continuous fiber ceramic composites (CFCCs) are attractive candidates. While not as high performance as SiC-based systems, oxide fiber ceramic composites (OFCCs), are advantageous for their oxidative stability, ease of manufacture, and lower cost [13,16]. However, OFCCs have their own environmental and temperature limitations, and require thermal and environmental barrier coatings (T/EBCs) of their own for components to have viable lifetimes [31]. T/EBCs for OFCCs bring unique challenges when compared to SiC-based or metallic components in current use. OFCCs have coefficients of thermal expansion (CTEs) that fall between those of superalloy components and SiC-based CFCCs, and materials with closely matched CTEs may not be thermochemically stable with the components of the OFCC [26,32,33]. OFCCs based on porous matrices to enable strain tolerance additionally complicate coating processing, adhesion, and the ensuing performance [34,35]. An overview of current knowledge of OFCCs and processing methods, examination of OFCC environmental limitations, approach to T/EBC challenges for OFCCs, and coating techniques are discussed in the following sections.

2.1 Overview of Oxide Fiber Ceramic Composites

2.1.1 Material composition of OFCCs

Typical OFCC constituents include mullite, an aluminosilicate with compositions typically in the range 75-80 mol%$AlO_{1.5}$, and/or alumina, both as fibers and the matrix phase. Common fibers are 3M Nextel™ 610 (N610), an all-alumina fiber, and Nextel™ 720 (N720), an alumina/mullite fiber containing about 70.5 vol% mullite at the higher alumina content, which would be in equilibrium with the alumina constituent at the relevant temperatures. N610 is stiffer and stronger, but has diminishing mechanical properties at elevated temperatures, especially in creep performance, with a maximum usage temperature of ~1000°C [36]. N720 fibers are not as stiff, but maintain properties at higher temperatures, and have better high temperature creep performance with a useful temperature limit of up to about 1150°C [13,36]. Matrices are typically porous alumina, but may contain different oxides such as silica, mullite, 3 mol.% Y_2O_3 stabilized zirconia (3YSZ), and yttria aluminum garnet (YAG) [18,21,37].

2.1.2 Damage tolerance in OFCCs

Achieving high toughness in CFCCs involves enabling matrix crack deflection around fibers, uncorrelated fiber failure, and frictional energy dissipation during subsequent fiber pullout. There are three common microstructural approaches to achieve this, described schematically in **Figure 2.2**. A first one involves using a fiber coating that forms a weak interface between the fibers and the matrix, as shown in **Figure 2.2** (b). This has been utilized extensively in SiC-based CFCCs with BN as the interphase coating. For OFCC systems, rare earth phosphates, such as monazite ($LaPO_4$), have been proposed as effective fiber coatings, bonding weakly to oxide fibers, and having a comparatively low hardness that enables plastic deformation during fiber-matrix sliding, further enhancing achievable toughness [38]. A second type of fiber coating is known as a "fugitive coating," illustrated in **Figure 2.2 (d).** These fiber coatings, typically based on carbon, oxidize and volatilize by the end of the composite fabrication process, leaving a physical gap between the fibers and the matrix [39,40]. The final microstructural design path, depicted in **Figure 2.2 (c)**, and the most common for OFCCs, is to have fine-scale porosity in the matrix while obviating the fiber coating. The porous matrix is inherently weakly bonded to the fibers. However, this creates some additional requirements of the matrix phase to ensure OFCC durability. The matrix must be diffusionally compatible with the oxide fibers, since the matrix and fibers will be in direct contact without a fiber coating. Additionally, the fine-scale nature of the porosity must be maintained at the target usage temperatures, so matrix materials must have sluggish sintering kinetics to prevent sintering and pore coarsening [16,21,41]. While porous matrix

OFCCs have advantages in reduced manufacturing costs by eliminating the fiber coating stage, they do have some limitations. The composite components are non-hermetic, being vulnerable ingress of corrosive gases, notably water vapor [16,33]. Two-dimensional fiber architectures, such as built from woven fiber plies, have very low interlaminar shear strengths between the layers that contain only matrix. Also, the porous matrix is expected to perform worse in compressive loadings than a matrix that is monolithic and dense, and is more susceptible to erosive and abrasive wear [42–44].

The porous matrices do bring additional benefits than just damage tolerance. Porous matrix OFCCs are light, about a third the weight of a metallic component, have resistance to thermal shock and vibration damping properties[18]. The ease of processability of porous matrix OFCCs has allowed very large components to be fabricated that are currently in service. These include exhaust diffusers and cones for the General Electric's Passport 20™ engine [17].

2.1.3 OFCC matrix design

OFCC matrices must have sufficiently low toughness to allow for crack deflection around the fibers, but also have enough strength for adequate performance of off-axis and interlaminar properties. Balancing these requirements is accomplished with evenly distributed, fine scale porosity. Fine matrix particle sizes allow for good packing density, uniform porosity distribution, and improve nominal matrix strength. However, small particle sizes make the matrix vulnerable to sintering and densification during processing and service, where undesirable cracking can occur due to the constraints of the fibers. The matrices must have thermally stable porosity to prevent cracks and defects to form during service or processing. The matrix processing must also be performed below temperatures that may degrade the microstructure of the oxide fibers.

2.2 Processing OFCCs: Precursor impregnation and pyrolysis (PIP)

2.2.1 PIP process

A precursor solution typically containing hydroxides, salts or metal-organic compounds, will decompose into an oxide upon pyrolysis at moderate temperatures [45]. Precursor solutions are often used to further densify partially sintered porous bodies by liquid impregnation and pyrolysis (PIP). The technique is a proven method to increase density at lower process temperatures while minimizing shrinkage from sintering [46,47].

A typical PIP process involves a vacuum-assisted full infiltration of the solution into the porous body, a gelling step to immobilize the solution within the body preventing segregation upon drying, a drying step to evaporate water from the solution, and the pyrolysis [21,48]. The process is repeated several times, as each cycle only yields a small amount of material [41,49]. A final firing at a higher temperature may be necessary depending on the material or precursor solution. Pyrolysis often yields metastable structures [50], especially with alumina precursors [41,49], and a final heat treatment at a higher temperature will allow transformation to the desired equilibrium phase.

2.2.2 PIP processing for porous matrix OFCCs

PIP processing is advantageous for densifying the porous matrices of OFCCs as the lower required processing temperatures will not damage fibers and help avoid introducing processing-related tensile stresses or cracking in the matrix from sintering shrinkage [41,49,51]. Previous work from [41,46] highlights how precursor solutions will segregate on drying when PIP processing without gelling. The aqueous precursor solution will gel with exposure to basic NH_4OH, either by adding the liquid directly to the precursor solution, or by exposing an infiltrated body to gaseous NH_4OH. This exposure creates a network of the precursor molecules, immobilizing the precursor molecules so they do not travel with the solvent on drying [46].

In both porous Si_3N_4 bodies in [46] and porous alumina/mullite OFCC matrices in [41], precursor solution is shown to segregate to the bodies' surface that face the heat lamp during the drying step. For OFCCs this segregation proved detrimental to overall mechanical properties [41]. There was a steep drop in overall toughness and visible fiber pullout, suggesting that precursor also segregated to the fiber-matrix interface, locally increasing the matrix density and hindering fiber pullout and matrix crack deflection [41,49]. Gelling the alumina precursor was shown to prevent segregation [52].

2.2.3 Infiltration processing for functional grading

PIP processing has been used elsewhere in literature to create a body of graded composition after densification [53–56]. A functionally graded ceramic body can be created with a differential in not only density, but also functional properties such as hardness, toughness, CTE, or thermal conductivity.

It has been demonstrated in literature that, adding 4 mol. % Y_2O_3 stabilized ZrO_2 via precursor impregnation to a porous alumina body, increased toughness with the creation of the transformable zirconia tetragonal phase [57]. The presence of monoclinic or cubic ZrO_2 structures do not contribute to toughness, only the transformable tetragonal phase, which was formed with a composition of 4 mol. % $Y_2O_3 – ZrO_2$ made from a precursor solution of zirconium acetate and yttrium nitrate.

2.3 *Volatility of oxides in high temperature water vapor*

While beneficial for their native oxidative stability, oxide materials are known to be vulnerable to hot corrosion in water vapor, which is a major component of combustion atmospheres, and especially in the high-pressure, high-gas velocity environments of GTE combustors. This phenomenon is important to understand not only for the oxide constituents of the OFCC, but also for the candidate oxide materials for the T/EBCs.

2.3.1 *Combustion and volatility reactions*

The combustion reaction for methane, the main component of natural gas, in air is as follows:

$$\mathrm{CH_4 + O_2 + N_2 \leftrightarrow CO_2 + CO + H_2O + NO_x + N_2} \qquad \mathbf{2.1}$$

This reaction is more efficient at higher temperatures, and produces less of the harmful byproducts of CO and NO_x. The average combustion atmosphere is about 10% water vapor [12]. So as the industry targets higher operating temperatures, it is increasingly important for the structural materials in the hot gas sections to withstand water vapor attack. The general reaction of a metal oxide, denoted as MO_x, with water vapor and oxygen to form an (oxy)hydroxide gaseous species is shown as follows [58]:

$$\mathrm{MO}_x(\mathrm{s}) + n\,\mathrm{H_2O(g)} + m\,\mathrm{O_2(g)} \leftrightarrow \mathrm{MO}_{x+m+2n}\mathrm{H}_{2n}(\mathrm{g}) \qquad \mathbf{2.2}$$

However, most of these types of reactions with structurally relevant oxides have negligible oxygen dependence, simplifying the reaction:

$$\mathrm{MO}_x(\mathrm{s}) + n\,\mathrm{H_2O(g)} \leftrightarrow \mathrm{MO}_{x+2n}\mathrm{H}_{2n}(\mathrm{g}) \qquad \mathbf{2.3}$$

This reaction causes material loss of the oxide from the volatility of the M-O-H gas species, and component recession is accelerated in high pressure, high gas velocity environments. The partial pressure of the (oxy)hydroxide can be calculated from the reaction equation[58] [REF]:

$$K_p = \frac{a_{M-O-H}}{a_{MO_x} a_{H_2O}^n} = \frac{p(M-O-H)}{p(H_2O)^n} \qquad \mathbf{2.4}$$

Where K_p is the equilibrium constant, the activities, a, of the gaseous species are given by their partial pressures, p, the activity of the pure oxide is unity in this case, and n is the stoichiometry of the water vapor dependence. Typically, this reaction produces the stoichiometric hydroxide, e.g. MO_x forming $M(OH)_{2x}$, but in certain systems, such as with SiO_2, the oxyhydroxide species need to be considered, especially at higher temperatures [59].

2.3.2 Performance of relevant oxides

A measure of the susceptibility of an oxide to volatilize in this environment is the partial pressure of the reaction product hydroxide or oxyhydroxide gas species at a relevant temperature. **Table 2.1** lists the partial pressure of hydroxide species of relevant oxides given a reaction with pH_2O = 1 atm, and with pO_2 = 0.5 atm, at 1200°C. (While oxyhydroxide species, especially $SiO(OH)_2$ [60], do become relevant at higher temperatures, the table illustrates the differences with just the hydroxides. The thermodynamic data available for $SiO(OH)_2$ is difficult to gather and unreliable.) This is a reasonable simulation of a GTE combustor environment where pH_2O ~ 0.5-2 atm and total pressure, P, is 5-30 atm [58]. (Oxy)hydroxide vapor pressures on the order of 10^{-7}–10^{-6} atm are enough to cause appreciable material loss over service times up to 30,000 h [58]. Of the relevant oxides listed in **Table 2.1**, the reaction of SiO_2 is in the realm of unacceptable material loss. Al_2O_3 volatilization is of less concern as the hydroxide partial pressure is over an order of magnitude lower than $Si(OH)_4$. Preventing the SiO_2 volatilization reaction is of primary concern, especially for OFCCs with mullite-containing N720 fibers. Y_2O_3 and ZrO_2 do not significantly volatilize at 1200°C, and are thus candidate materials for barrier coatings.

2.3.3 SiO₂ activity in mixed oxides

Oxide volatility in water vapor is a concern in mixed oxides, as well. When a mixed oxide containing a vulnerable species such as SiO_2, the material loss depends on the activity, a, of the vulnerable species within the mixed oxide. In **Equation 2.3**, there is an assumption that a_{MO_x} is unity, but in mixed oxides the activity of the volatile oxide would be less than one, and need to be included in the equation. For a volatile species in a mixed oxide, p(M-O-H) is directly proportional to a_{MO_x}. Therefore, a lower activity will result in lower (oxy)hydroxide pressure and less material loss. For example, a mixed oxide silicate, the reaction equation is as follows:

$$K_p = \frac{a_{M-\mathrm{O-H}}}{a_{\mathrm{MO}_x} a_{\mathrm{H_2O}}^{n}} = \frac{p(\mathrm{Si(OH)_4})}{a_{\mathrm{SiO_2}}\, p(\mathrm{H_2O})^2} \qquad \mathbf{2.5}$$

In the case of mullite, an aluminosilicate given by $Al_6Si_2O_{13}$, $a_{SiO2} = 0.54$ [58], so appreciable material recession by loss of SiO_2 would be expected. Rare-earth (RE) -silicates tend to have far lower a_{SiO2}, and have been extensively studied as EBC materials for SiC-based composite components. According to a Mao et al. CALPHAD assessment of the Y_2O_3-SiO_2 system, $a_{SiO2} = 0.083$ for $Y_2Si_2O_7$, yttrium disilicate (YDS), and $a_{SiO2} = 1.1 \times 10^{-4}$ for Y_2SiO_5, yttrium monosilicate (YMS) at 1200°C [61]. The lower a_{SiO2} of these materials lead to reduced recession rates in combustion environments, and their subsequent study as EBC materials for SiC-based components [62]. Regardless of the SiO_2 content of a mixed oxide, a_{SiO2} is an important consideration in the lifetime of Si-based structural materials in combustion environments.

2.4 Coating insights and challenges

The previous sections highlighted the material restraints for OFCCs limiting their use in high temperature, water vapor-laden environments. The temperature limitations of N610 and N720 fibers, as well as the ability to mitigate sintering of the matrices to maintain the fine-scale porosity necessary for matrix crack deflection and fiber pullout. Thermal barrier coatings (TBCs) will be required to for OFCC components to be implemented in the hot gas sections of GTEs to maintain the maximum temperature within the composite below 1200°C, which is arguably the allowable limit for N720. Also, at 1200°C, SiO_2 from the mullite in the N720 fibers is vulnerable to volatilization from water vapor attack. Because the porosity of the composites allows for gas ingress and selective SiO_2 loss, with concomitant degradation of the fibers, environmental barrier coatings (EBCs) are needed for protection against component degradation in combustion atmospheres. Balancing the tradeoffs for the material and microstructural 'requirements' for thermal and environmental protection is necessary for effective T/EBC systems for OFCCs.

2.4.1 TBC considerations

A TBC needs to have low thermal conductivity to maintain the substrate within its allowable temperature, dictated in OFCCs by the maximum capability of current oxide fibers (~1200°C). In conventional applications TBCs are effective because the substrate has a much higher thermal conductivity and is actively cooled, so the TBC is the primary barrier to heat transfer. The standard material is ZrO_2-7wt%$YO_{1.5}$,or ZrO_2-7.6mol%$YO_{1.5}$, (7YSZ), which has a thermal conductivity in the operating range (1000-1200°C) of ~2.5 W/m·K, reduced to 1-2 W/m·K upon incorporation of porosity [29]. Conversely, porous matrix OFCCs also have thermal conductivity of order 2 W/mK [51], can be several millimeters thick and are not planned to be actively cooled, so the temperature gradient through the TBC may be much smaller than that typical of coatings on metallic substrates. The implication is that if the maximum OFCC temperature must be ≤1200°C, a surface temperature of order 1300-1400°C may require a considerably thicker coating than that in current GTEs for aircraft or power generation. As the TBC thickness increases, the CTE mismatch with the OFCC becomes more critical to the durability.

2.4.2 EBC considerations

The ideal EBC would be a dense, hermetic layer that mitigates any gas ingress through to the component, while also being comprised of materials having strong resistance to reactivity or volatility in combustion environments. If the coating material is a mixed oxide containing a component vulnerable to corrosion, such as SiO_2, the activity of the vulnerable constituent must be necessarily low to prevent EBC recession. A hermetic EBC is of particular importance for OFCCs, as porous matrices allow pathways for gas ingress deep into the composite, possibly resulting in accelerated material loss [34]. For this reasoning, a dense EBC is preferred for protection, but might be more at risk for mechanical failure if there is a significant CTE mismatch. The denser coatings would not have the engineered porosity that give in-plane compliance and strain tolerance, so the EBC must have a CTE closely matched to that of the composite to minimize thermal stresses.

2.4.3 Thermochemical stability

Thermochemical stability of the barrier coatings with the underlying substrate materials is also an important concern, especially with the long service times desired for these OFCC components. Extensive reaction can create new phases that are detrimental, by damaging the fibers and/or the matrix, possibly bonding the fibers to the matrix, and will also consume the coating material or the fibers and matrix. Additionally, the presence of the reaction phases can complicate the thermal stress landscape, as the phases will have different CTEs and toughness values. Multilayer coatings have been used with next-generation TBCs for turbine airfoils, using 7YSZ as a diffusional barrier between the gadolinium zirconate (GZO) topcoat and the thermally grown alumina on the surface of the alloy, as GZO and alumina are not thermochemically compatible [63–65]. Higher Y_2O_3 – content YSZs used as barrier coatings, such as $Y_4Zr_3O_{12}$ (YZO) also use 7YSZ as a diffusion barrier to separate it from alumina [66]. Despite the CTE differences between 7YSZ and these higher rare earth – containing zirconias, 7YSZ has proven to be an effective diffusion barrier to protect underlying alumina, and could be applied to OFCCs for barrier coating systems to prevent coating reaction with the composite substrate.

Balancing the necessary barrier coatings requirements, namely an adequate porosity content to reduce thermal conductivity and a pore architecture suitable to minimize CTE mismatch, thicker coatings for better thermal protection, denser coatings with a well matched CTE for environmental protection, and assuring prospective materials will not react with the OFCC is a challenge. Multilayers are likely necessary to balance these system needs.

2.5 Air plasma spray (APS) coating

2.5.1 Overview

Atmospheric plasma-spraying (APS) is a widely-utilized technique for deposition of environmental and thermal barrier coatings. It is a higher deposition rate and less expensive process than EB-PVD, and is typically used to coat larger components such as combustors, shrouds, and land-based GTE airfoils that require thicker coatings, upwards of 1 mm thick. Powder of the desired oxide is injected into a plasma jet, and the melted droplets are sprayed onto a preheated substrate, typically to about 300°C [29,67], but can be upwards of 1000°C for coatings with the dense, vertically cracked (DVC) microstructure [29]. The process is performed in ambient conditions, hence the name ‘air’ or ‘atmospheric.’ The droplets form “splats” when they impact and deposit on the substrate surface, and layers of these “splats” build up like bricks with porosity in between, and microcracking within from the rapid solidification of the droplets. The lamellar nature of the porosity, parallel to the substrate surface, greatly reduces thermal conductivity, potentially as low as 20% of the base oxide[29]. The microcracking and inter-splat porosity do allow for some strain tolerance in the coating; however, since most of it is lamellar and parallel to the substrate, it is not as effective as segmentation that is perpendicular to the substrate.

2.5.2 Coating adhesion

Adherence of APS coatings is often of concern, as the process is performed at moderate temperature. Metallic substrates are often grit blasted prior to coating to increase the surface roughness of the substrate allowing for mechanical bonding with the sprayed coating [68]. More elegant means of surface roughening have also been studied and implemented, such as using laser ablation to create a pattern on the substrate surface [69,70]. This makes regular anchor points on the substrate for mechanical interlocking. The porous matrix surface of OFCCs is a notable concern for APS adhesion as surfaces lack anchoring points for the coating splats and usually have drying and sintering cracks within the matrix near the surface. The surfaces result in overall poor adherence and the cracks can make the as-fabricated composites prone to erosion during APS [26]. Laser surface patterning .has been used to increase surface roughness to improve adherence of APS coatings on OFCCs [71,72]. Examples of patterns used in practice are shown in **Figure 2.3.**

Another method of improving APS coating adhesion on porous matrix OFCCs has been to use a bond coat to make a more robust surface for the coating process. The bond coat is typically reaction bonded aluminum oxide (RBAO), which creates a layer on top of the porous OFCC that is resistant to erosion during the spraying process [20,26,34]. RBAO is processed at moderate temperatures with simultaneously oxidizing aluminum metal and partially sintering aluminum oxide, the balance of the volumetric shrinkage from the oxide sintering is offset by the expansion of the metal oxidizing, creating a coating without shrinkage cracking from sintering. The RBAO layer brings added benefit of a low permeability layer, ‘sealing’ the top of the porous OFCC, providing environmental protection in addition to promoting good bonding for APS coatings [34,51].

2.6 EB-PVD

2.6.1 Overview

Electron beam-physical vapor deposition (EB-PVD) is a thin film coating technique that has been widely utilized for coating hot-zone components of GTEs with TBCs [28,29]. As a “physical vapor deposition” process, it involves the evaporation of a source material, and the coating deposition occurs through condensation from the vapor phase. In EB-PVD, the source material is heated to evaporation using an electron beam, and pre-heated substrates are coated while being in line of sight to the vapor source. Oxides tend to dissociate on evaporation, and the O species will segregate to the periphery of the vapor cloud, leading to a sub-stoichiometric oxide. Oxygen gas is bled in during deposition to promote a stoichiometric coating [73]. Substrates are typically rotated during deposition, both to allow for conformal coverage during the line-of-site coating process, and also to aid with producing the desired microstructure. EB-PVD produces a columnar grain microstructure, with high aspect ratio grains growing out from the substrate, and this microstructure is especially prevalent when substrates are rotated. The different pore structures giving reduced thermal conductivity and compliance in standard APS and EB-PVD coatings are compared in **Figure 2.4**. The microstructure of EB-PVD coatings is especially sensitive to the process parameters [74].

2.6.2 Structure Zone Model

The generally accepted model relating PVD film microstructure evolution to deposition temperature is the "structure zone map" proposed by Movchan and Demchishin [75] and illustrated in **Figure 2.5** (a). The model divides the microstructure of thick PVD films into three "zones" based on the temperature of deposition. The transition temperatures, T_1 and T_2, are related to the homologous temperature of the evaporant, which is the temperature at the growth surface normalized by the melting point of the evaporant, T/T_M. For metals, T_1 and T_2 were experimentally determined to be ~$0.3T_M$ and ~$0.5T_M$, respectively. The microstructures characteristic of these zones are illustrated schematically in **Figure 2.5(a)**. Zone 1 films, for temperatures up to T_1, typically have cone-shaped domains of poor crystallinity separated and rounded tops that have a botryoidal morphology. These domains have a fibrous structure with significant internal porosity. Zone 2 microstructures, between T_1 and T_2, have parallel, columnar grains with faceted column tips, where the column width is seen to increase with temperature. Lastly, zone 3 microstructures are characterized by noncolumnar, equiaxed grains.

Sanders [76] proposed a similar model, but was based on the activation of physical processes instead of microstructure characteristics, relating the transition temperatures, T_1 and T_2, to the activation of surface diffusion and bulk diffusion, respectively. Where zone 1 microstructures below T_1 result from conditions where surface diffusion is slow, the zone 2 microstructures are dominated by surface-diffusion based growth. The microstructures of zone 3 in metals occur when bulk diffusion allows for recrystallization. The microstructural landscape is influenced by more than just surface temperature. Thornton[77] showed modifying the pressure during deposition will change the film microstructure, where increasing inert gas pressure pushes the observed microstructure transition temperatures higher, shown schematically in **Figure 2.5 (b)**. Higher chamber pressure can cause scattering and add oblique components to the vapor flux, which also increases coating porosity [78].

More recent work by Schulz et al. [79] has shown that changing other process parameters can alter the zone map. Substrate rotation during the evaporation of 7YSZ is shown to create zone 2-type microstructures at temperatures where zone 3 microstructures would be expected. The substrate rotation introduces a range of vapor incidence angles, which push the microstructure transitions to higher temperatures, shown schematically in **Figure 2.5 (c)**. This is advantageous as the parallel columnar grains associated with the zone 1-2 transition are ideal microstructures for allowing in-plane compliance and strain tolerance, and deposition at the zone 2/3 transition temperature promotes better adhesion to the substrate.

2.6.3 Evolutionary selection

As columnar grains grow in the desired zone 1-2 microstructure, a crystallographic texture evolves with the coating thickness. Growth initially begins with nucleation of randomly oriented grains, and the film becomes columnar with an out-of-plane texture that increases in sharpness with the film thickness. The mechanism of initially randomly oriented grains becoming increasingly oriented with film thickness is known as ‘evolutionary selection’ [80], illustrated in **Figure 2.6**. The process is particularly prevalent in surface diffusion-controlled growth, such as the growth of EB-PVD TBCs.

During film growth by this process, grains with favorable orientations with respect to the vapor incidence grow fastest, crowding out other orientations. Thick films characterized by the evolutionary selection mechanism would have grains comprising the entire film thickness with near identical crystallographic growth axis, giving the film a strong out-of-plane orientation. PVD coating texture development, especially in the surface diffusion–controlled zone 2 microstructures, can be understood by considering the preferred, or fastest growing growth directions; preferred growth directions are bound by facets such that growth normal is minimized, and fast laterally. Insight on these preferred growth facets can be gathered from performing a periodic bond chain (PBC) analysis of the crystal structure of the deposited material [81]. A PBC analysis looks at the chains of strongest bonds in a structure, and these chains will define the preferred growth ledges in the system. Planes containing to two or more PBC vectors maximize in-plane bonding. Kinks are rare, so growth normal to the facet is slow, but fast in the lateral direction [81]. PBC analysis of the fluorite structure, identified $\langle 110 \rangle$ as the PBC directions, connecting the anion tetrahedra coordinating the cations [82], this is illustrated schematically in **Figure 2.7**. The expected dominant facets would then be the $\{111\}$ as they contain multiple $\langle 110 \rangle$ directions and multiple PBCs. The pseudo-cubic, tetragonal *t'* structure of 7YSZ is very close to cubic fluorite, the c-axis deviation, ~2%, is small enough the PBCs in this structure are still expected to be $\langle 110 \rangle$, and dominant facets will still be $\{111\}$. Multiple types of idealized column tips in the fluorite structure with $\{111\}$ facets and the corresponding growth directions are illustrated in **Figure 2.8** [73]. The mechanisms and conditions for the presented column tips is discussed in the following section.

2.6.4 Growth morphology

Understanding the geometries and growth modes of the well-studied system of 7YSZ can help with the understanding and interpretation of the EB-PVD growth of systems with more novel compositions and crystal structures. Understanding the growth of the optimal microstructures in the industry workhorse system can help grow those microstructures with novel systems.

Since EB-PVD growth of TBCs typically occurs at a temperature where surface diffusion controls the growth and evolutionary selection of crystallographic texture, the observed facets on the surface of the coatings bring insight to growth behavior of the coatings. The {111}-faceted column tip geometries presented in **Figure 2.8** have been observed in the EB-PVD growth of 7YSZ, depending on the substrate orientation and process parameters [73,83]. The 'flat' and 'stepped' geometries are observed during stationary growth, with the {111} facets normal both to the substrate and the vapor incidence, and the growth direction of the columns is also ⟨111⟩ [73]. The formation of '[110] rooftop' column tips is observed in stationary substrates oblique to the vapor incidence at a 45° angle, and the column growth direction is ⟨110⟩ [73]. The '[001] rooftop' tip morphology was observed at a very small scale in the stationary deposition of 7YSZ on single crystal sapphire substrates where 7YSZ was able to template off the sapphire [83].

The square pyramidal tip geometry with a growth direction of ⟨100⟩ is observed with rotated substrates, and is consequently observed in the growth of industrial TBCs. These column tips form as a direct result from substrate rotation. As the substrate rotates, the vapor incidence angle, α, will change from -90° to 90°. This can be divided into two segments, $-90° \leq \alpha \leq 0°$ and $0° \leq \alpha \leq 90°$, where the average angle of vapor incidence is -45° and +45°, respectively. They can also be thought of 'sunrise' and 'sunset', as the vapor source rises up from one horizon of the substrate and sets on the other side. The two segments, with average vapor incidences of -45° and +45°, each separately feed a pair of the four $\{111\}$ facets of the square pyramid. The pairs are $\langle 110 \rangle$ type column tips forming from the ± 45° average vapor incidence, as previously described, and the pairs together create a square pyramid tip with a growth direction of $\langle 100 \rangle$ normal to the substrate[73]. This is depicted in **Figure 2.9.** In this configuration, all facets receive the same amount of vapor flux, which is key to the surviving column growth directions and tip morphologies.

With single axis substrate rotation, the columns will align themselves, giving the coatings biaxial texture, having an in-plane texture in addition to the [100] out of plane texture. This type of alignment is shown schematically in **Figure 2.10.** Biaxial texture is only seen in single axis substrate rotation, and is lost, even to the extent of a random, fiber texture in-plane with different rotation modes [84].

Surface temperature on deposition will influence the column tip morphology. Column tips become rougher and elongated in the direction of the substrate rotation axis at lower temperatures, and are more isotropic and sharply facetted at higher temperatures. This phenomenon was demonstrated by Terry [73], and is shown in **Figure 2.11** with depositions of 7YSZ where the square pyramidal column tips become more isotropic and sharper when going from surface temperatures of 900°C to 1100°C. Higher energy configurations are also possible at higher surface temperatures, even with substrate rotation, such as the triangular pyramidal – tipped $\langle 311 \rangle$ growth direction [73,85].

Square pyramid column tips is an optimal morphology for TBCs, signifying a well-formed columnar microstructure, with porosity between the columns giving the coating strain tolerance and in-plane compliance. As more novel compositions are deposited by EB-PVD as TBCs for OFCCs, the objective is to create this microstructure.

2.7 Summary and scope

OFCC components are oxidation resistant, cost-effective, lightweight materials that are promising materials for GTE applications to increase operating temperatures and efficiency. While some OFCC components are already flying in current aeroengines, there is a motivation to use OFCCs for higher temperature, combustion area components. These materials are not without temperature and environmental limitations, so T/EBCs are required for their use in the combustion atmospheres. APS and EB-PVD are both effective techniques for depositing T/EBCs for OFCCs, but each have tradeoffs to consider, and the porous nature of these materials brings additional issues with coating adhesion.

This dissertation focusses on addressing the challenges with creating an effective barrier coating system for OFCCs. The research works on understanding the limitations of APS coated composites, and addresses the issues with different coating and processing methods. Concerns with T/EBC adhesion are addressed using PIP processing to strengthen the porous matrices near the OFCC surface to promote coating adhesion and durability. The dissertation has a focus on using EB-PVD to create more compliant coatings with materials more closely CTE matched to the OFCC, and the growth behavior of these materials is studied, analyzed, and compared with 7YSZ. Difficulties of the EB-PVD process on OFCC substrates are highlighted. The durability and effectiveness of these coated composites were tested in simulated combustion environments. The dissertation explores the necessary balancing of material properties and processing requirements for creating effective barrier coatings for OFCCs.

2.8 Tables and Figures

Table 2.1: Partial pressures of hydroxide vapor species for select oxides. Adapted from [58].

Volatilization reaction	$p_{\text{hydroxide}}$ **(atm) for** p_{H2O} **= 1 atm at** T **= 1200°C**
$SiO_2(s) + 2H_2O(g) \leftrightarrow Si(OH)_4(g)$	3.75×10^{-6}
$0.5Al_2O_3(s) + 1.5H_2O(g) \leftrightarrow Al(OH)_3(g)$	1.42×10^{-7}
$ZrO_2(s) + 2H_2O(g) \leftrightarrow Zr(OH)_4(g)$	2.81×10^{-11}
$0.5Y_2O_3(s) + 1.5H_2O(g) \leftrightarrow Y(OH)_3(g)$	9.15×10^{-11}

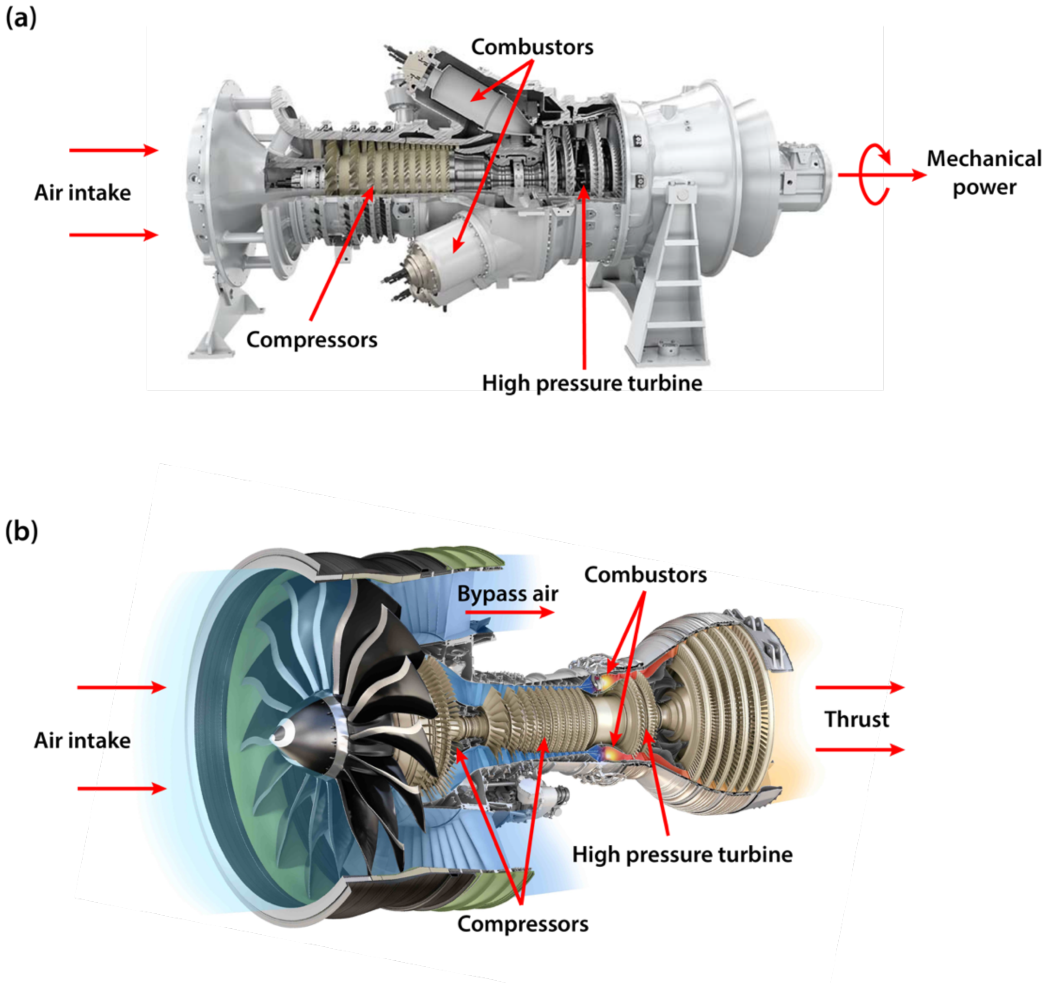

Figure 2.1: Schematic diagram of (a) a power generation GTE (Siemens SGT-300, adapted from [86]) and (b) an aero-GTE (General Electric GEnx, adapted from [87]) with major sections labelled.

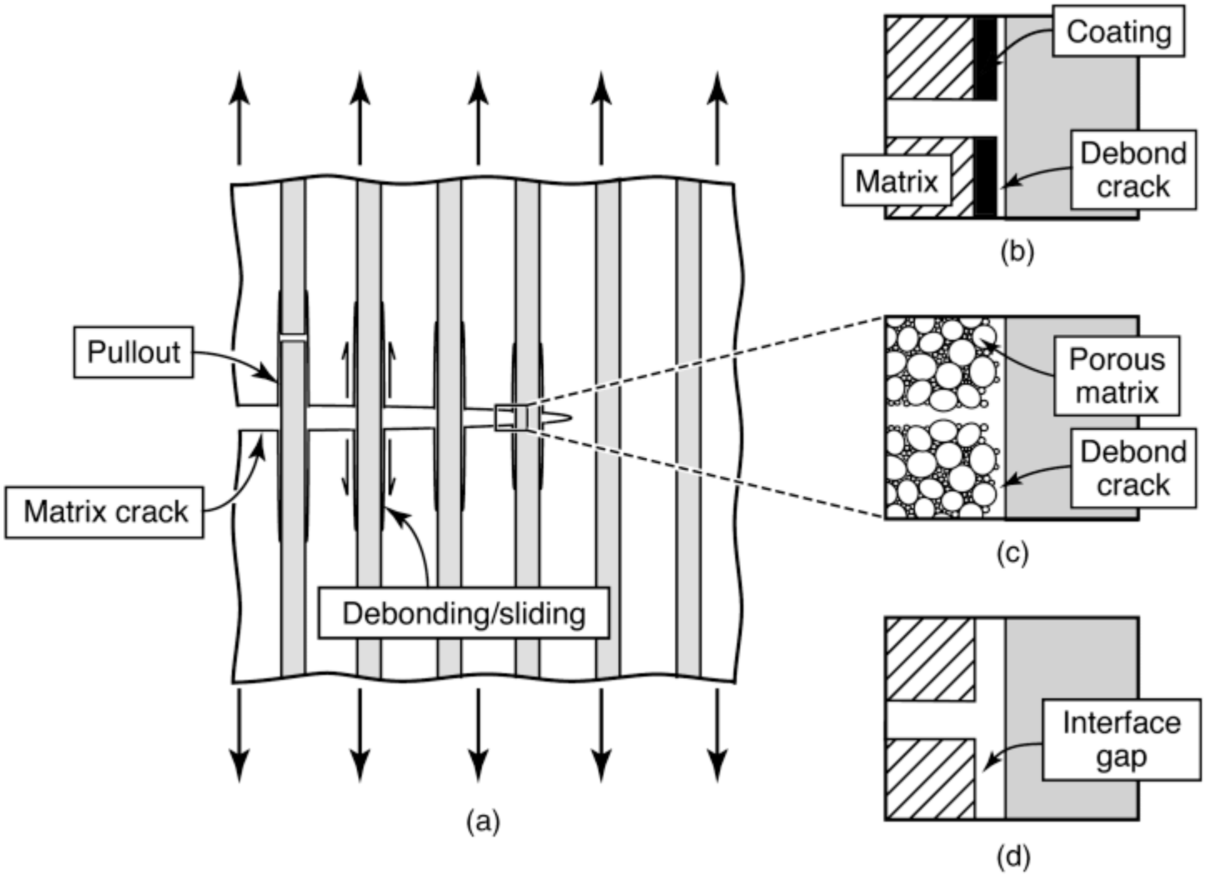

Figure 2.2: Schematic depiction of load transfer in OFCCs, illustrating (a) matrix cracks deflecting around fibers, and the microstructural design methods to promote debonding, (b) fiber coatings, (c) porous matrices, and (d) an interface gap from fugitive fiber coatings. From [13].

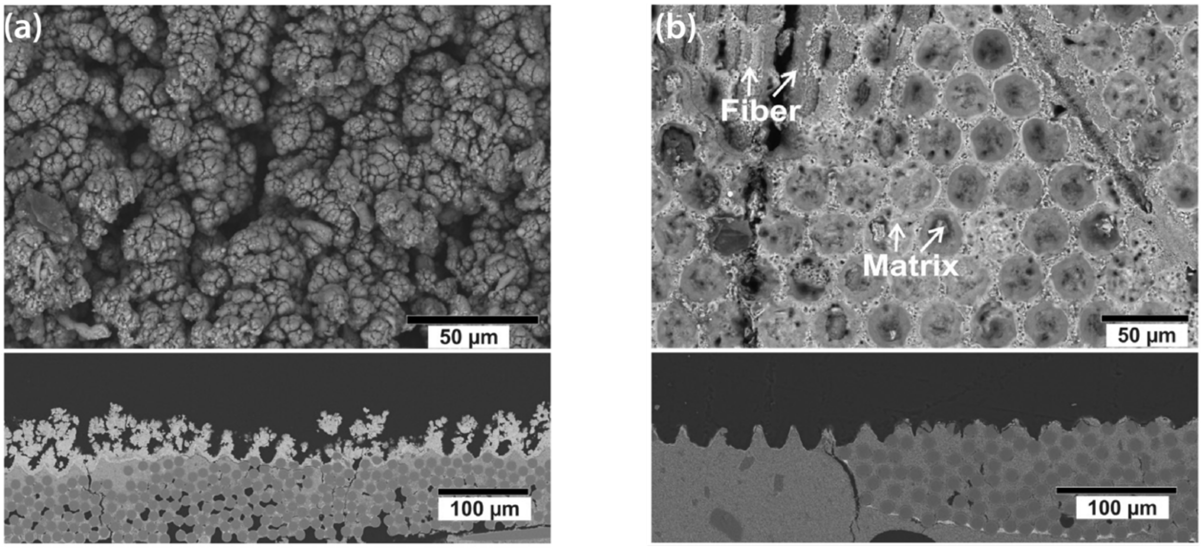

Figure 2.3: SEM micrographs showing two different styles of laser surface patterning on OFCCs: (a) 'cauliflower' and (b) 'honeycomb' structures. Both aid in the adhesion of APS coatings. Adapted from [72].

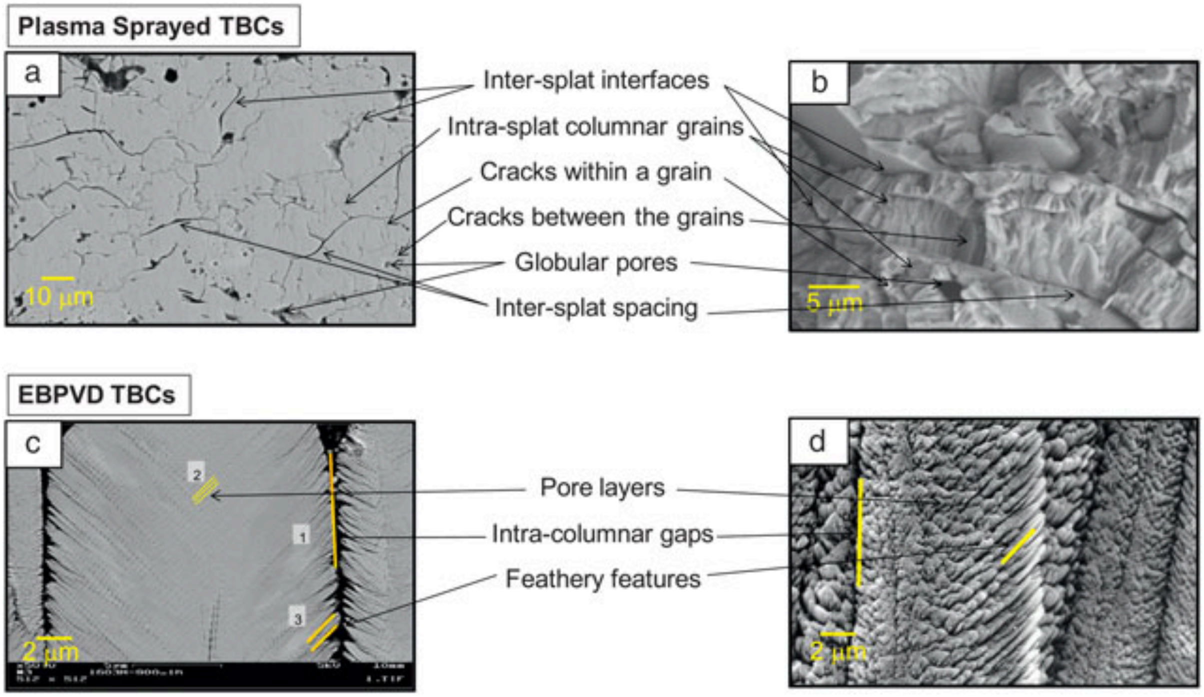

Figure 2.4: SEM micrographs showing the pore structures of (a,b) APS coatings and (c,d) EB-PVD coatings. The porosity serves to increase strain tolerance and decrease thermal conductivity. From [29].

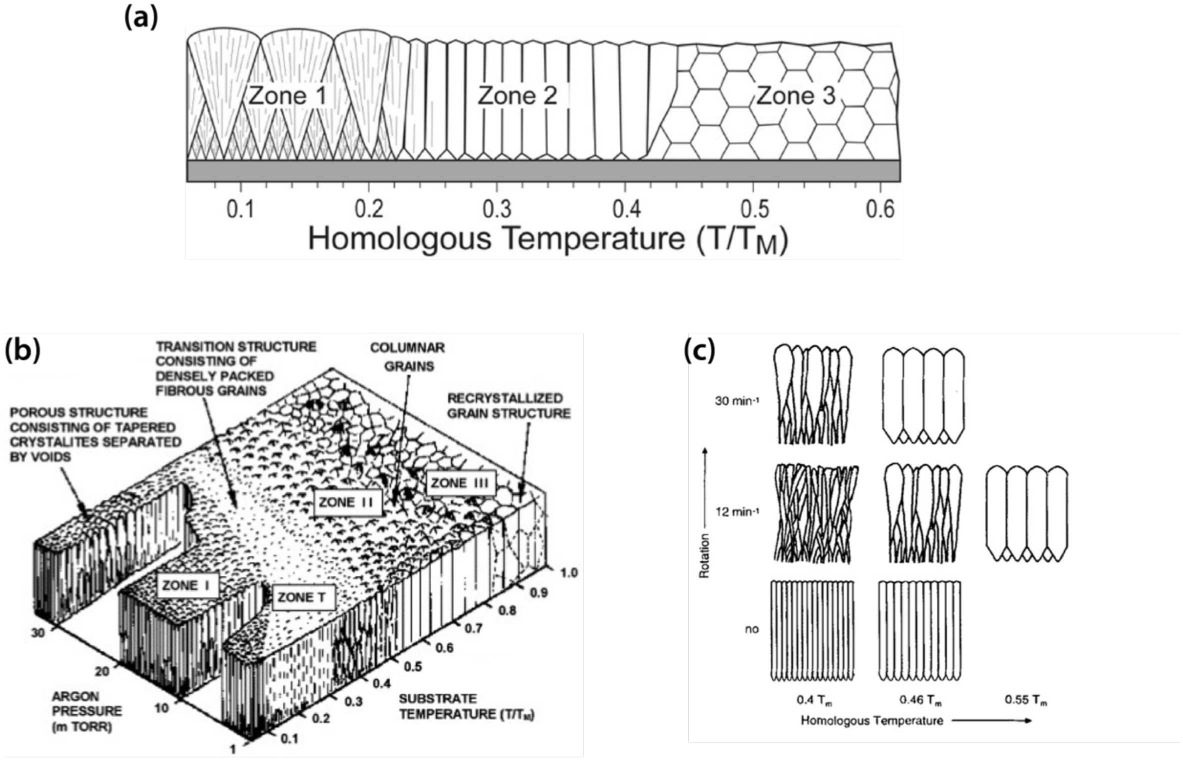

Figure 2.5: Illustrations of the (a) structure zone model relating homologous temperature to deposition microstructure for PVD coatings (adapted from [75]) and how changing process parameters such as (b) chamber pressure [77] and (c) substrate rotation[79] change the microstructure landscape and push the zone transition temperatures higher.

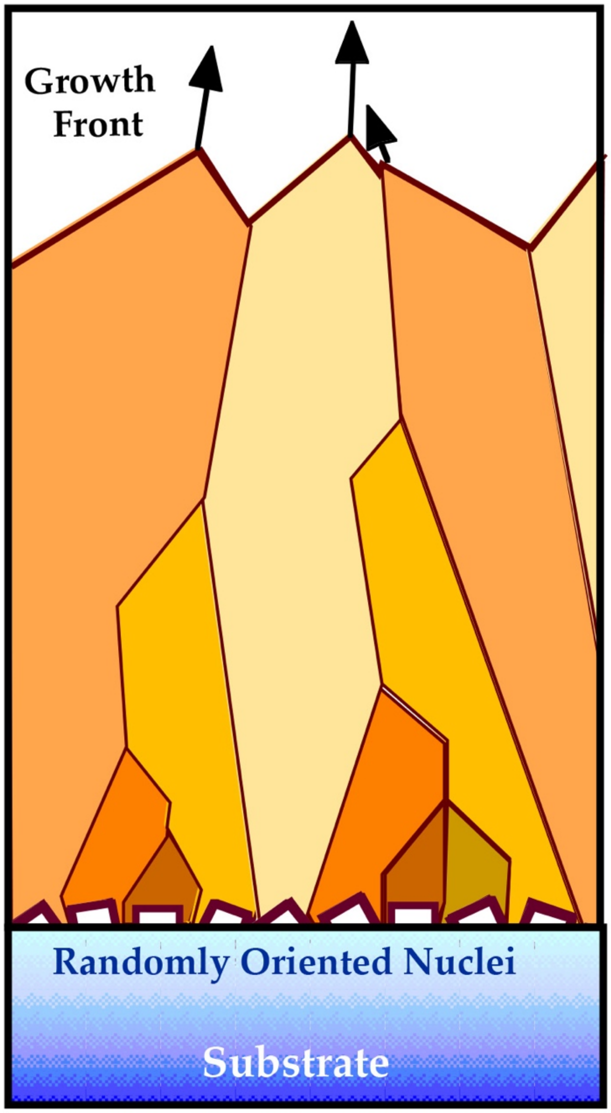

Figure 2.6: Schematic illustration of a coating growing with the evolutionary selection process. Nuclei initially deposit with random orientations, and favorable orientations with relation to the vapor flux crowd out others, leading to a highly textured coating out of plane. From Levi, adapted from [80]

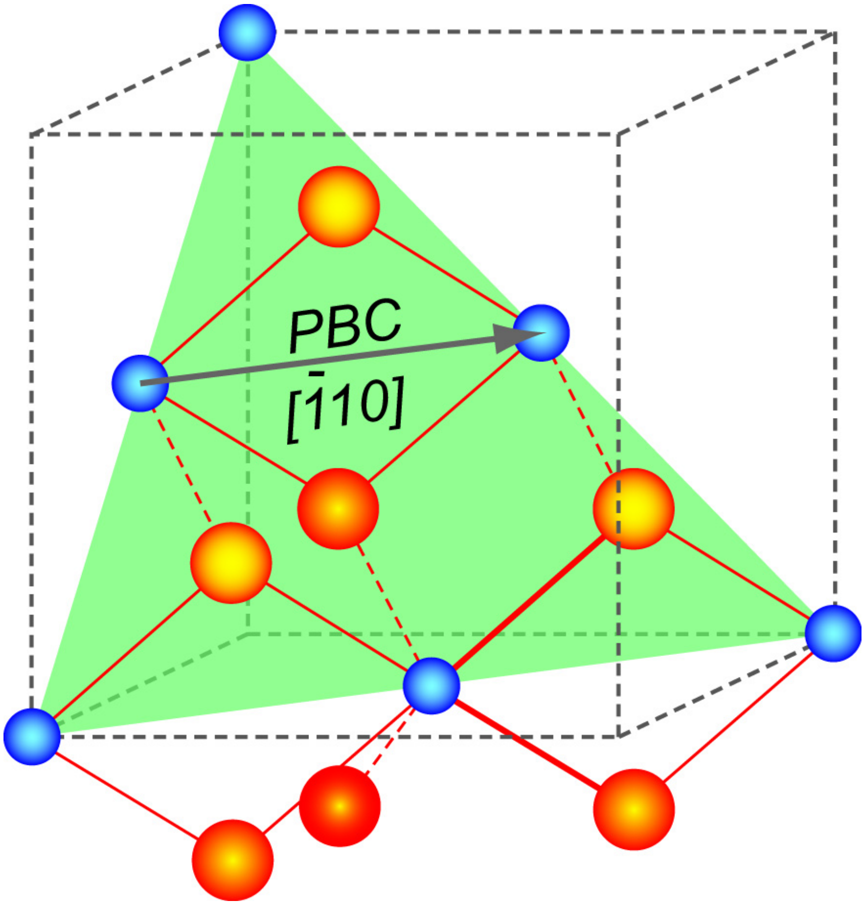

Figure 2.7: Illustration of the ⟨110⟩ periodic bond chain (PBC) direction in the fluorite structure, contained in a (111) plane. From [73].

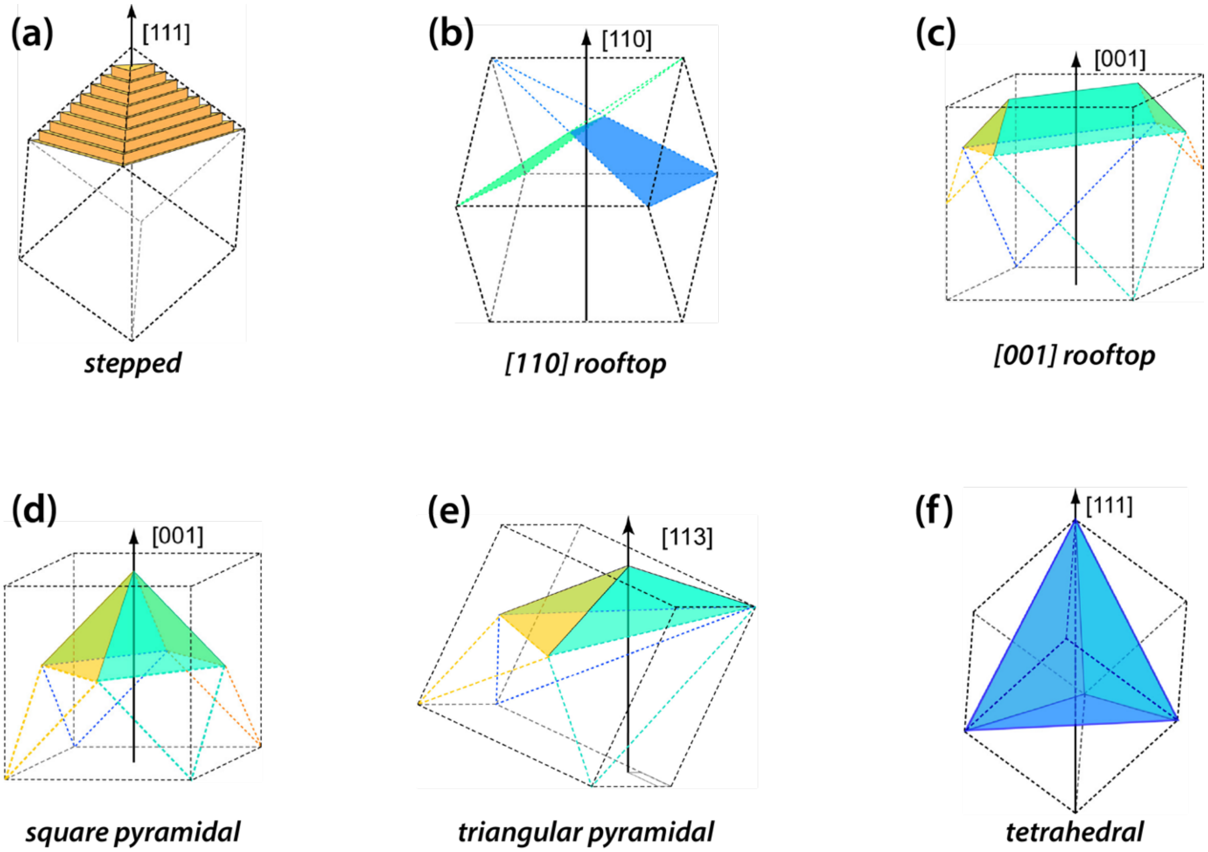

Figure 2.8: Examples of faceted column tip geometries with {111} faces corresponding to different growth directions, labelled (a) ’stepped’, (b) ‘[110] rooftop’, (c) ‘[001] rooftop’, (d) ‘square pyramidal’, (e) ‘triangular pyramidal’, and (f) tetrahedral. Adapted from [73].

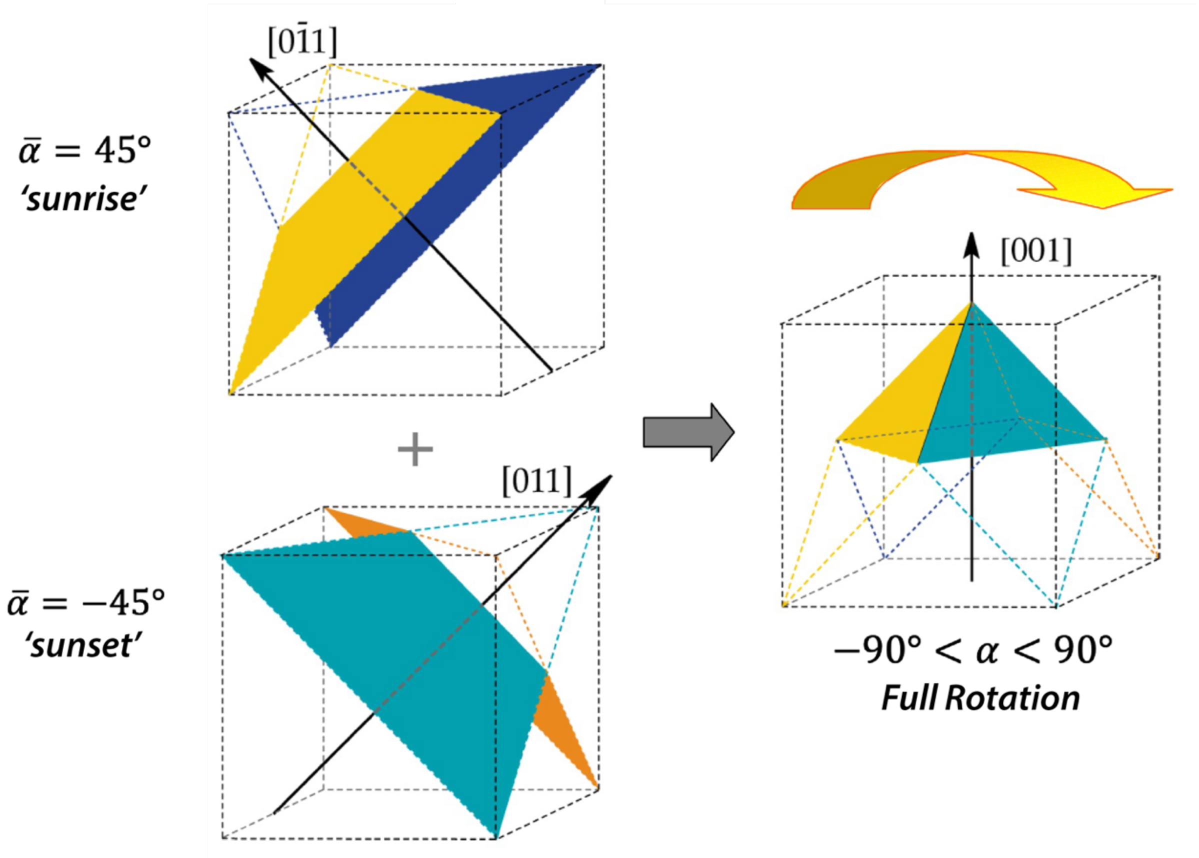

Figure 2.9: Illustration of how the square pyramidal [100] geometry forms in single axis substrate rotation. Two {110} directional 'rooftop' type tips corresponding to the 'sunrise', $\bar{\alpha}$ = 45°, and 'sunset', $\bar{\alpha}$ = -45°, segments of the vapor flux. The two rooftop type tips are each two faces of the square pyramidal tip. Adapted from [73].

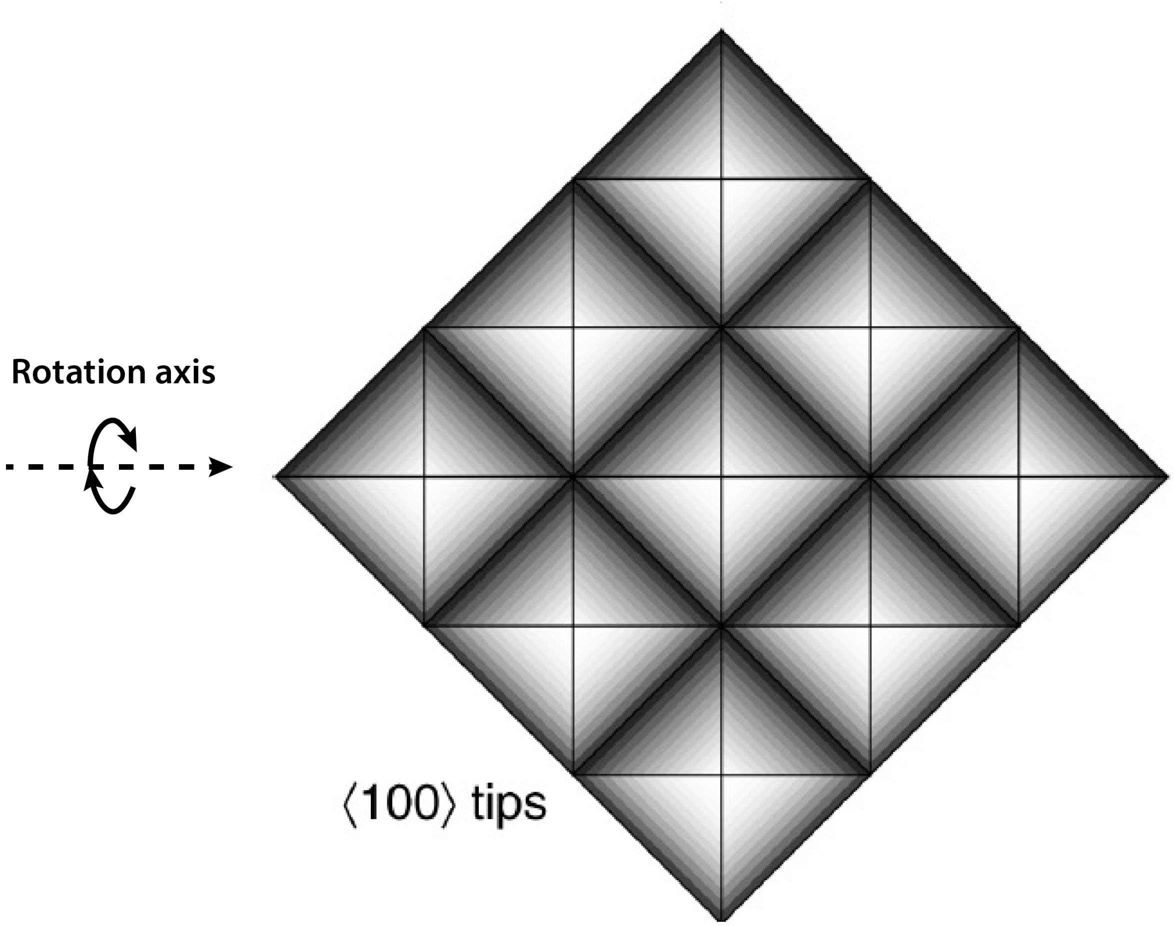

Figure 2.10: Top-down schematic of the alignment of square pyramidal ⟨100⟩ column tips in single axis substrate rotation, giving the coating a biaxial texture. Adapted from[73].

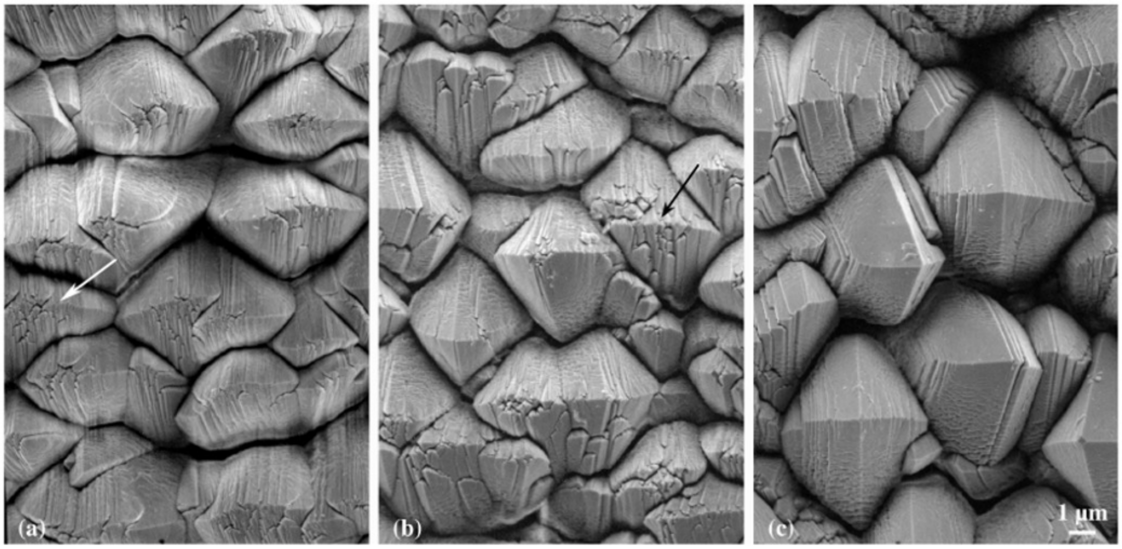

Figure 2.11: Column tips of EB-PVD grown 7YSZ at surface temperatures of (a) 900°C, (b) 1000°C, and (c) 1100°C. The axis of substrate rotation is parallel to the horizontal direction. The tips become sharper and less elongated as the surface temperature increases. From [73].

Chapter 3: Experimental Methods

The processing and assessment of thermal and environmental barrier coating (T/EBC) systems for OFCCs in this work involved an extensive experimental approach. OFCCs produced in industry were coated in-house by EB-PVD and tested by furnace cycling alongside specimens coated by APS in industry. Precursor processing was employed on uncoated OFCCs to improve interlaminar strength and durability under thermal cycling. Coating microstructures were analyzed and related to process parameters and coating performance. The equipment and characterization techniques that were used are described in this chapter, with additional information or techniques provided in subsequent chapters as necessary.

3.1 Materials supplied by industry and processing methods

3.1.1 Supplied uncoated OFCCs

Two generations of OFCC coupons were supplied by Siemens Corporate Technology for processing and coating at UCSB. Both generations were comprised of porous alumina matrices and N720 fibers. First generation composites were precut into 25 mm square coupons, 3.2 mm thick. The coupon surface was a smooth, with no surface structuring or exposed fibers, shown in **Figure 3.1 (a)**. In cross-section, presented in **Figure 3.1 (b)**, many large voids, upwards of 1 mm in length, were observed between fiber tows, in addition to visible poor matrix filling around fibers within the tows. Second generation composites were also precut into 25 mm square coupons but were thinner, at 2.7 mm in thickness. The coupons were left with a fabric imprint after processing on both surfaces, leaving a pattern of impressions each about 300 μm x 600 μm, with a depth of about 25 μm. The imprint pattern is seen on the surface in **Figure 3.1 (c)**. In cross-section, presented in **Figure 3.1 (d)**, there were similar large voids between some fiber tows, but about half the size, as well as similar instances of poor matrix filling around fibers within some tows. The pockets of porous alumina matrix between the tows were thinner in the second generation coupons. Overall porosity of the coupons was reported at about 25%. This porosity includes the fibers, meaning the matrix is more porous. The level of matrix porosity lends itself to increased densification by precursor infiltration.

3.1.2 Precursor solution preparation and calibration

Two compositions of precursor solutions were used for the matrix densification procedures. Alumina precursor solutions were made from dissolving $Al_2Cl(OH)_5 \cdot 2H_2O$ (Spectrum Chemical, Gardena, CA) in deionized (DI) water, until the desired concentration was reached. Yttria stabilized zirconia (YSZ) precursors were made from dissolving $Y(NO_3)_3 \cdot 6H_2O$ (Sigma Aldrich, St. Louis, MO) and zirconium(IV) acetate hydroxide (Sigma Aldrich) in DI water with a target final composition of 4 mol. % $Y_2O_3 – ZrO_2$. Volumetric yields of the precursor solutions were calculated from pipetting 10.0 ml of each solution into a pre-weighed 50 ml alumina crucible with a cap. The solutions were dried and the residue calcined, and the mass of each covered crucible was taken after pyrolysis. The mass of oxide left in the crucibles was converted to volume of oxide using the density of the relevant materials, and volumetric yield was calculated from the initial 10.0 ml of solution.

3.1.3 Precursor impregnation and pyrolysis

Following a procedure adapted from Mattoni [41], uncoated OFCC coupons were fully impregnated with precursor solution. This method is described schematically in **Figure 3.2**, with details elaborated below. Coupons were immersed in a glass dish of the alumina precursor solution, and the mass of the dish, solution, and coupons were taken together. The dish was covered with Parafilm (Beemis, Neenah, WI), and holes were poked into the film to accommodate some water evaporation out of the precursor solution. The covered dish was placed into a vacuum chamber, and vacuum was pulled down to 10-20 torr and held for 30 min. The dish was monitored, and vacuum would be reduced if aggressive boiling was observed. The dish was removed from the vacuum chamber after ~30 min, and the parafilm removed. The dish, solution, and coupons were weighed again, and any lost water mass was re-added with a dropper of deionized water. Impregnated coupons were placed under a heat lamp, such that only the corners or edges of the coupons were supported, and there was no surface in direct contact with back of the coupons. Coupons were dried under the heat lamp for at least 6 hours, before being moved to a furnace for pyrolysis, first heating to 550°C at 8°C/min and dwelling for 2 h, then heating to 900°C at 6°C/min and dwelling for another 2 hours, before ramping down in the furnace to room temperature at 10°C/min. This has described one PIP cycle. After the desired number of cycles, *N*, there was a final heat treatment of 6°C/min to 900°C, dwell for 1 h, and a final heating up to 1200°C, and anneal for 2 h, before ramping back to room temperature at 10°C/min.

3.1.4 Surface application of precursor solutions

A surface application method was developed to better realize a matrix density gradient without densifying deep into the composite, without limiting matrix crack deflection, and while having a reasonable processing timeframe. The technique is illustrated schematically in **Figure 3.3** and described in detail as follows. The precursor solution was applied to the surface of the composite coupons with a small camelhair brush in a painting motion to cover the entire surface of the coupon. The coat was allowed to sit for 5 minutes before the next was applied, with a total of 4 ‘coats’ per cycle. After the fourth coat, excess solution was wiped off the surface with a rubber glove. Painted coupons were suspended by their corners upside-down, about 5 mm over a hotplate set to ~100°C for 6 h before firing. The pyrolysis procedure was identical to the full immersion process described in the previous section. Coupons saw 4 cycles of this precursor application method.

3.1.5 EB-PVD

EB-PVD coatings for the OFCCs were deposited at UCSB using an in-house laboratory scale evaporator (Consarc, Inc., Rancocas, NJ), depicted in **Figure 3.4,** using ingots procured from TCI Ceramics, Inc. (Bethlehem, PA). Ingots of three different compositions, 7YSZ, $Y_4Zr_3O_{12}$, and Y_2O_3 were evaporated and films deposited on 25 x25 mm square OFCC substrates (Siemens Corporate Technology, Munich, Germany). The substrates were carefully surface ground with 800 then1200 grit SiC abrasive paper (Allied High Tech Products, Inc., Rancho Dominguez, CA) to remove asperities on the surface that would give rise to undesirable coating microstructures. OFCC substrates were secured to an alumina tube (McDanel Ceramics, Beaver Falls, PA) using refractory wire, either FeCrAlloy® (Goodfellow Corporation, Coraopolis, PA) or Chromel® (Omega Engineering, Inc., Norwalk, CT). The tube was mounted on a stage that allows for rotation above the evaporation source, heated by a cylindrical SiC heating element (I Squared R, Akron, NY) within the tube that heated the backside of the specimens by radiation.

Once the assemblage was in place the chamber was first evacuated to ~5 x 10^{-6} torr, before oxygen was introduced at a rate of 40 sccm to maintain a pressure of 5 mTorr. Substrates were then heated to either 1000°C or 1100°C, with temperature monitored in-situ by a two-wavelength pyrometer (Stratonics, Inc., Lake Forest, CA). The substrate heater assembly was mounted such that substrates were centered 18 cm above the evaporating source ingot, and rotated at 8 rpm during heating and deposition. The system operated with an electron beam accelerating voltage of 40 kV, and a beam power of 130-180 mA. Deposition rates varied from 0.3 – 2 μm/min depending on the material.

When performing bilayer depositions, source ingots were changed in-situ with an ingot switching device within the chamber below the hearth, detailed in **Figure 3.4** and designed for this project. The 7YSZ layer was deposited first, typically with thickness of 20-30 μm. The electron beam was powered down, but the specimen assemblage was kept at temperature to prevent thermally induced cracking on cooling. The source ingots were then switched, the electron beam powered back up, and a top layer of $Y_4Zr_3O_{12}$ or Y_2O_3 was deposited on the 7YSZ layer. In bilayer depositions where a denser interlayer was desired, 7YSZ was deposited without substrate rotation, then the rotation was started for the topcoat.

Y_2O_3 ingots often broke during initial preheating with the electron beam, in such a way that complicated or prevented ingot feed, rotation, and melting, and the deposition would need to be aborted. To prevent this type of catastrophic ingot cracking, a 5-10 mm thick 'cap' of Y_2O_3 ingot was placed on top of the ingot during loading prior to deposition. This cap did not crack, and would eventually melt and fuse to the rest of the ingot, and evaporation would run uninterrupted.

3.2 Coating durability testing

3.2.1 Furnace Cycle Testing in air

Thermochemical and thermomechanical stability were assessed using furnace cyclic testing (FCT) in lab air. A horizontal tube furnace (Lindberg/Blue M, Thermo Fischer Scientific, Waltham MA) illustrated in **Figure 3.5** was used with a programmable rail system powered by a stepper motor (Parker Compumotor, Petaluma CA) that inserted the specimen at a prescribed rate into the hot zone of the furnace for a set amount of time. A software program was used to control the speed in which the sample was moved in and out of the furnace to maintain a consistent heating and cooling rate. The system was able to run for several days uninterrupted. The thermal cycles had a dwell temperature of either 1200°C or 1300°C, a dwell time of 1 hour, a heating and cooling rate of 100°C/min, and an external, room temperature dwell of 3 minutes. A digital camera (Nikon D5100, Nikon USA, Melville, NY) was automated using software (Capture Control Pro 2, Nikon USA) and synchronized with the external dwell to automatically take an image of the specimen to monitor its condition after every cycle.

3.2.2 Furnace Cycle Testing in flowing water vapor

The performance of OFCC T/EBC systems in simulated combustion atmospheres was assessed by performing FCT in a high temperature, flowing water vapor environment. The set up used, specifically designed and built for this research, is depicted in **Figure 3.6**. A tube furnace (Lindberg/Blue M, Thermo Fischer Scientific, Waltham, MA) with a 3” outer diameter (OD) alumina tube (Coorstek, Golden CO), 32” in length, was mounted vertically with the tube standing on its own weight on an aluminum baseplate, sealed with a mica gasket. A second, smaller alumina tube, 2” OD, was suspended above the furnace, and positioned in the center of the larger tube. This tube contained the reactant atmosphere. A peristaltic pump (FH 100, Thermo Fischer Scientific, Waltham, MA) fed DI water at 8 ml/min, and dry lab air at 1.42 L/min was fed into a 3 kW steam generator (Infinity Fluids, Worcester, MA) set to a temperature of 320°C, the outlet of which was routed to the inner tube above the furnace. This mixture of 10% air and 90% superheated steam flowing down the inner tube was the environment used for testing. Simultaneously, dry lab air was fed at 30 14.2 l/min into a second 1kW steam generator (Infinity Fluids, Worcester, MA) set to 300°C, which served to preheat the lab air. This air was directed to a stainless-steel flange that directed the flow to the annular region between the outer and inner tubes. This air was necessary to direct the reactant atmosphere through the effluent flow at the bottom of the furnace. The flange also served to cap the top of the outer alumina tube. When fully inserted, the specimen sat normal to the vapor flow atop a stage made from rigidized (Cotronics, Brooklyn, NY) zirconia foam (Zircar, Florida, NY) on a third alumina tube, 1.5” OD within the inner, 2” OD tube. This small tube was secured to a steel plate that seals with the bottom of aluminum baseplate with a silicone gasket. A hole in the bottom of the steel plate allowed for effluent flow of both the water vapor reactant atmosphere and the lab air. The sample support tube and stainless-steel seating were fixed to a programmable stepper motor (Haydon Kerk Pittman, Waterbury CT) and rail system to allow for automatic insertion and removal from the furnace. A type-B thermocouple (Omega Engineering, Inc., Norwalk, CT) was suspended from the top to monitor the interior furnace temperature, referred as the “flow TC” and a second type-B thermocouple was in contact with the back of the composite sample, wired through the sample support tube, referred as the “sample TC.” When fully removed, the specimen sat about 10 cm below the baseplate.

The typical thermal cycle involved a dwell temperature of 1200°C as read by the suspended thermocouple, with an insertion and extraction time of 13.5 min, for a heating and cooling rate of ~87°C/min. The dwell at temperature was 30 min, and the external dwell was 3 min, for a total cycle time of 60 min. Dwell time was shorter than the lab air FCT experiments to have more thermal cycles in a shorter experimental time.

3.3 Characterization techniques

3.3.1 Preparation of specimen cross-sections

Specimens were sectioned using a slow speed saw (TechCut 4, Allied High Tech Products, Inc., Rancho Dominguez, CA) using a Low Concentration Diamond Metal Bond wafering blade, with deionized water used as cutting lubricant. Cut samples were dried for at least 30 minutes under a heat lamp prior to evaporate any adsorbed water prior to epoxy infiltration. Due to the porous nature of the EB-PVD coatings and the OFCC specimens, samples were double mounted in epoxy (EpoxySet), such that they were infiltrated, sectioned again, and the cut surface embedded in epoxy a second time. The goal was to minimize material pull-out on subsequent polishing of the porous OFCCs and coatings. Specimens were polished down to 0.25 μm diamond slurry (Allied High Tech Products, Inc.) for microscopic examination. Cross-sections mounted in epoxy were sputtered Au/Pd for 90 s for conductivity prior to examination.

3.3.2 Scanning Electron Microscopy

Coating microstructure observations and general specimen cross-section imaging were conducted using scanning electron microscopy (SEM) on a FEI Nova Nano 650 FEG SEM (FEI, Hillsboro, OR) and an Apreo C SEM (Thermo Fischer Scientific, Waltham, MA). Secondary electron imaging (SEI) and back-scattered electron imaging (BSEI) were conducted on both microscopes. Chemical analysis was performed by electron energy dispersive spectroscopy (EDS) within the Apreo C with an AMETEK EDAX system. (Berwyn, PA). The EB-PVD coating surfaces were imaged without a sputtered conductive coating, so samples could be used in future experiments. To prevent charging, Low accelerating voltage and beam current were used, 2 kV and 25 pA, respectively.

3.3.3 Transmission Electron Microscopy

Lamellae for transmission electron microscopy (TEM) were extracted using focused ion beam (FIB) in a Helios Dualbeam Nanolab 600 (FEI). Transmission electron microscopy was performed using a 200kV Tecnai G2 Sphera (FEI) for brightfield imaging and compositional analysis. A FEI Titan 80-300 kV FEG TEM/STEM microscope with a spherical aberration corrector for the objective lens were used for high-resolution work involving bright field, high angle annular dark field (HAADF), and scanning tunneling electron microscopy (STEM) imaging and diffraction analysis. A Thermo Fisher Talos G2 200X TEM/STEM was used for high resolution EDS and mapping. (Assisted by Drs. Daesung Park and Megan Emigh)

3.3.4 Dilatometry

The bulk, linear coefficient of thermal expansion (CTE) of OFCC specimens was measured using a push-rod type Orton 2016 HU differential dilatometer in lab air. A 25 mm alumina rod with 9.5 mm diameter was used as a standard. 25 mm x 6 mm x 3 mm bars of OFCC, as well as pieces of EB-PVD ingot 25 mm in length and roughly 5 mm in cross section were characterized. Samples were measured in a temperature range of 30°C-1300°C with a heating and cooling rate of 3°C/min. The mean CTE for a given temperature interval is calculated using:

$$\alpha_{\mathrm{mean}} = 1/\mathrm{L}_0 * (\Delta\mathrm{L}/\Delta\mathrm{T}) \qquad \textbf{3.1}$$

where L_0 is the length of the bar at the reference (ambient) temperature, ΔL is the change in length from ambient to the temperature of interest, and ΔT is the difference between the temperature of interest and ambient temperature.

3.3.5 X-ray diffraction

Phase analysis was conducted by standard x-ray diffraction techniques on sample surfaces (Empyrean Powder Diffractometer, PANalytical, Westborough, MA). Phases were identified with comparison to published powder diffraction data (ICCD PDF-4 database). A goniometer was used to scan reciprocal space, typically from $2\theta = 14°$ to $90°$ with a step size of 0.013° and 15 min scan time.

3.3.6 Pole Figures

EB-PVD coating texture was characterized by collecting pole figures using a diffractometer capable of rotating in Φ (phi, in-plane) and φ (psi, out-of-plane) (Hypix 2000, Rigaku, Tokyo, Japan). A step size of 1° was used for Φ, and a step size of 2.5° was used for φ. Total scan time was 45 minutes. Various peaks were used to gather both in-plane and out-of-plane texture information.

3.4 Figures

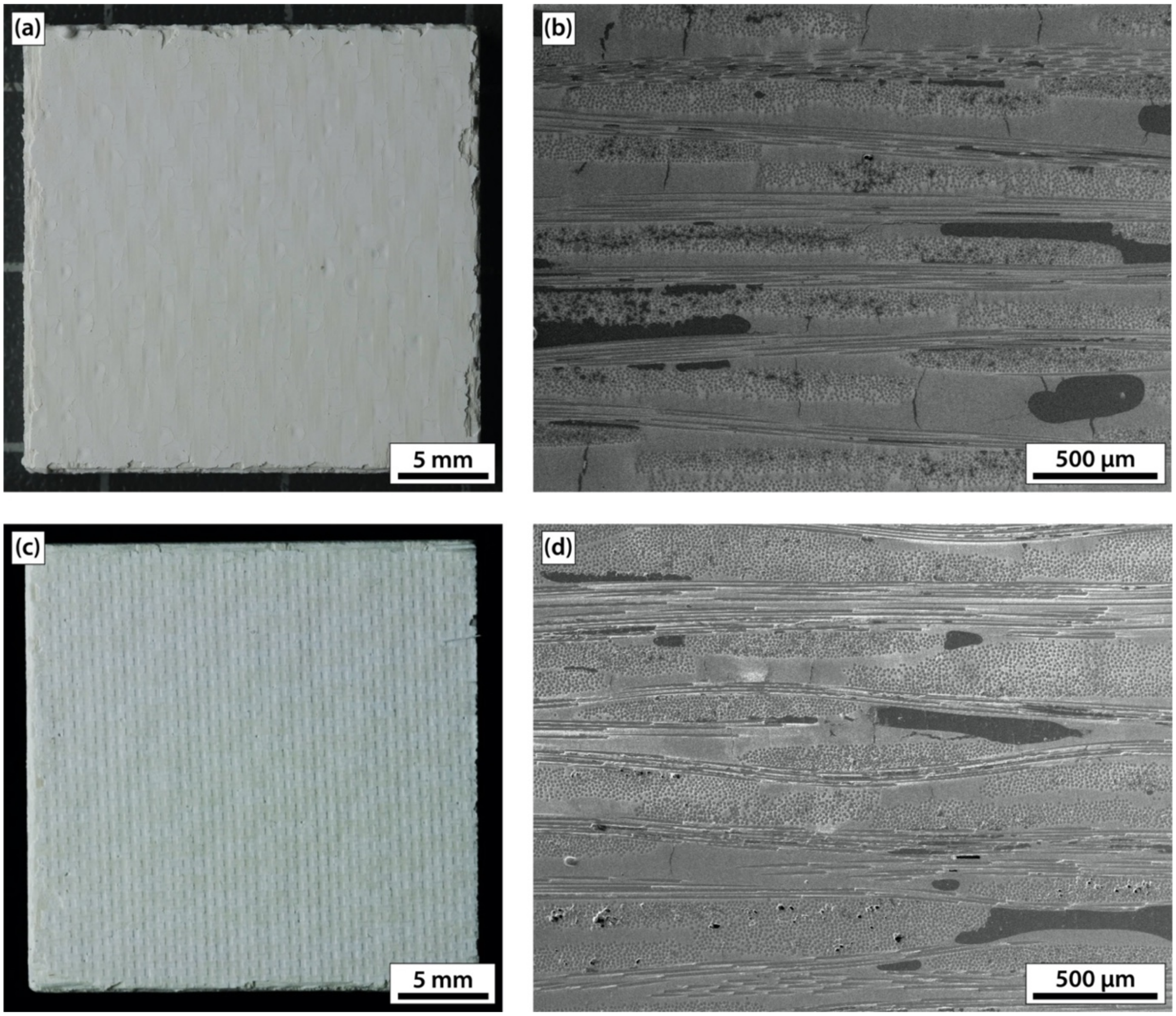

Figure 3.1: Two generations of as-received composites from Siemens. First generation coupons have a smooth surface, seen by optical imaging (a), and in cross-section (b) many large voids are visible between fiber tows, as well as some poor matrix filling between fibers within the tows. Second generation composites have an surface imprint in the matrix leftover from processing, visible in the optical image in (c) and the cross-section in (d) also reveals large inter-tow voids and pockets of poor matrix filling within the tows. Matrix pockets between fiber tows are smaller in the second-generation composites.

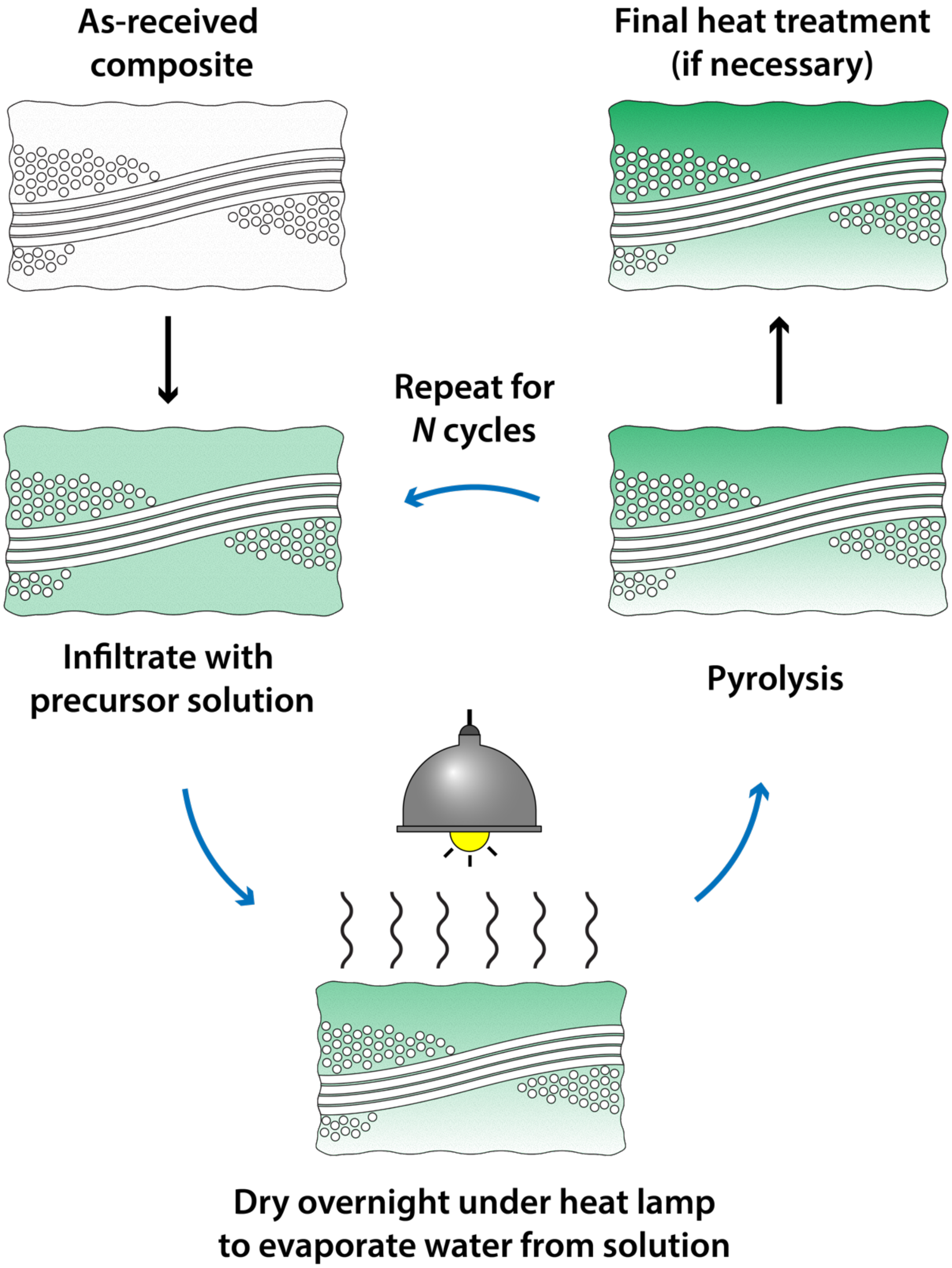

Figure 3.2: Schematic description of the full impregnation PIP process for OFCC matrices

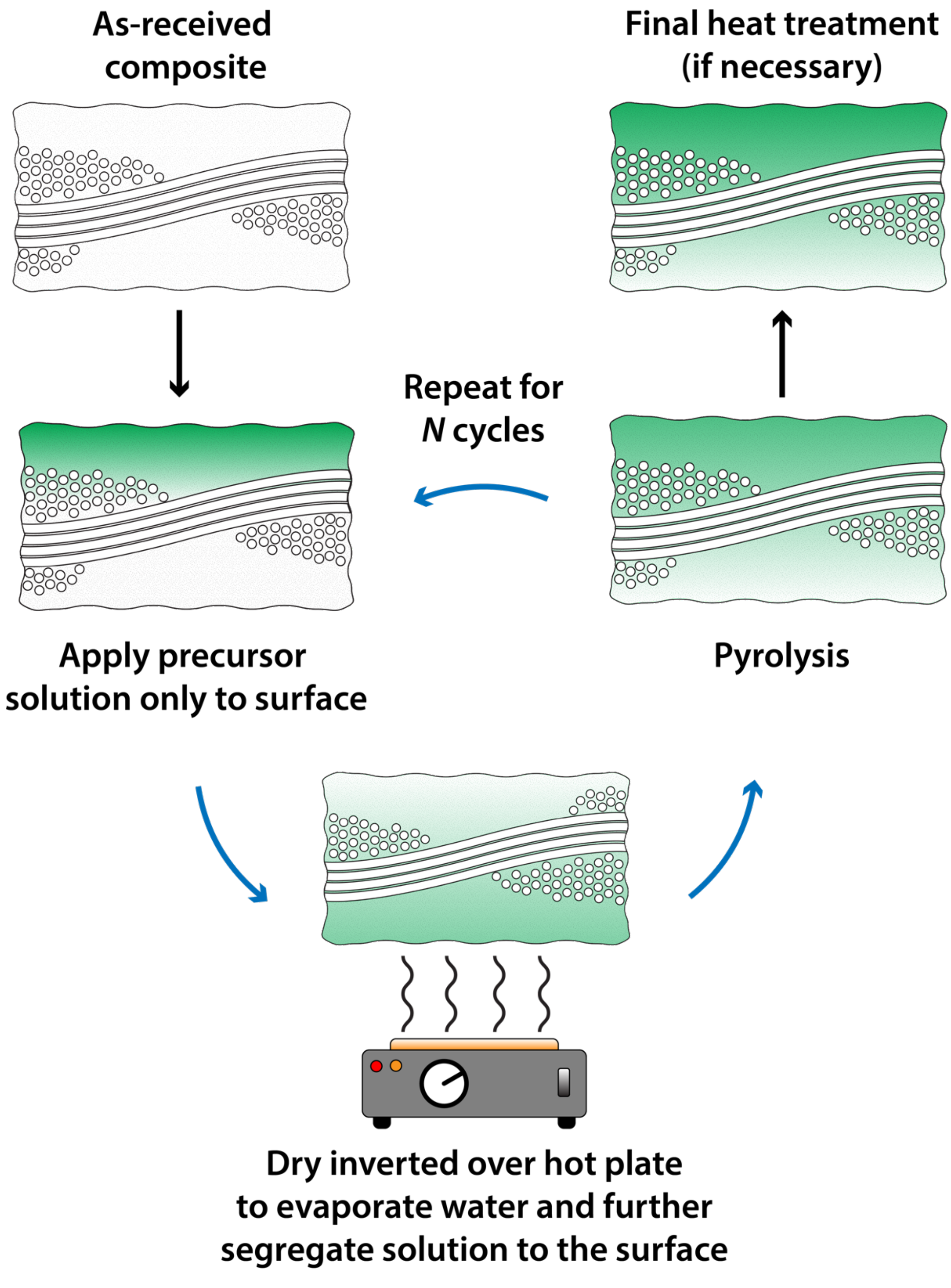

Figure 3.3: Schematic depiction of the surface application, "painting" PIP technique for OFCC matrices.

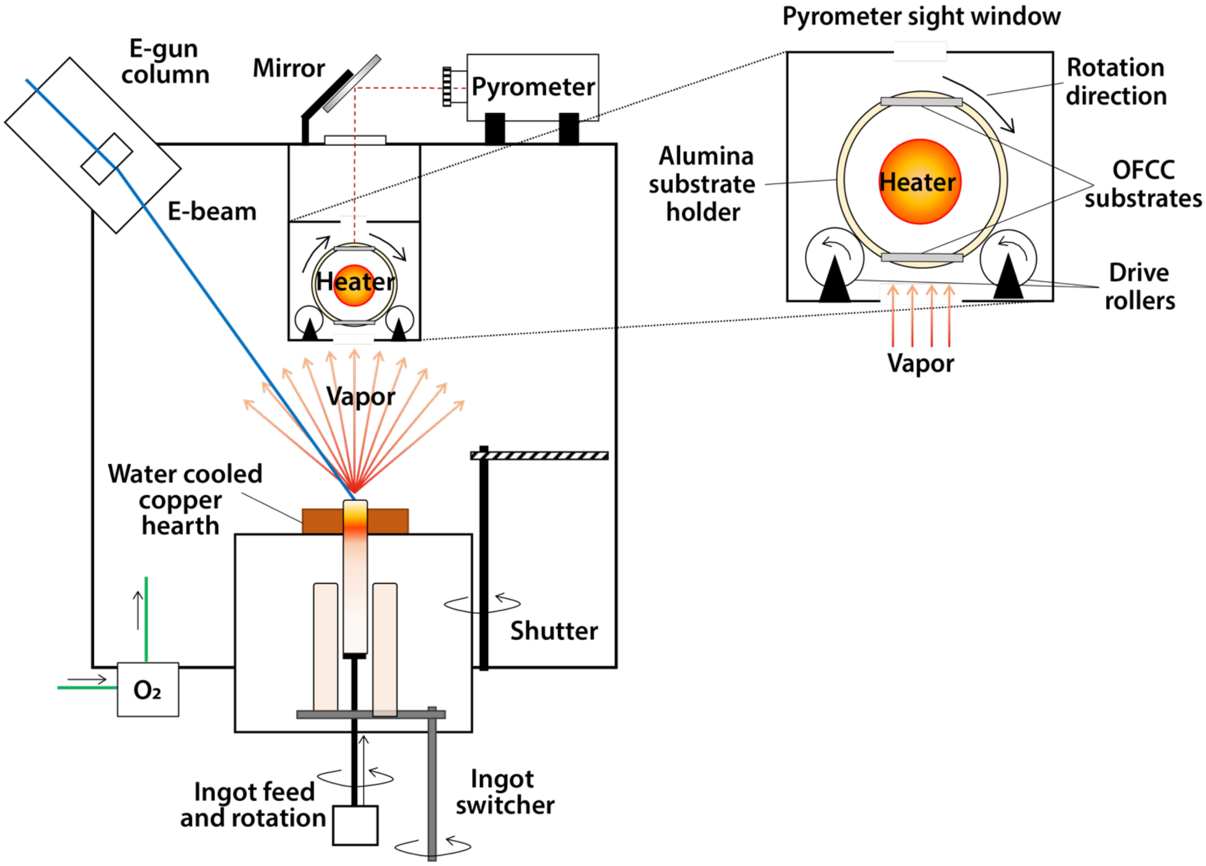

Figure 3.4: Schematic of the UCSB EB-PVD apparatus configured for deposition on rotating substrates and in-situ source ingot switching, with inset highlighting the substrate heater assembly.

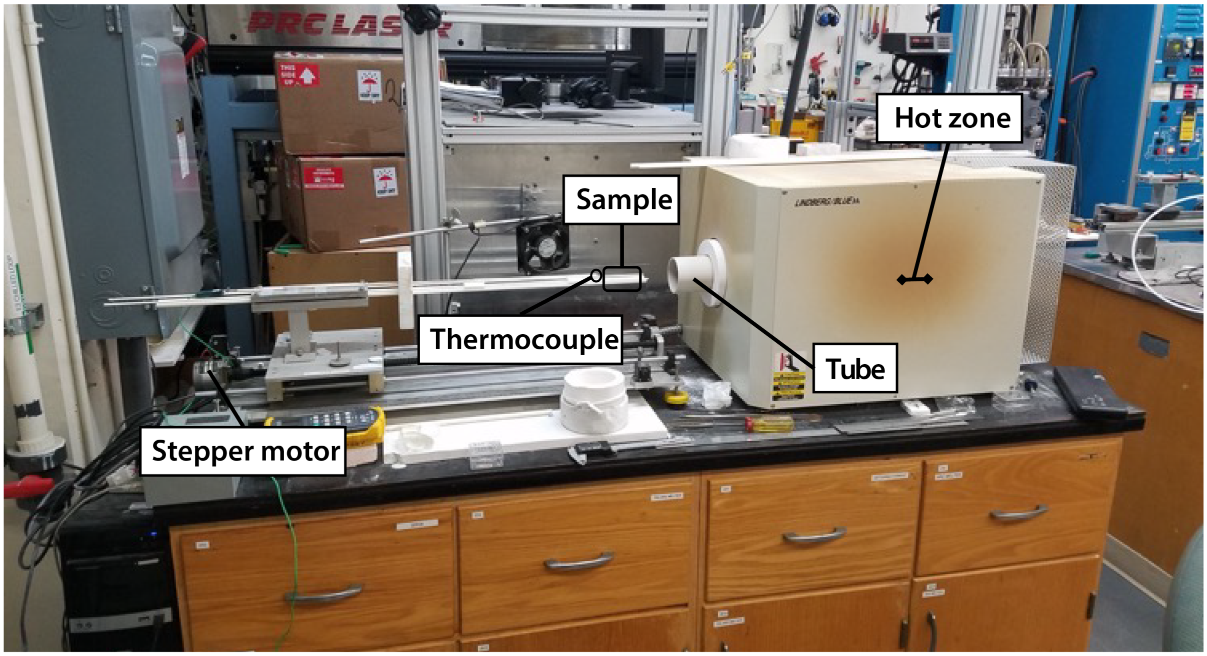

Figure 3.5: Image of the automatic thermal cycling furnace at UCSB with important components labelled.

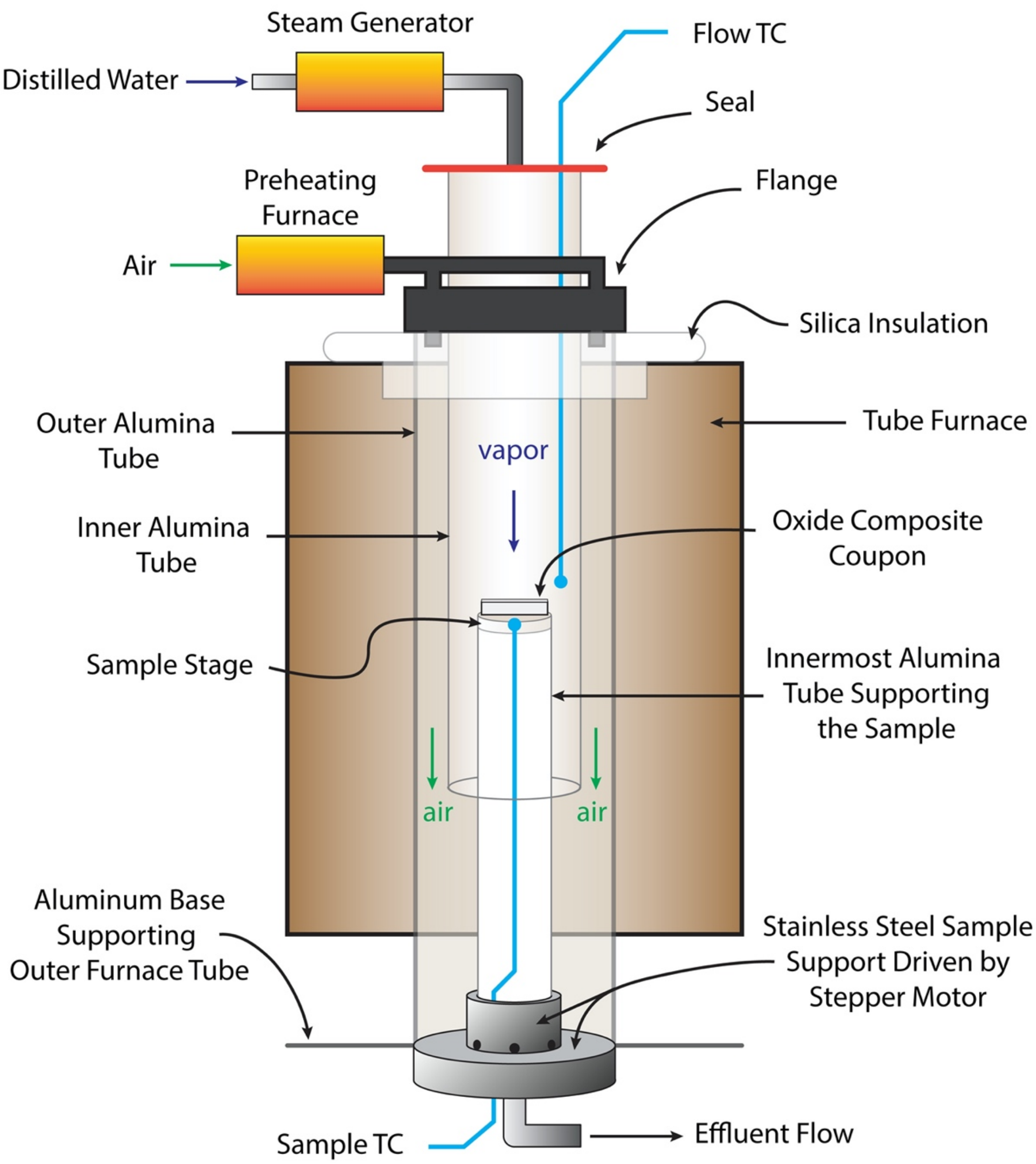

Figure 3.6: Schematic of the high temperature water vapor rig at UCSB with important components labelled.

Chapter 4: Furnace Cycle Testing of Coated OFCC's

Creating protective coating systems for oxide fiber ceramic composites (OFCCs) poses unique challenges when compared to other turbine engine materials, such as SiC -based composites and metallic superalloys. The thermal expansion coefficient (CTE) of the constituent materials, viz. alumina (8 ppm/°C) [88,89] and alumina/mullite N720 fibers (6 ppm/°C) [36], are substantially different from that of SiC-based ceramic composites (~4.5 ppm/°C) [90] and metallic superalloys (15+ ppm/°C) [91], as well as the industry standard thermal barrier oxide, 7YSZ (12 ppm/°C) [92], New coating materials are clearly needed for OFCCs to minimize CTE mismatch, or compliant coatings would need to be engineered to mitigate the effects of thermal stresses between the coating materials and the composite. Thermochemical compatibility between the coating and OFCC is also essential for the long-term performance of components. As noted in **Chapter 2**, atmospheric plasma spray (APS) is a favored technique for the deposition of protective coatings on gas turbine components. However, adhesion of APS coatings can be an issue, especially under thermal cycling and when coating porous substrates, such as the OFCCs matrices of interest to this dissertation. Electron-beam physical vapor deposition (EB-PVD) offers an alternative to circumvent some of these problems as candidate coating materials adhere well to alumina at the deposition temperatures [93]. In this chapter the performance and limitations of APS coated OFCCs will be assessed by furnace cyclic testing (FCT) experiments, both in air and water vapor, and compared to similar experiments on EB-PVD coatings deposited on similar OFCCs.

4.1 Materials Tested

4.1.1 APS coated OFCCs

As noted in **Chapter 3**, Siemens corporate technology supplied two plates of N720 fiber ($85\%Al_2O_3$-$15wt\%SiO_2$) [36] porous alumina matrix OFCC, about 3 mm thick and 50 mm square. Both plates were APS coated, with the coating composition differentiating the two samples, designated 'Gen1-234' and 'Gen1-237.' Both were sprayed with about 1 mm of 48 wt.% Y_2O_3 stabilized ZrO_2 (48YSZ or $\sim Y_{0.5}Zr_{0.5}O_{1.75}$) with Gen1-234 having a 100 µm interlayer of co-deposited 48YSZ + Al_2O_3, and Gen1-237 having a 100 µm interlayer of 7YSZ. The OFCC surface was laser patterned prior to coating deposition in both plates. The purpose of the laser patterning was to provide a tailored surface topology for mechanical interlocking of the deposited coating. The samples were sectioned by slow speed diamond saw into 25 mm square coupons for testing and analysis. Schematics of the sectioned samples are shown in **Figure 4.1 (a)**.

Second generation OFCC samples, designated 'Gen2,' were also based on N720 fiber with a porous alumina matrix. The plates were about 2.7 mm thick and precut into 25 mm square coupons. Gen2 samples were sprayed with a monolayer of about 500 µm of APS 7YSZ. The composite surface was also laser patterned prior to spraying. Schematics of the Gen2 samples are shown in **Figure 4.1 (b)**.The patterning was more pronounced than Gen1-234 or Gen1-237, with a coarser pattern of laser ablation as shown in **Figure 4.2**. Gen1 samples have a pattern with troughs every ~200 µm that are ~60 µm deep. Gen2 samples had a pattern with troughs every ~400 µm that are ~200 µm deep. While the fibers and matrix materials of the two generations of samples were the same, processing of Gen2 composites differed from the previous samples. The plates were thinner, and there were a greater number of large inter-tow voids in the Gen2 plates. **Figure 4.2** also highlights the difference in the matrices of the two generations of supplied composite samples. Details of the OFCC manufacture were proprietary.

4.1.2 EBPVD coated OFCCs

Uncoated OFCC coupons, precut into dimensions of 25mm x 25mm x 3mm, were supplied by Siemens. These composites were similar to the supplied Gen2 composites with porous alumina matrices and N720 fibers, but without the APS coatings or surface structuring. Two of these coupons were coated with a monolayer of 7YSZ using the in-house evaporation system at UCSB, described in detail in **Chapter 3**. No additional surface preparation was performed on the composite coupons prior to deposition, but surface modification alternatives are explored in **Chapter 5**. Targeted surface temperature on deposition was 1100°C (measured at 1085°C), and coatings were 240 μm in thickness. Details on the EB-PVD process and apparatus were described in **Chapter 3.**

4.1.3 Furnace Cyclic Tests (FCT)

Thermochemical and thermomechanical stability of the supplied APS coating systems were first assessed using furnace cyclic testing (FCT) in lab air. A horizontal tube furnace was set up with automatic thermal cycling capabilities. Hot zone temperatures of 1200°C and 1300°C were chosen as they are considered realistic OFCC component temperatures for industrial gas turbine operation. During one cycle, coupons were inserted such that the heating rate experienced was about 100°C/min, and held at the prescribed temperature for 1 hour. Coupons were removed at the same rate as insertion, and when completely out of the tube furnace, held for 3 minutes with cooling assisted by a small fan to return the specimen to room temperature before the next cycle. The FCT runs were stopped after 100 cycles, and 100 h at peak temperature. A more detailed description is given in **Chapter 3.**

To assess the performance of the different coated OFCCs in simulated combustion atmospheres, FCT experiments on a subset of coated specimens, a Gen2 sample and an EB-PVD sample, were also undertaken in a flowing water vapor environment. Details of the furnace apparatus and operation have been described previously in **Chapter 3**. Specimens were subjected to 30 cycles, each with a 30 min. dwell at 1200°C, for a total time at temperature of 15 hours.

4.2 Results

4.2.1 FCT of first generation APS specimens

First generation OFCC coupons, samples Gen1-234 and Gen1-237, were subjected to FCT in air at 1200°C and 1300°C. At 1200°C, samples exhibited delamination cracking along the entire cross section, as well as some channel cracking through the thickness of the coating. There was no clear difference in the cracking seen in Gen1-234 and Gen1-237, suggesting the different interlayer compositions have no effect on coating performance at comparable number of cycles. Edge-on optical images in **Figure 4.3 (a)** and **(b)**, as well as cross-section SEM micrographs, presented in **Figure 4.3 (c)** and **(d)**, show much of the delamination cracking in the two samples occurs *below* the coating/matrix interface, often cutting through or propagating below the patterned composite surface.

At 1300°C, similar types of cracking were observed as at 1200°C, but the delamination was more severe. Delamination was extensive in both Gen1-234 and Gen1-237, seen by the edge-on optical images in **Figure 4.4 (a)** and **(b)**, with the different interlayer composition having no impact on coating performance. The cross sections in **Figure 4.4 (c)** and **(d)** show cracking initiating at the edges and propagating within the composite, below the coating interface. As at 1200°C, the delamination cracking occurred within the composite matrix, below the coating/composite interface. Despite the extensive cracking, the coatings did not spall.

4.2.2 Interlayer interactions in first generation specimens

While the difference in interlayer materials did not seem to impact the thermomechanical performance, there are concerns about the thermochemical stability of the materials in the interlayer of sample Gen1-234. The high yttria content of the 48 YSZ topcoat raises concerns of reactivity with the alumina and mullite constituents the of the interlayer and composite. The simultaneously sprayed interlayer of sample Gen1-234 not only has 48YSZ in direct contact with alumina within the interlayer, but also in contact with the composite matrix and N720 fibers because of the surface patterning, seen in **Figure 4.2 (a)**. After FCT at both 1200°C and 1300°C there was visible interaction between the APS 48YSZ and alumina within the interlayer, as well as interactions with the alumina matrix and N720 fibers. Cross-section backscattered electron (BSE) images in **Figure 4.5 (a)** and **(b)**, illustrate the aforementioned interactions, which are far more extensive at 1300°C. Reaction phases are visible within the APS 48YSZ layers of the interlayer, and within fibers that were in contact with APS 48YSZ. No reaction phases were observed within the APS alumina layers of the interlayer or the alumina matrix in contact with APS 48YSZ. In contrast, sample Gen1-237 with a 7YSZ interlayer revealed no reactions between coating materials and composite constituents, as illustrated in **Figure 4.5 (c).**

Closer examination of the reacted fibers after the 1300°C testing, in **Figure 4.5 (b),** shows a layer of reaction product at the interfaces of 48YSZ and N720 fibers, as well as distinct new phase within the fibers themselves. Additionally, extensive grain growth is visible in the reacted fibers. Analysis of the reaction phases was performed using TEM EDS. A lamella was lifted from the cross-section using FIB, and thinned for TEM imaging and microchemical analysis. **Figure 4.6 (a)** shows the location of the lamella liftout, which was chosen to capture the reaction phases within the APS 48YSZ, at the interface of the APS 48YSZ and an N720 fiber, and the reaction phases and grain growth within the N720 fiber. TEM EDS analysis of the lamella is presented in **Figure 4.6 (b)**. The chemical composition of the reaction phase within the 48YSZ, and at the interface with the APS alumina or alumina matrix, was consistent with $Y_3Al_5O_{12}$ (yttrium aluminum garnet, YAG). Within the fiber, and at the interface between the fiber and the 48YSZ the reaction phase analysis suggests it is $Y_2Si_2O_7$ (yttrium disilicate, YDS), and the large grains in **Figure 4.6 (b)** are coarsened alumina. This is shown in **Figure 4.7**, with the relevant phases labelled on the inset of the micrograph from **Figure 4.5 (b)**.

4.2.3 Behavior of Gen2 APS specimens after 1200°C FCT

Gen2 samples were tested only at 1200°C, with an identical FCT schedule. From the edge-on optical image (not cross-section) in **Figure 4.8 (a)**, the Gen2 sample showed far more damage than the first generation Gen1-234 or Gen1-237. There is extensive cracking in the matrix, even up to 1mm below the coating interface. The APS coating also began to spall on one side, leaving the laser surface imprint visible in the separated coating, seen in the inset in **Figure 4.8 (b)**. However, the coating remained attached to the substrate and did not spall.

4.2.4 As-deposited EB-PVD microstructure

EB-PVD coatings remained well adhered upon cooling from the deposition temperature of 1085°C. However, cross-sections viewed under SEM revealed numerous vertical penetrating cracks in the EB-PVD coating, as illustrated in **Figure 4.9 (a)**. Many of these vertical cracks initiated at pre-existing cracks and gaps on the matrix surface of the OFCC substrate, as evident by the presence of deposited 7YSZ inside the crack. Moreover, the cracks are widest at the coating interface, and get narrower going to the coating surface and into the composite. There was no sign of decohesion of the coating from the porous matrix on the composite surface, illustrated by the higher magnification image in **Figure 4.9 (b)**. A complete analysis of the coating microstructure, texture, and growth behavior is out of the scope of this chapter and is presented in **Chapter 6**.

4.2.5 Water vapor effects on thermal cycling of EB-PVD and Gen2 APS coated OFCCs

The water vapor exposures were performed on two coupons, one coated with Gen2 7YSZ and the other with EB-PVD 7YSZ. After 30 cycles, the APS sample showed delamination cracking on all edges, two of which shown in optical images in **Figure 4.10 (b)** and compared with the pristine condition in **Figure 4.10 (a)**. SEM imaging of polished cross-sections in **Figure 4.11 (a)** and **(b)**, show delamination cracks initiating at the edges and propagating into the matrix below the coating/composite interface. Images near the center in **Figure 4.11 (c)** and **(d)**, revealed several vertical penetrating cracks in the APS coated sample.

Optical inspection of the EB-PVD sample presented in **Figure 4.12**, revealed no significant damage after cycling, in contrast with that found in the APS specimen. There was no visible difference between the as-deposited condition in **Figure 4.12 (a)** and after cycling in **Figure 4.12 (b)**, or any observable damage on the coupon edges in **Figure 4.12 (c).** The cross section in **Figure 4.13** exhibits multiple channeling cracks penetrating the coating into the matrix. However, there is no noticeable increase in the number density of these cracks from that in the as-deposited condition in **Figure 4.9**. There was also no sign of delamination or spallation at the matrix/7YSZ interface after cycling. However, some of the channel cracks penetrating the composite in **Figure 4.13** appear to have grown during the thermal cycling and kinked into the fiber tows. These could potentially lead to delamination at larger number of cycles.

4.3 Discussion

4.3.1 Delamination cracking calculations

Some quantitative calculations are useful for providing additional insight into the observed results of the FCT experiments. The software package "LayerSlayer" developed by Dr. Matthew Begley and his group at UCSB, was used to generate a few basic calculations for the stresses and energy release rates (ERR) for delamination cracking in the coating systems tested in this Chapter. Some assumptions were made to simplify the calculations: the specimens 'Gen1-234' and 'Gen1-237' were simplified to a 1.1 mm thick 48YSZ monolayer, the Poisson's ratio for all materials is assumed to be 0.2, the Young's modulus for all coating materials is 40 GPa, and the OFCC substrate is 3.0 mm in all cases. **Table 4.1** lists the relevant properties of each layer. Presented in **Figure 4.14** are the stresses and ERR for delamination cracking in the coating and OFCC substrate upon cooling to 20°C from an assumed stress-free state at 1200°C, the hot zone temperature of the FCT experiments.

In all three cases, both the maximum stress and ERR occurred at the interface between the T/EBC material and the OFCC substrate. The stresses in the coating are tensile, as each of the coating materials has a greater CTE than the substrate and will try to shrink more than the OFCC substrate on cooling. However, delamination cracking was observed experimentally within the OFCC below the interface in the APS coatings, and not observed at the interface in the EB-PVD coating. This suggests there are factors contributing to the cracking that are not captured by the assumptions in the calculations, such as the poor strength of the porous matrix, voids in the composite matrix, residual stresses from the surface patterning in the APS specimens, the increased adhesion and provided by said surface patterning, and the microstructural differences in the columnar EB-PVD coating. However, the calculations do show that the ERR for delamination cracking increases within the composite substrate as one moves closer to the coating interface. While the maximum ERR is at the interface, the ERR in the composite could be such to initiate cracking in regions of the composite with localized residual stresses or flaws. Additionally, these calculations do not account for the channel cracking after deposition in the EB-PVD coating, which would lower the net elastic modulus for that sample, and further lower both the stresses and ERRs for delamination.

4.3.2 Thermal cycling in air

Damage resulting from cycling of the first generation OFCCs was far more extensive at 1300°C than at 1200°C, as expected from the larger temperature excursion and ensuing thermal strain. There is a comparatively moderate CTE mismatch between the 48YSZ topcoat (9-10 ppm/°C) [94] and the alumina/N720 OFCC (6-8 ppm/°C) [51,95]. Given the thickness of the coating—upwards of 1 mm or about 1/3 of the OFCC substrate—it is not surprising to find more severe cracking at the higher temperature. Despite the extensive cracking, however, the coatings did not spall. This is arguably a consequence of the surface patterning on the composite, intended to serve as anchor points for adhesion of the APS coating. The pattern physically cuts into the first ply of the composite, as seen in **Figure 4.2**, bringing the coating in direct contact with the fiber tows near the surface. The intimate contact with the fibers increases the resistance to crack propagation as the fibers are anchored in the composite but can also bridge delamination cracks propagating parallel to and below the surface OFCC ply. While this structuring does improve adhesion, especially to the porous matrix, and can improve resistance to coating spallation, it is also damaging to the composite near its surface. The laser ablation process cuts into the fiber tows near the surface, sinters the porous alumina matrix, and could leave residual tensile stresses in the composite. The stresses may promote delamination cracking that initiate within the matrix rather than at the coating interface. These cracks can then propagate readily though the low shear strength porous matrix between the woven fiber plies, typically those closest to the surface.

The different interlayer materials in the Gen1-234 and Gen1-237 samples did not have appreciable impact on the overall coating performance. While the CTE of 7YSZ (12 ppm/°C)[92] is significantly greater than that of the alumina/N720 OFCC (6-8 ppm/°C) [51,95] and therefore a source of strain incompatibility, its thickness was apparently not large enough to significantly impact the thermomechanical response. The interlayers were only ~10% of the total coating thickness so the difference in CTE of the interlayers with the substrate was negligible compared with that of the 48YSZ top coat. When comparing the FCT results of the Gen1 and Gen2 samples, damage is far more extensive in the Gen2 sample. Even when compared to the first-generation composites cycled at 1300°C, the Gen2 damage at 1200°C was far more severe despite having a thinner barrier coating and smaller temperature excursion. There was more extensive cracking in the matrix below the coating interface, both in severity and depth into the composite; cracking upwards of 1 mm below the interface was observed in the Gen2 sample in **Figure 4.7**. Differences between the Gen1 and Gen2 samples, in both the APS coatings and the composites themselves between the two generation samples are likely responsible for the differences in performance. First, while the APS coating in Gen2 samples was thinner, ~500μm compared to 1.1mm thick first-generation coatings, the Gen2 coating was a 7YSZ monolayer, which has a higher CTE (12 ppm/°C) than the 48YSZ (9-10 ppm/°C) that was the bulk of the first-generation samples. The greater CTE difference between the OFCC substrate (6-8 ppm/°C) resulted in more damage than the thicker coating with a closer matched CTE. Secondly, as shown in **Figure 4.2**, the matrices of the two generations were different, with the Gen2 matrix having larger inter-tow pores than the first generation samples. These large pores make the composite more susceptible to interlaminar cracking through the matrix. (Not enough samples were supplied for interlaminar strength testing of coated OFCCs). Thirdly, also shown in **Figure 4.2**, Gen2 samples featured a more pronounced patterning than the first-generation samples. The patterning was coarser and extended deeper into the composite than the first-generation patterning, cutting though more fibers and exposing more matrix deeper into the composite to the sintering effects of the laser patterning. The combination of the greater CTE, the weaker matrix, and the more intensive surface structuring lead the Gen2 sample to perform far more poorly than the first-generation samples in FCT. This is also represented in the delamination cracking calculations in **Figure 4.14**, where the Gen2 coatings showed nearly twice the stress and nearly four times the ERR at the interface that the Gen1 coatings.

4.3.3 Diffusional interactions

While the nature of the interlayers in the OFCC coatings do not seem to influence significantly the durability, they do introduce different forms of thermochemical interactions that may play a role at longer lives. The 7YSZ interlayer of Gen1-237 was intended to serve as a diffusion barrier between the 48YSZ topcoat and the composite constituents. The interlayer of Gen1-234, comprising a mixture of 48YSZ and alumina splats was designed in an attempt to enhance the CTE compatibility between the 48YSZ top coat and the alumina-based composite. While the interlayer may help alleviate the CTE mismatch in theory, the constituents of the interlayer would need to be *thermochemically* compatible for long-term stability of the T/EBC, which was not the case for the interlayer of Gen1-234.

The reaction phase within the 48YSZ/Al_2O_3 interlayer, identified as $Y_3Al_5O_{12}$ (YAG) by TEM EDS, is consistent with a likely diffusion path in the ZrO–Y_2O_3–Al_2O_3 isothermal section at 1250°C by Lakiza et al [96] in **Figure 4.15**.

$$10.5\ Y_{0.5}Zr_{0.5}O_{1.75} + 2.5\ Al_2O_3 \rightarrow Y_3Al_5O_{12} + 7.5\ Zr_{0.7}Y_{0.3}O_{1.85} \qquad \mathbf{4.1}$$

The diagram also indicates that no reaction should occur between 7YSZ and alumina, which was the observed result from sample Gen1-237. In the Gen1-234 interlayer, the YAG reaction phase is exclusively within the 48YSZ, along the interface with the alumina, and at splat and grain boundaries within the APS 48YSZ. There is no evidence of YAG within the APS alumina or porous matrix, indicating that alumina is the mobile species, diffusing into the 48YSZ along the grain and splat boundary interfaces where YAG nucleates and grows through further diffusion of alumina and yttria leaving Y-depleted YSZ.

The reaction phases get more complicated when looking at the N720/48YSZ interactions. When in direct contact with the fiber, the 48YSZ, approximated by $Y_{0.5}Zr_{0.5}O_{1.75}$, decomposes with Y migration into the fiber, where it apparently reacts with the mullite to yield YDS and alumina:

$$4\ Y_{0.5}Zr_{0.5}O_{1.75} + Al_6Si_2O_{13} \rightarrow Y_2Si_2O_7 + 3\ Al_2O_3 + 2\ ZrO_2 \qquad \mathbf{4.2}$$

This reaction will also lead to Y-depleted YSZ in the coating material, and result in the coarsening of the alumina grains within the N720 fibers. While initial alumina grains in the

N720 fibers average only 70 nm [97] in size, grains up to 2-3 μm in size are observed in reacted fibers at 1300°C, e.g. **Figure 4.7**. Further details of the reaction mechanisms of the alumina and N720 interactions with 48YSZ are beyond the extent of this work. However, the results highlight the necessity for a diffusional barrier in the T/EBC system, such as 7YSZ that is thermodynamically stable with the composite constituents and the top coating layer.

4.3.4 Thermal cycling in water vapor

Issues arising from the required surface preparation for APS coatings can be avoided using EB-PVD, which does not require surface patterning and mechanical interlocking for good adhesion. Additionally, the columnar microstructure produced from EB-PVD is more compliant in-plane and allows for the mitigation of thermal stresses arising from CTE mismatch between the coating and composite.

Although this particular set of tests was limited to 30 cycles, equivalent to only 15 hours of hot time, the experiments were long enough in duration to reveal significant difference between the APS and EB-PVD coated samples. With visible cracking on all edges, both on the as deposited as well as the cut edges, the APS Gen2 sample showed signs of incipient failure after 30 cycles. In contrast, the EB-PVD coated OFCC showed no visible signs of any cracking, spalling or delamination, both in the optical images and in cross-section. The columnar structure of the EB-PVD coatings provided sufficient in-plane compliance, and in addition to the lack of deleterious surface structuring, created an adherent coating that did not show significant signs of damage after FCT. There were many channel cracks observed, however, just as in the as-deposited condition. There were not noticeably more of this cracking after cycling than prior to it, suggesting that these cracks form on cooling after coating deposition, and not during the FCT process. The existence of these channel cracks prior to FCT allows for further accommodation of thermal strains on cycling without forming additional penetration or delamination cracking. The penetrating cracks kinking into the fiber tows is of concern, as it again highlights the weak porous matrix that is susceptible to delamination cracking in and around the fiber tows near the coating interface. These preexisting channel cracks could also be a likely path for water vapor ingress, but this experiment was not long enough to observe any effects. Although the EB-PVD coating was less than half the thickness of the Gen2 APS coating, 240 µm to 500 µm, respectively, the aforementioned coating microstructure, lack of surface structuring, and preexisting channel cracks are factors for the superior performance of the EB-PVD coatings in this preliminary FCT experiment. This was partially picked up in the LayerSlayer calculations in **Figure 4.14,** where the driving force for delamination cracking in the EB-PVD sample was half that of the Gen2 sample. The calculations do show there is more stress at the interface in the EB-PVD sample, but the delamination stresses do not take into account stress being relieved from channel cracking.

4.4 Synopsis

Higher Y_2O_3 containing YSZs have a lower CTE than the industry workhorse 7YSZ, better matched to a porous matrix alumina/N720 composite and consequently do perform better in thermal cycling . However, the greater Y_2O_3 content coatings are no longer thermochemically stable with the alumina and mullite constituents of the composite. Reaction phases form, consuming coating material, further complicating the CTE landscape, and damaging fibers with formation of reaction phases and extensive grain coarsening.

While necessary for adhesion during the APS coating process, the laser surface structuring damages the porous matrix and the topmost bundles of fibers of the composite.

The laser ablation process cuts through fibers and locally sinters the porous alumina matrix. This leaves residual tensile stresses in the composite near the coating interface, evident by delamination cracking both initiating and propagating within the composite below the coating interface. Coarser and deeper cutting surface patterns may exacerbate this problem, extending the damage and residual stresses from the patterning deeper into the composite.

EB-PVD can circumvent some of the issues that lead to shorter lives in APS coatings. EB-PVD does not require deleterious surface structuring for good adhesion, and initial depositions show coatings can be effectively grown on the porous alumina matrix OFCC substrate. The columnar microstructure of EB-PVD provides in-plane compliance and mitigation of thermal stresses, accommodating a CTE mismatch between the coating material and the composite without sacrificing durability in thermocyclic environments.

While the initial results and performance of EB-PVD coatings is promising, further action can be taken to produce a more robust and durable barrier coating system. In addition to utilizing a coating deposition technique that does not require damaging the composite for adhesion, strengthening the porous matrix of the composite to help reduce damage within the composite below the coating interface. Care should be exercised, however, to do so without reducing toughness and damage tolerance through the thickness of the composite. This porous matrix strengthening will be discussed in detail in **Chapter 5**.

4.5 Tables and Figures

Table 4.1: Relevant values for the stress and ERR calculations from **Section 4.3.4**

Material	*Thickness*	*CTE (ppm/°C)*	*Poisson ratio*	*Young's Modulus (GPA)*
Gen1 (48YSZ)	1.1 mm	9.5	0.2	40
Gen2 (7YSZ)	500 μm	13	0.2	40
EB-PVD 7YSZ	240 μm	13	0.2	40
OFCC	3.0 mm	7.3	0.2	50

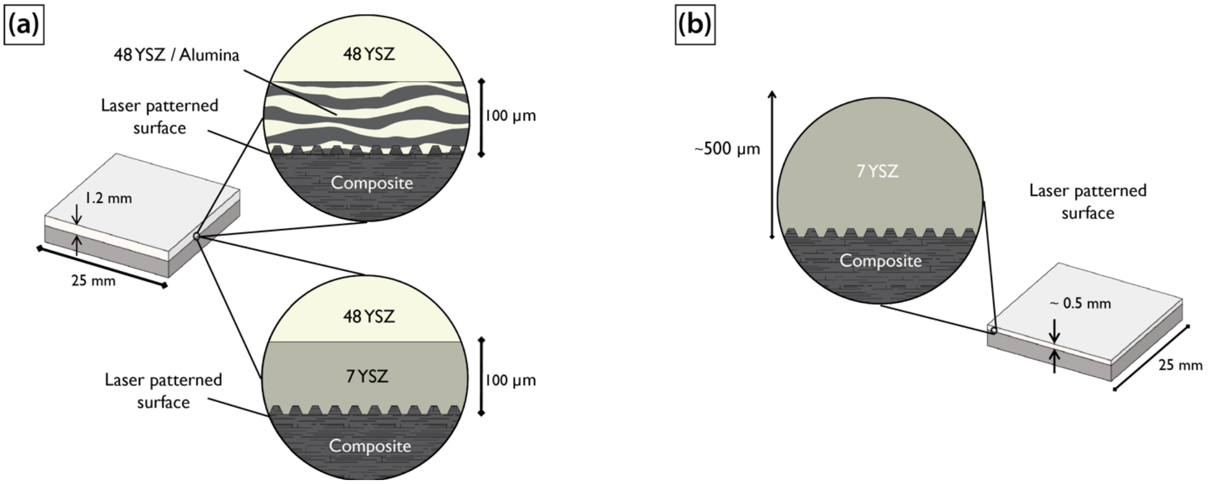

Figure 4.1: Schematic depiction of (a) the first-generation samples Gen1-234 and Gen1-237, highlighting the difference in interlayer materials, and (b) the Gen2 samples being a 7YSZ single layer.

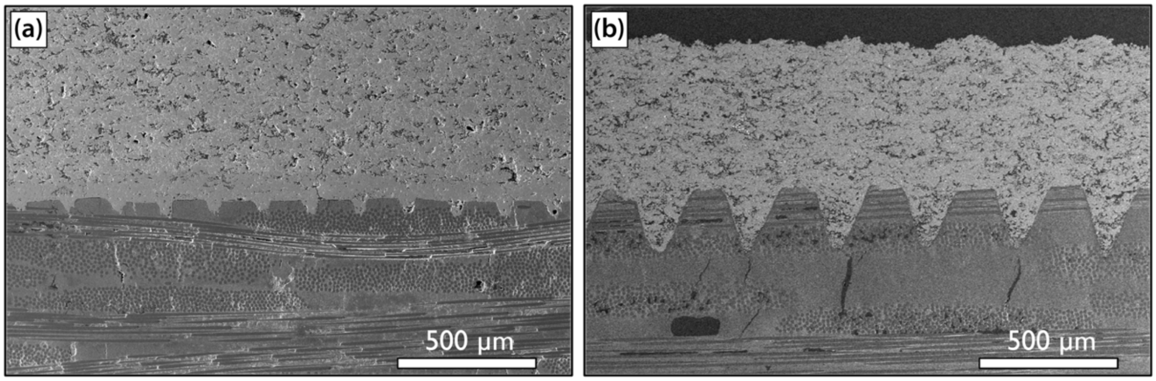

Figure 4.2: The difference in the laser surface structuring between (a) the first generation, samples Gen1-234 and Gen1-237 and (b) the Gen2 samples. In addition to the size difference in the surface structuring, also noted is the difference in the composite itself, within the fiber tows, and greater amount of intratow porosity and large, intertow voids.

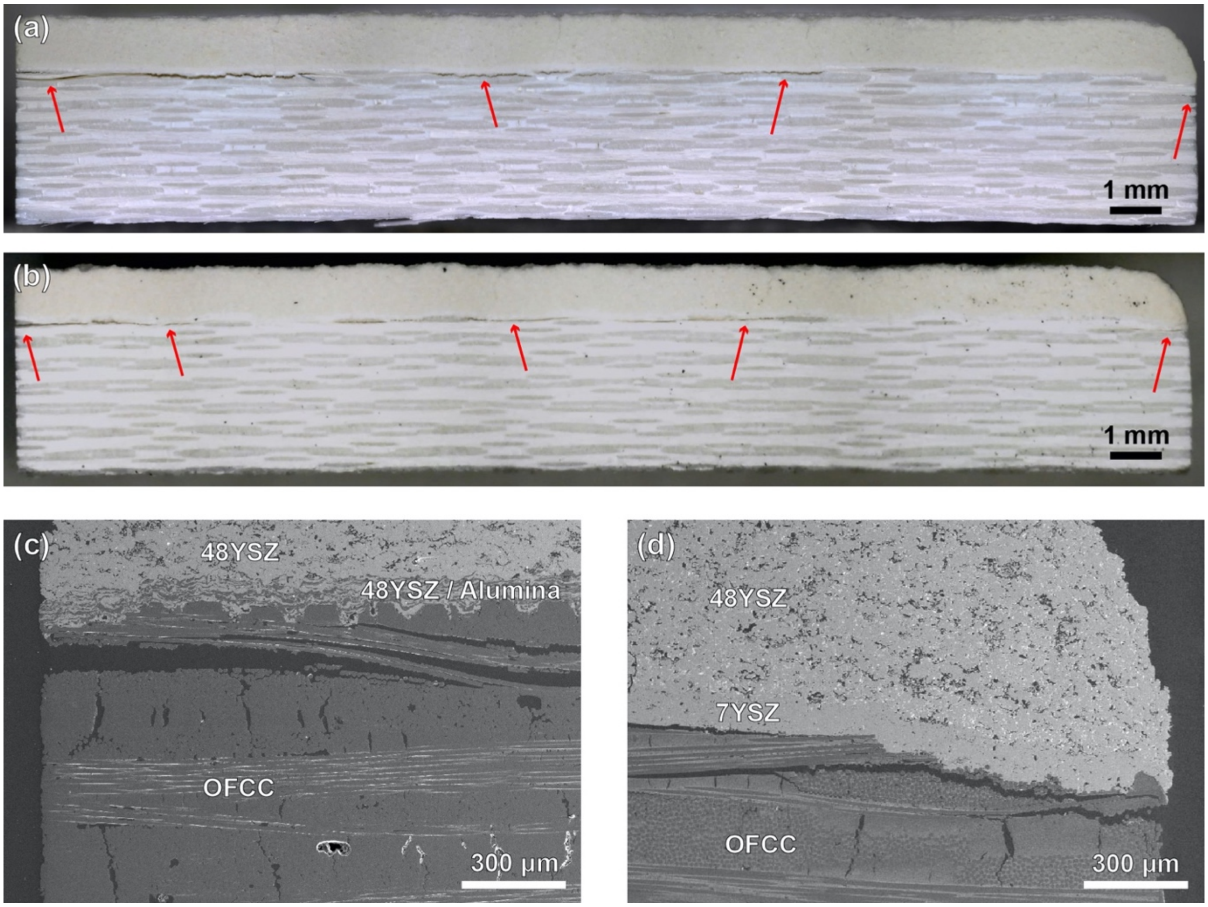

Figure 4.3: Edge-on optical images of (a) Gen1-234 and (b) Gen1-237 after FCT at 1200°C. Cross-section images of the cracking at the edges of the composites for (c) Gen1-234 and (d) Gen1-237, and. Cracking appeared to initiate below the coating interface in both samples, and arrows highlight cracking within the composite below the coating interface in (a) and (b).

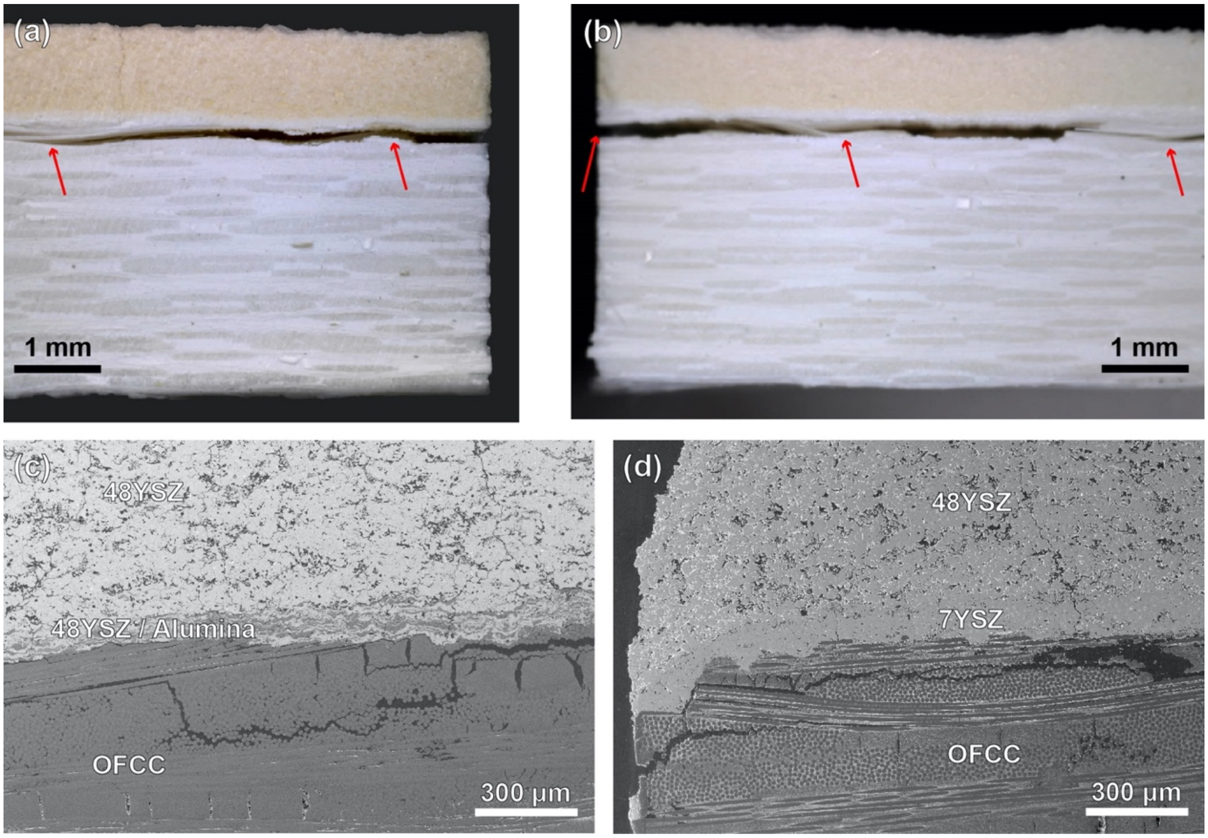

Figure 4.4: Edge-on optical images of (a) Gen1-234 and (b) Gen1-237 showing cracking within and at the edges of the composites after 100 cycles at 1300°C, with arrows highlight cracking within the composite, below the coating interface. Cross-section images for (c) Gen1-234 and (d) Gen1-237, again showed cracking that appeared to initiate and propagate below the coating interface in both samples,

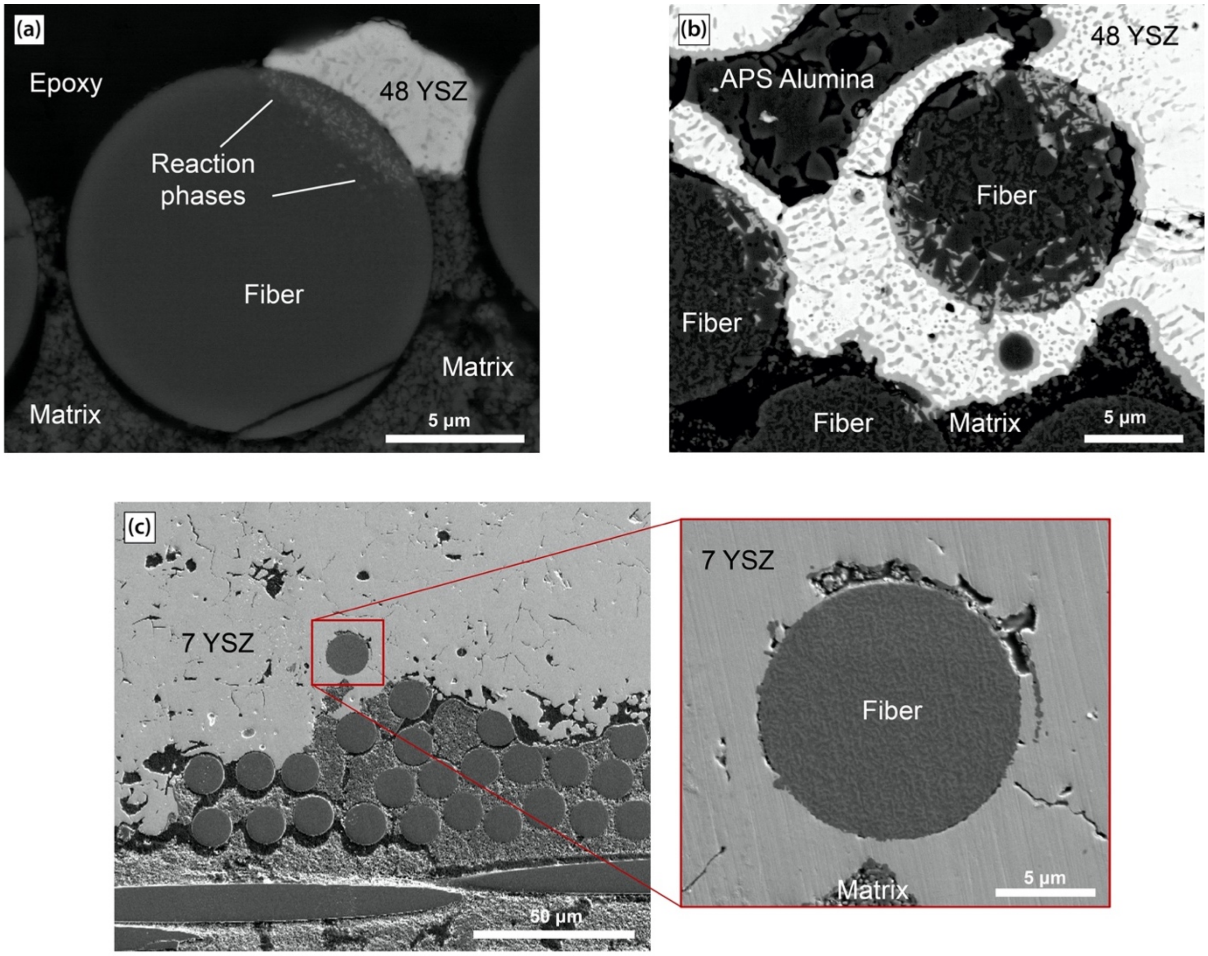

Figure 4.5: The interaction between APS 48YSZ and the APS alumina, matrix, and N720 fibers in sample Gen1-234 after FCT at (a) 1200°C and far more extensive reaction at (b) 1300°C. After FCT at 1300°C, the (c) 7YSZ interlayer in Gen1-237 showed no interaction with the matrix or N720 fibers.

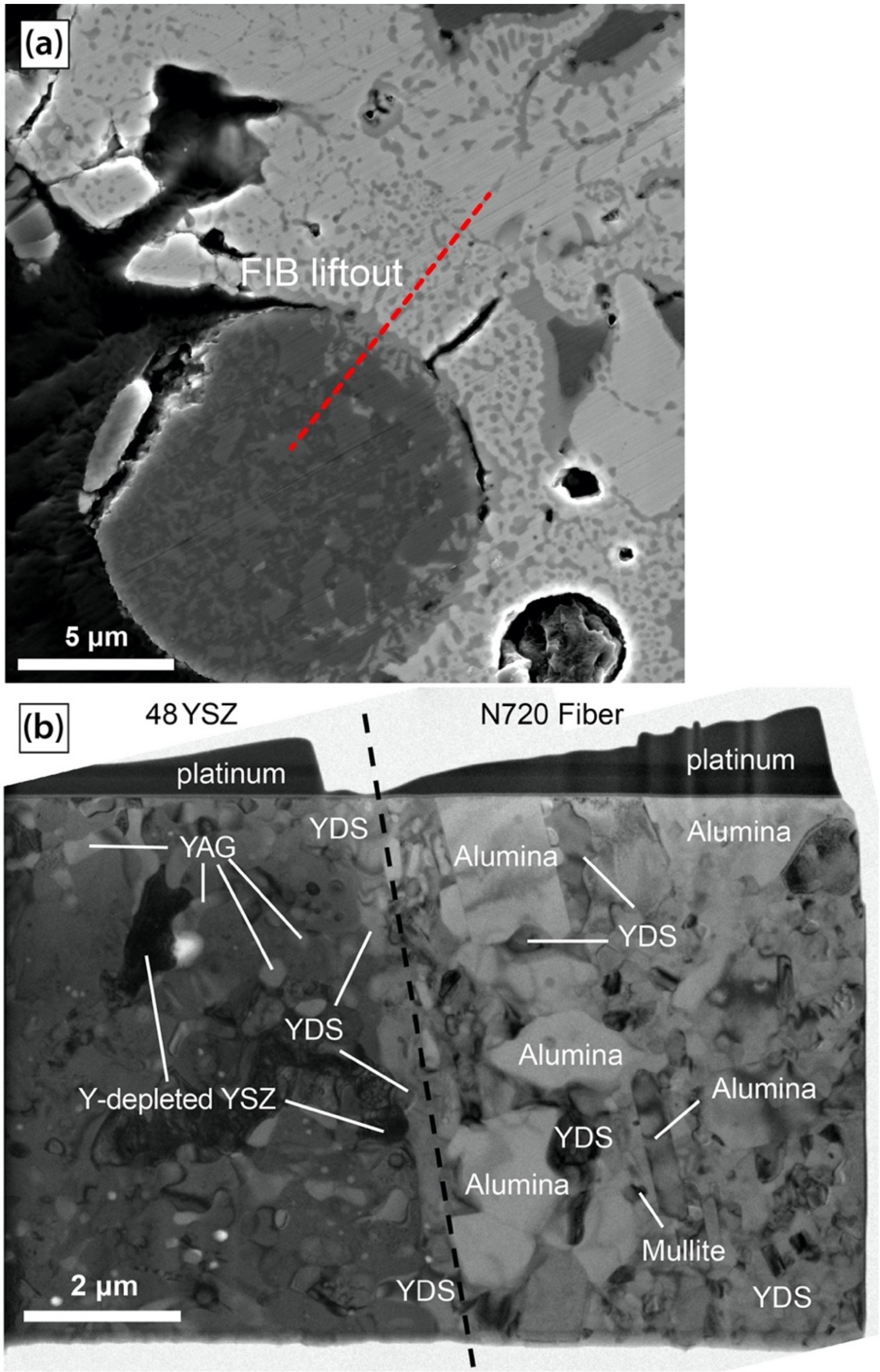

Figure 4.6: (a) The location of the FIB lamella liftout from the 1300°C run of sample Gen1-234 capturing the reaction phases in both the APS 48YSZ and the N720 fiber. Bright field TEM stitched image of the lamella is shown in (b) with TEM EDS identified phases labelled on the individual grains.

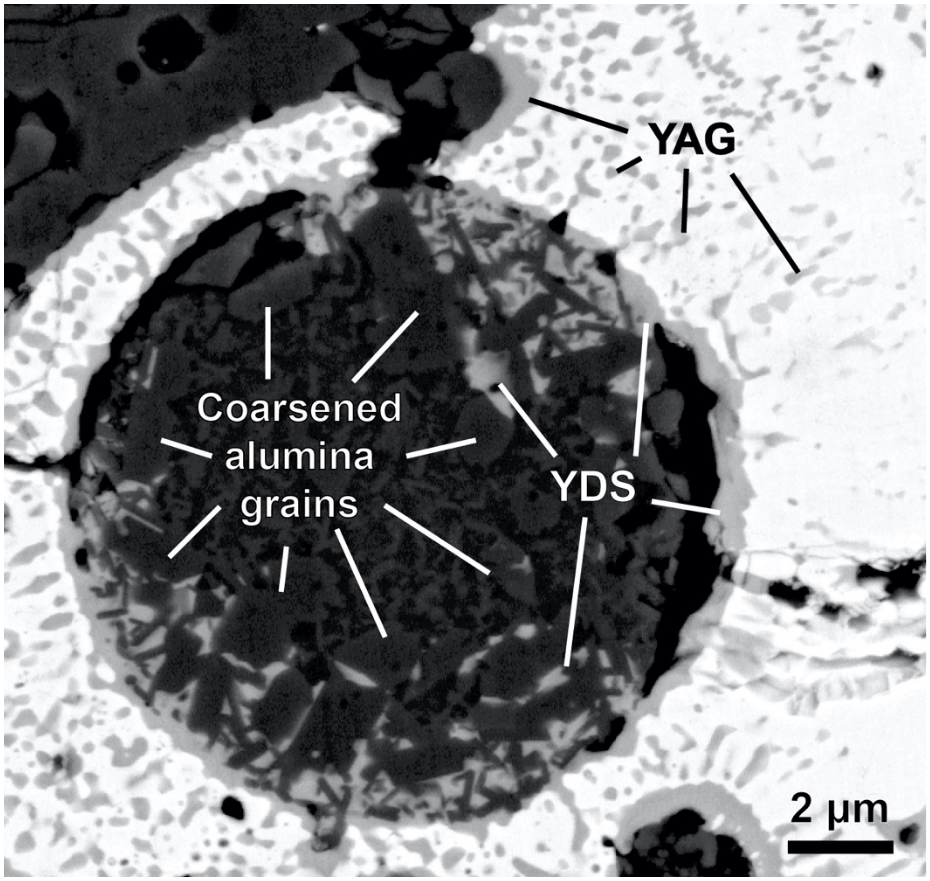

Figure 4.7: Higher magnification inset of the reacted fiber from **Figure 5(b)** with phases labelled as determined from TEM EDS. YAG forms within the APS 48YSZ and at the interface with the alumina matrix and APS alumina, YDS forms at the interface between the N720 fiber and the APS 48YSZ, as well as within the fiber. Alumina grains coarsen within the reacted fibers as SiO_2 is consumed to form YDS.

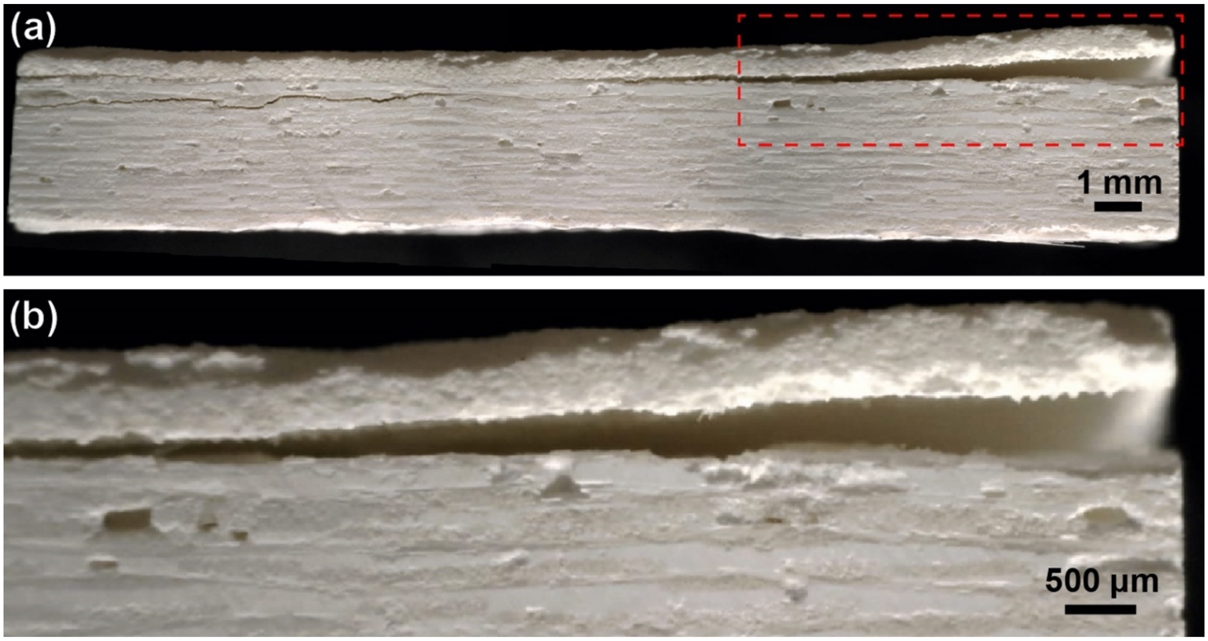

Figure 4.8: (a) Edge on view (not a cross-section) of the 'Gen2' sample after 100 1h cycles at 1200°C exhibiting significant delamination on the right side and cracking nearly 1mm into the matrix on the left side. Inset in (b) shows the imprint of the surface patterning on the section of spalled coating.

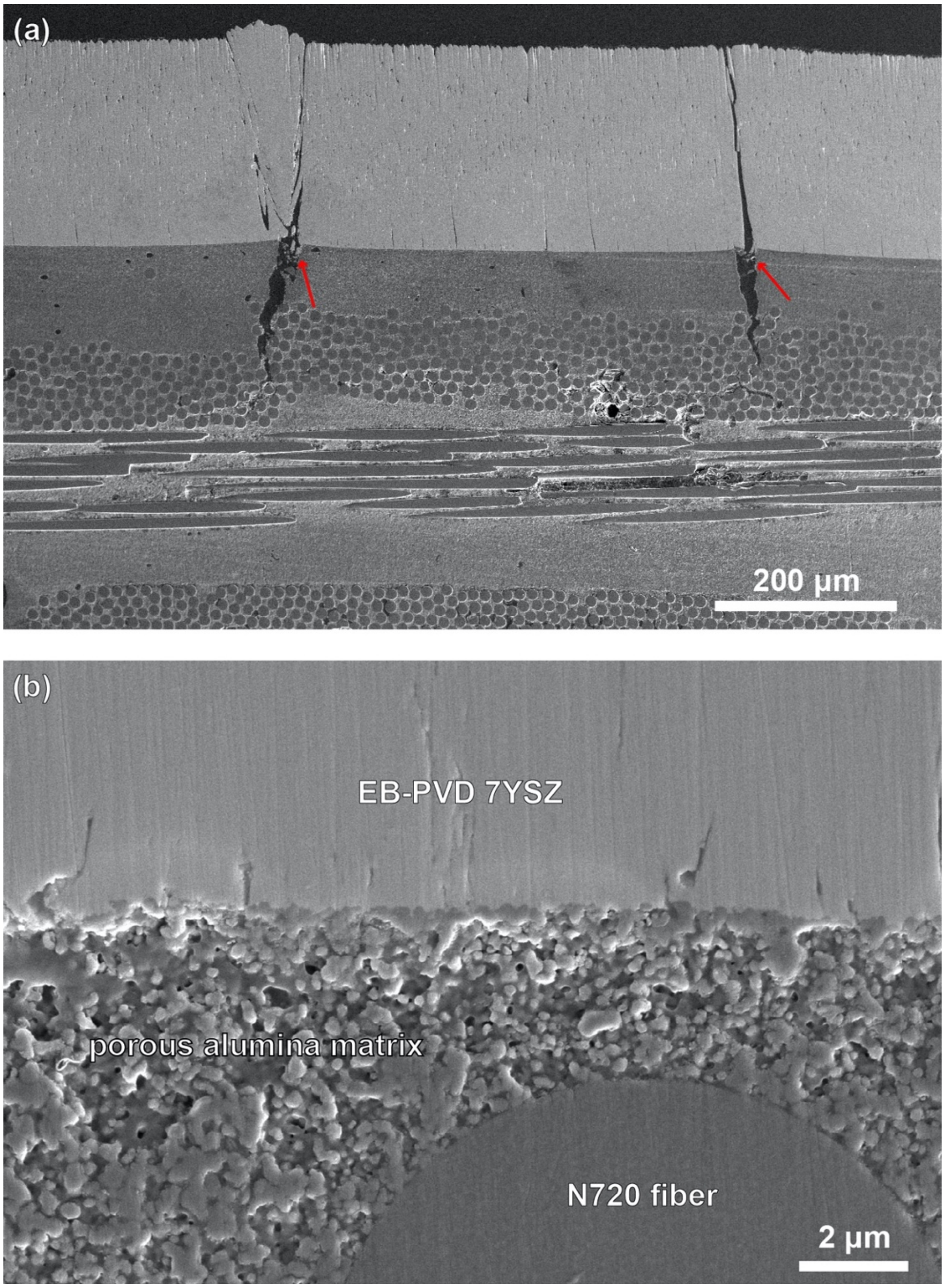

Figure 4.9: (a) Example channel cracks penetrating the matrix and fiber tows. Highlighted are some cracks that initiated at pre-existing mudcracks on the the composite surface, evident by the widest opening at the coating/composite interface, and narrow going into the composite and toward the coating surface, and also by the presence of deposited 7YSZ in the composite crack, highlighted with arrows. Higher magnification image in (b) shows good adhesion between the coating and the porous matrix.

Figure 4.10: Optical edge-on images (not cross-sections) of two edges of the Gen2 coated OFCC (a) before FCT in water vapor and (b) the same two edges after 30 cycles, with visible delamination cracking. The darker region in the upper right corner of (a) is small region on the corner of the supplied OFCC that was not APS coated. The region was a semi-circular with a radius of about 3 mm.

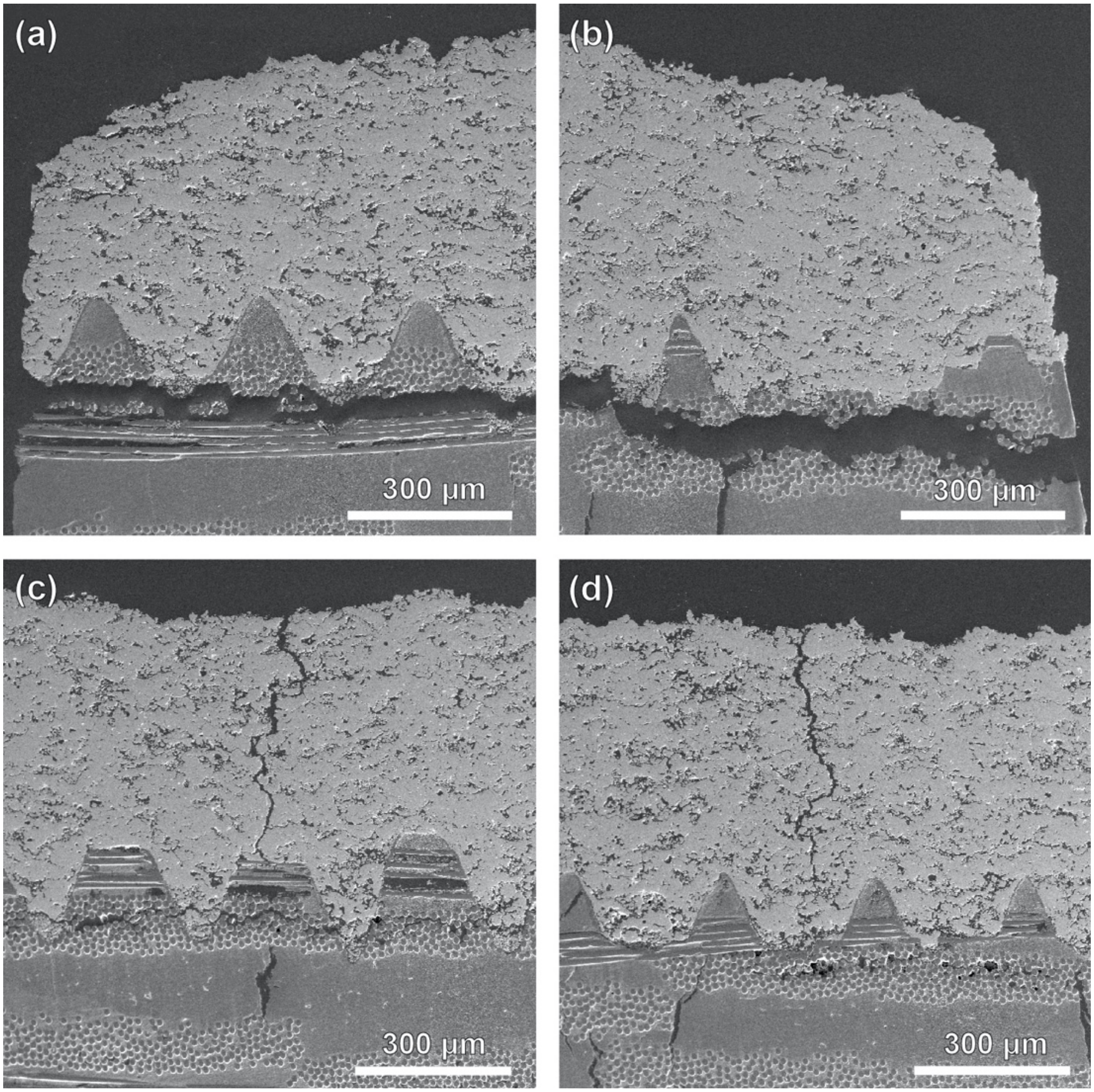

Figure 4.11: Cross-section SEM images of a Gen2 sample after FCT at 1200°C highlighting the (a & b) delamination cracking at the composite edges and (c & d) examples of channel cracks penetrating through the coating into the matrix.

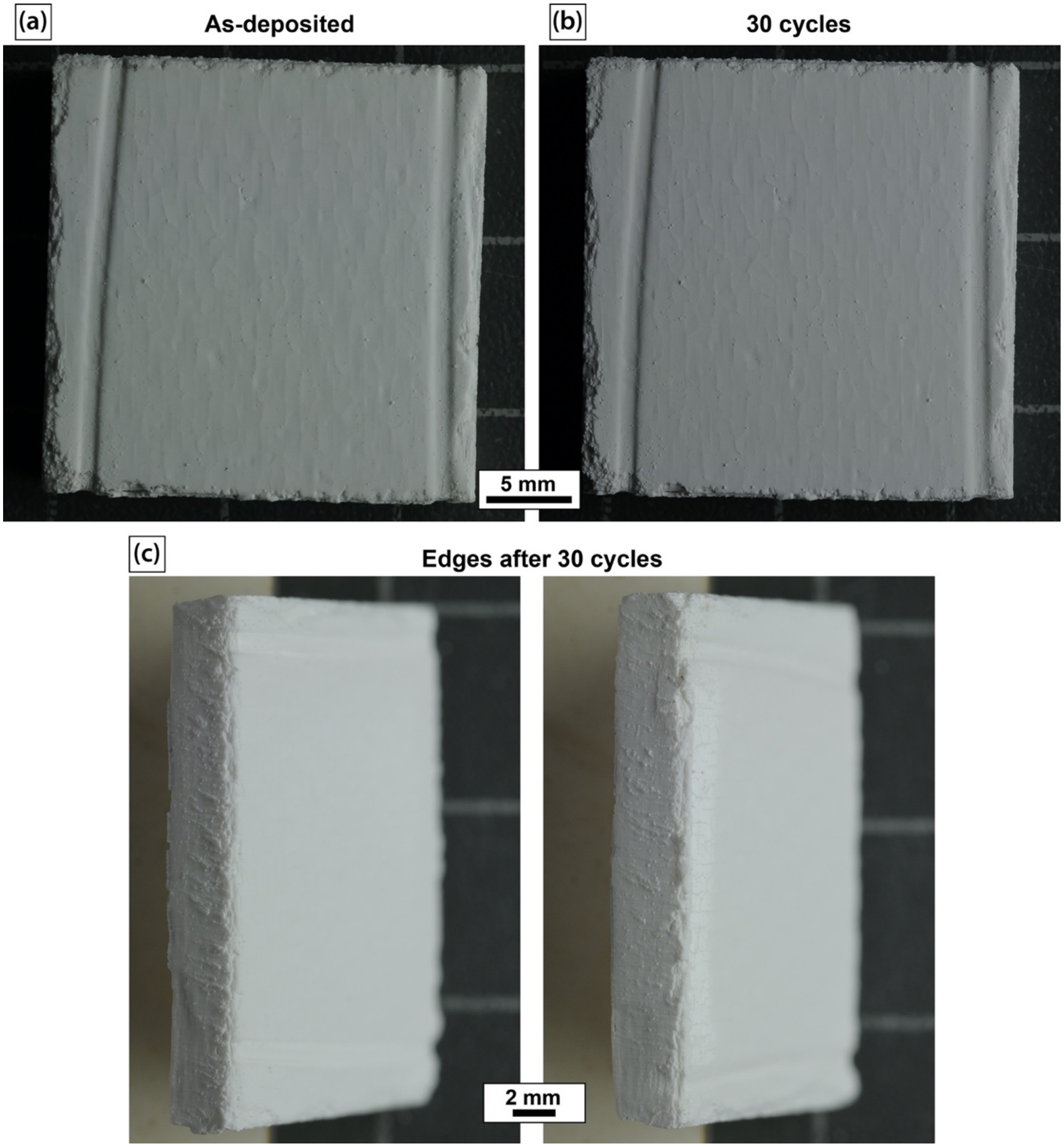

Figure 4.12: Optical images of the EB-PVD 7YSZ coupon (a) as-deposited and (b) after 30 cycles. The edges of the coupon in (c) do not show any sign of cracking or other damage after exposure.

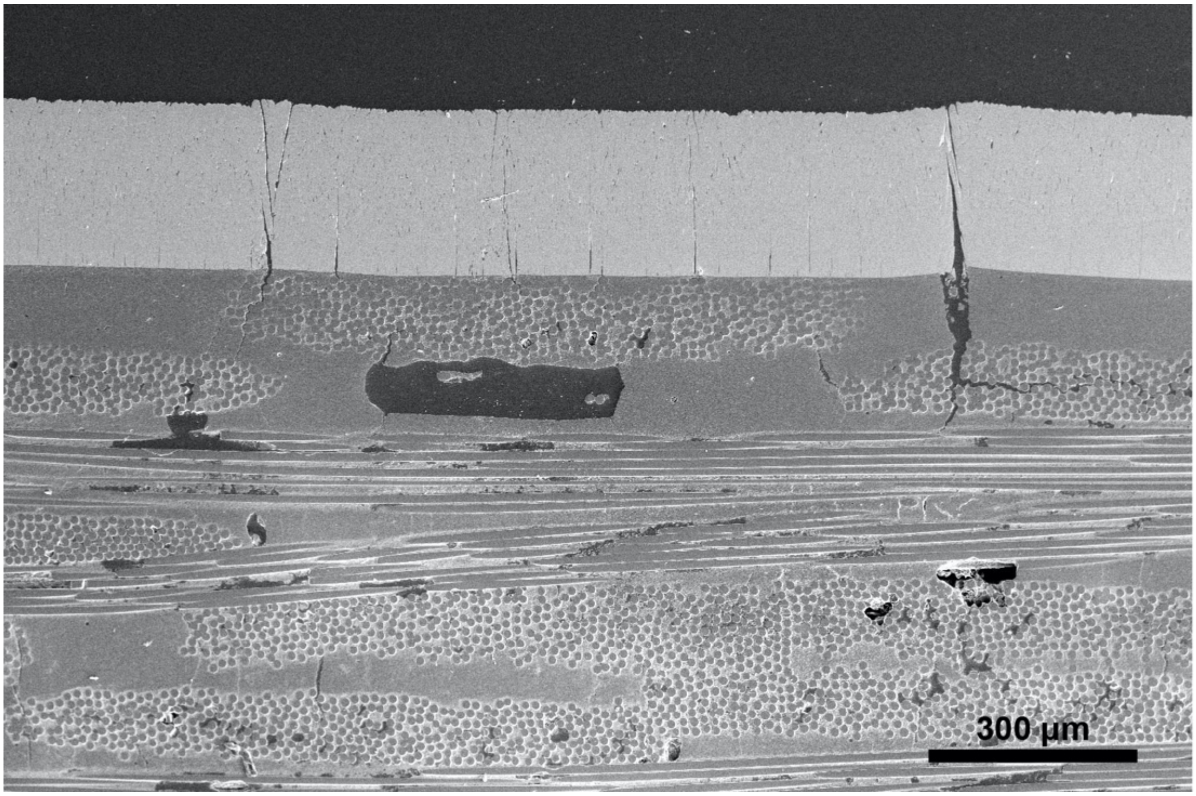

Figure 4.13: Cross-section image(s) of the 7YSZ EB-PVD coated sample after 30 cycles of FCT in water vapor showing a few channel cracks penetrating the coating. There are not noticeably more cracks than the as-deposited condition. Some cracks appear to kink horizontally into the fiber tows after cycling.

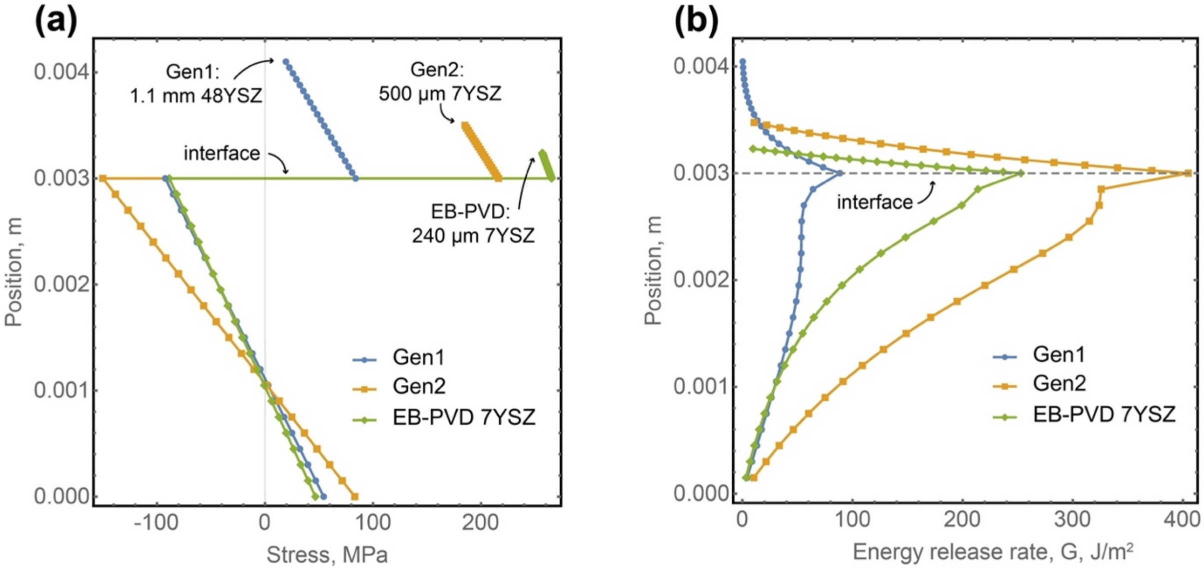

Figure 4.14: (a) Stress and (b) ERR calculations using the LayerSlayer software package. The results are for a 3 mm thick OFCC with various topcoats: Gen1, 1.1 mm of 48YSZ, Gen2, 500 µm of 7YSZ, and EB-PVD 7YSZ, 240 µm of 7YSZ. The calculations are representative of a single thermal cycle from an assumed stress-free state at 1200°C down to 20°C. The origin of the y-axis of the plots the bottom of the OFCC, so 0.003 m (3 mm) is the interface between the OFCC and the coating material. Below this line represent stress and ERR within the OFCC, and above represent stress and ERR within the coating material.

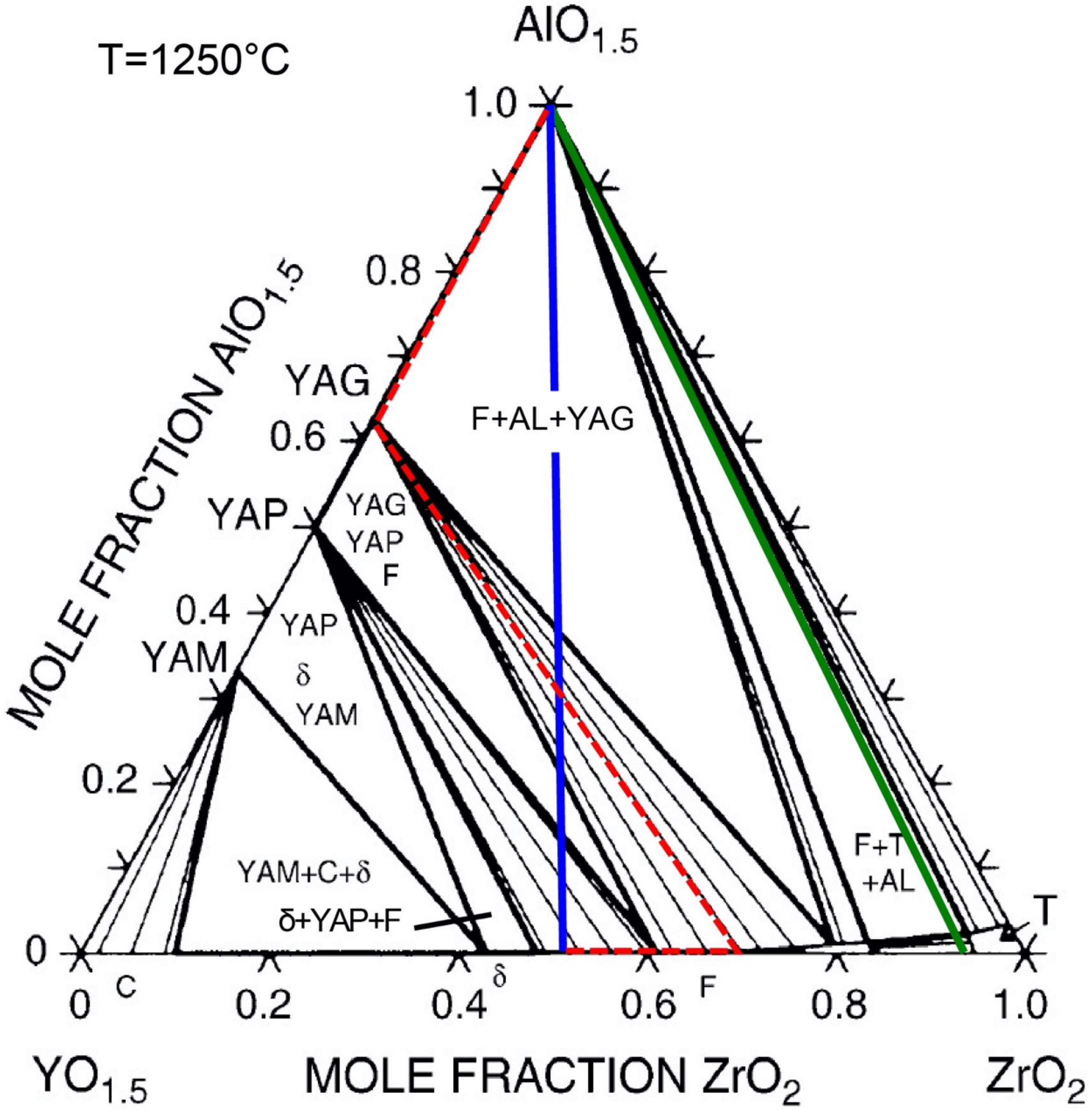

Figure 4.15: Experimental yttria-alumina-zirconia ternary phase diagram isotherm at 1250°C from Lakiza et al.[25]. Also shown are tie lines between alumina and 7 YSZ (green) and 48 YSZ (blue) and the reaction pathway (red dashed) between 48YSZ and alumina, where the reaction phase YAG will form, as well as Y-depleted fluorite. This highlights the lack of thermodynamic stability between high yttria-containing materials and alumina. It is expected from the binary systems that the phase diagram will not be significantly different at 1300°C

Chapter 5: OFCC Matrix Enhancement by Precursor Processing

EB-PVD has shown its advantages over APS in T/EBC durability in initial FCT testing, but there is still need to improve the robustness of the T/EBC system. The EB-PVD process produced well-adherent coatings, even after FCT, without surface structuring. However, the relatively weak porous matrix still presented issues that could be detrimental to long-term T/EBC durability if left unaddressed. Channel cracks penetrating the matrix into fiber tows are pathways for accelerated gas ingress, and the cracks kinking into the surface tows or neighboring matrix after cycling raise long term durability concerns. The approach to improving the robustness of coated OFCCs is multi-fold. Presented schematically in **Figure 5.1**, the research objective is to create a layered T/EBC *system* that begins within the composite itself. Modifying and strengthening the top layers of the porous composite to create a more robust surface for EB-PVD, which will be deposited in bilayers, with a thin diffusion barrier before a thicker topcoat with a reduced CTE mismatch. **Chapter 2** described how PIP processing can segregate on drying, creating both a density differential between the surface and bulk of an OFCC plate, and a sharp decrease in toughness due to microsegregation to the fiber-matrix interface. However, this commonly deleterious mechanism can be used creatively to generate a functionally graded porous matrix for OFCCs, with a gradient in strength and toughness in addition to density.

The research objective is the utilization of PIP and precursor segregation to selectively strengthen the porous OFCC matrix near the surface that is to be coated by EB-PVD, while maintaining damage tolerance through the thickness of the composite. This chapter discusses the development and analysis of different impregnation methods and precursor solution concentrations and compositions.

5.1 Precursor solution processing and experimental methods

5.1.1 Precursor solutions

The creation and calibration of the precursor solutions used for the infiltration experiments were described in detail in **Section 3.1.2**. Two alumina precursor solutions were used for the infiltration experiments, made from $Al_2Cl(OH)_5$ in water**.** One solution had a lower concentration (18 wt. % $Al_2Cl(OH)_5$) with a 3.3 % volumetric yield of alumina, and a second one with higher concentration (36 wt. % $Al_2Cl(OH)_5$), with 6.2 % volumetric yield of alumina. A 4 mol. % Y_2O_3 – ZrO_2 precursor solution was also used to infiltrate the OFCC matrices. This composition was used to introduce a second phase to the porous matrix, creating a 'composite' matrix with a functional second phase to add toughness. This solution was made from zirconium acetate and yttrium nitrate in water, with a 5.2 % volumetric yield. Due to experimental limitations, the YSZ precursor was not used for matrix hardening in subsequent EB-PVD depositions.

5.1.2 Vickers Microhardness of modified Matrix

The extent of precursor segregation within the porous matrices was assessed using Vickers microindentation. Samples were cross-sectioned, mounted in epoxy, and polished with the procedure described in **Section 3.3.1**. The polished cross-sections were sputter coated with Au/Pd for 30 s to improve contrast in the optical microscope of the Vickers microindenter apparatus (Zwick 3212, ZwickRoell, Kennesaw, GA). Indentations were made within the pockets of matrix between the fiber plies and in the near-surface regions of matrix, through the thickness of the composite. Load size was selected so it would create indents around half the size of the matrix pocket. Loads of 300 or 400 g were applied with a pyramidal diamond indenter for a duration of 30 s. The two diagonals of each indent, d_1 and d_2, were measured using SEM, and the surface area of the indents, A, was calculated using:

$$\boldsymbol{A = \frac{((d_1 + d_2)/2)^2}{2\sin(136°/2)} \approx \frac{d_{avg}^2}{1.8544}} \qquad \textbf{5.1}$$

The Vickers hardness value, HV, was calculated from the applied load, F, over A:

$$HV = \frac{F}{A} \approx \frac{1.8544\,F}{d_{avg}^2} \qquad \textbf{5.2}$$

F is given in kg, and A in mm^2, giving the standard units for HV of kg/mm^2. An SEM micrograph of a typical indent is shown in **Figure 5.2.**

5.2 Results

5.2.1 Full impregnation – alumina precursor

Coupons of the first generation of uncoated OFCCs, described in **Section 3.1.1**, were fully infiltrated with $N = 0$, 2, and 4 cycles, of the precursor solution with the lower volumetric yield of alumina (3.3%). The full precursor impregnation and pyrolysis procedure is described in detail in **Section 3.1.3**. Samples were then mounted in epoxy and cross-sectioned. The matrices were analyzed by Vickers microindentation with a load of 400 g, and plots of the matrix hardness versus the distance into the composite of the three samples are presented in **Figure 5.3**. The sample with no precursor cycles was presented for a baseline of matrix hardness, which was averaged as 392 ± 75 kg/mm^2. There was a moderate trend of increased hardness near the surface, about 1.5 times the base hardness.

There were inconsistencies in the matrix hardness measurements, especially near the composite surface. **Figure 5.4** presents two images of indents near the surface of the $N = 2$ sample for the fully impregnated 3.3% volumetric yield alumina precursor solution. The measured hardness from the two indents is very different, mostly due to the significant cracking extending from the indent to the surface in **Figure 5.4 (b)**, whereas the indent shown in **Figure 5.4 (a)** does not have the associated significant cracking and measures a greater hardness value. This type of cracking was observed in several of the indents in the near-surface matrix pockets, and made acquiring consistent hardness measurements from the surface difficult.

The infiltration experiment was repeated with the more concentrated precursor solution with the higher volumetric yield of alumina (6.2%). The same procedure was followed, and coupons of 2, 4, and 6 PIP cycles were analyzed. Presented in **Figure 5.5** are plots of the matrix microhardness measurements against the depth into the composite for the higher concentration precursor solution, with the average matrix hardness marked on each plot. Aside from a weak trend in the $N = 4$ sample in **Figure 5.5 (b)**, there was an increase in matrix hardness through the entire thickness of the composites, from a 1.5 – 2 fold increase for $N = 2$, to a, albeit scattered, 2-3 fold increase for $N = 6$. This indicated the process had densified the matrices more than was desired, deep into the composite.

5.2.2 Surface application – alumina precursor

Vickers microhardness of polished cross-sections of painted coupons, the surface application procedure is detailed in **Section 3.1.2**, are presented in **Figure 5.6.** Both the first generation in **Figure 5.6 (a)** and the second generation in **Figure 5.6 (b)** showed significant hardening in the top ~500 μm of the matrix, without appreciable hardening deeper into the composite. There were inconsistencies in the near surface measurements as before, but the trend is still clear. Additionally, cracking from the indents was not observed to penetrate nearby fibers anywhere through the thickness of the composite, indicating a retention of the weak fiber-matrix interface allowing for matrix crack deflection and overall composite damage tolerance.

5.2.3 Surface application – 4 mol. % Y_2O_3 – ZrO_2 precursor

The 4 mol. % Y_2O_3 – ZrO_2 precursor solution was applied to the surface of OFCC coupons in the same manner as described in the previous section, with a different pyrolysis profile for the 4 mol. % Y_2O_3 – ZrO_2 precursor. Painted coupons were first heated to 300°C at 5°C/min and held for 2 hours, then to 500°C at 5°C/min with a 2 hour dwell, and lastly up to 1000°C at 8°C/min and held for 2 hours, before ramping to room temperature at 10°C/min. Coupons were subjected to 4 cycles of application and pyrolysis.

Painted coupons were mounted in epoxy, cross-sectioned and polished for Vickers microhardness of matrix pockets. The resulting plots are presented in **Figure 5.7**. There is a well-defined trend that there is significantly more hardening in the top ~400 μm of the matrix. Measurements near the surface were inconsistent as the same type of cracking was observed, shown in **Figure 5.8**.

5.3 Discussion

5.3.1 Vickers analysis

In addition to the significant horizontal cracking seen from the near-surface in **Figure 5.4** and **Figure 5.8**, Cracks emanating from the indents in the bulk, not surface, which can be seen in the example indent in **Figure 5.2**, are a result of residual tensile stresses in the matrix from processing. The alumina matrix has a greater CTE than the N720 fibers, so on cooling from an assumed stress-free state, the matrix will want to contract more than the fibers, and there will be residual tension in the matrix pockets because that shrinkage will be restricted by the network of neighboring fibers [48] .

The Vickers hardness measurement model is not entirely accurate because of the extensive cracks from the indents, especially in the near-surface indents, but the values do provide a semi-quantitative insight on the extent of densification, even without being able to correlate the hardness values to the matrix density/porosity. Despite the measurements' inconsistency, there was still an observed trend that the near surface matrix is hardening more than that deeper into the composite, although arguably not to the optimum extent desired.

The cracks from the indents can also bring insight to potential loss of damage tolerance in the composite. **Figure 5.9** presents images of indents from the impregnation experiment with the higher concentration, $y_p = 6.2$ % alumina precursor solution, of the $N = 2$, 4 and 6 samples, where cracking from the corners of the indents propagate through the matrix and penetrate nearby fibers. In this case there is no longer a de-coupling of the fibers and matrix, caused by an increase in the matrix density, either in bulk, or locally at the fiber-matrix interface, such that matrix cracks will no longer deflect around fibers. This is particularly concerning in **Figure 5.9 (c)** where an indent deep in the middle of the OFCC of the $N = 6$ sample showed this behavior, indicating a loss of damage tolerance in the bulk of the OFCC.

Even at equivalent matrix hardness values, it is possible for the cracks emanating from the indents to penetrate nearby fibers, instead of deflecting around, IF the fiber-matrix interface has been locally densified such that there is no longer sufficient decoupling of the fiber and matrix **Figure 5.9 (a)** shows an example of this, with a crack from the bottom side propagating to penetrate a fiber, whereas the crack from the top corner propagates and deflects around a fiber.

Precursor segregation to fiber-matrix interfaces on drying has been observed in previous studies of precursor densification of porous OFCC matrices [41,49], even after a few cycles. However, observing this so deep into the composite is further indication that there is not sufficient segregation to produce hardening only at the composite surface, and without jeopardizing damage tolerance into the bulk of the OFCC.

5.3.2 Defects in OFCC matrices

The absence of sufficient precursor segregation to the surface in the fully impregnated PIP experiments, while preserving the desired damage tolerance in the composite bulk, is attributed to the large void defects in the OFCC matrices resulting from the fabrication procedure (whose details are proprietary). The supplied, uncoated OFCC coupons had large voids in the intertow regions of the matrix, and many pores within the fiber tows themselves. The description of the as-received OFCC coupons in **Section 3.1.1** highlights these pores. The matrices of these uncoated coupons appear similar to that of the Gen2 coated coupons described in the previous chapter. These large pores and voids serve as reservoirs for the impregnated precursor solution and reduce the effectiveness of the capillary forces driving segregation of the solution to the surface during drying. An example in **Figure 5.10** shows a large pore in the matrix of the $N = 4$ sample of the greater concentration precursor solution, $y_p = 6.2$ %, full impregnation experiment, that is filled with the precursor derived alumina that was not able to segregate to the surface. The implication is that regions of the matrix next to those large pores, which are present throughout the cross section, would also be strengthened and their bonding to the fibers increased, degrading the damage tolerance mechanism.

5.3.3 Comparison with precursor surface application technique

The results of this approach are more promising than those of the full infiltration as precursor solution does not reach the bulk of the composite or the pores that can act as reservoirs. The result is a denser layer at the surface of the composite while maintaining matrix crack deflection and composite damage tolerance throughout the thickness of the composite. Ideally, the region of strengthened matrix would extend to ~500 µm deep into the thickness to strengthen in and around the first ply of the composite, where cracking was observed after FCT of the EB-PVD 7YSZ sample in **Chapter 4**. This technique can be improved and optimized, but the results are promising, having strengthened the top layer of the composite matrix without significantly hardening deep into the composite, and without locally densifying around the fibers, reducing matrix crack deflection.

The 4 mol. % Y_2O_3 – ZrO_2 precursor impregnated composite matrix hardness measurements in **Figure 5.7,** when compared to the alumina precursor surface application data in **Figure 5.6**, had similar hardening in terms of the upper limit, but there does appear to be more hardening deeper into the composite than with the alumina precursor solution. However, the trend is clear that the 4 mol. % Y_2O_3 – ZrO_2 precursor solution can produce a similar density gradient as the alumina precursor solution when applied using the ‘surface application' technique.

5.3.4 Difference in composites

The second generation, Gen2, composites were processed using the ‘surface application' technique for subsequent EB-PVD coating. However, the differences in the OFCCs required some differences in processing. As described previously in **Section 3.1.1**, the Gen2 coupons had smaller matrix pockets between the fiber tows, and when performing matrix hardness probing, the smaller matrix pockets necessitated a lighter Vickers load of 300 g to create smaller indents. The baseline matrix hardness of the newer received coupons was lower, measured to be 245 ± 51 kg/mm^2. The hardness values have more variation, partially due to the reduced amount of matrix pockets to test, and the smaller load on indentation. The upper limit of the matrix hardness is lower, as with the baseline hardness, however the trend is still clear that the surface is being preferentially strengthened without appreciable hardening through the composite thickness.

5.4 Synopsis

The described PIP techniques have demonstrated the creation of a strength gradient within a porous matrix OFCC. The very top layers of matrix were strengthened, as well as moderate hardening into the first ply, 200-400 μm into the composite. The desired segregation was achieved using a technique based on 'painting' the surface of the porous OFCC coupons with just enough precursor solution to limit the impregnation to the surface but not affecting the interior of the OFCC. Full impregnation yielded significant hardening, but without the expected segregation leading to hardening observed deep into the OFCC cross-section, as well as evidence of loss of crack deflection at the matrix/fiber interfaces, due to the large voids in the OFCC matrix serving as reservoirs for the precursor solution and inhibiting capillary forces driving the segregation. There is room to improve the surface application technique, to extend the hardening deeper into the first ply, in which observed cracking from EB-PVD coating and FCT was present. However these results are sufficiently promising to create a stronger and denser surface region for improved EB-PVD coating growth and performance. Although there is much room to improve the precursor process, the objective of creating a stronger surface for EB-PVD coating, shown in **Figure 5.1**, as part of the layered T/EBC system has been shown to be feasible. Subsequent EB-PVD in the following chapters are coated on OFCC substrates that are hardened using the surface application precursor method.

5.5 *Figures*

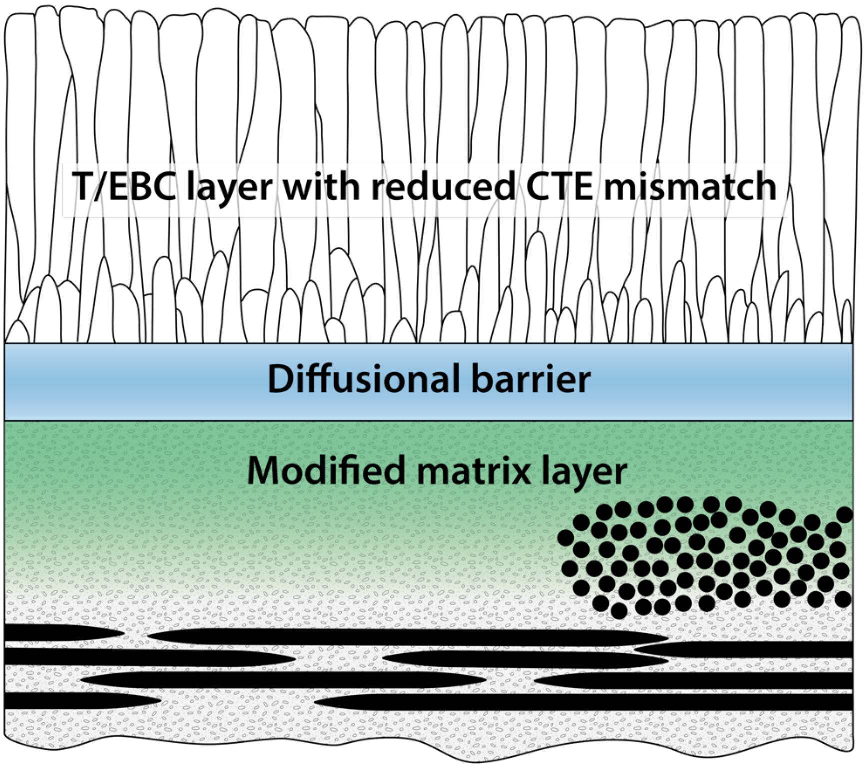

Figure 5.1: Schematic of the T/EBC system for OFCCs: a modified matrix layer to reduce delamination cracking, a diffusional barrier to prevent interaction between the main coating material and the composite constituents, and the main T/EBC layer with a reduced CTE mismatch with respect to the OFCC.

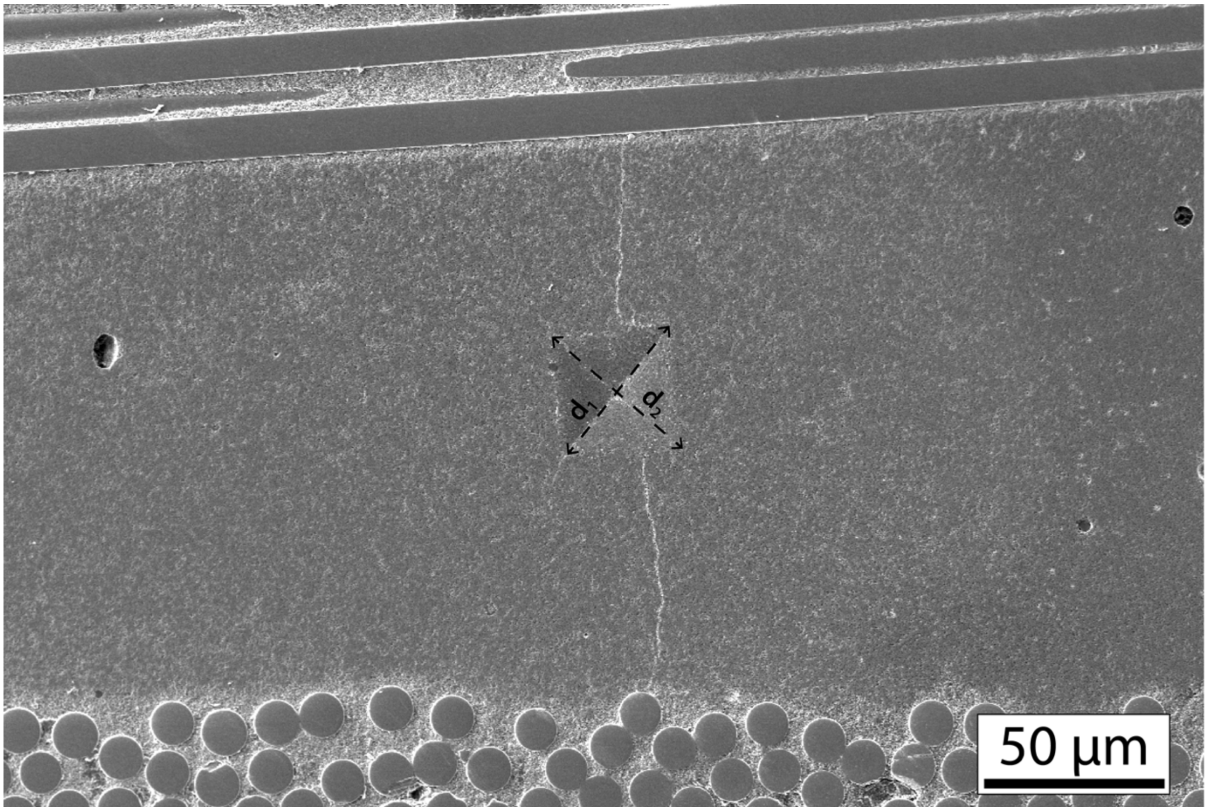

Figure 5.2: Example indent in a matrix pocket for matrix hardness analysis, with labelled distances used to calculate the Vickers Hardness Number (VHN).

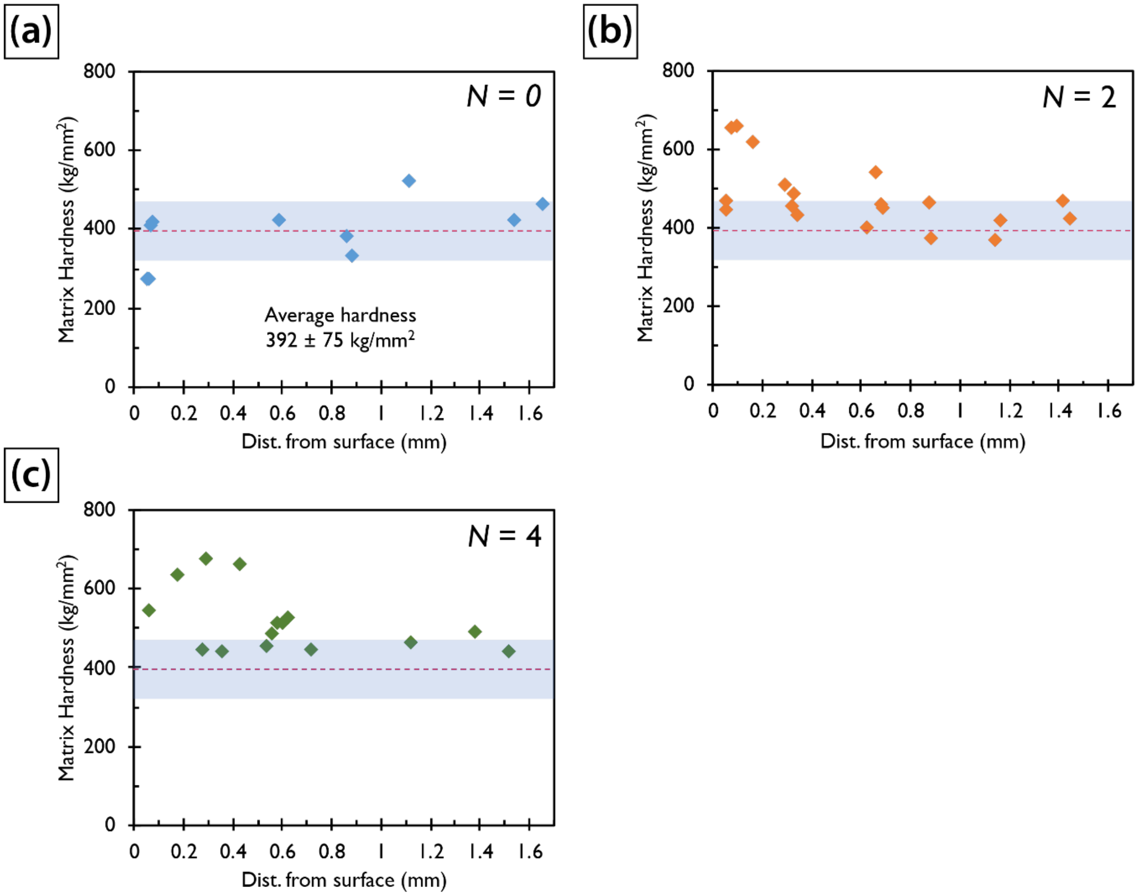

Figure 5.3: Plots of matrix hardness against distance from coupon surface for (a) no impregnations, *N* = 0, (b), *N* = 2, and (c) *N* = 4 impregnation cycles with the y_p = 3.3% alumina precursor solution.

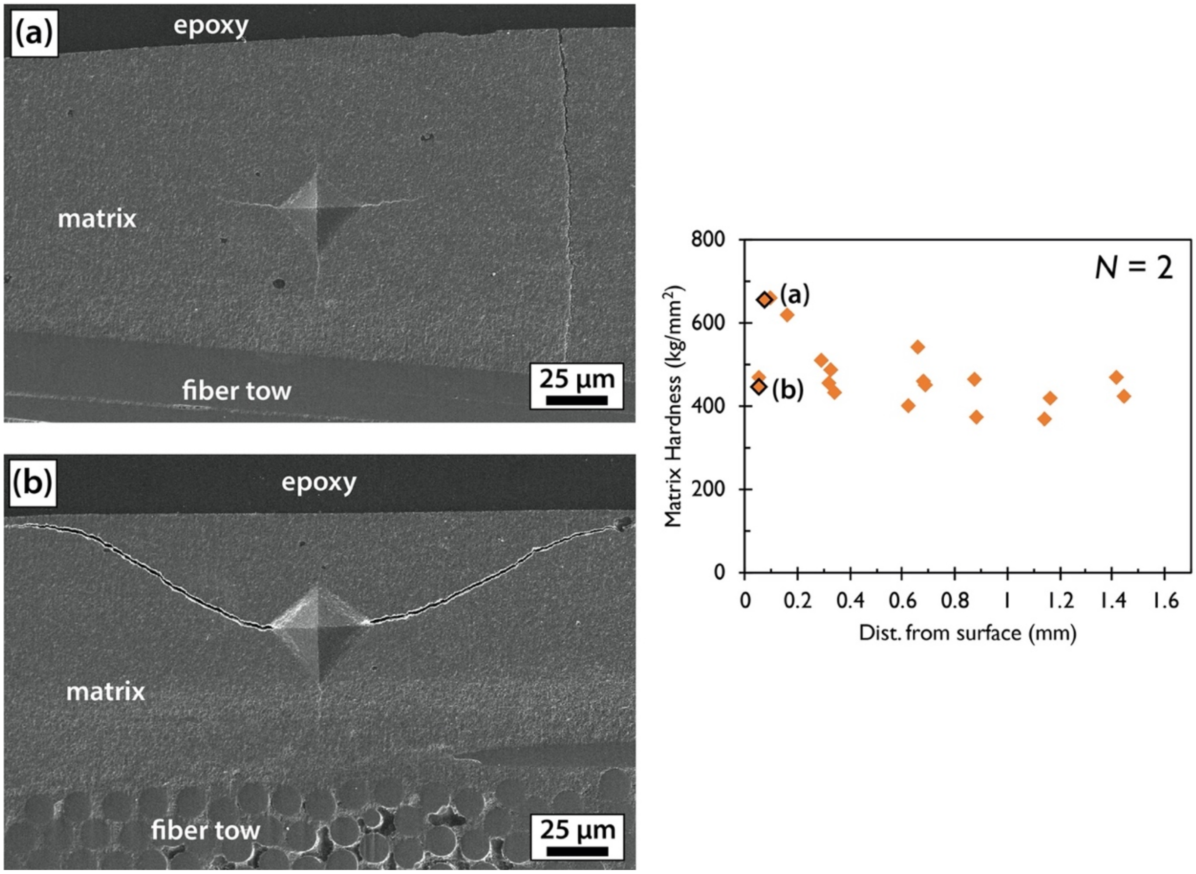

Figure 5.4: Two indents from the *N* = 2, fully impregnated with y_p=3.3% alumina precursor solution sample near the surface. Highlighted is the difference in measured hardness for (a) an indent without significant cracking, and (b) an indent with significant cracking from the indent corners to the surface.

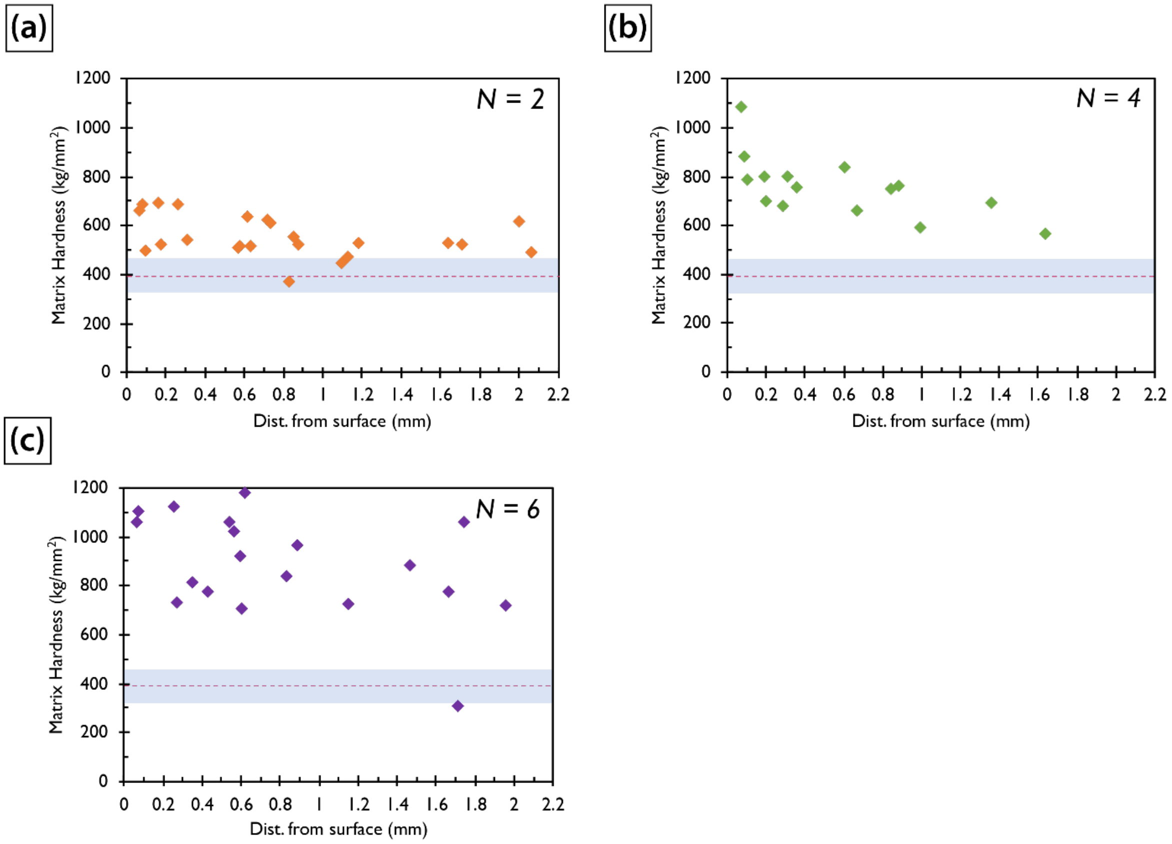

Figure 5.5: Plots of matrix hardness against distance from coupon surface for (a) $N = 2$, (b), $N = 4$, and (c) $N = 6$ impregnation cycles with the $y_p = 6.2\%$ alumina precursor solution, with the initial harness value shown on each plot.

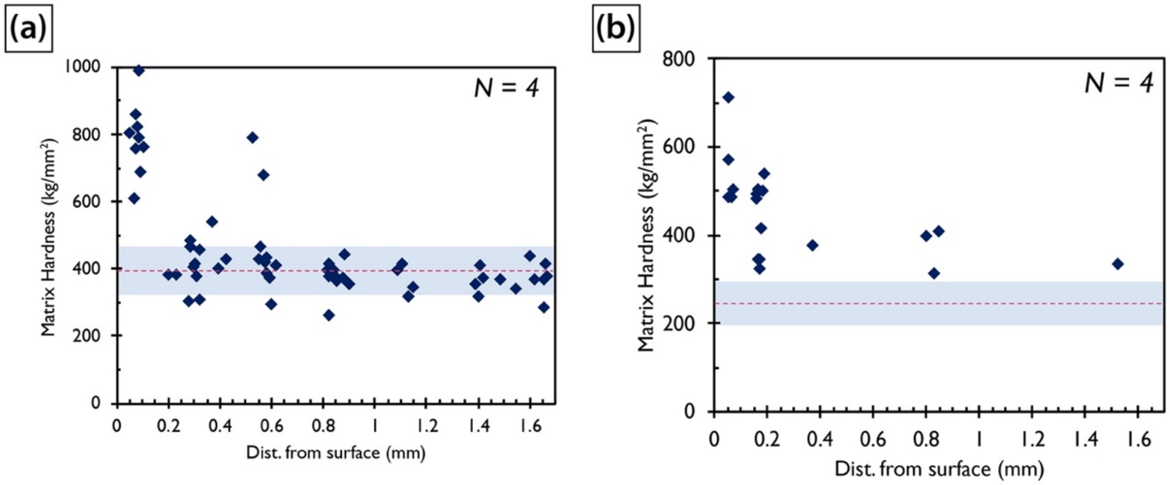

Figure 5.6: Matrix hardness after four cycles of the surface application technique plotted against distance from coupon surface for (a) first generation and (b) second generation supplied OFCCs with initial hardness of each shown on the plots.

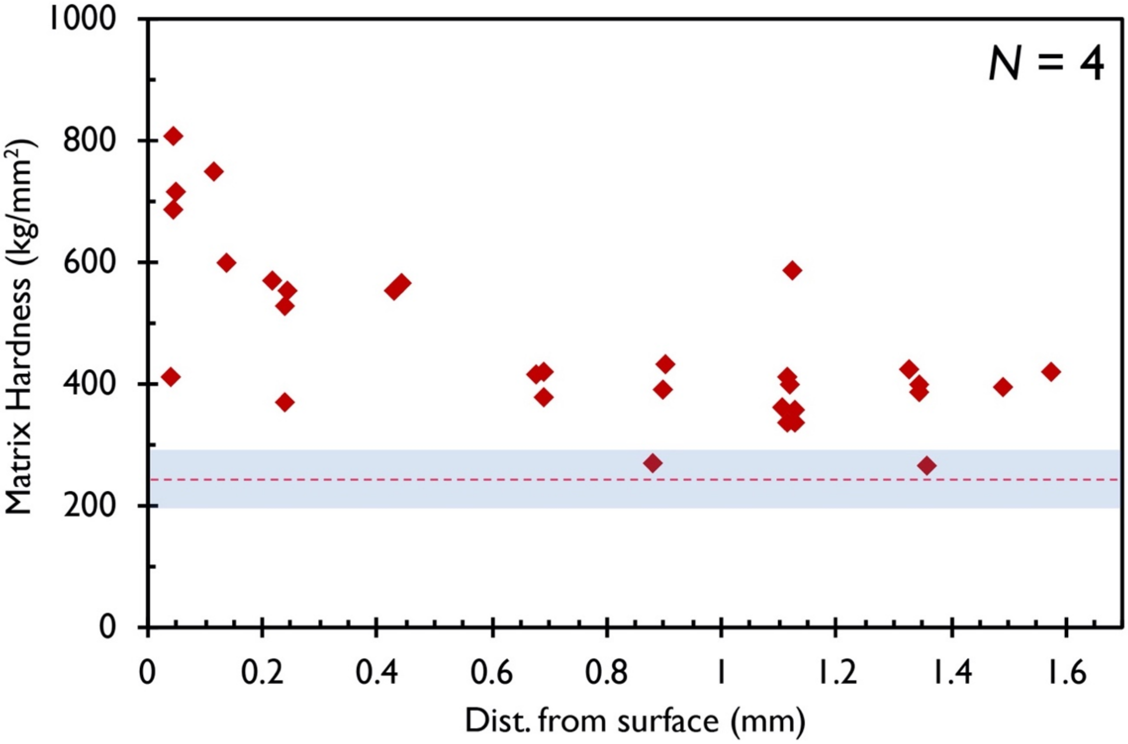

Figure 5.7: Matrix hardness after four cycles of the surface application technique with the 4 mol.% $Y_2O_3 - ZrO_2$ precursor plotted against distance from coupon surface for a second generation supplied OFCC plots.

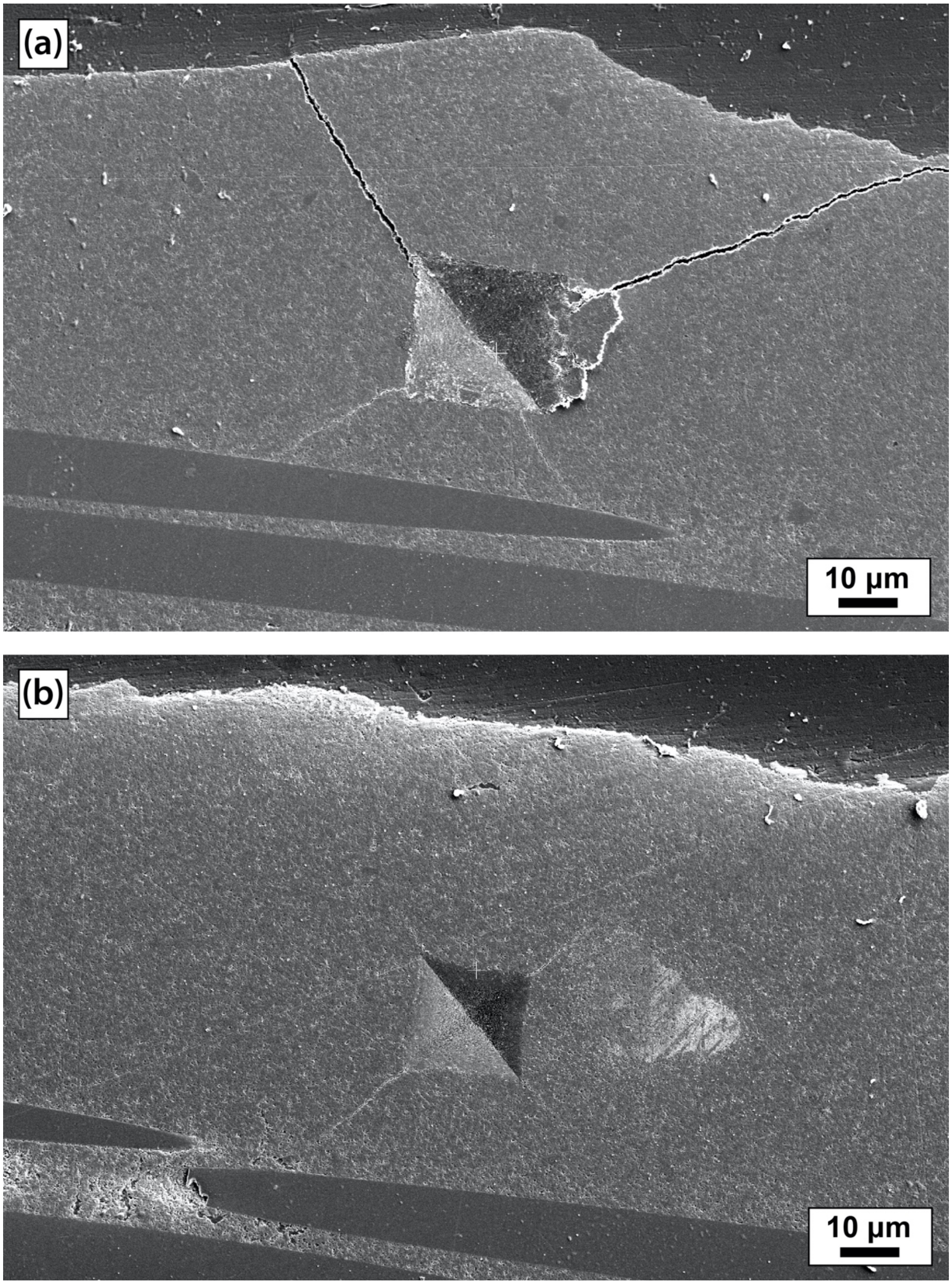

Figure 5.8: Example indents for the surface application of the YSZ precursor, showing similar inconsistent indents near the surface with (a) a larger indent with significant cracking from indents to the surface, and (b) a smaller indent with limited cracking.

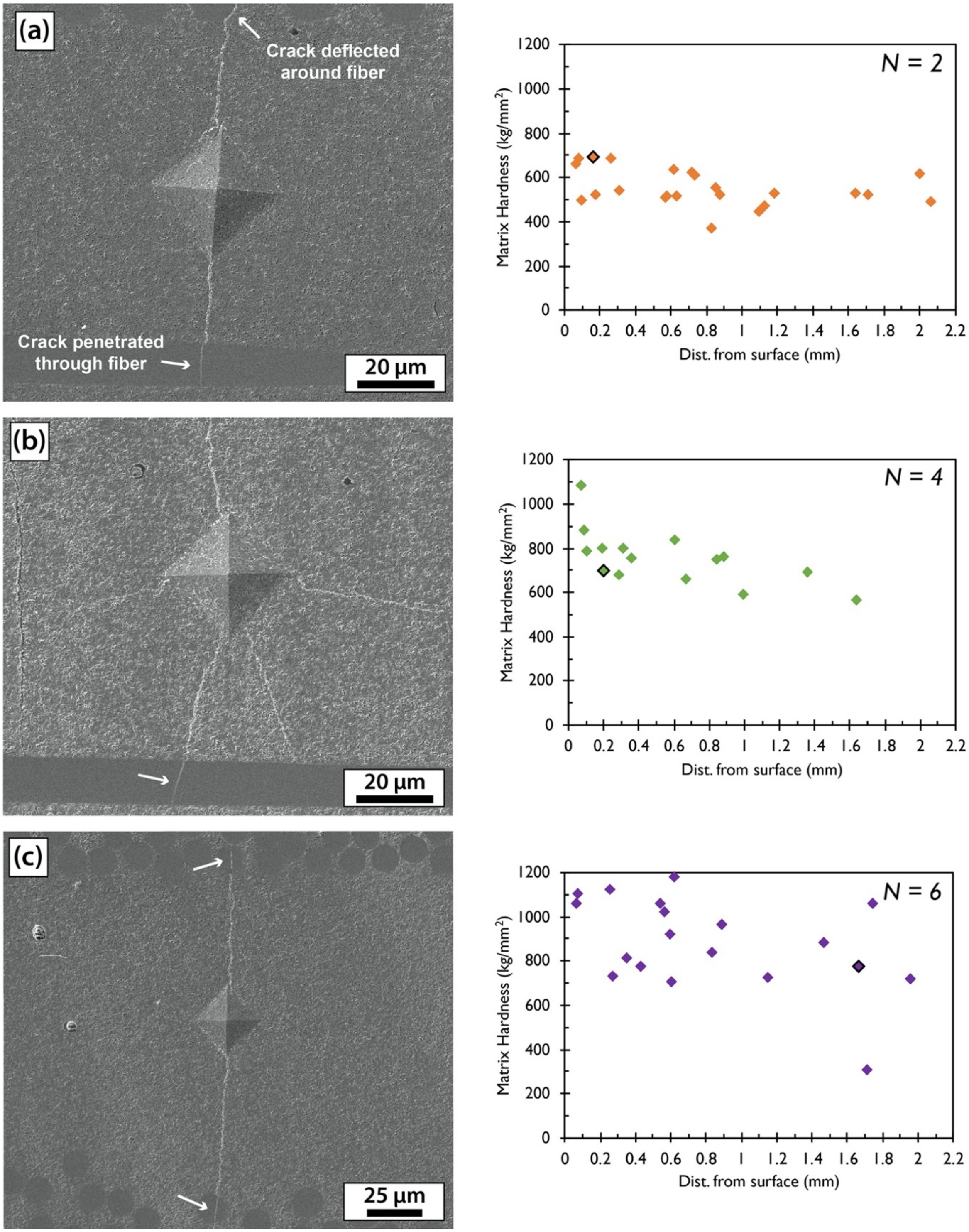

Figure 5.9: Selected indents from the plots of matrix hardness against distance from coupon surface for (a) *N* = 2, (b), *N* = 4, and (c) *N* = 6 impregnation cycles with the y_p = 6.2% alumina precursor solution. Arrows highlight where cracks from indents penetrate nearby fibers.

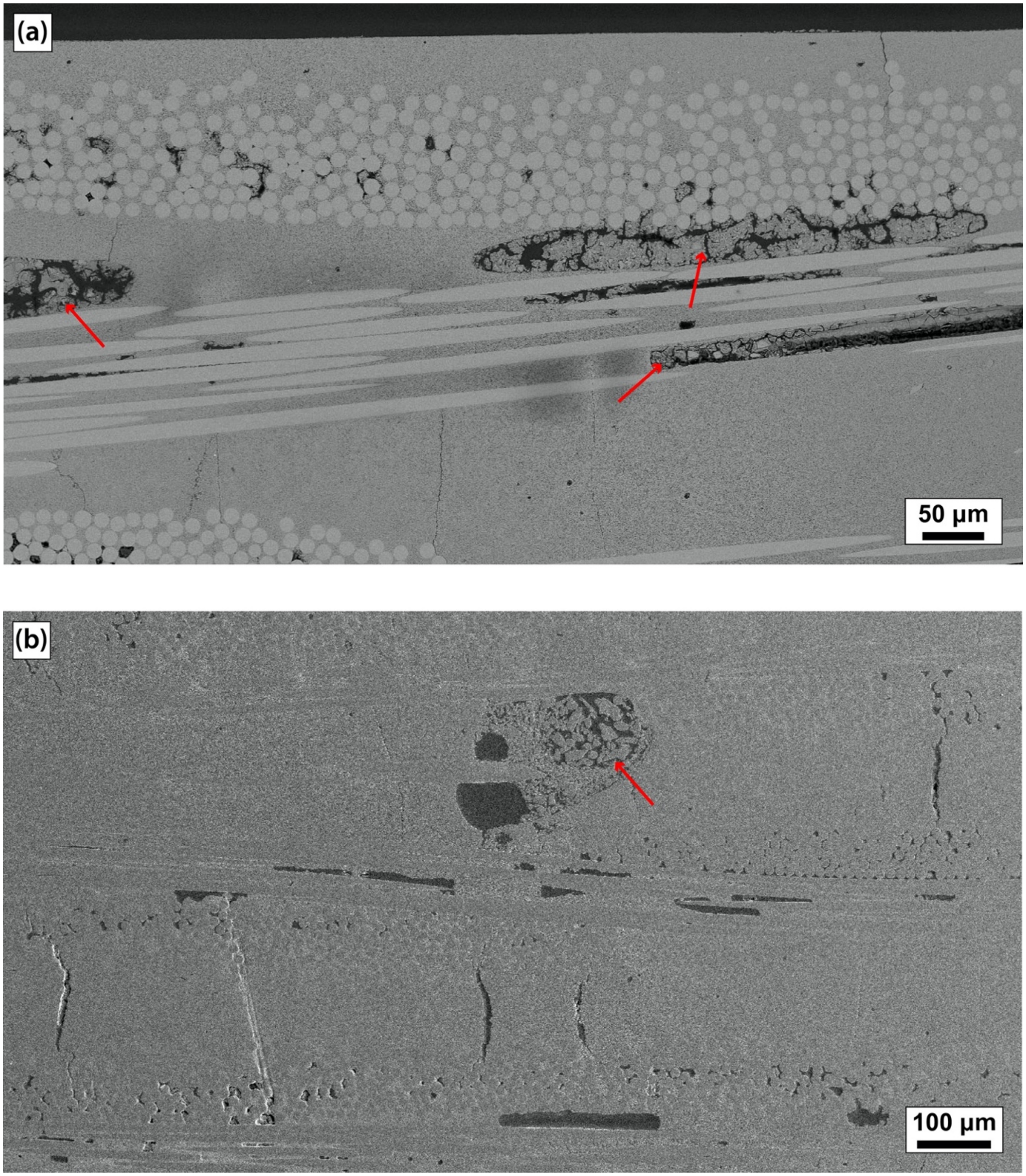

Figure 5.10: SEM cross-section of the *N* = 4, fully impregnated, $y_p = 6.2\%$ alumina precursor sample, with arrows highlighting large voids filled with precursor derived alumina (a) near the surface and (b) deep in the middle of the composite.

Chapter 6: Structure of EB-PVD coatings

Electron beam – physical vapor deposition (EB-PVD) is an advantageous technique for processing thermal barrier coatings (TBCs) on metallic components. EB-PVD produces a columnar microstructure with high in-plane compliance, reducing stresses from the thermal expansion mismatch with the substrate and promoting strain tolerance during thermal cycling. There is much less experience, however, on the use of EB-PVD for improving the thermomechanical compatibility between a T/EBC and an underlying OFCC [33,35]. Additionally, these coatings have good adhesion to alumina when deposited at sufficiently high temperature, which bodes well for adherence to the porous matrix of the OFCCs without requiring detrimental surface preparation or structuring that can damage the composite, as illustrated in **Chapter 4**. While the microstructure generated from EB-PVD promotes the thermomechanical compatibility between the coating and the OFCC, the coating material must still be thermochemically compatible with the OFCC and its constituents for long-term component durability and performance.

The yttria – zirconia system is a favorable system for EB-PVD because of amenability to preserve composition during vapor processing and the resulting favorable properties[98]. Both oxides and their solutions also exhibit superior resistance to volatilization in high temperature water vapor [58]. The yttria – rich side of the system has coefficients of thermal expansion (CTEs) closer to the N720/alumina OFCC, with Y_2O_3 (8 ppm/°C) [99], and $Y_4Zr_3O_{12}$ (YZO) (8-9 ppm/°C) [94] being closer to the OFCC (6-8 ppm/°C) than that of 7YSZ (~12 ppm/°C) [51,92,95], However, as described in **Section 2.4.3**, and demonstrated in **Chapter 4**, the reactivity of all high-yttria candidate T/EBC materials, such as 48YSZ, with both alumina and the N720 fibers would requires a thermochemically compatible diffusion barrier between the top coat and the OFCC for long term stability of the system. It is well established that 7 wt.% yttria stabilized zirconia (7YSZ) is thermochemically compatible with alumina, the primary thermally grown oxide on the superalloys, and would therefore be a candidate for the diffusion barrier between higher yttria-containing materials and OFCCs [64,66]. Because the 7YSZ diffusion barrier would have to be dense to be effective, the CTE mismatch would have to be mitigated by limiting its thickness so the thermal stresses can be tolerated.

While the EB-PVD growth behavior of 7YSZ has been extensively studied, and process parameters reasonably optimized to produce the desired columnar microstructures, there is much less information available in the open literature about the higher yttria-content coatings [33,35]. Understanding their growth behavior is necessary for creating robust and effective T/EBCs. This chapter presents the growth behavior of monolayer 7YSZ, and bilayers of 7YSZ/YZO and 7YSZ/Y_2O_3 on OFCCs and model alumina substrates, highlighting the effect of surface temperature on coating growth, morphology, and texture in all three systems.

6.1 Substrate preparation for EB-PVD

Uncoated OFCC coupons were prepared for EB-PVD using four cycles of the surface application of precursor described in **Chapter 5** to strengthen the surface prior to coating deposition. The hardened surface was then lightly ground with 800 and 1200 grit sandpaper to remove any small residue of precursor or other coarse surface irregularities that could be detrimental to the columnar growth of the EB-PVD coating. Moreover, 500 μm thick dense polycrystalline alumina plates were cut to 25 mm x 25 mm to fit the rotating substrate holder for EB-PVD described in **Section 3.1.5**. Alumina plate substrates were used as a substitute for a alumina thermally grown oxide (TGO) to demonstrate a prototypical 7YSZ TBC in the

UCSB evaporator, as well as to provide a baseline for comparison to growth on OFCC substrates.

6.2 Results

Seven 7YSZ monolayer coatings, two 7YSZ/YZO bilayers, and five 7YSZ/ Y_2O_3 bilayers were deposited and analyzed. Relevant information such as coating thickness and substrate type, and process parameters such as measured surface temperature (T_S), deposition rate, and electron beam power are listed in **Table 6.1**. 7YSZ results are presented first, followed by the two groups of bilayer systems. Because of uncertainty in the pyrometer readings, which had been calibrated for metallic substrates with thin alumina scales, the substrate heater power was also reported to give another qualitative comparison of the surface temperature.

6.3 7YSZ growths on alumina plate substrates

6.3.1 Coating morphology

Alumina plate substrates were used as a surrogate for an alumina thermally grown oxide (TGO) to demonstrate a prototypical 7YSZ TBC in the UCSB evaporator, as well as to provide a baseline for comparison to growth on OFCC substrates. Depositions labeled in **Table 6.1** as 7YSZ-A and 7YSZ-B were both grown on the alumina plates, as previously described, with surface temperature differentiating the two. The observed surface temperature for 7YSZ-A was 1140°C, with a substrate heater power of 56%. The heater power was set to 99% for 7YSZ-B, but the read surface temperature was only 20°C higher, at 1160°C.

The coating surfaces are presented in **Figure 6.1.** The columnar growth tips in 7YSZ-A are consistent with those deposited on pre-oxidized metallic substrates, exhibiting roughened pyramidal shapes.[84] The idealized geometry for ⟨100⟩ columnar growth in cubic systems, with single axis substrate rotation, comprises a pyramidal tip with a square base defined by an arrangement of {111} facets, with one of the sets of [110] colinear ridges along the rotation axis. Elongation of the pyramidal tips is typically seen along the ridge parallel to the rotation axis due to shadowing effects when there is no periodic tilt perpendicular to the rotation axis, as in these experiments and described in more detail in Chapter 2 and [73].

The tips are generally micro-faceted but the crystallographic effects are still present. The ridges are coarsely rounded, and are elongated parallel to the substrate rotation axis, producing a two-fold symmetry football-like shape, (or the keel grooving of a ship hull). Additionally, the nominal apexes of the tips are not sharp but rather exhibit a rough or corrugated morphology. The corrugated centers of the larger columns are a collection of small facets that look like the tips of many “mini-columns.” The football shaped column tips are consistent with a [100] growth direction in 7YSZ, and has been observed in depositions at temperatures of order 900-1100°C. [73], seen in **Section 2.6.4** and **Figure 2.11**. “Roughened, elongated pyramidal tips” is used henceforth as a descriptor for this morphology. The 7YSZ-B coatings in **Figure 6.1 (c,d)** exhibit two directions of roof-top-like tips, aligned ± 60° off the substrate rotation axis, along with trigonal pyramidal column tips. This deviates from typical morphologies but it has been previously reported in the literature, and is discussed in **Section 2.6.4** and illustrated in **Figure 2.8**.

In cross-section, seen in **Figure 6.2**, the columns of 7YSZ-A appear more regular in width and shape, whereas the columns of 7YSZ-B are irregular in morphology, which agrees with the observation of competing column growth directions. It is noted that in these images the axis of rotation is out of the page, so it is possible there may be tilts in the column orientation in 7YSZ-B. This issue is discussed later.

6.3.2 Coating texture

X-ray reflections for the tetragonal 7YSZ are presented as pseudo-cubic (PC), rather than as the conventional tetragonal unit cell for easy comparison to the cubic phases presented later in the chapter and in literature. Surface XRD scans of 7YSZ-A and-B in **Figure 6.3** exhibit substantial (200_{PC}) peaks for both coatings. However, 7YSZ-B shows an additional and stronger (311_{PC}) peak, indicating that the latter growth direction becomes strongly competitive with (200_{PC}). 7YSZ-A shows only the strong (200_{PC}) peak, indicating the more conventional growth direction in EB-PVD of 7YSZ.

Pole figures for 7YSZ-A show the intensity patterns in the (200_{PC}) pole, **Figure 6.4 (a)**, and the (220_{PC}) pole, **Figure 6.4 (b)**, as expected for the ⟨100⟩ pyramidal columnar growth, with a single intensity spot near the origin in the (200_{PC}) pole, and a pattern of four intensity spots at $\varphi = 0°$, 90°, 180°, and 270°, each 45° from the origin ($\rho = 45°$) in the (220_{PC}) pole, a variation of the ideal 4-fold symmetry of aligned square pyramidal column tips, with intensity stretching in the axis of substrate rotation, which is also consistent with the elongated column tips. The pole figures for 7YSZ-B in **Figure 6.4 (c)** do show a strong (200_{PC}) intensity out-of-plane. The intensity pattern is off center due to an artifact with mounting the thin plate in the diffractometer. The (220_{PC}) pole in **Figure 6.4 (d)** shows a combination of the patterns for the two different 60° oriented roof-top column tips, with intensity spots in the (220_{PC}) pole at ($\rho = 45°$) and ideally $\varphi = 60°$, 150°, 240°, and 330° for one orientation, and $\varphi = 30°$, 120°, 210°, and 300° for the other. One of these eight intensity spots is missing, likely due to a tilt in the thin plate when it was mounted in the diffractometer, as no tilt was observed in the columns in the cross-section images. The (311_{PC}) pole was acquired as well, shown in **Figure 6.4 (e)**. The intensity pattern is not a single spot in the middle, but four spots near the center. These spots are close enough to normal to contribute to the intensity of the (311_{PC}) peak in the surface XRD scan. The three pole figures for 7YSZ-B show there is competition between the $\langle 100_{PC} \rangle$ and $\langle 311_{PC} \rangle$ growth directions despite the large intensity the (311_{PC}) peak in the surface XRD scan.

6.4 Comparing 7YSZ growth on OFCC versus alumina plate substrates

6.4.1 Coating morphology

The coatings 7YSZ-C and 7YSZ-D were samples from the same EB-PVD run but with different substrates, with 7YSZ-C deposited on a 25 mm x 25 mm x 0.5 mm alumina plate, and 7YSZ-D on an OFCC coupon. Both coatings are 50 μm thick 7YSZ. While both being from the same run of the evaporator, there are some expected differences in the surface temperature between 7YSZ-C and 7YSZ-D because of the differences in coating material and microstructure. The primary means of increasing surface temperature in the system is backside heating, so 7YSZ-C, which was deposited on a 0.5 mm thick, dense alumina plate, would be expected to have a higher growth surface temperature than 7YSZ-D, which was deposited on a 2.7 mm thick, porous alumina matrix OFCC, not just because of the thicker substrate, but also because of the lower thermal conductivity of the porous OFCC.

The surfaces of both coatings are shown in **Figure 6.5**. The surface of 7YSZ-C, in **Figure 6.5 (a)** and **(b),** showed two column tip geometries, one being the ‘roof-top’ tip morphology oriented ± 60° from the substrate rotation axis, and the secondary observed column tip geometry are triangular pyramidal tips, corresponding to a $\langle 311_{PC} \rangle$ column growth direction, although these are less extensive than the roof-top tips. The tip geometries are identified and labelled in **Figure 6.5 (b)**. The OFCC substrate, 7YSZ-D, shown in **Figure 6.5 (c)** and **(d)**, also had two dominating column tip morphologies: sharply faceted square pyramidal tips, and two orientations of 'rooftop' tips, aligned ± 60° off the substrate rotation axis.

In cross-section, the columnar growth of 7YSZ-C and -D appeared less uniform than that in **Figure 6.2**, as shown in **Figure 6.6 (a)** and **(c)**, respectively. About halfway through the thickness of the coatings, there was a discontinuity in the column growth because of an electron beam instantaneous shut down and re-start issue about halfway through the deposition process. However, the interruption did not appear to have a significant impact in the continued growth of the 7YSZ. Higher magnification of the column tips of 7YSZ-C and -D in **Figure 6.6 (b)** and **(d)**, respectively, also show multiple column tip morphologies.

6.4.2 Coating texture

Surface XRD scans of the 7YSZ-C and -D shown in **Figure 6.3** reveal a strong (200_{PC}) peak in both coatings, suggesting a strong ⟨100⟩ out-of-plane texture. The (002_{PC}) reflection is also present in both coatings, slightly more intense in 7YSZ-D. A small (311_{PC}) peak is present in 7YSZ-C, reminiscent of those found for 7YSZ depositions in literature at $T_S \approx$ 1100°C [73]. The pole figures of these coatings in **Figure 6.7** provide additional insight on the crystallographic texture. The (200_{PC}) pole figures in **Figure 6.7 (a)** and **(c)** confirm the expected ⟨100⟩ texture albeit much less defined. The strong intensity pattern near the edges of **Figure 6.7 (a)** were an artifact of how the coated plate was mounted in the diffractometer, but the figure still showed the intensity spot near the origin of the pole, so the presumed out-of-plane texture is ⟨100⟩. The intensity pattern of the (220_{PC}) pole figure for 7YSZ-C in **Figure 6.7 (b)** suggests a competition of in-plane orientations, consistent with the multiple observed column tip morphologies on the surface in **Figure 6.5 (a)** and **(b)**. The (200_{PC}) pole figure for 7YSZ-D in **Figure 6.7 (c)** and the (220_{PC}) pole in **Figure 6.7 (d)** have much cleaner patterns consistent with ⟨100⟩ texture, expected from the observed square pyramidal – type column tips, both in- and out-of-plane. This suggests that the texture corresponding to square pyramidal tips was dominant in 7YSZ-D despite the observation of rooftop column tips in **Figure 6.5 (c)** and **(d)**.

6.5 7YSZ depositions on OFCCs

6.5.1 Coating morphology

EB-PVD single layers of 7YSZ were deposited on OFCC substrates, with targeted deposition surface temperatures of 1000°C and 1100°C, and average measured surface temperatures of 1030°C and 1085°C respectively. SEM images of the coating surfaces are presented in **Figure 6.8**. The surface of 7YSZ-E, seen in **Figure 6.8 (a, b)**, exhibits a column tip morphology similar to the roughened, elongated pyramids of 7YSZ-A presented in **Figure 6.1 (a, b)**; however, the tips are somewhat coarser and have rougher surfaces. Despite the irregular shape of the column tips , they still show evidence of octahedral {111} microfacets, and are elongated in the direction of the substrate rotation axis.

The column tips elongation, and the rough or 'corrugated' surfaces are consistent with lower temperature 7YSZ depositions in literature [73]. The surface of 7YSZ-F, presented in **Figure 6.8 (c,d)**, shows a very different morphology. The observed column tips appear to be one orientation of the roof-top type with the long axis of the tip aligned about 60° off the substrate rotation axis. This ridge also exhibits a similar corrugated morphology of small facets as 7YSZ-E. This type of column growth has been observed in stationary 7YSZ depositions [83], However, the expected morphology was sharply faceted, square pyramidal column tips given the substrate rotation and a surface temperature near 1100°C [73].

In cross-section, shown in **Figure 6.9 (a,b)**, coating 7YSZ-E shows well-formed columnar growth with expected feathery porosity within the columns themselves. Higher magnification of column tips in **Figure 6.9 (b)** reveal the columns terminate with rounded tips which is again consistent with a lower surface temperature 7YSZ columnar growth in EB-PVD rather than the more typical 1000°C [73]. Cross-sections of coating 7YSZ-F in **Figure 6.9 (c,d)** show the columnar growth that terminates with the roof-top tips. The columns appear finer, as the cross-section does not cut through the long axis of the roof-top columns.

6.5.2 Coating texture

Surface x-ray diffraction (XRD) scans of the coatings are presented in **Figure 6.3.** The scans from the two coatings both have strong (200_{PC}) peaks, and the 7YSZ-F Coating exhibits a weak peak at (311_{PC}). The scans reveal a strong ⟨100⟩ out-of-plane texture in both coatings, which are in agreement with the observed columns tips; both the roof-top and roughened, elongated pyramidal column tips correspond to a ⟨100⟩ growth direction and out-of-plane texture. Pole figure scans presented in **Figure 6.10** provide a more complete description of the coatings' texture. The 7YSZ-E (200_{PC}) and (220_{PC}) pole figures presented in **Figure 6.10 (a,b)**, respectively, confirm the expected (100) out-of-plane texture and in-plane texture corresponding to the growth suggested by square pyramidal – derived column tips. Both pole figures show intensity stretching along the direction of the rotation axis, which is consistent with the observed elongation of the column tips. It is a phenomenon reported with EB-PVD growth with single axis substrate rotation, and is more severe at lower surface temperatures [73,84,100], with the stretching reduced at higher surface temperatures. The 7YSZ-F (200_{PC}) and (220_{PC}) pole figures presented in **Figure 6.10 (c,d)**, respectively, tell a different story. The out-of-plane texture is ⟨100⟩ as suggested by surface XRD, albeit with a ~10° column tilt also observed in cross-section in Error! Reference source not found. **(c)**. The in-plane texture revealed by the (220_{PC}) in **Figure 6.10 (d)** is consistent with the observed 60° off-rotation-axis orientation of the roof-top column tips in the surface images. There was not the same type of intensity stretching in either of the 7YSZ-F pole figures that was observed in the 7YSZ-E pole figures.

6.6 25 μm coating growth

7YSZ-Gwas analyzed after 25 μm of deposition at 1085°C. This was the targeted thickness for the 7YSZ barrier layers in the bilayer depositions presented later in this chapter. The surface, seen in **Figure 6.11**, show both square pyramidal type column tips and roof-top tips visible. Surface XRD in **Figure 6.3** shows a very strong (200_{PC}) peak, but a small (002_{PC}) peak, corresponding to the longer, *c*-axis of the t-7YSZ, is also present, suggesting that some of the square pyramidal tips exhibit the *c*-orientation in the tetragonal structure of 7YSZ. The dimensional difference is only ~2% larger than the *a* or *b* directions, so there is not a suspected morphology difference for the *c* orientation [73]. The (200_{PC}) and (220_{PC}) pole figures in **Figure 6.12** exhibit clean intensity patterns much closer to the ideal in-plane and out-of-plane texture for the idealized square pyramidal tipped columnar growth[73], suggesting they are the dominant morphology. The intensity streaking along the axis of substrate rotation is also seen, although it is not as severe as in 7YSZ-A and 7YSZ-E. At this thickness, only 25 um, evolutionary selection is still ongoing, so the c-axis has not been superseded by the a- and b- axes. This can also explain the larger intensity dispersions in the pole figures.

6.7 7YSZ / YZO bilayer coatings

6.7.1 YZO coating morphology

Two 7YSZ/YZO bilayers were studied, designated YZO-A and YZO-B, deposited at target temperatures of 1000°C and 1100°C, respectively, with average measured temperatures of 1050°C and 1095°C, respectively. Surface images of the two bilayers are shown in **Figure 6.13**. Both coatings exhibit column tips that are closer to the idealized square pyramidal column tips than those observed for any of the 7YSZ coatings, with more defined facets and sharper tips with less corrugation. The tips are still slightly elongated along the rotation axis. The column tips are larger in YZO-B due to the thicker coating, but, overall, the surfaces of the coatings are similar.

Cross-section images in **Figure 6.14** show good columnar growth and well-formed feathery porosity within the columns up to the tips. There is some column tilt in YZO-B, roughly 10°, with none seen in YZO-A. Higher magnification reveals differences at the 7YSZ/YZO interface of the two coatings, shown in **Figure 6.15.** YZO-A, in **Figure 6.15 (a)**, has a discontinuity in the columnar growth between the two materials, evident by the fan-like structures on the YZO side of the interface indicating some renucleation with epitaxial growth in some cases, manifested as continuity of the feather arms from the YSZ to the YZO. The interface in YZO-B, in **Figure 6.15 (b)**, exhibited fewer fan-like structures, and the columnar growth was uninterrupted between the 7YSZ and YZO layers. Regardless of the morphology of the 7-YSZ interlayer, YZO grew with the desired microstructure of well-formed ⟨100⟩ columns with square pyramidal tips.

6.7.2 Coating texture

Surface XRD scans in **Figure 6.16** are similar, with both YZO-A and YZO-B having very strong (200) peaks, with a weak (311) reflection present in both scans. (200) pole figures for both samples in **Figure 6.17** confirm strong ⟨100⟩ out of plane texture expected from the surface morphology and XRD scans. The (220) poles exhibited four spot intensity patterns that were also as suggested from the square pyramidal – like tip morphology. YZO-A had greater intensity streaking in the direction of the substrate rotation axis in both poles, which was also likely from the lower deposition temperature. The intensity spots were more circular in the poles of YZO-B.

6.8 7YSZ / yttria bilayer coatings

6.8.1 Yttria coating morphology

Coating surfaces in **Figure 6.18** show the surface morphology of Y_2O_3-A and Y_2O_3-B, the two coatings deposited at a target of 1000°C, both with measured surface temperature of 1035°C. The main differences between the two separate depositions were the yttria topcoat deposition rate and thickness. These coatings showed well-defined, sharply facetted square pyramidal column tips. The tips appear less aligned in Y_2O_3-B arguably because of the less developed evolutionary selection in the thinner coating. Cross sections in **Figure 6.19** and **Figure 6.20** further confirm observations of the surface images. The 1000°C depositions in (a) and (b) show good columnar growth with distinctly visible feather arm porosity that is characteristic of the desired EB-PVD microstructures. Close examination of the 7YSZ/yttria interface in **Figure 6.19 (d)** and **Figure 6.20 (d)** show an interruption of columnar growth at the transition between the 7YSZ and yttria layers, manifesting in a fan-like pattern of renucleation of the yttria before columnar growth takes over. The lack of continuity in the columnar structure suggests absence of epitaxy in the growth of yttria on 7YSZ, but the texture still develop in the top layer owing to evolutionary selection.

The higher temperature depositions, Y_2O_3-C, -D, and -E, were deposited with a target temperature of 1100°C, with measured surface temperatures of 1080°C, 1070°C, and 1095°C, respectively. Surface micrographs of Y_2O_3-C, -D, and -E in **Figure 6.21** show more irregular microstructures in the higher temperature coatings, with much finer column tips with some distorted and curved pyramidal column tips observed.

Cross-sections of Y_2O_3-C and Y_2O_3-D in **Figure 6.22** and **Figure 6.23** show fairly narrow columns that further segmented into smaller columns during growth, and without much feather arm porosity visible. The yttria growth seen in cross-section of Y_2O_3-E in **Figure 6.24** are significantly branched with diverging crystallites, more so than Y_2O_3-C and Y_2O_3-D, but the columns similarly terminate in the fine column tips seen in the surface images. All three coatings show a defined columnar structure despite the irregular surface morphologies. The 7YSZ/yttria interface in all of the higher temperature coatings, seen in **Figure 6.22 (d)**, **Figure 6.23 (d)**, and **Figure 6.24 (d)**, show the evidence of renucleation at the beginning of the yttria layer also seen in the lower temperature depositions, also indicating a general absence of epitaxial growth.

6.8.2 Yttria coating texture

Surface XRD scans in **Figure 6.25** provide some insight into coating texture but are not sufficient to fully characterize it. Scans of the two lower temperature depositions, **(a)** and **(b)**, show strong (400) peaks that dwarf all other reflections. The (400) reflection for yttria in the bixbyite structure is equivalent to the (200) reflection in the fluorite phase because of the reduced symmetry and enlarged unit cell for bixbyite. The higher temperature depositions,

(c), **(d)**, and **(e)** have more visible peaks, and in the case of **(e)**, peaks and intensities that are closer to those of an yttria powder scan, suggesting no strong texture. However, **(c)** and **(d)** exhibit a greater-than-normal intensity of the (400) reflection, but other peaks are present, suggesting a weakly textured coating.

Pole figures are necessary to better characterize the crystallographic texture. Pole figures generated using the (400) and (440) reflections in **Figure 6.26** indicate a strong texture in the yttria layers in Y_2O_3-A and Y_2O_3-B with a strong ⟨100⟩ texture along the growth direction normal to the substrate. The pattern of the (440) pole figures are consistent with the morphology of the surface images. The intensity patterns in both (400) and (440) pole figures in **Figure 6.26** are slightly elongated in the direction parallel to the substrate rotation.

The (400) pole figure for Y_2O_3-C in **Figure 6.27 (a)** showed broad intensity near the center, with the peak intensity ~20° off normal, along the rotation axis. This can be a result of tilted columnar growth, however such severe tilt was not observed in cross-section normal to the rotation axis. The (440) pole figure in **Figure 6.27 (b)** showed an intensity pattern that looked similar to that of square pyramidal – tipped ⟨100⟩ columns, but tilted ~20°. Once again, evidence of such column tilt was not observed in cross-section. These intensity patterns are attributed to many competing growth directions. The pole figures for Y_2O_3-D in **Figure 6.27 (c)** and **(d)** are more complicated. The (400) pole shows a broad intensity dispersion, especially parallel to the substrate rotation axis, centered about the substrate normal. The dispersion pattern seen in the (440) pole figure is likely from the competition of multiple competing column growth directions. Pole figures of Y_2O_3-E in **Figure 6.27 (e)** and **(f)** show an intensity dispersion characteristic of a lack of texture, in both the (400) and (440) reflections. This agrees with the apparent lack of texture seen in the surface XRD scan in

Figure 6.25, as well as the observed branching of the columns seen in cross-section. Contrary to other segmented microcolumns these do not share a relatively common orientation.

6.8.3 Extensive N720 grain growth

An additional effect of higher temperature depositions was found with the backsides of the 1100°C targeted growths on OFCC substrates after deposition. **Figure 6.28** shows the backside, the surface facing the heating element, of **(a)**, 7YSZ-A, deposited at 1035°C, and **(b)**, sample Y_2O_3-E, deposited at 1095°C, and Despite a measured surface temperature difference of only 60°C, the backside in **Figure 6.28 (b)** shows significant signs of matrix sintering, with surface mudcracks visible on the entire surface. **Figure 6.28 (a)** does not show any visible signs of sintering, only some discoloration from the SiC heating element. In cross-section, N720 fibers in the OFCC near the backside surface show extensive grain growth, shown in **Figure 6.29 (a)**, and an SEM EDS elemental map in **Figure 6.30** confirmed the larger grains were alumina. The 3-5μm size of these alumina grains in the N720 fibers is significantly larger than the initial grain size of 70 nm [97]. Using a parabolic grain growth model [45] which follows the form:

$$\mathrm{d}^{\mathrm{n}} - \mathrm{d_0}^{\mathrm{n}} = \mathrm{Kte}^{-\mathrm{Q/RT}} \qquad \textbf{6.1}$$

Where d is grain size, d_0 is initial grain size, n is the grain growth exponent, K is a constant, t is time, Q is the activation energy, R is the gas constant, and T is temperature. Using values from Hay et al.[97] on the growth of alumina grains within N720 fibers, listed in **Table 6.2**, the backside temperature can be approximated. The deposition time for the sample in **Figure 6.29** was 2 hours. Using the values from Hay et al., and given a time at temperature of 2 hours, the approximate temperature of the backside surface was calculated to be 1608°C.

There was no visible grain growth in the fibers at or near the coated surface that faced the vapor plume. As seen in **Figure 6.29 (b)**, there is no visible grain growth in the N720 fibers near the coated surface of the same coated sample. Based on the model and results of Hay, it can be assumed that that surface reached a temperature no greater than 1300°C. To test this calculation, an uncoated OFCC coupon was annealed for 2 h at 1600°C. **Figure 6.31** shows fibers from this coupon in cross-section. The alumina grains in these fibers are noticeably larger than the backside of the EB-PVD coated substrate OFCC in **Figure 6.29**. This suggests the backside temperature was close to, but below 1600°C.

6.9 Discussion

6.9.1 Overall comparisons

EB-PVD coatings of all compositions have been grown on a porous substrate, with microstructures known for strain tolerance. The structures of the three compositions, 7YSZ, YZO, and Y_2O_3, are all derivatives of the fluorite crystal structure. 7YSZ is a tetragonal distortion, YZO is a variant of fluorite with partial anion and cation ordering [101], and yttria is a ordered anion vacancy derivative typically known as bixbyite [102]. The well-related structures behave in the expected manner given their crystallography, and generally grow with a $\langle 100 \rangle$ orientation with square pyramidal – type column tips, given the correct temperature range. Morphology variations are seen at higher temperatures: roughening and microfacetting of the tips, different column growth geometries and directions showing up in 7YSZ, and column branching in Y_2O_3 growth. Some of these other morphologies seen may not be as strain compliant.

When comparing the EB-PVD growth morphology of 7YSZ, YZO, and yttria to each other, one must consider both surface diffusion and competing growth directions. Greater surface diffusion will lead to sharper facets and more isotropic columnar growth, even with single axis substrate rotation. However, with increased surface diffusion, higher energy growth directions and morphologies become more competitive.

Homologous temperature, or temperature relative to that material's melting point (T/T_{M}), can explain some of the morphology characteristics in the yttria depositions. Yttria has a lower melting point (2454°C, or 2707 K), than 7YSZ (~2800°C, or 3073 K) or YZO (~2625°C, or 2898 K). The homologous temperature for each of the topcoat materials is presented in **Table 6.1** for each deposition. At the surface temperatures of the depositions presented in this chapter, yttria was at a higher homologous temperature. Surface diffusion is known to scale with homologous temperature [75], and the increased surface diffusion in yttria can explain the sharpest faceted, and most isotropic square pyramidal column tips, compared to 7YSZ or YZO, at the lower surface temperature depositions. However, homologous temperature is not the whole rationale for explaining the irregular surface morphology and loss of strong texture at the higher surface temperature depositions. Likewise, homologous temperature cannot be the explanation for the difference in the 7YSZ and YZO morphologies, notably the sharper faceted column tips in the YZO coatings at the lower temperature. Increased surface diffusion is still likely the explanation, but the difference is a consequence of the different crystal structures between the two compositions. Schulz et al. [103] suggested that RE-zirconates in the fluorite structure, like YZO in the presented work, have greater surface diffusion than tetragonally structured RE-stabilized zirconias, like 7YSZ. The slight difference in the coordination of the tetragonal phase changes the surface energies and thus the crystal growth conditions. They concluded that growth in the cubic phase, 20YSZ, has sharper facets and more regular topography, which is consistent with the observations in the presented work.

The crystallographic differences, namely the reduced symmetries in the tetragonal 7YSZ and bixbyite yttria, are the likely reason behind the prevalence of competing growth directions in 7YSZ and yttria coatings. In 7YSZ there is a progression of prevalent growth directions and morphologies with increasing surface temperature, where in yttria the reduced symmetry in the bixbyite structure leads to irregular column tip morphology, and weakly textured, or untextured coatings, with narrow, branching columns at higher temperatures. The fluorite structure of YZO does not appear to have growth directions competitive with the ⟨100⟩, like the ⟨311⟩ in 7YSZ. The ⟨100⟩ square pyramidal-tipped configuration is lower in energy in this system such that no other configurations are prevalent at the greater surface temperature depositions.

6.9.2 Origins of 7YSZ column growth morphology

The column morphologies observed in the presented 7YSZ depositions are consistent with previous observations – the roughened pyramid, rooftop, and triangular pyramidal geometry have all been reported in literature [73,83,85]. However, the conditions in which these geometries are observed, and the orientation of the roof-top tips are not well established or understood as column orientations compete through evolutionary selection along the thickness of the coating. Small variations in surface temperature, deposition rate, rotation rate, coating thickness, and substrate can cause the roof-top type column tips to be prominent. In EB-PVD growth with substrate rotation, column tips form in a geometry to balance the vapor flux to each face. Growth models for non-square pyramidal column tips are not well-developed, and would be useful for investigating the evolutionary prevalence of the ± 60° orientation of the rooftop tips. As is, there is not enough information to elucidate the origin of the ± 60° orientation off the substrate rotation axis of the rooftop tips observed.

The dominance of these tips is partially a result of increased surface temperature, as that was the primary difference in process parameters among the presented 7YSZ coatings, and the roof-top tips were only observed in the depositions with a higher reported temperature or greater backside heater power. Especially when comparing 7YSZ-C and 7YSZ-D, where the only difference between the two was the substrate, as they were both from the same run of the evaporator. As described above, the thinner, denser alumina plate substrate, 7YSZ-C, was at a higher surface temperature because of the backside heating. 7YSZ-C showed no square-pyramidal tips, and only rooftop tips, whereas 7YSZ-D showed many square pyramidal tips. Additionally, the major difference between coatings 7YSZ-A and 7YSZ-B, both on alumina plates, was surface temperature. While the pyrometer surface temperature readings of the two depositions were inconsistent, there was a qualitative difference in the surface temperature given the much greater heater power in 7YSZ-B. Roughened, elongated pyramidal tips were observed in 7YSZ-A, and the oriented rooftop tips were observed in 7YSZ-B.

6.9.3 7YSZ EB-PVD growth morphology progression

Three surface temperature regimes were probed with these 7YSZ growths. Target temperature of 1000°C on OFCC substrates, (observed temperatures 1035°C, heater power 62%), target temperature of 1100°C on OFCC substrates, (observed temperatures of ~1085°C, heater power 95%), and 1100+°C on alumina plate substrates. While there was doubt in the accuracy of the pyrometer readings, as described earlier in this section, the backside heater power gives another qualitative comparison between the temperatures of the depositions. Through analyzing coatings in these temperature regimes and the different thicknesses of the growths, insight will be given into the morphology progression of 7YSZ as thickness and temperature increase.

At the target T_S of 1000°C on OFCC substrates, measured temperature 1035°C, the ⟨100⟩ direction, growth morphology with roughened, elongated pyramidal column tips dominate with little to no presence of additional growth directions. The column tips are rough and corrugated, a sign of reduced surface diffusion at the lower deposition temperatures. Despite the measured temperature of 1035°C, the roughness of the column tips, along with the intensity streaking in the pole figures were characteristic of lower temperature 7YSZ growths in literature at 900°C [73].

With an increase to a target surface temperature of 1100°C on OFCCs, the expected growth morphology would have still been square pyramidal column tips, but with sharper faceted tips, like those seen in work by Terry [73], with occasional ⟨311⟩ triangular pyramidal tips. Instead, roof-top tips were extensively observed. At lower coating thicknesses, in 7YSZ-C and 7YSZ-E, at 50 µm and 25 µm, respectively, $\langle 100_{PC} \rangle$ columnar growth, with column tips resembling the square pyramidal geometry are still dominant, seen by the pole figures for 7YSZ-C and 7YSZ-E, despite the significant presence of the roof-top-tipped columns observed in the surface images in both coatings. As the 7YSZ grows thicker, the roof-top-tipped columns start to dominate, and by evolutionary selection, crowd out most of the square pyramidal columns. Two directions of the roof-top tips, ± 60° off the substrate rotation axis, were initially present, but as the 7YSZ thickness further increased, one of the directions became dominant, and was the only orientation observed.

Even greater surface temperatures were achieved when 1100°C was targeted on alumina plate substrates. At lower thicknesses, up to 50 μm, the angular tips were more prevalent than square pyramidal tips at 1140°C in 7YSZ-D. As 7YSZ grew thicker at the higher temperature, up to 120 μm thick, both orientations of angular tips were still visible, along with many $\langle 311_{PC} \rangle$ growth direction triangular pyramidal column tips, in 7YSZ-G. Pole figures did show that the angular tips were dominant, but the relatively large (311_{PC}) peak in the surface XRD scan indicated that the $\langle 311_{PC} \rangle$ columns could become dominant over a thicker or higher temperature growth. A rationale based on the accumulation of vapor deposited during a sunrise-sunset cycle is not available for the $\langle 311_{PC} \rangle$ orientation, as it is for the $\langle 100_{PC}]$ as discussed in Chapter 2.

6.9.4 YZO based coatings

The two YZO bilayer coatings both had uninterrupted columnar growth with the desired morphology, columns terminating in a tip morphology more closely resembling the idealized square pyramidal geometry. When compared to the 7YSZ growths, the YZO layers grew with much sharper facetted column tips, especially at the lower deposition temperatures. Deposition temperature did not appear to have a strong impact on the surface morphology of the coating. The column tips of the 1095°C deposition did not appear more sharply facetted, although the pole figures in **Figure 6.17** did show less intensity streaking along the rotation axis, likely because of the greater deposition surface temperature compared to YZO-A. Overall, the growth morphology of YZO coatings appear relatively insensitive to surface temperature in the explored range.

YZO did show some evidence of growing epitaxially on the 7YSZ interlayer in the higher temperature deposition. Epitaxial growth is preferred for bilayer EB-PVD coatings [64] to minimize excess porosity at the interface that may coarsen over time and lead to ready fracture paths parallel to the coating. Therefore, performance of 7YSZ/YZO bilayer coatings that have epitaxial growth of the YZO layer are expected to have better performance and longevity in operation at high temperatures and long durations. However, further experimental testing of this hypothesis was out of the scope of the presented dissertation.

6.9.5 Yttria based coatings

Yttria coating morphology was found to be particularly sensitive to process parameters, specifically surface temperature and deposition rate. At lower surface temperatures in Y_2O_3-A and Y_2O_3-B, the yttria layer grows in a clean microstructure of sharply facetted, square pyramidal – tipped, ⟨100⟩ columns. The texture and morphology manifested quickly, as evident by the well-defined surface morphology and in- and out-of-plane texture in Y_2O_3-B, after only 25 μm of growth. Additionally, the columnar morphology appeared insensitive to the deposition rates of 1.30 and 0.73 μm/min for Y_2O_3-A and Y_2O_3-B, respectively.

There are notable differences in the three higher temperature depositions, coatings Y_2O_3-C, -D, and -E, when compared to the lower surface temperature depositions. While all coatings have irregular surface morphologies, with fine features resulting from column branching, coatings C and D appear to have more column tip geometries that resemble square pyramidal-type column tips, although they appeared curved and distorted on growth. Coatings C and D also appear to have a weak ⟨100⟩ texture given by a greater-than-normal intensity of the (400) reflection in the surface XRD scans shown in **Figure 6.25**, and the (400) pole figures in **Figure 6.27**. Whereas coating E has such significant branching on growth that neither the surface XRD scan nor the pole figures show any evidence of a dominant growth direction or texture. The broad peaks in the surface XRD scans all three coatings in **Figure 6.25** suggest small crystallites at the surface of these coatings, likely a result from branching, even in the weakly ⟨100⟩ textured coatings C and D. In cross-sections presented in **Figure 6.22**, **Figure 6.23**, and **Figure 6.24** there is not as much branching observed in coatings C and D, as in coating E, resulting in a structure that appears somewhat more columnar. The columns in all three coatings terminate in a much finer structure when compared to the well-formed columns in coating A.

The main difference in the process parameters between coatings C, D, and E was the deposition rates, 1.1, 2.18, and 0.7 μm/min respectively. The surface temperature was read higher for coating E, 1095°C, than coatings C or D, 1080°C, but the 15°C difference is likely within error of the pyrometer. While a similar change in deposition rates between coatings Y_2O_3-A and -B resulted in minimal microstructural differences, interplay between the deposition rates and the greater surface temperature could influence the microstructure to the extent seen in coatings C, D, and E. However, there is not enough information to definitively determine the origin of the microstructural irregularities in the higher temperature yttria growths.

These findings further highlight the surface temperature sensitivity of the microstructure and morphology of EB-PVD coatings, especially with materials that are structurally related but deviate crystallographically from the well-studied fluorite and tetragonal structures. At greater temperatures, increased surface diffusion leads to more growth directions becoming competitive [73,85] and other process parameters can have an influence on dominant growth directions, or lack thereof. Despite the microstructural irregularities in the higher temperature growths, it is important to note that yttria is observed to grow in the ideal square pyramidal-tipped, ⟨100⟩ columnar microstructure like what is seen with fluorite-structured materials and *t*-7YSZ.

Significant epitaxial growth of yttria on 7YSZ was not observed in any of the yttria coatings, as indicated by the fan-like structures of renucleation are observed at the bilayer interface in all depositions. Epitaxial growth is desired in bilayer EB-PVD coatings to create an intimate bond between the layers and to have continuity of the columnar growth. Re-nucleation of the topcoat material enhances porosity near the interface which, as noted earlier, can coarsen upon prolonged thermal exposure and provide paths for preferential cracking [64]. Yttria has been shown to grow epitaxially on ⟨100⟩ textured 7YSZ substrates in molecular beam epitaxy experiments [104], so epitaxial growth of yttria by EB-PVD is feasible, but this highlights the sensitivity of epitaxy to surface temperature and deposition rate. The lattice mismatch between the two materials is only 3-4% difference between the yttria lattice parameter and two times the 7YSZ *a* & *b* directions (the reduction in symmetry in the bixbyite structure of yttria leads to a unit cell that is twice as large)[16].

6.9.6 Temperature determination in EB-PVD

As evident by the coatings grown in this work, surface temperature is a key process parameter that will influence the morphology of the coating, and also evident in this work is the challenge of effectively monitoring surface temperature during deposition. The pyrometer used for temperature monitoring in the EB-PVD apparatus used two wavelengths of 800 nm and 950 nm, which are effective for reading the temperatures of most metals, emissivity is consistently high in that range of lower wavelength infrared. However, alumina has a very low emissivity in that range [105], so inadequate calibration will lead to incorrect temperature readings. A low emissivity also increases the potential for error in the pyrometer reading. While a narrow band of the two wavelengths will reduce the potential for error because of the material's emissivity will likely be consistent in a narrow spectral range. A two-color pyrometer can read temperatures that are independent of materials' emissivities and are less sensitive to environmental effects, especially if the materials emissivity is high (close to unity) in the range and consistent [106]. Longer wavelength pyrometers, 8-14 μm for example, are better suited for reading ceramics because of their high and consistent emissivity in that range [107].

Additionally, porosity of the OFCC will change the emissivity as well, especially in low wavelength infrared, which can complicate accurate temperature readings [105]. When combined with the lower thermal conductivity of the OFCC compared to the thin alumina plate,

Surface temperature is important for producing desired and effective coating microstructures from EB-PVD. Accurately determining the substrate surface temperature during the deposition process is extremely challenging: thermocouples are difficult to secure to a rotating substrate, and intimate contact between the surface and the thermocouple would be difficult to maintain on ceramic substrates without the ability to spot weld the thermocouple to the surface as one can with a metallic substrate. Additionally, electric interference from the high-powered E-beam can interfere with thermocouple reading. Infrared pyrometry is also a challenge with (1) difficulty pointing a pyrometer at the surface being coated, as this surface will see a greater temperature facing the evaporating source; (2) the signal to the pyrometer must travel through multiple glass windows/mirrors before it is interpreted by the camera, and each material the signal passes through will affect the temperature reading; (3) the EB-PVD coating will have different optical properties (emissivity, transmissivity, absorbance, etc), and as the material grows on the surface, the properties of the coating will increasingly influence the pyrometer readout [108,109].

6.10 Synopsis

The results from this chapter highlight the sensitivity of surface temperature on the morphology of EB-PVD coatings, and that monitoring this temperature is challenging, yet critically important for growing novel materials with desired microstructures that will best protect an underlying OFCC.

7YSZ growth was shown to be sensitive to temperature in the range tested. The roof-top morphology of ⟨100⟩ type column tips was observed with single axis substrate rotation that had not been previously observed with similar process parameters. This, plus evidence of fiber grain growth in the OFCC substrates, and inconsistencies in observed temperature and observed morphology on alumina plate substrates, suggests the surface temperature of deposition was greater than the observed 1100°C. The observed morphology evolution of 7YSZ growth in EB-PVD with single axis substrate rotation, as temperature increases is ⟨100⟩ square pyramidal, ⟨100⟩ roof-top, ⟨311⟩ trigonal pyramidal. With, even at higher temperatures, ⟨100⟩ square pyramidal being dominant earlier in thinner growths, with ⟨100⟩ roof-top and ⟨311⟩ trigonal pyramidal tips dominating as the coating grows. The ⟨100⟩ roof-top columns, in single axis substrate rotation, grow with an orientation of ± 60° off the substrate rotation axis, with one of the two orientations dominating with increased coating thickness.

YZO, in the disordered fluorite phase, grows in the desired ⟨100⟩ columnar microstructure, and the microstructure is not sensitive to surface temperature in the range tested. YZO does show some evidence of growing epitaxially on 7YSZ at higher surface temperatures, but further testing, and likely TEM, will need to be done to confirm.

Yttria can grow with the desired columnar microstructure and ⟨100⟩ texture. However, yttria's growth morphology is particularly sensitive to surface temperature on deposition, where greater surface temperatures lead to irregular morphologies and branched columnar growth. Growth of the desired columnar microstructure requires lower temperatures than previously studied 7YSZ and RE – zirconates, likely because of yttria's lower melting point and the resulting increase in surface diffusion. Epitaxial growth of yttria on 7YSZ was not observed, but may be possible with EB-PVD with the correct process parameters.

While accurately determining surface temperature during this process is challenging, It was still possible to find the correct parameters to produce the desired columnar microstructures in all materials studied. Despite the surface morphology irregularities in 7YSZ, desired columnar microstructures of the lower CTE materials of YZO and yttria were grown on top of the irregular 7YSZ. Replicating these microstructures would require substrate rotation and surface temperatures around 1030°C for all materials. The ideal microstructures have been produced with a range of deposition rates between 0.7 and 3.1 μm/min, suggesting that deposition rate may not be a critical factor for producing the desirable microstructures, provided the rate is within that range. In-situ source ingot switching is ideal for the process as it will reduce the amount of shrinkage cracking from cooling a 7YSZ layer to room temperature.

6.11 Tables and Figures

Table 6.1: Single layer and bilayer depositions investigated, with relevant process parameters. Chamber pressure and substrate rotation rate were 5 mtorr O_2 and 8 rpm, respectively, in all depositions.

Material(s) (designation)	***Thickness(es) (μm)***	***Substrate***	***Top coat deposition rate (μm/min)***	***Beam current (mA)***	***Subst. temp (°C)***	***Subst. heater (%)***	***Homologous temp. (Ts/Tm)***
7YSZ-A	130	Alumina plate	2.17	158	1140	58	0.460
7YSZ-B	125	Alumina plate	2.08	160	1160	95-99	0.460
7YSZ-C	50	Alumina plate	1.67	157-160	1160	95	0.466
7YSZ-D	50	Hardened OFCC	1.67	157-160	1085	95	0.442
7YSZ-E	150	Hardened OFCC	2.50	168-174	1030	62	0.424
7YSZ-F	240	OFCC	2.03	180-187	1085	95	0.442
7YSZ-G	25	Hardened OFCC	1.67	175	1060	95	0.434
7YSZ / YZO (YZO-A)	25 / 135	Hardened OFCC	2.05	162	1050	59	0.457
7YSZ / YZO (YZO-B)	25 / 200	Hardened OFCC	3.13	167-195	1095	95	0.472
7YSZ / Y_2O_3 (Y_2O_3-A)	30 / 50	Hardened OFCC	1.30	157	1035	65	0.483
7YSZ / Y_2O_3 (Y_2O_3-B)	25 / 25	Hardened OFCC	0.73	140	1035	48	0.483
7YSZ / Y_2O_3 (Y_2O_3-C)	26 / 87	Hardened OFCC	2.18	150	1080	97.5	0.500
7YSZ / Y_2O_3 (Y_2O_3-D)	25 / 45	Hardened OFCC	1.1	156	1080	95	0.500
7YSZ / Y_2O_3 (Y_2O_3-E)	30 / 50	Hardened OFCC	0.63	150-158	1095	90	0.505

Table 6.2: Tabulated values for the grain growth equation

Grain growth equation: $\mathrm{d}^{\mathrm{n}} - \mathrm{d_0}^{\mathrm{n}} = \mathrm{Kte}^{-\mathrm{Q/RT}}$		
Variable	***Definition***	***Value***
d	Grain size	~2 μm
d_0	Initial grain size	70 nm
n	Grain growth exponent	0.50
K	Pre-exponent constant	3000
t	time	2 h
Q	Activation energy	370 $kJ^{-1}\cdot mol^{-1}$
R	Gas constant	8.314 $J\cdot K^{-1}\cdot mol^{-1}$
T	Temperature	1880 K (1607°C)

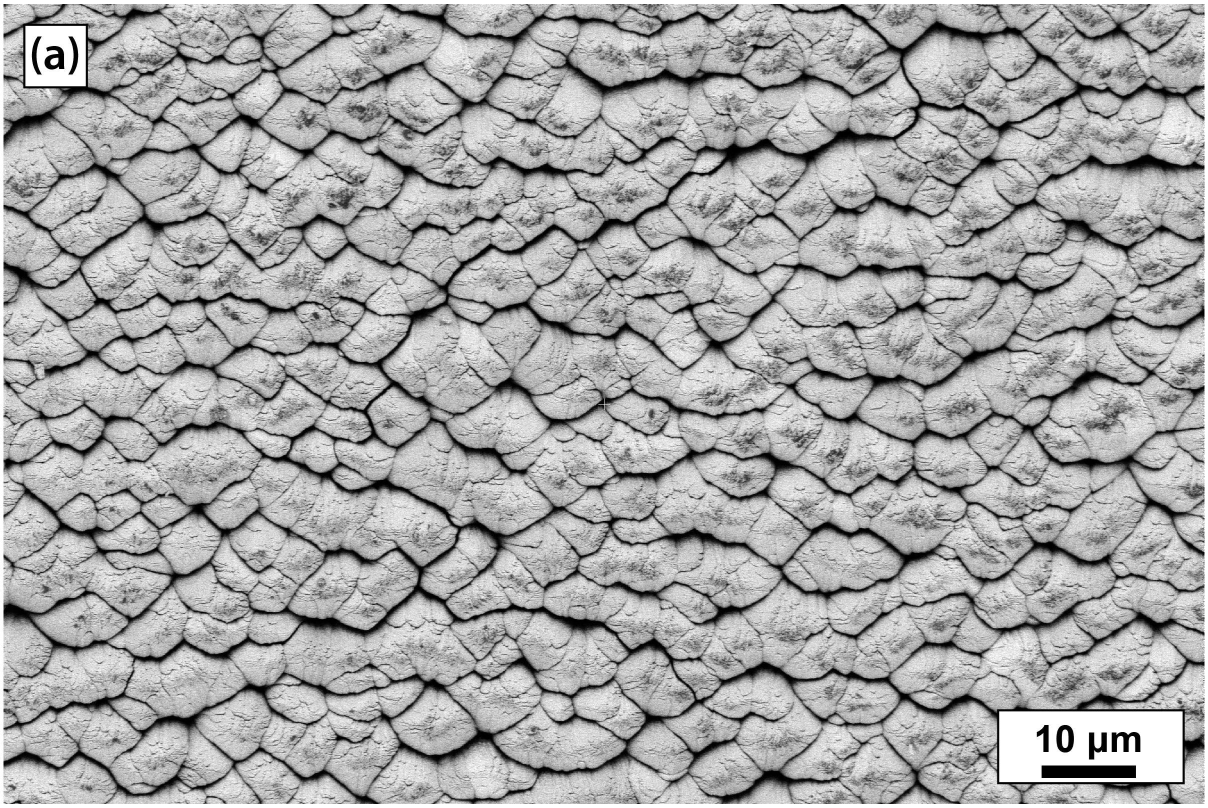
(a)
10 µm

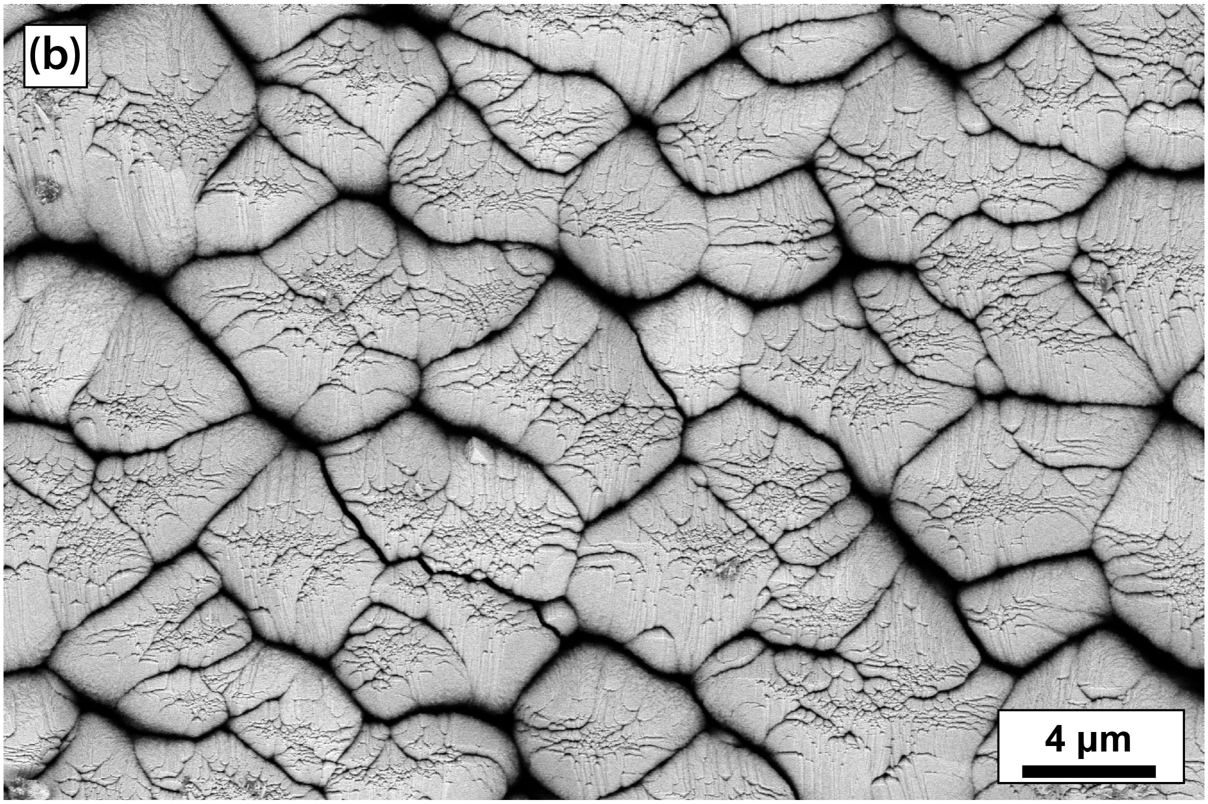
(b)
4 µm

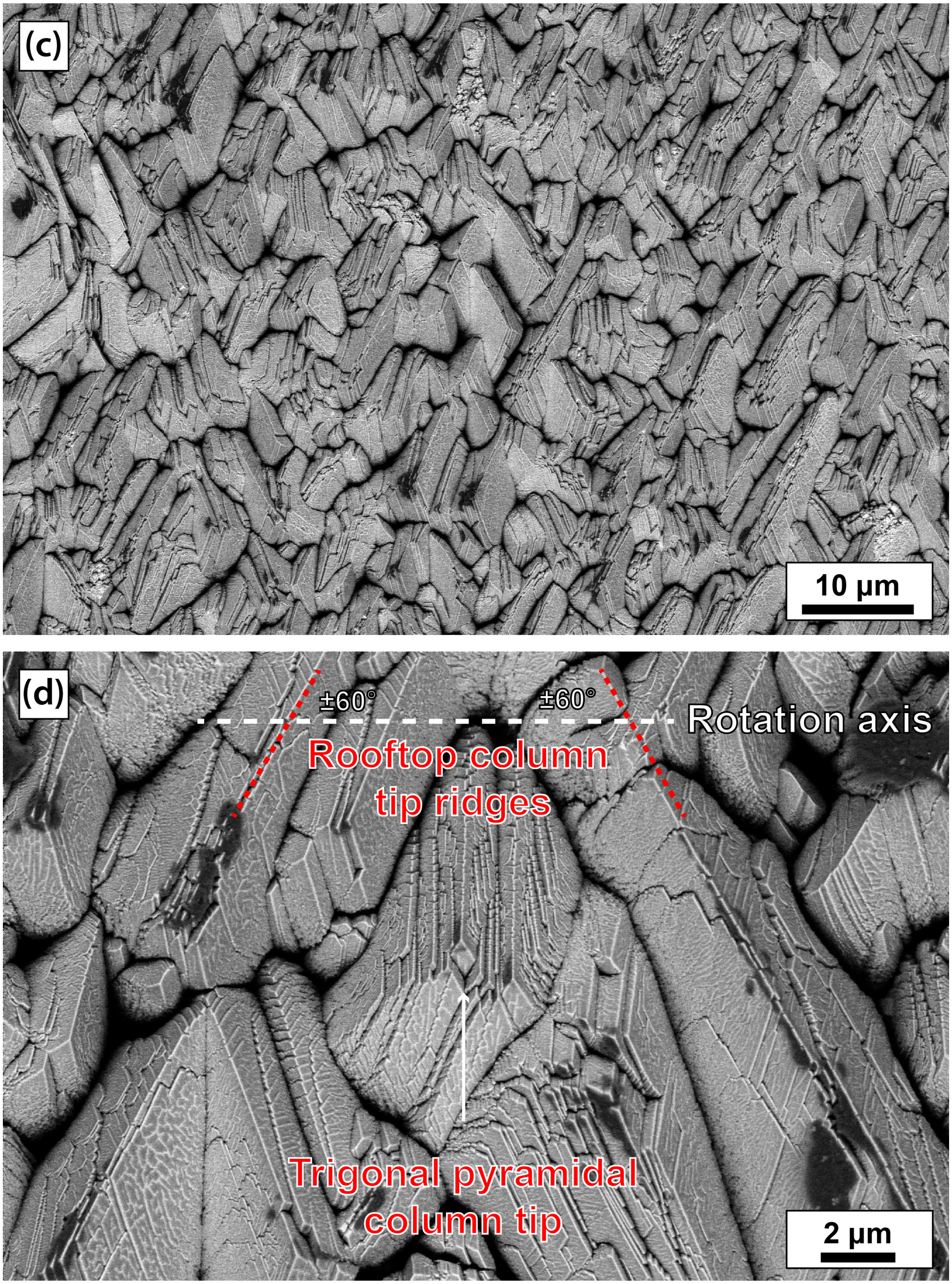

Figure 6.1: Surface images of (a) and (b) 7YSZ-A, and (c) and (d) 7YSZ-B, deposited on alumina plate substrates. The axis of substrate rotation is parallel to the horizontal direction.

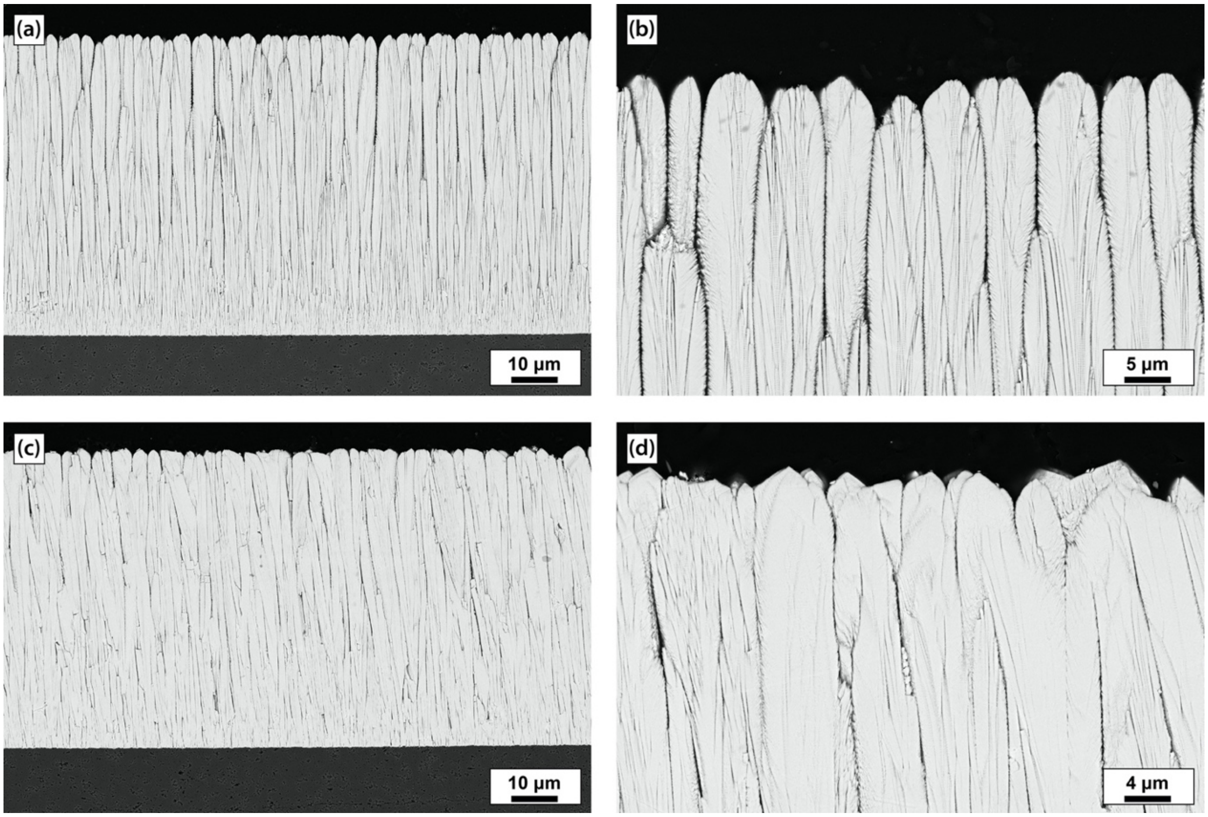

Figure 6.2: Cross-section images of (a) and (b) 7YSZ-A, and (c) and (d) 7YSZ-B, deposited on alumina plate substrates. The axis of substrate rotation is out of the page.

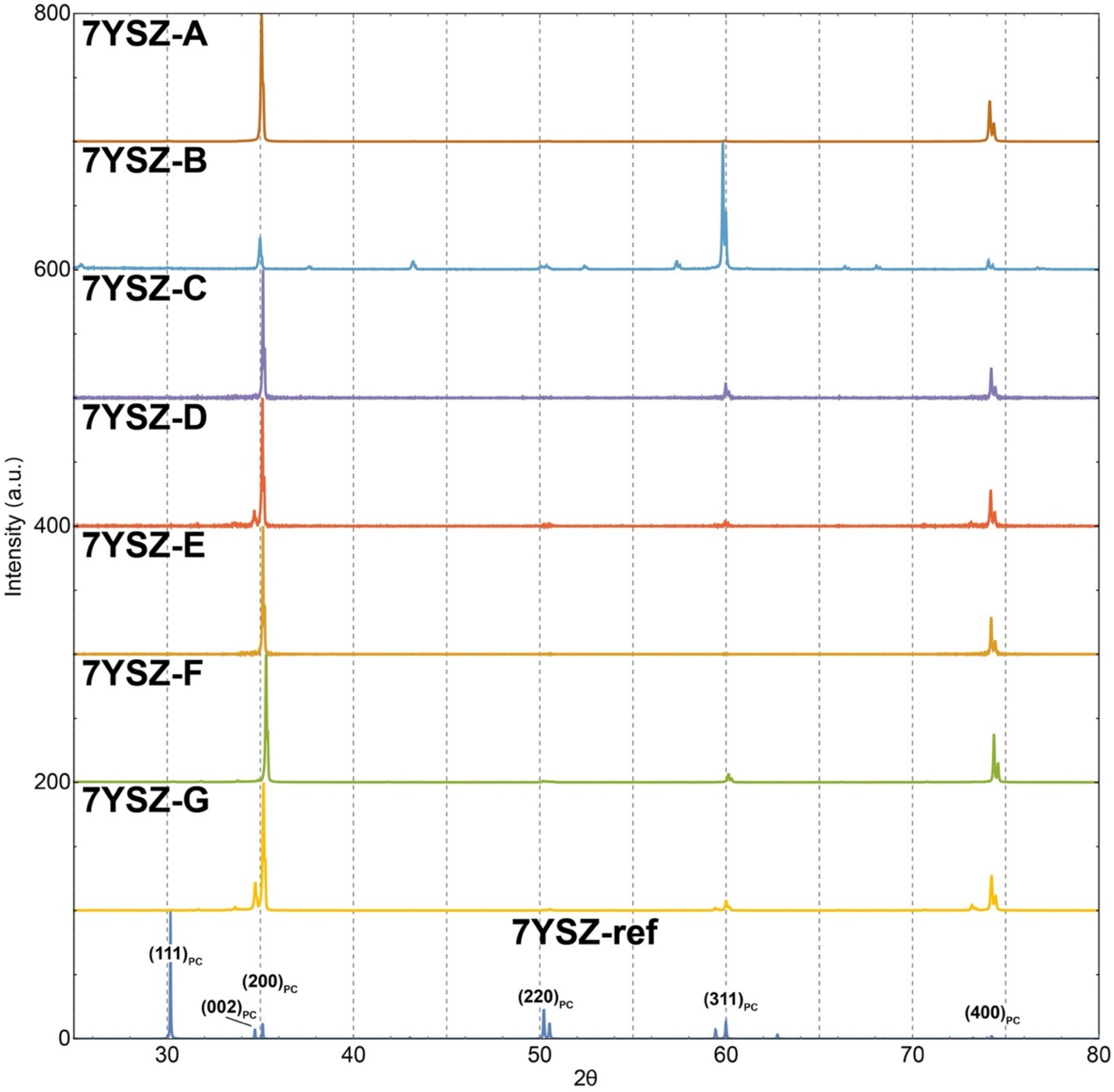

Figure 6.3: Surface XRD scans of all presented 7YSZ coatings and a reference t-7YSZ from [110].

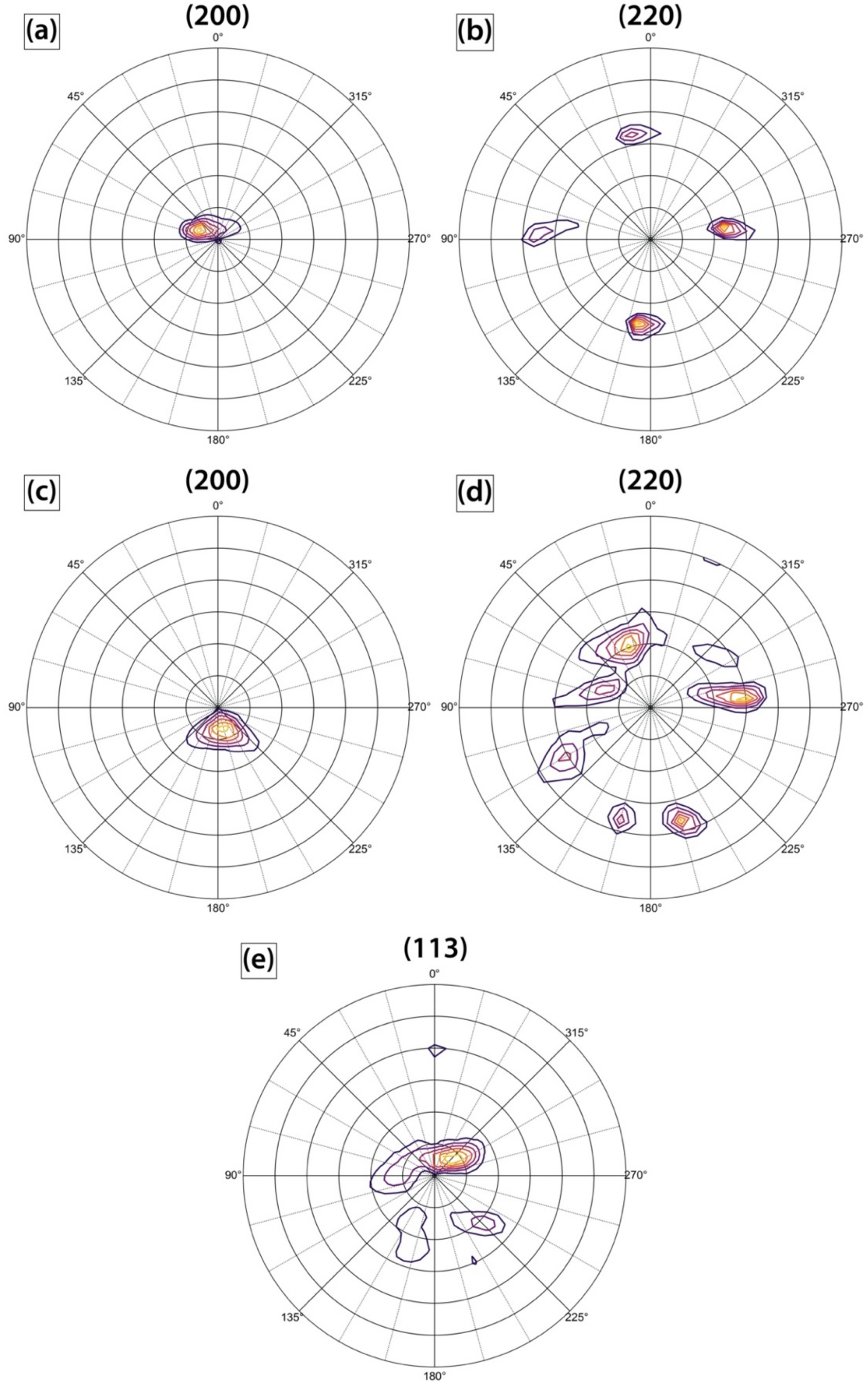

Figure 6.4: Pole figures for (a) and (b) 7YSZ-A and (c), (d) and (e) 7YSZ-B. The axis of substrate rotation is parallel to the horizontal direction.

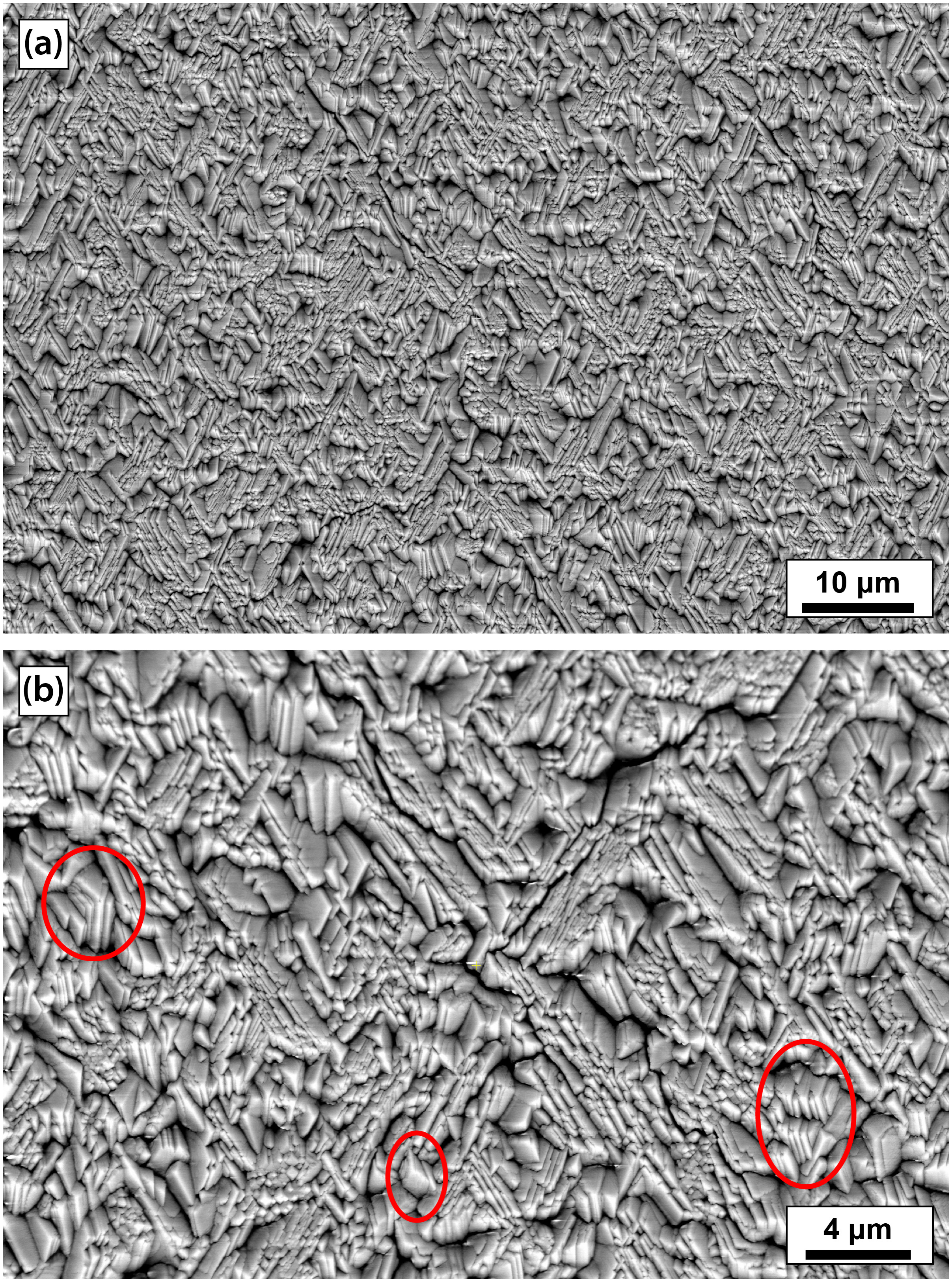
(a)
10 µm
(b)
4 µm

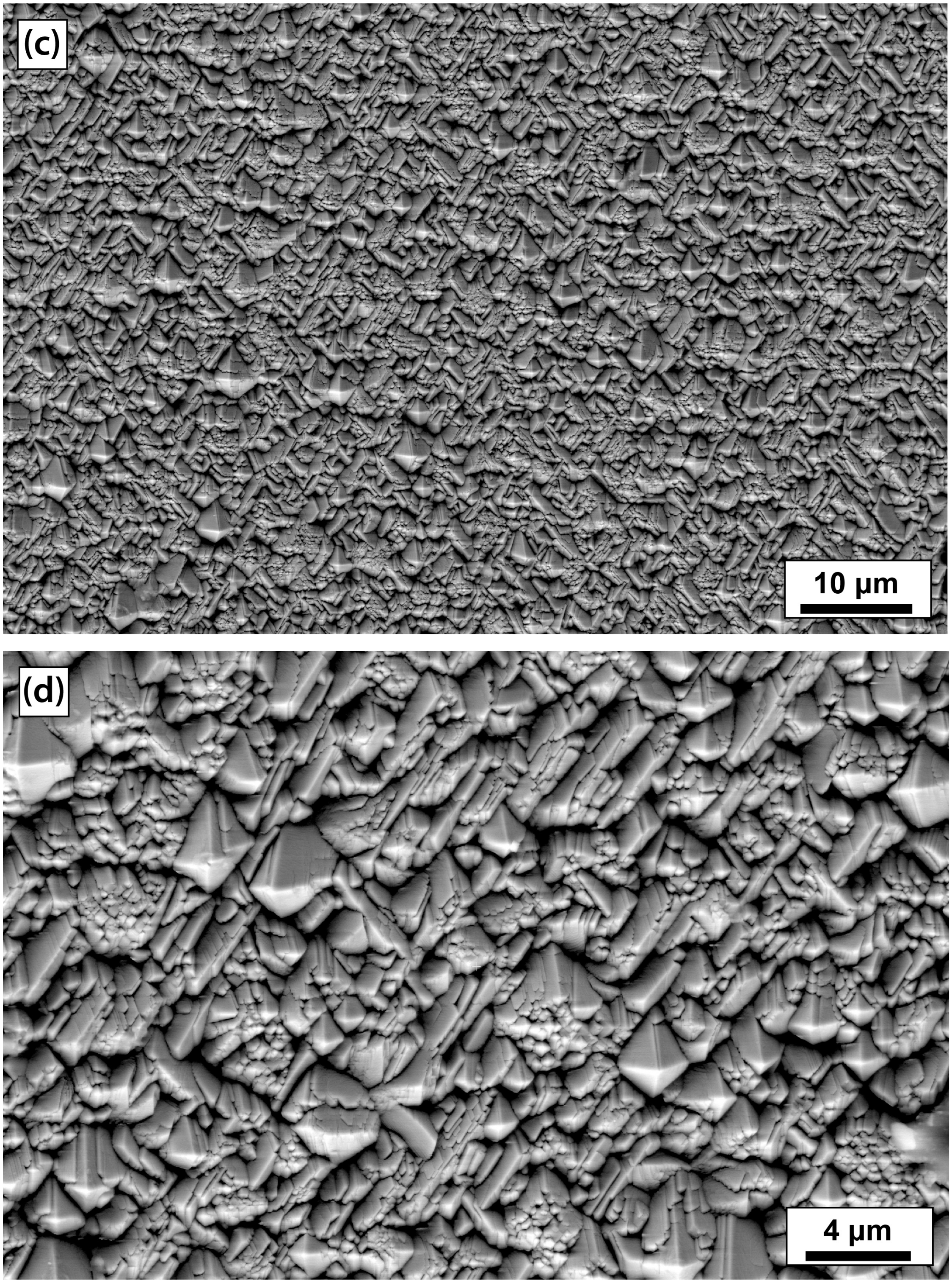

Figure 6.5: Surface images of (a) and (b) 7YSZ-C, deposited on an alumina plate substrate, and (c) and (d) 7YSZ-D, deposited on an OFCC substrate. The axis of substrate rotation is parallel to the horizontal direction. Marked with ovals in (b) are examples of trigonal pyramidal column tips.

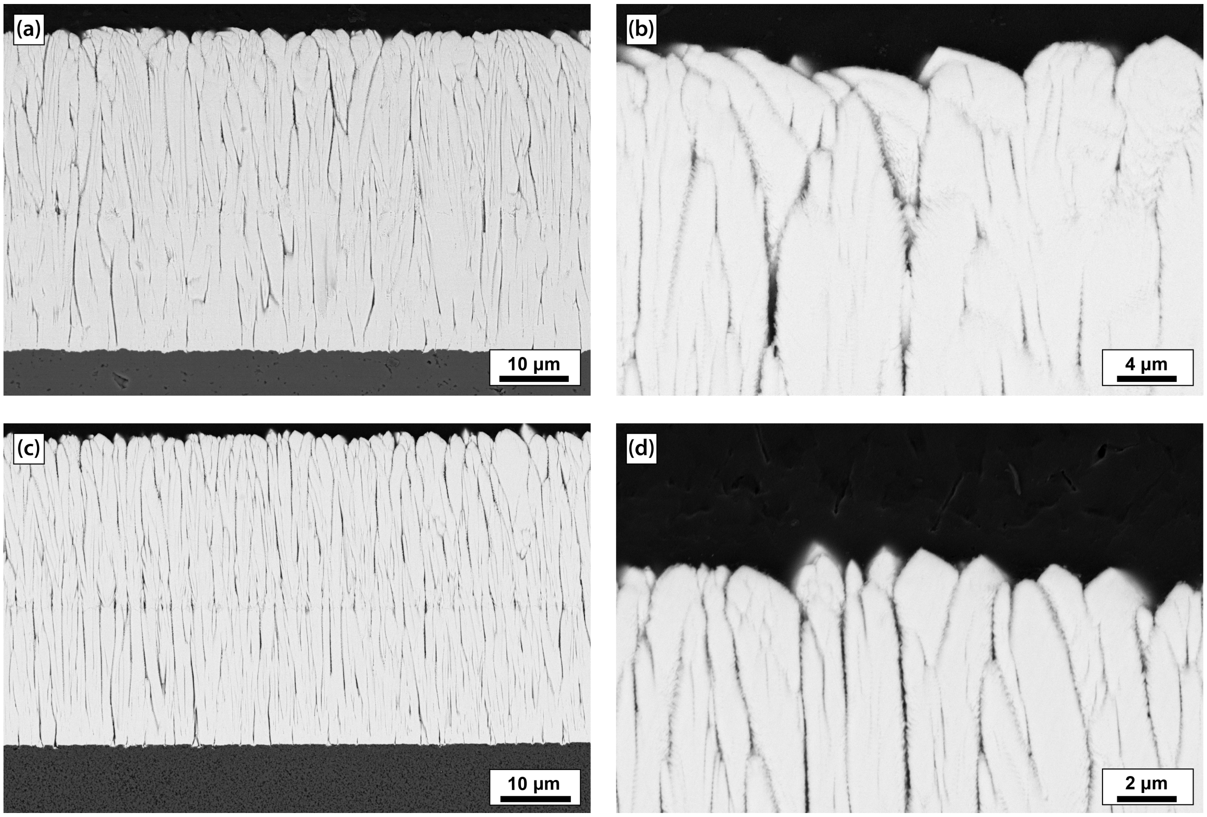

Figure 6.6: Cross-section images of (a) and (b) 7YSZ-C, deposited on an alumina plate substrate, and (c) and (d) 7YSZ-D, deposited on an OFCC substrate. The axis of substrate rotation is out of the page.

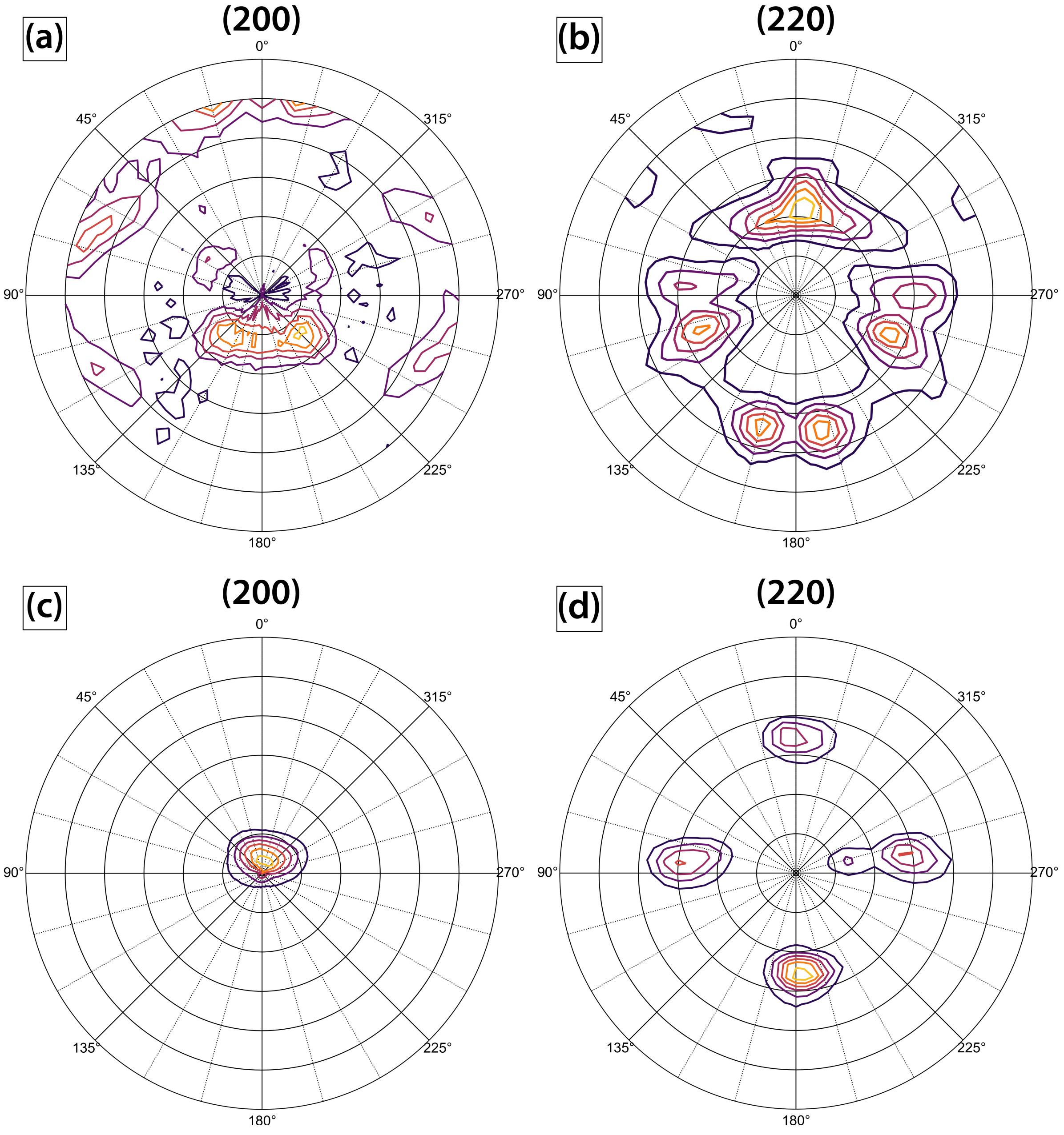

Figure 6.7: Pole figures of (a) and (b) 7YSZ-C, deposited on an alumina substrate, and (c) and (d) 7YSZ-D, deposited on an OFCC substrate. The axis of substrate rotation is parallel to the horizontal direction.

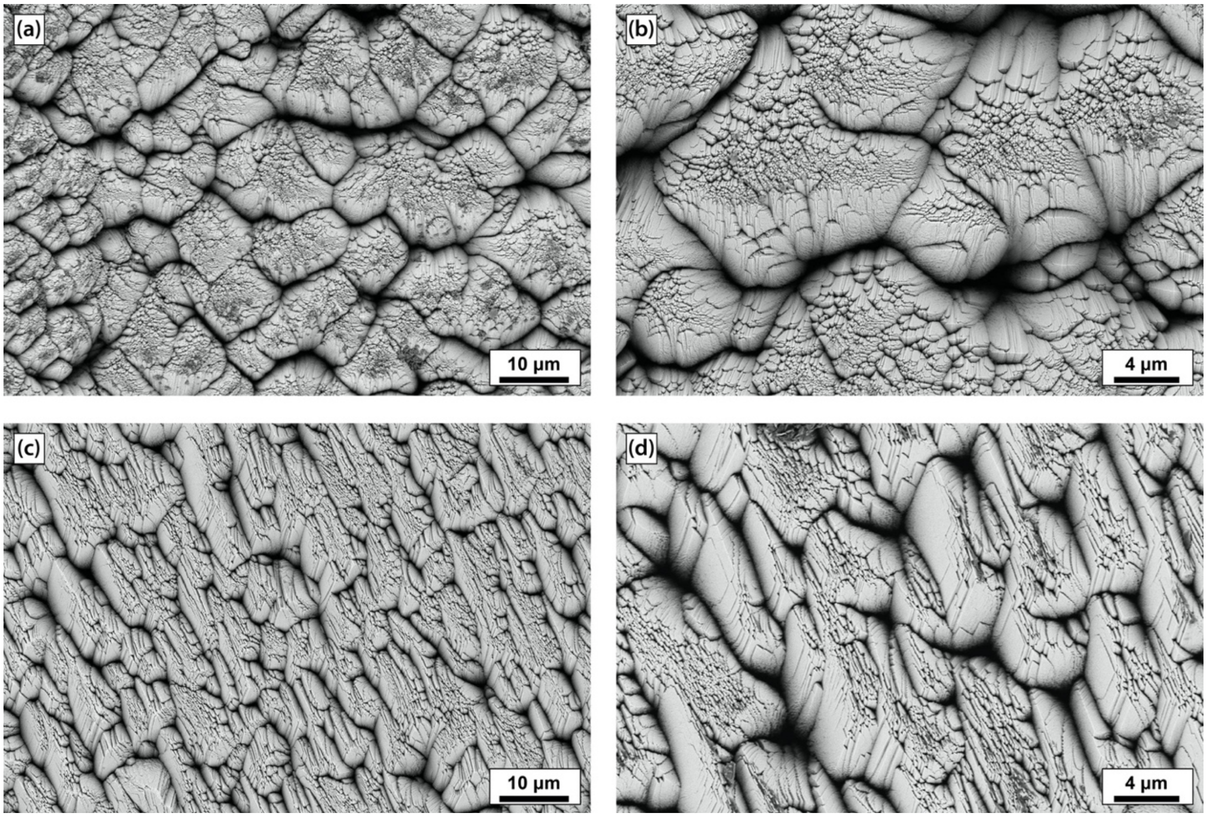

Figure 6.8: Surface images of (a) and (b) 7YSZ-E, and (c) and (d) 7YSZ-F. The axis of substrate rotation is parallel to the horizontal direction. The coating surfaces in (a) and (b) show roughened, elongated pyramidal column tips. Surfaces (c) and (d) show roof-top tips with a consistent orientation of ~60° off the rotation axis.

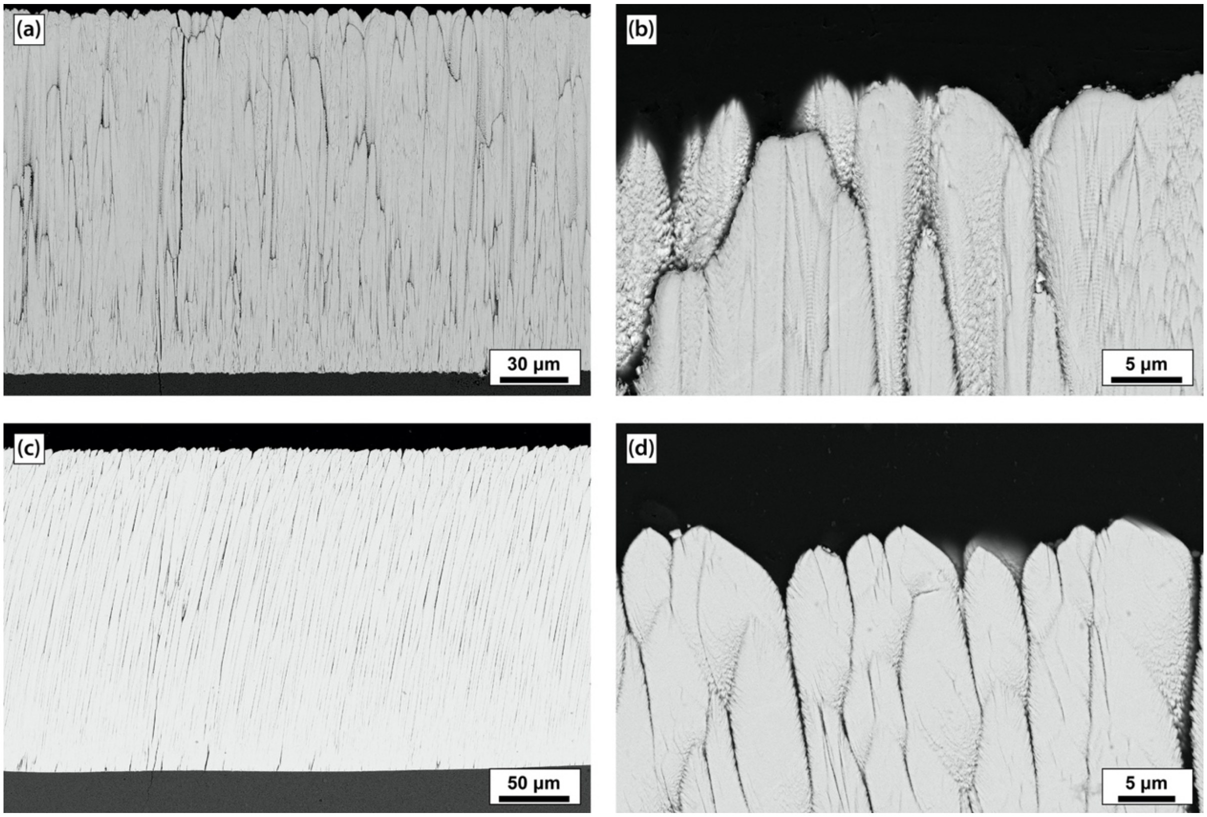

Figure 6.9: Cross-section images of (a) and (b) 7YSZ-E, and (c) and (d) 7YSZ-F. The axis of substrate rotation is out of the page. (a) and (b) show the columnar growth of 7YSZ-E, terminating in square pyramidal-type tips. (c) and (d) show the columnar growth of 7YSZ-F, terminating in 'angular' tips, with ~10° tilt in the columns.

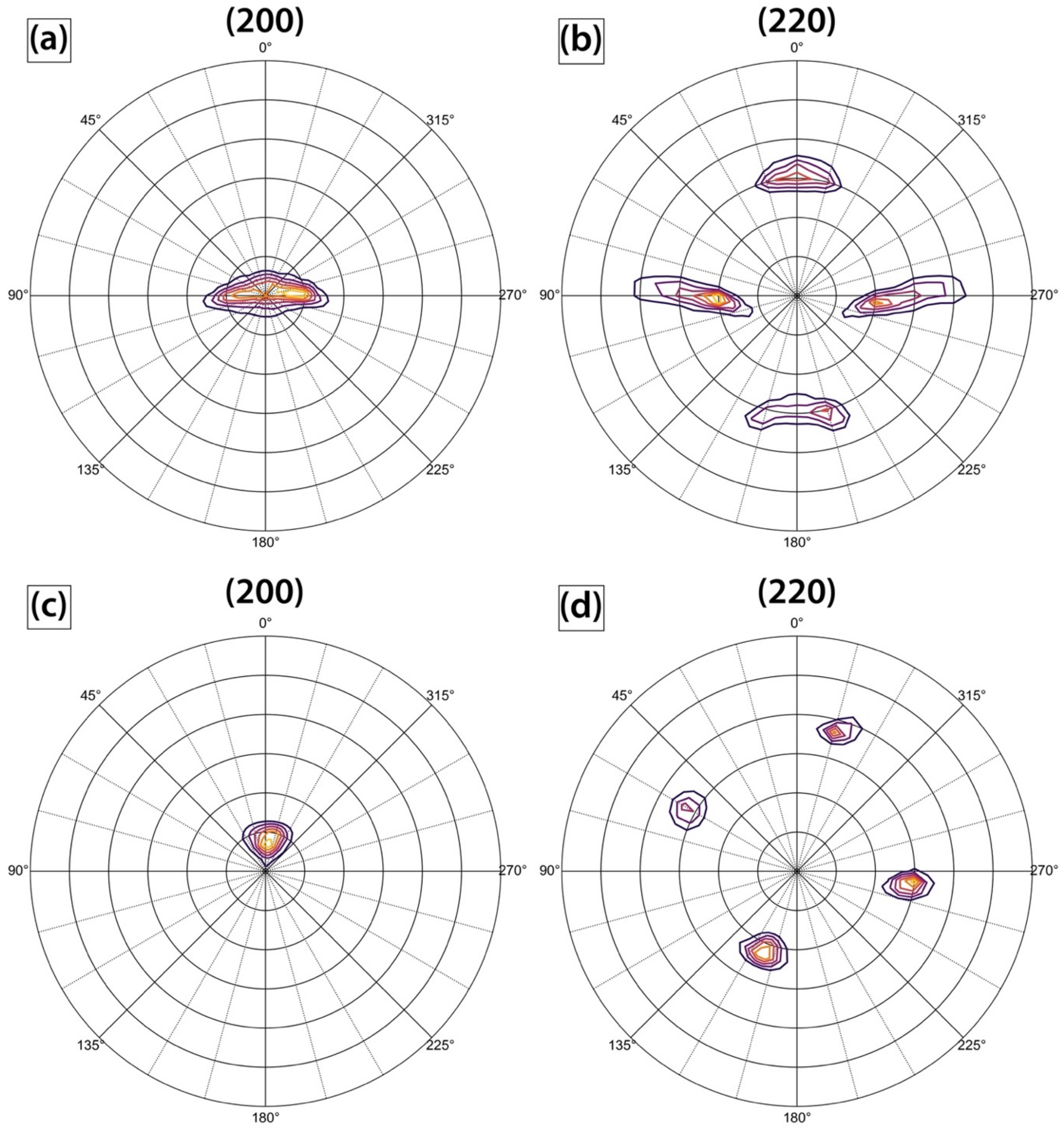

Figure 6.10: Pole figures for (a) and (b) 7YSZ-E and (c) and (d) 7YSZ-F. The axis of substrate rotation is parallel to the horizontal direction.

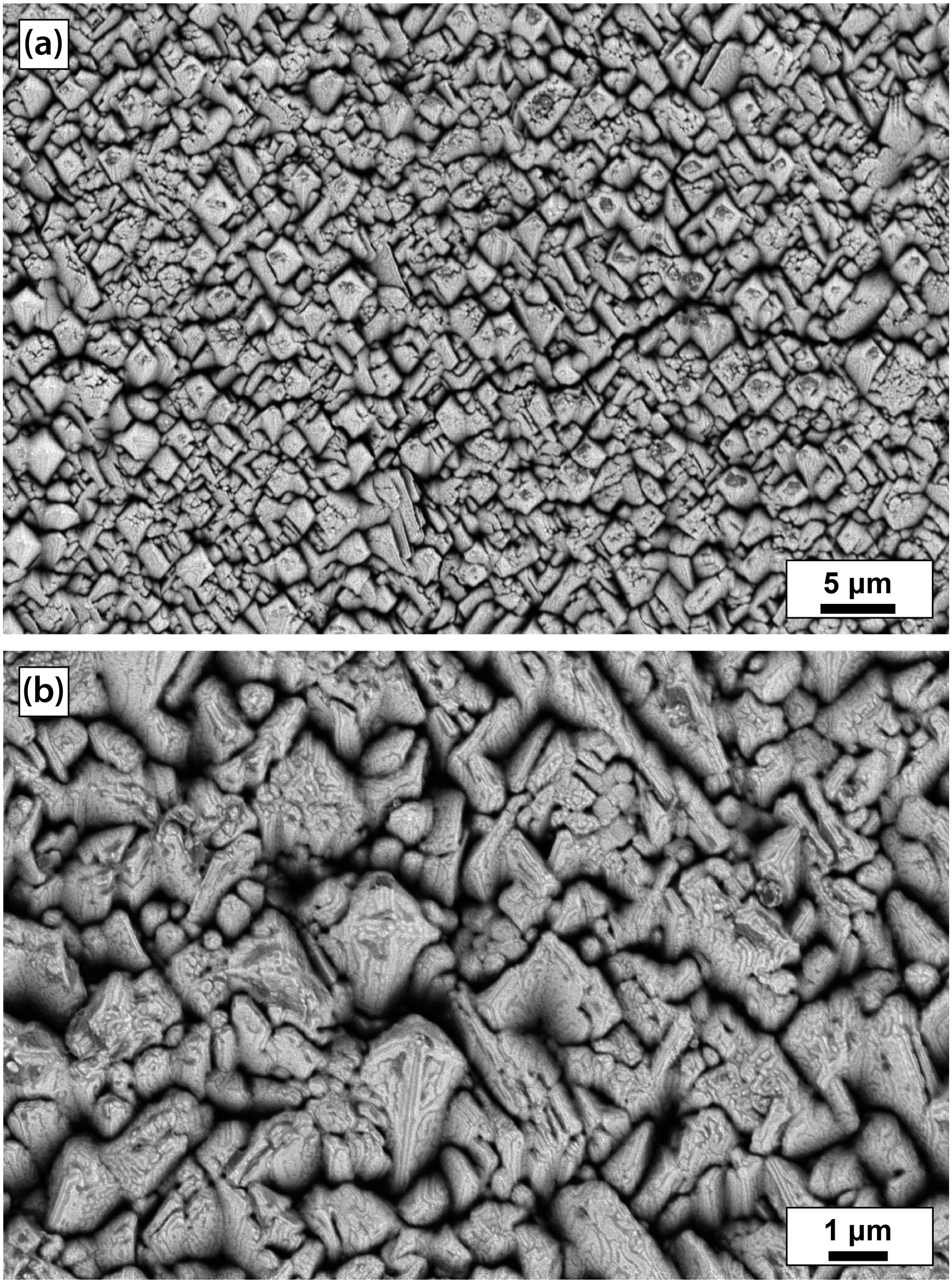

Figure 6.11: Surface images of (a) and (b) 7YSZ-G, the 25 μm coating on an OFCC substrate. The axis of substrate rotation is parallel to the horizontal direction.

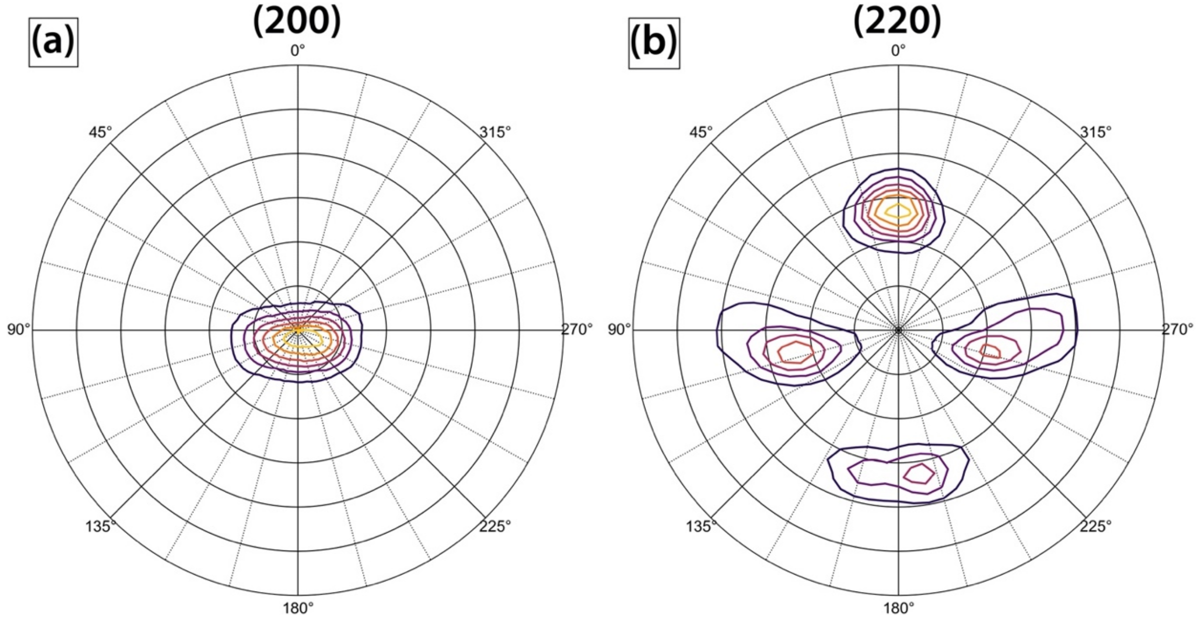

Figure 6.12: Pole figures for (a) and (b) 7YSZ-G, the 25μm coating on an OFCC substrate. The axis of substrate rotation is parallel to the horizontal direction.

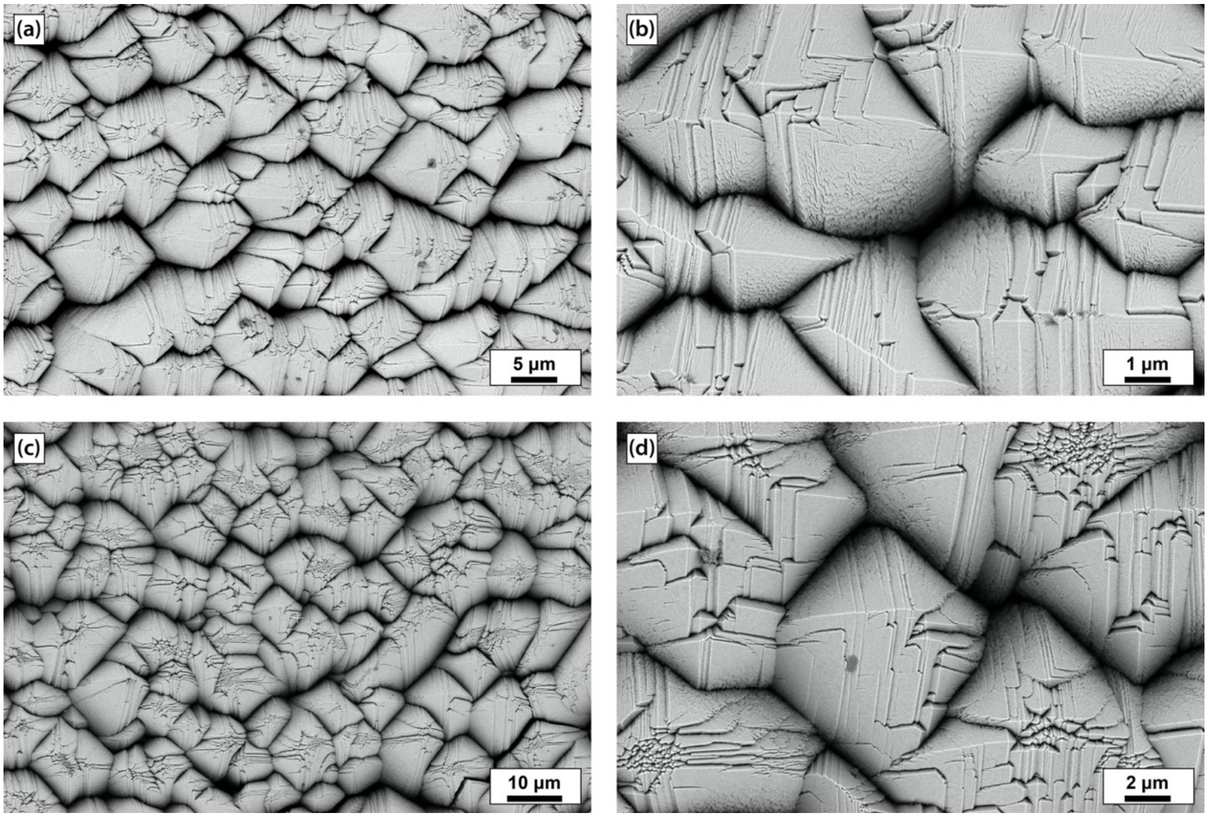

Figure 6.13: Surface images of the two 7YSZ/YZO bilayer coatings, (a) and (b) YZO-A and (c) and (d) YZO-B. The axis of substrate rotation is parallel to the horizontal direction.

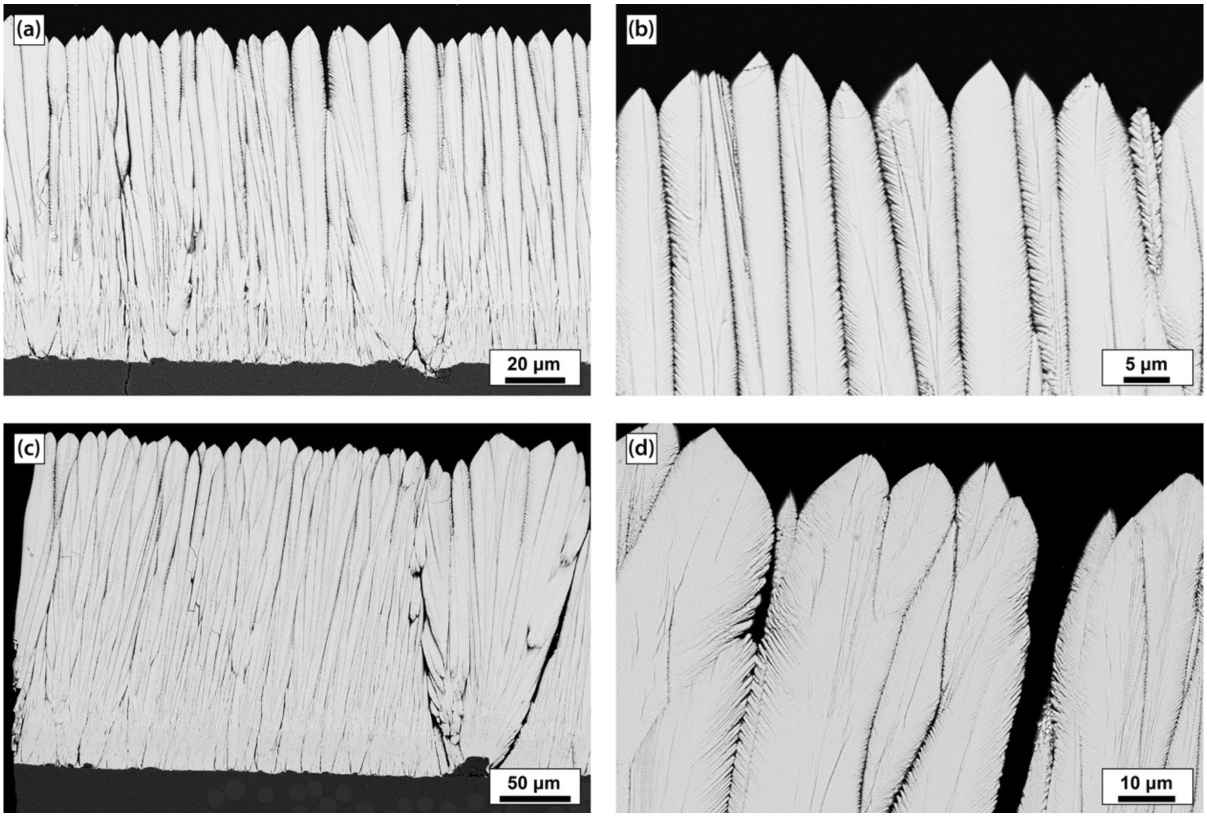

Figure 6.14: Cross-section images of the two 7YSZ/YZO bilayer coatings, (a) and (b) YZO-A and (c) and (d) YZO-B. The axis of substrate rotation is out of the page.

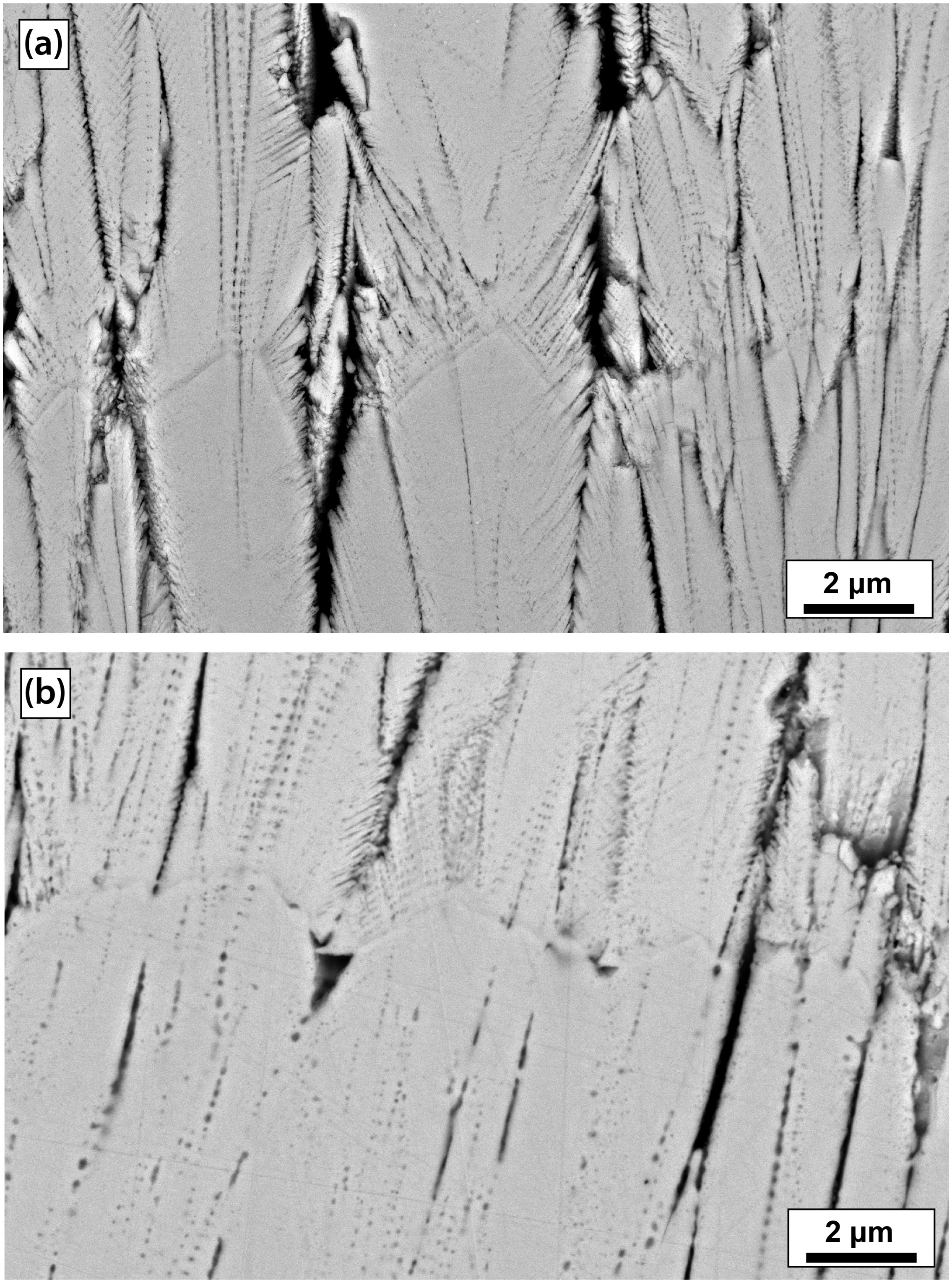

Figure 6.15: Cross- section images of the bilayer interfaces of the two 7YSZ/YZO bilayer coatings, (a) YZO-A, and (b) YZO-B. The axis of substrate rotation is out of the page.

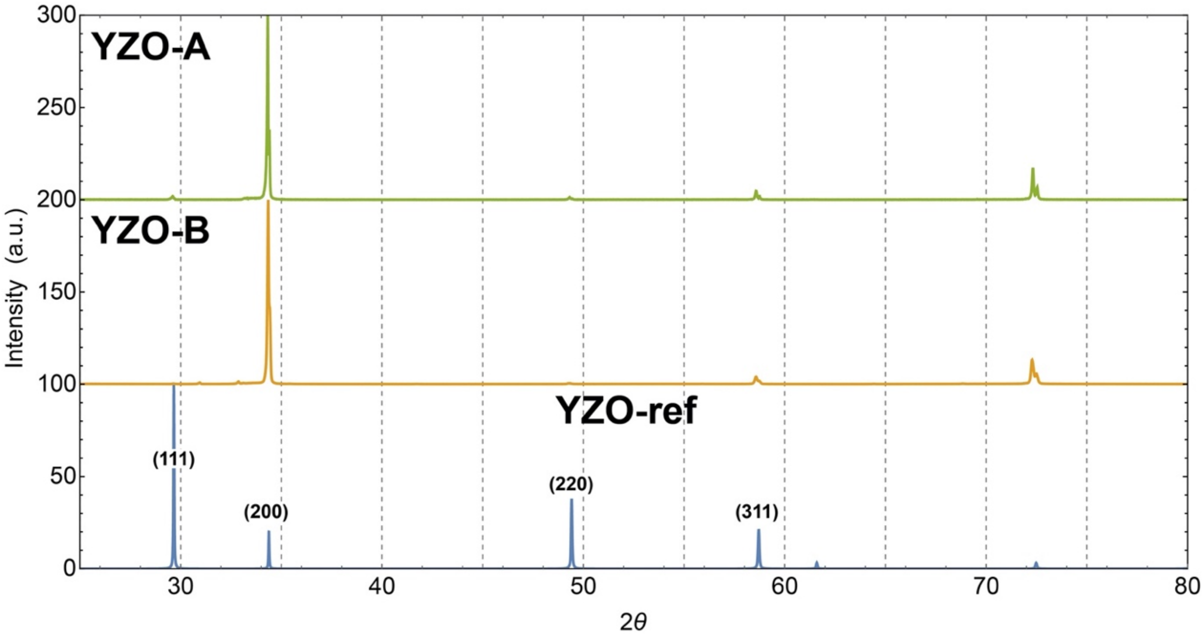

Figure 6.16: Surface XRD scans for the presented YZO coatings, including a reference scan for 50YSZ.

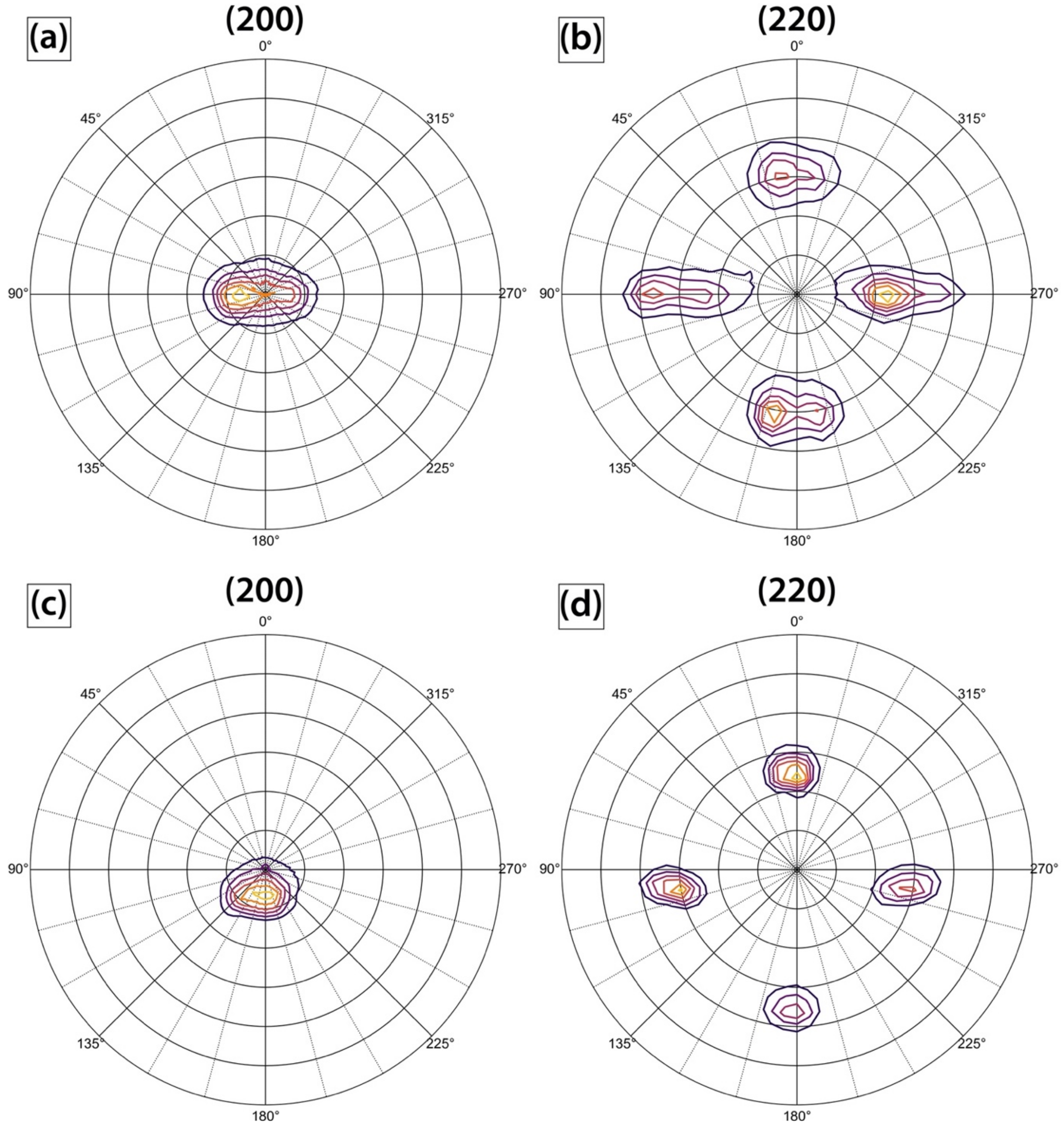

Figure 6.17: Pole figures for (a) and (b) YZO-A and (c) and (d) YZO-B. The axis of substrate rotation is parallel to the horizontal direction.

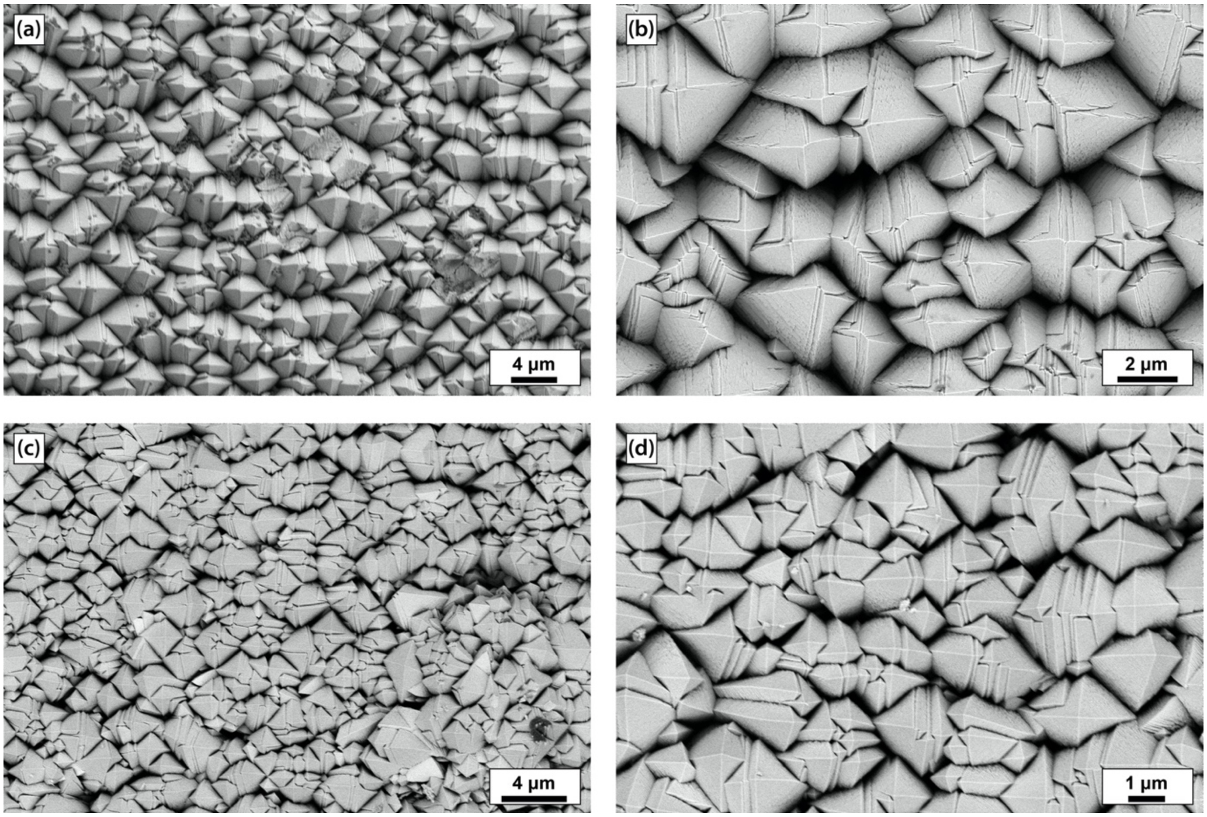

Figure 6.18: Surface images of 7YSZ/Y_2O_3 bilayer coatings, (a) and (b) Y_2O_3-A and (c) and (d) Y_2O_3-B. The axis of substrate rotation is parallel to the horizontal direction.

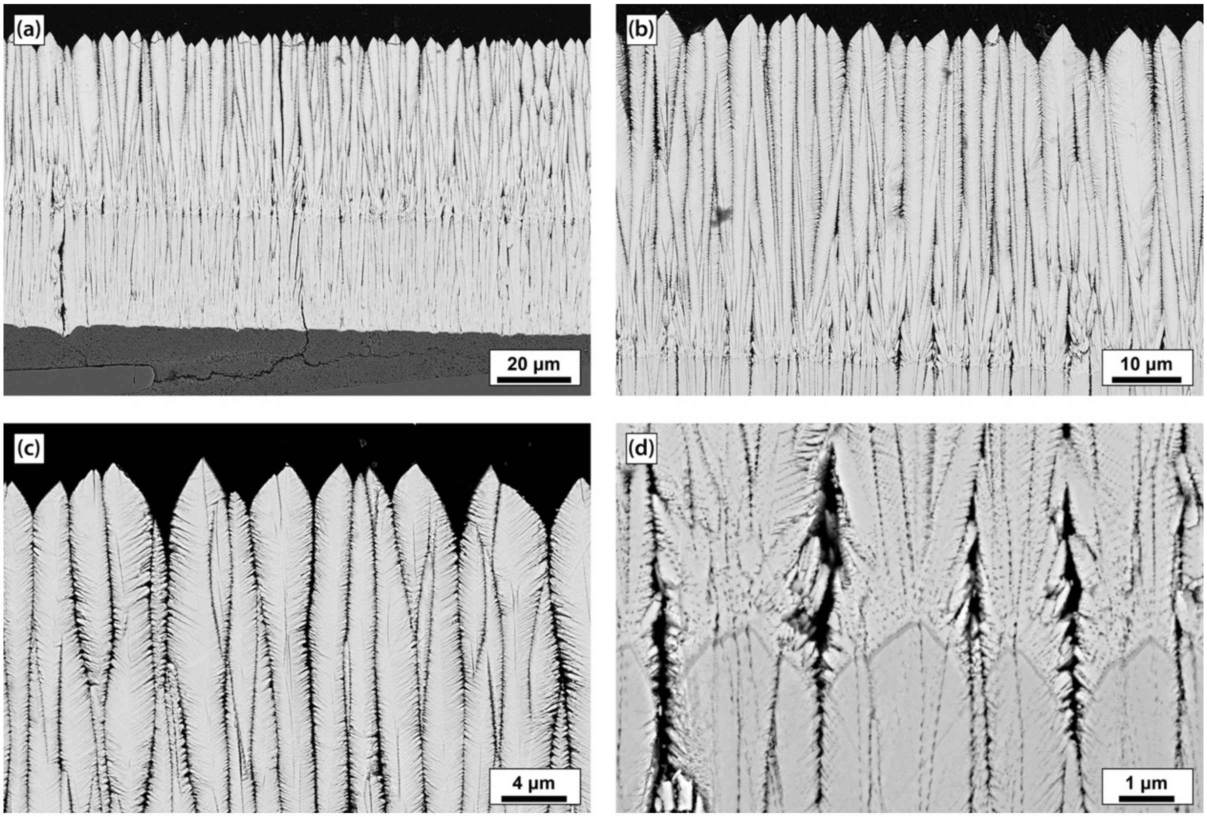

Figure 6.19: Cross-section images of Y_2O_3-A, showing (a) the overall morphology, (b) columnar growth of the Y_2O_3 layer, (c) the column tips, and (d) the bilayer interface between the Y_2O_3 and the 7YSZ. The axis of substrate rotation is out of the page.

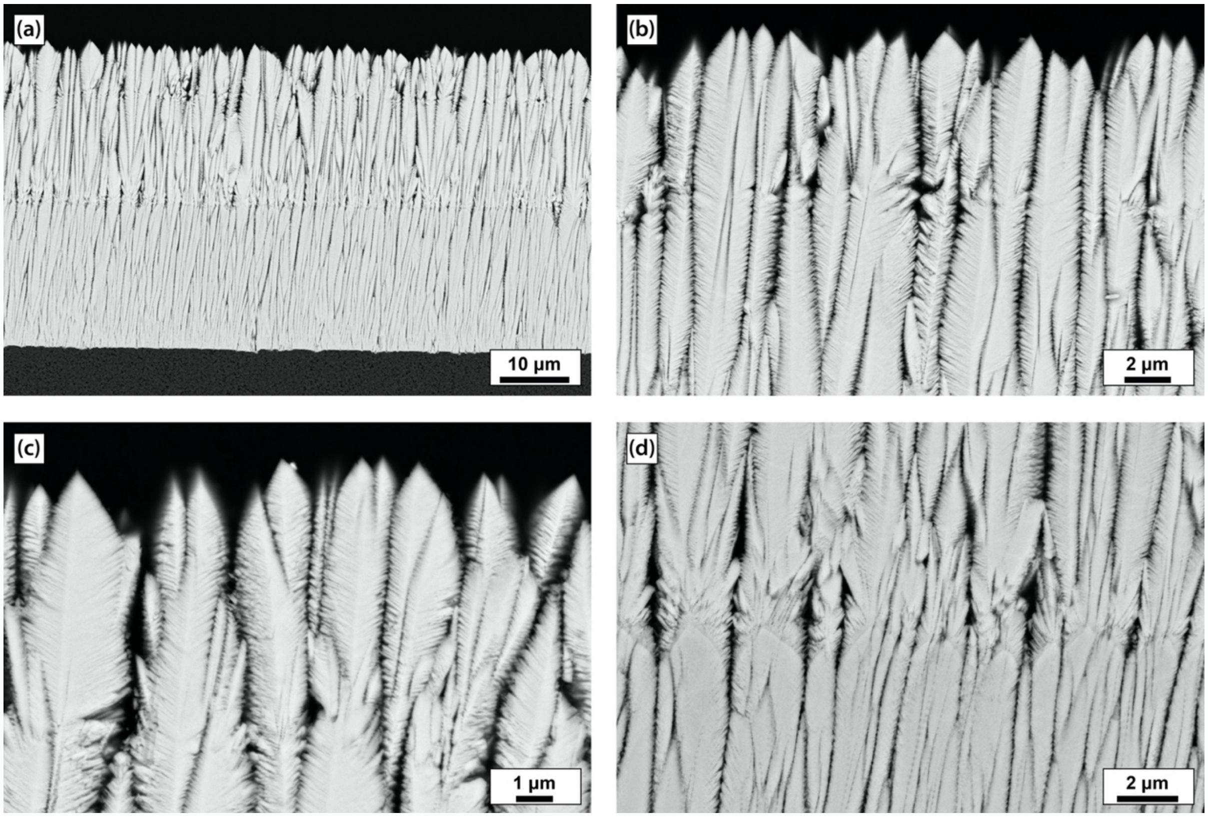

Figure 6.20: Cross-section images of Y_2O_3-B, showing (a) the overall morphology, (b) Columnar growth in the Y_2O_3 layer, (c) the column tips, and (d) the bilayer interface between the Y_2O_3 and the 7YSZ. The discontinuity observed in the columnar growth ~10 μm from the surface was due to an interruption in the electron beam power during deposition. The axis of substrate rotation is out of the page.

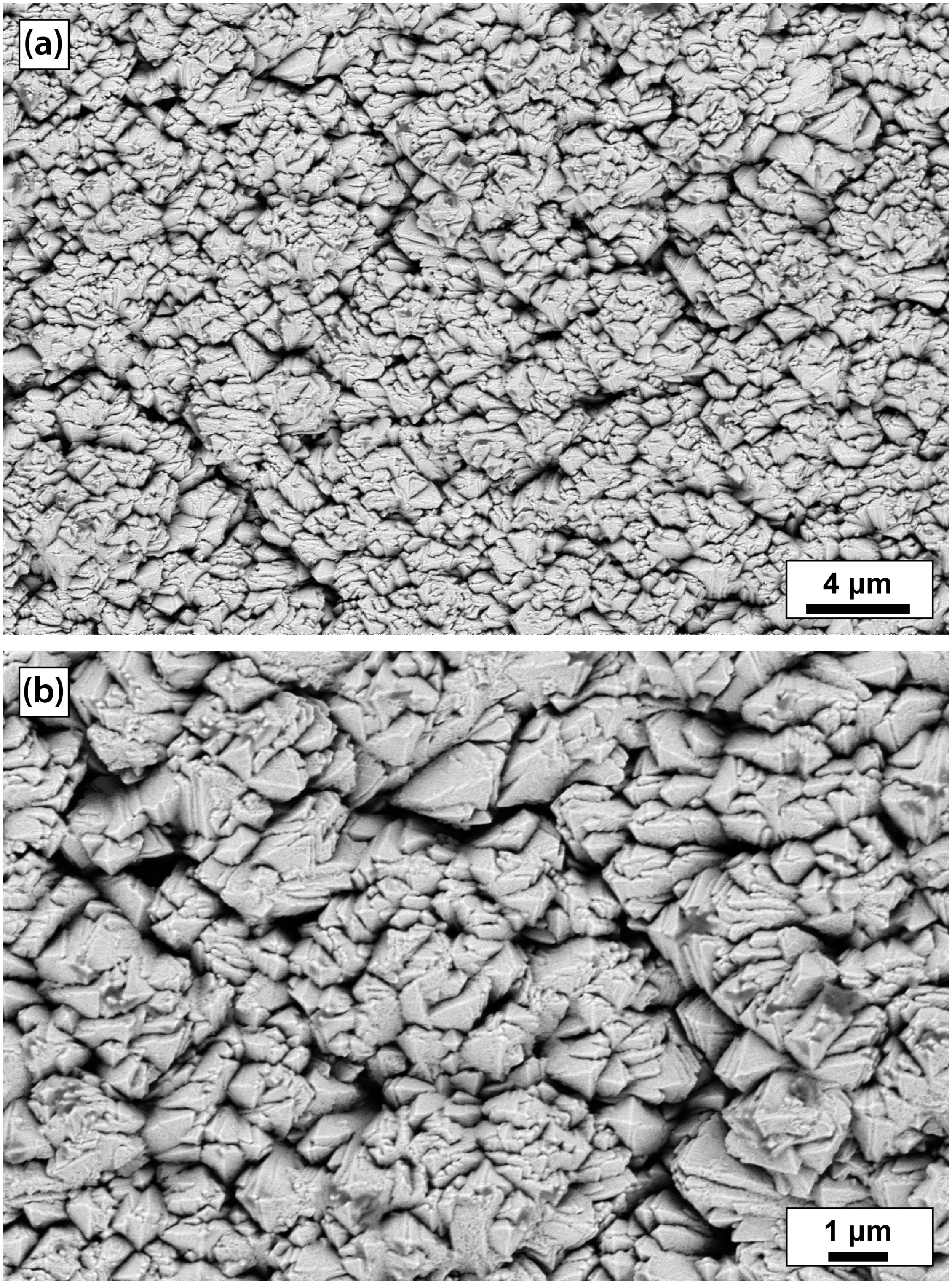
(a)
4 μm
(b)
1 μm

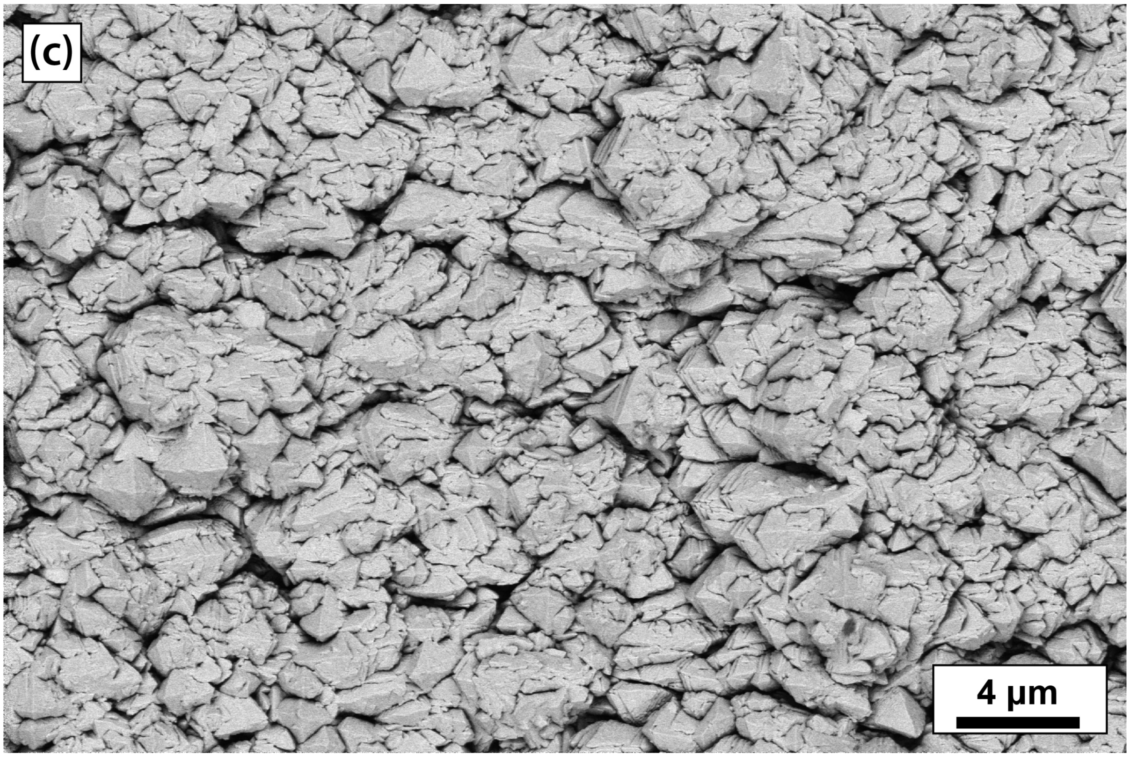
(c)
4 µm

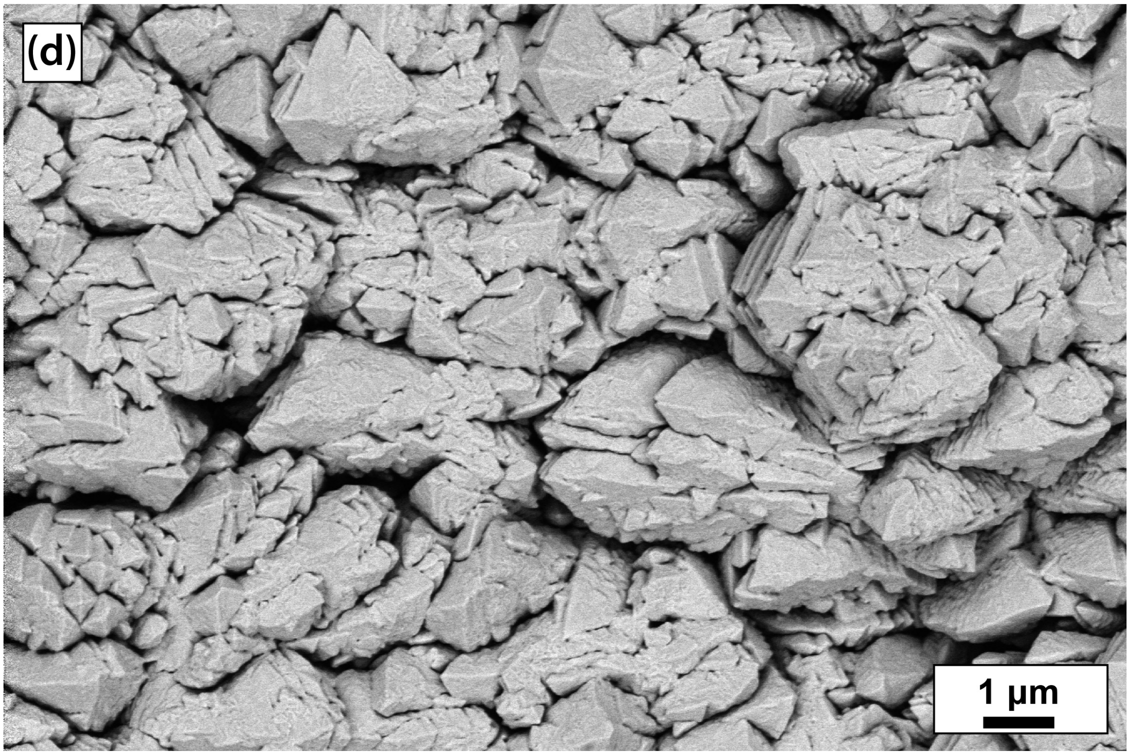
(d)
1 µm

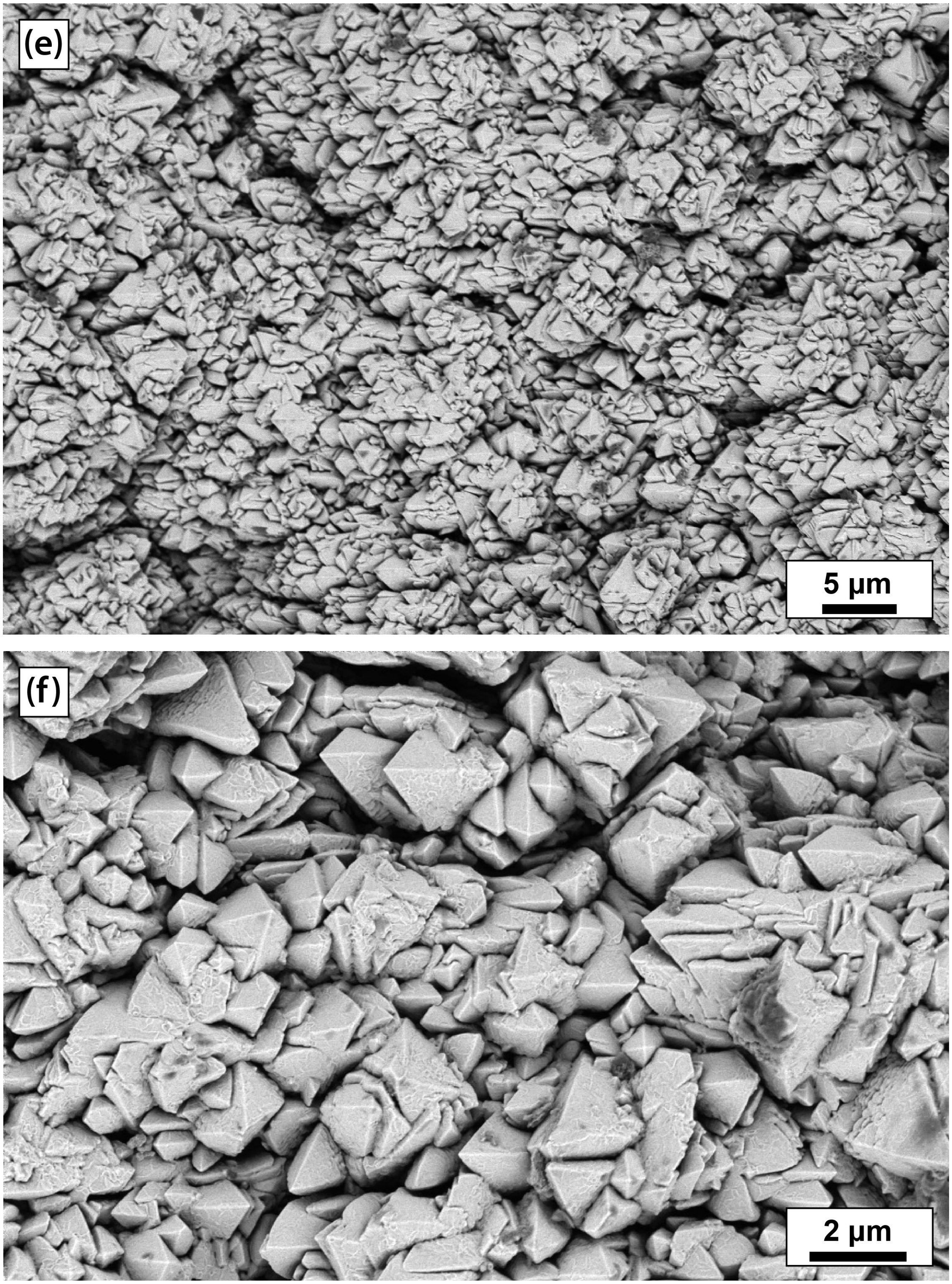

Figure 6.21: Surface images of the 7YSZ/Y_2O_3 bilayer coatings, (a) and (b) Y_2O_3-C, (c) and (d) Y_2O_3-D, and (e) and (f) Y_2O_3-E. The axis of substrate rotation is parallel to the horizontal direction.

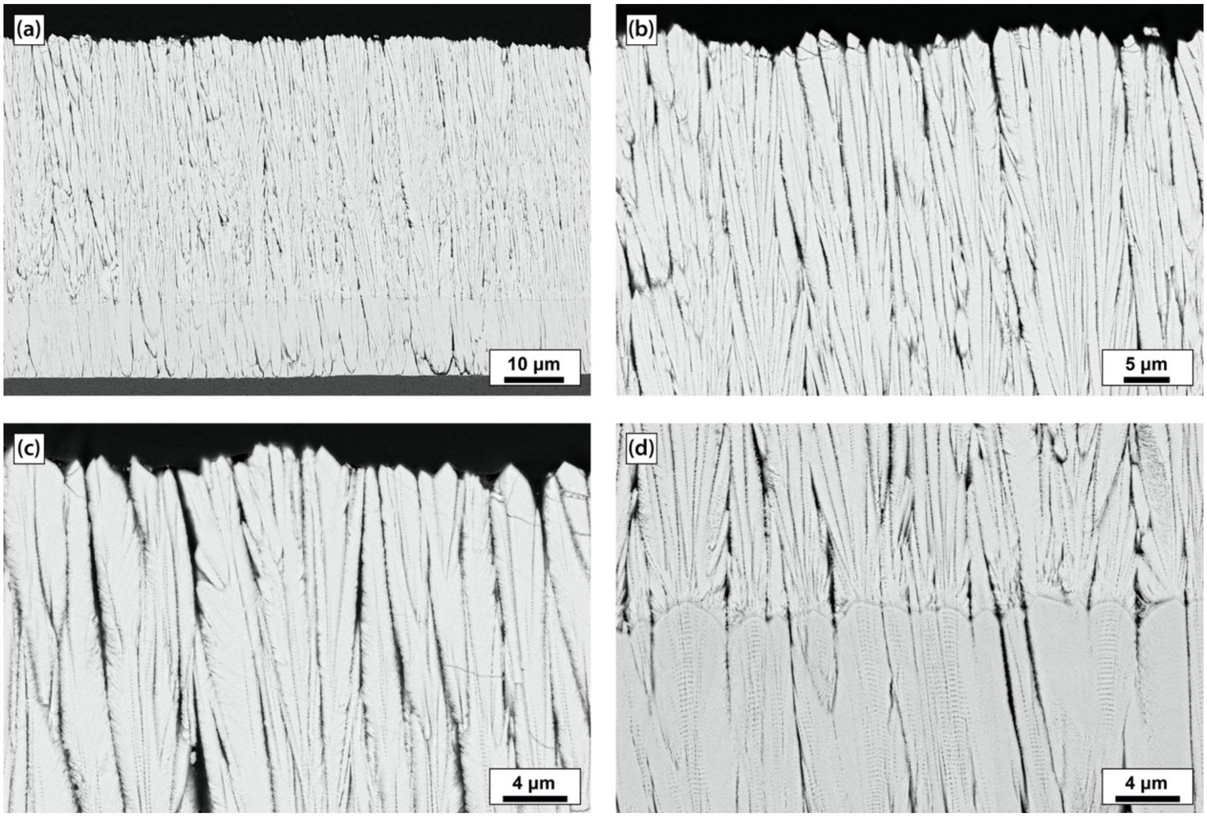

Figure 6.22: Cross-section images of Y_2O_3-C, showing (a) the overall morphology, (b) growth in the Y_2O_3 layer, (c) the column tips, and (d) the bilayer interface between the Y_2O_3 and the 7YSZ. The axis of substrate rotation is out of the page.

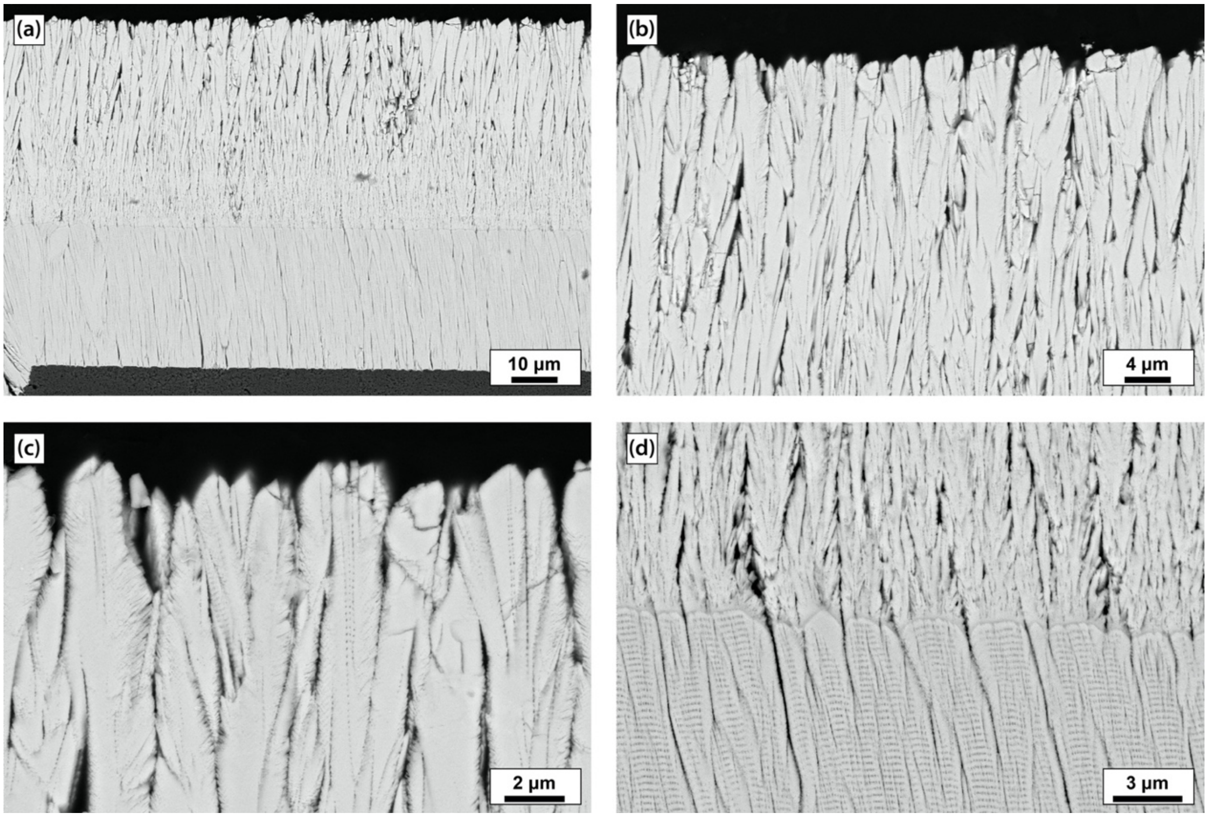

Figure 6.23: Cross-section images of Y_2O_3-D, showing (a) the overall morphology, (b) columnar growth in the Y_2O_3 layer, (c) the column tips, and (d) the bilayer interface between the Y_2O_3 and the 7YSZ. The axis of substrate rotation is out of the page.

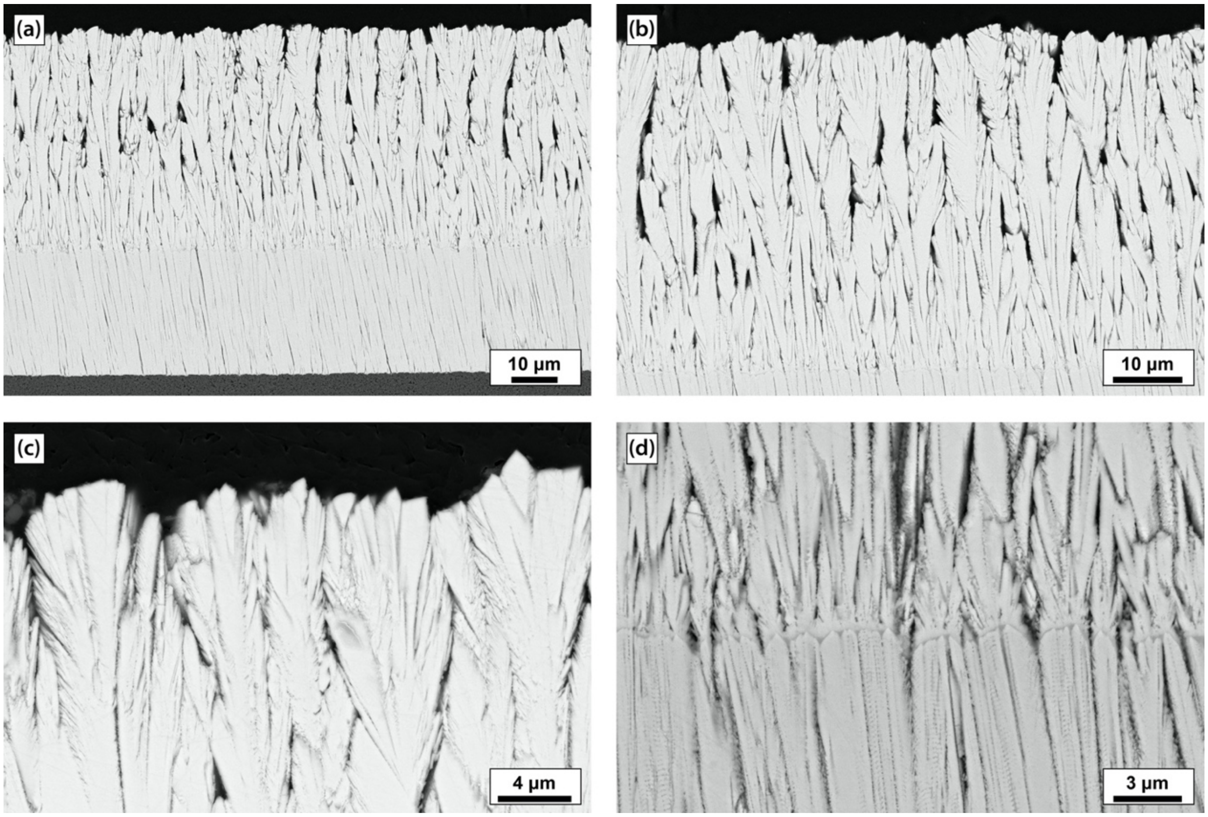

Figure 6.24: Cross-section images of Y_2O_3-E, showing (a) the overall morphology, (b) branched columnar growth in the Y_2O_3 layer, (c) the column tips, and (d) the bilayer interface between the Y_2O_3 and the 7YSZ. The axis of substrate rotation is out of the page.

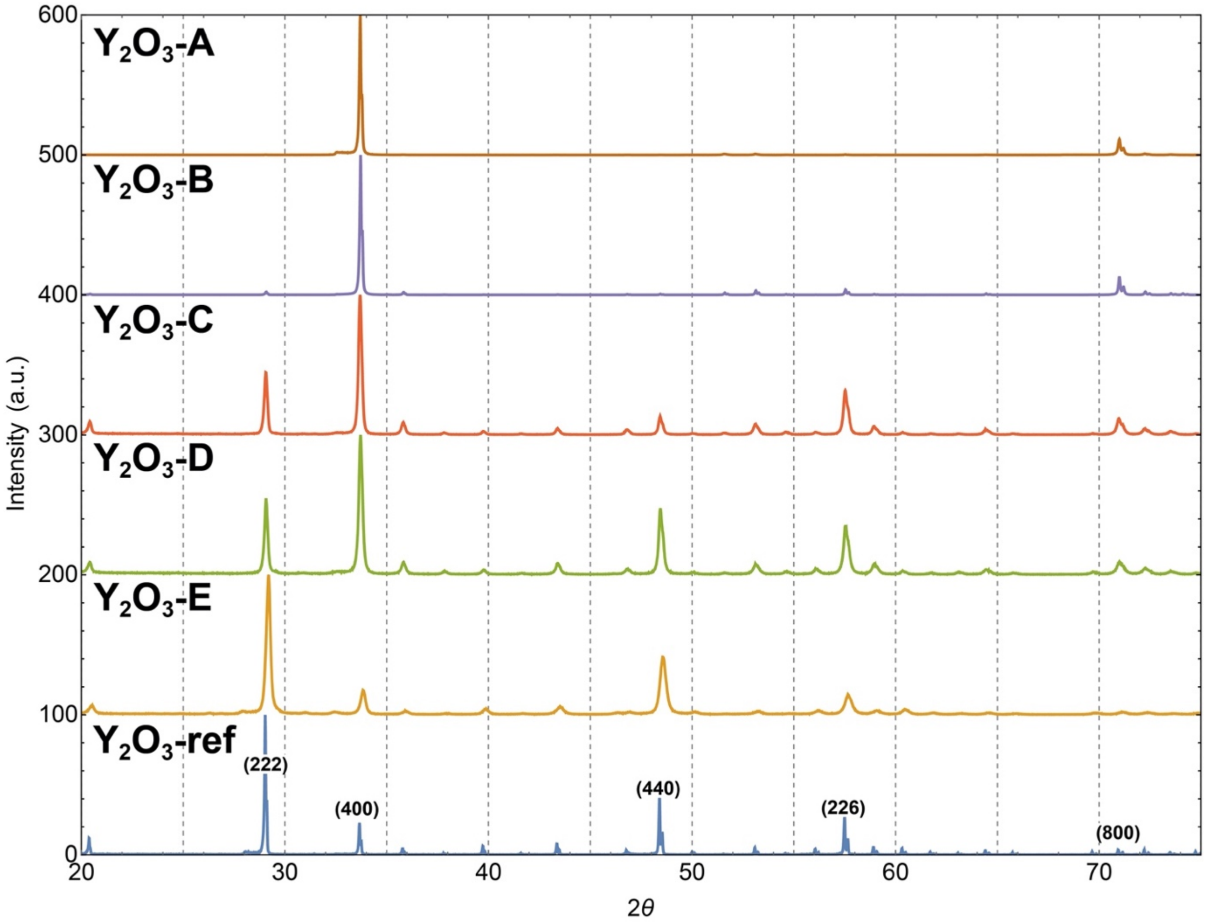

Figure 6.25: Surface XRD scans of the presented Y_2O_3 coatings. Reference scan from a Y_2O_3 ingot used for EB-PVD.

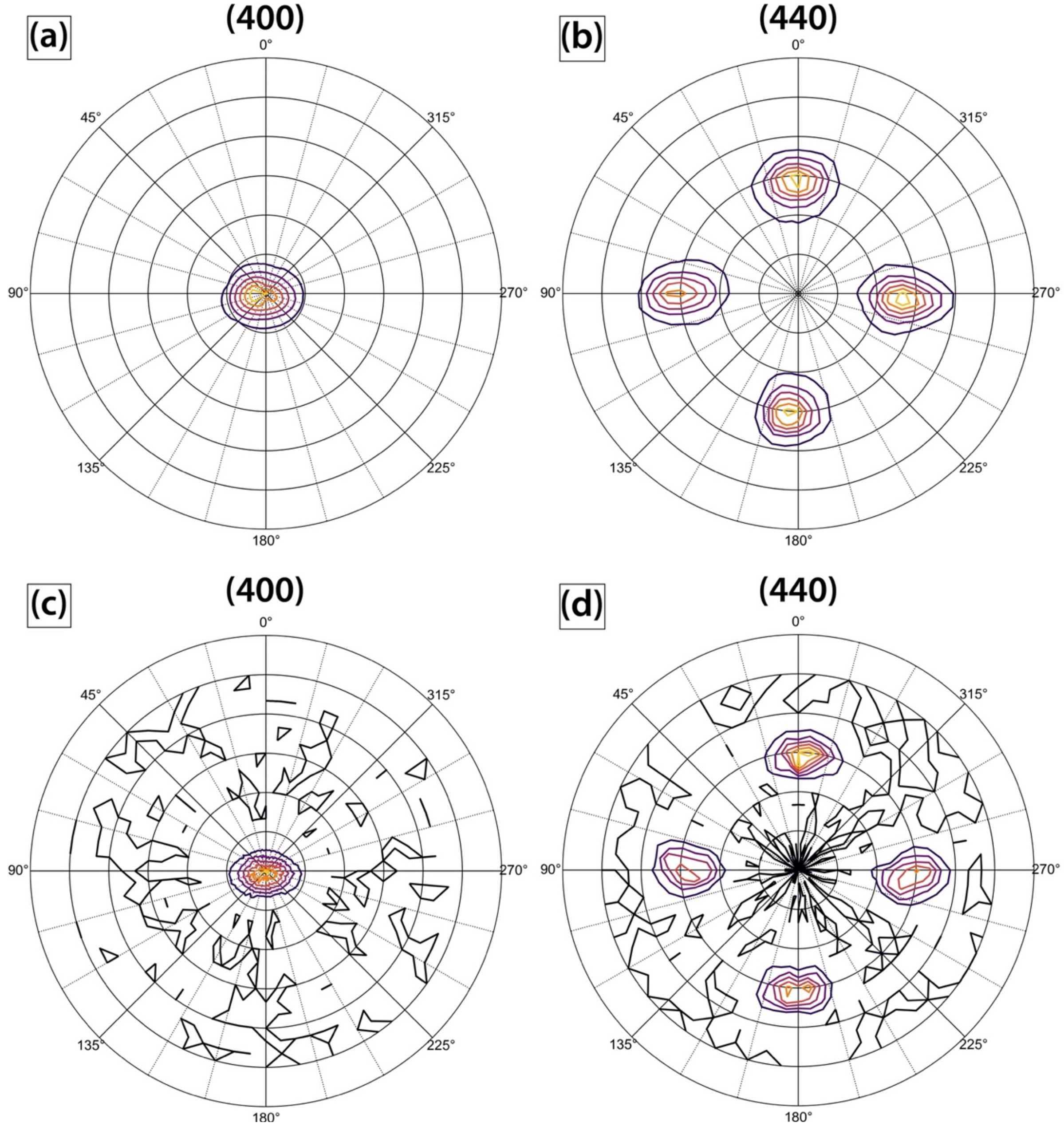

Figure 6.26: Pole figures for (a) and (b) Y_2O_3-A, and (c) and (d) Y_2O_3-B. The axis of substrate rotation is parallel to the horizontal direction.

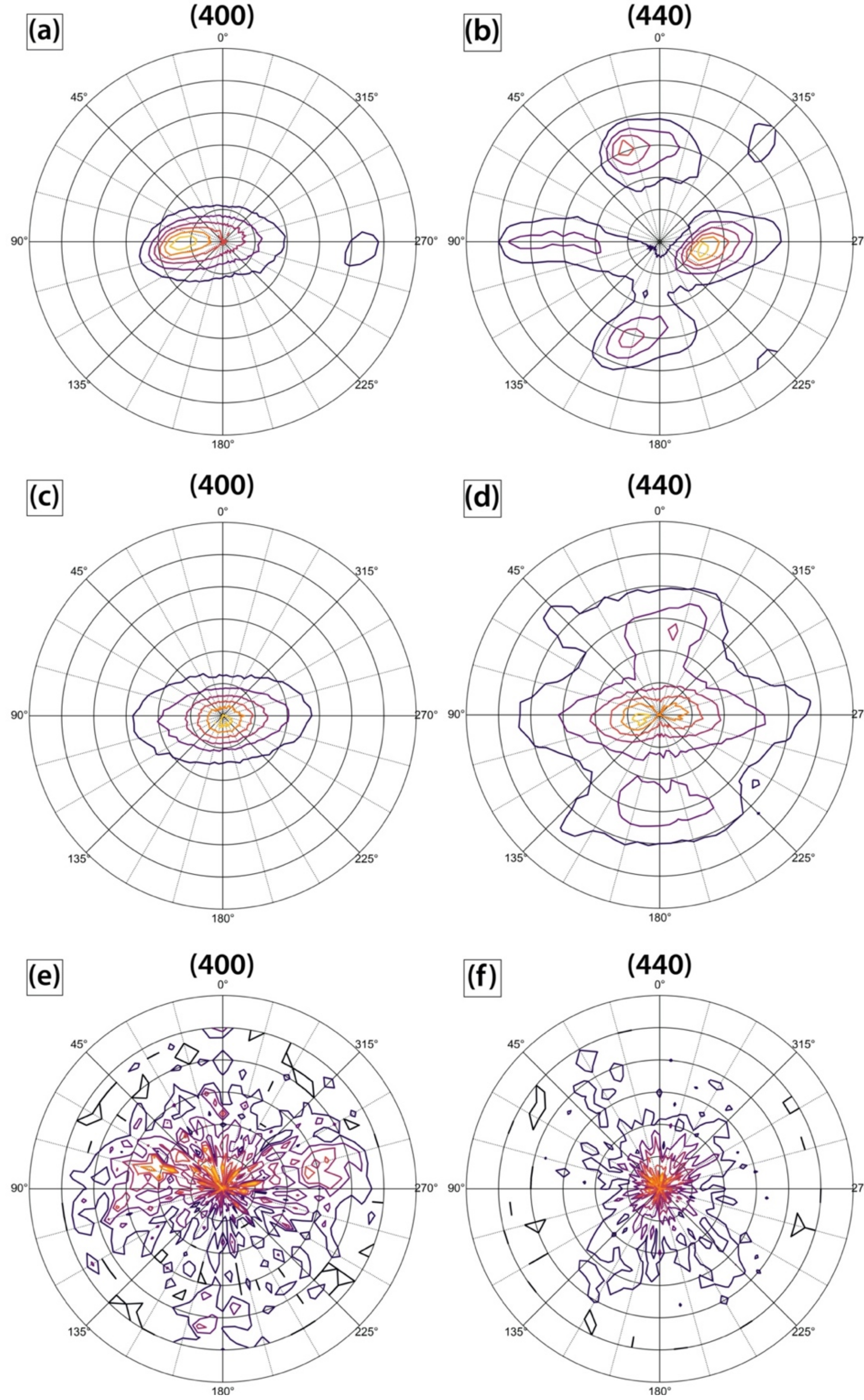

Figure 6.27: Pole figures for (a) and (b) Y_2O_3-C, (c) and (d) Y_2O_3-D, and (e) and (f) Y_2O_3-E. The axis of substrate rotation is parallel to the horizontal direction.

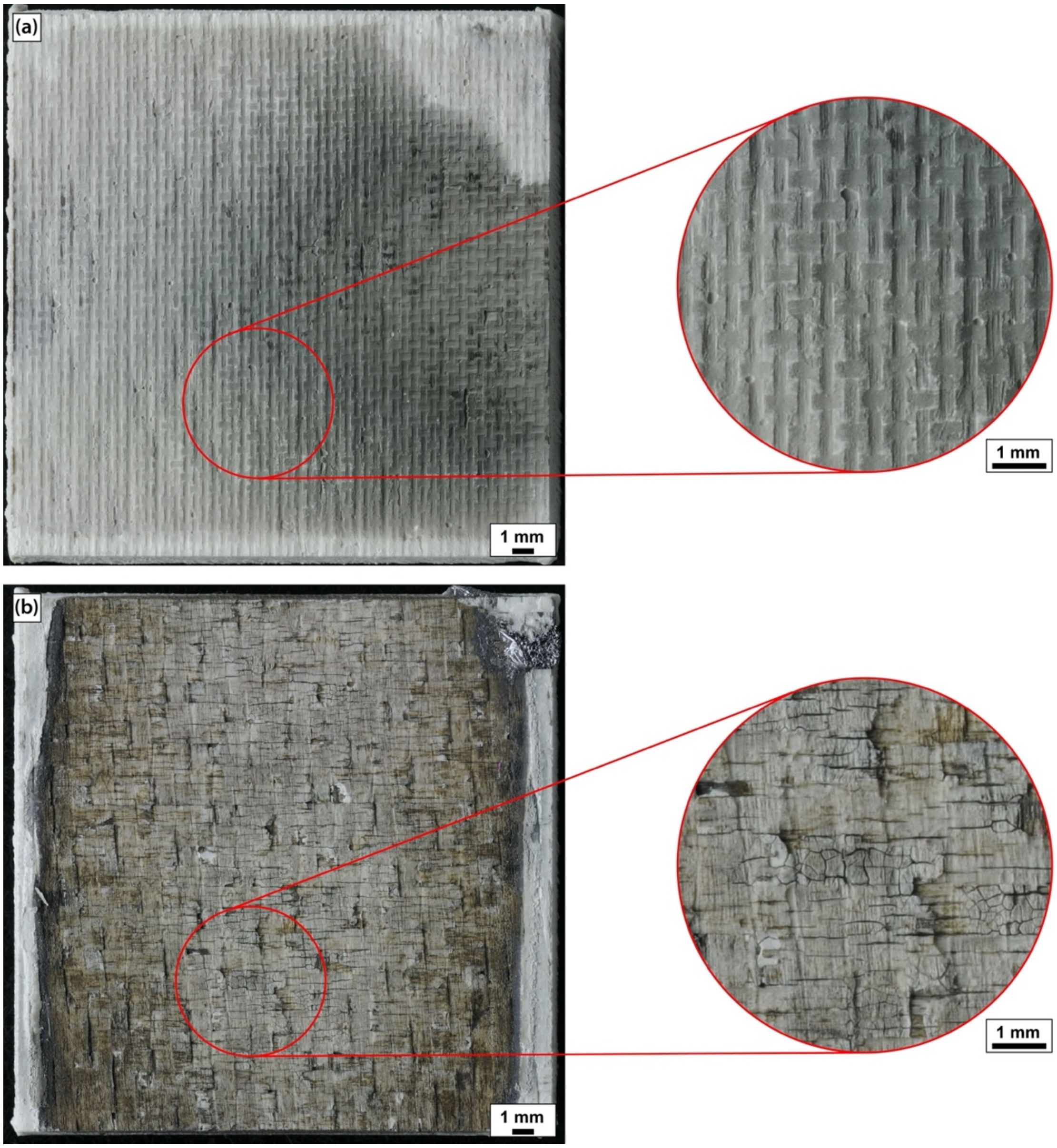

Figure 6.28: Backsides (the side facing the heating element) of two OFCC substrates after deposition, (a) 7YSZ-E grown at 1030°C, and (b) Y_2O_3-E grown at 1095°C. Insets highlight evidence of sintering in (b) and lack thereof in (a).

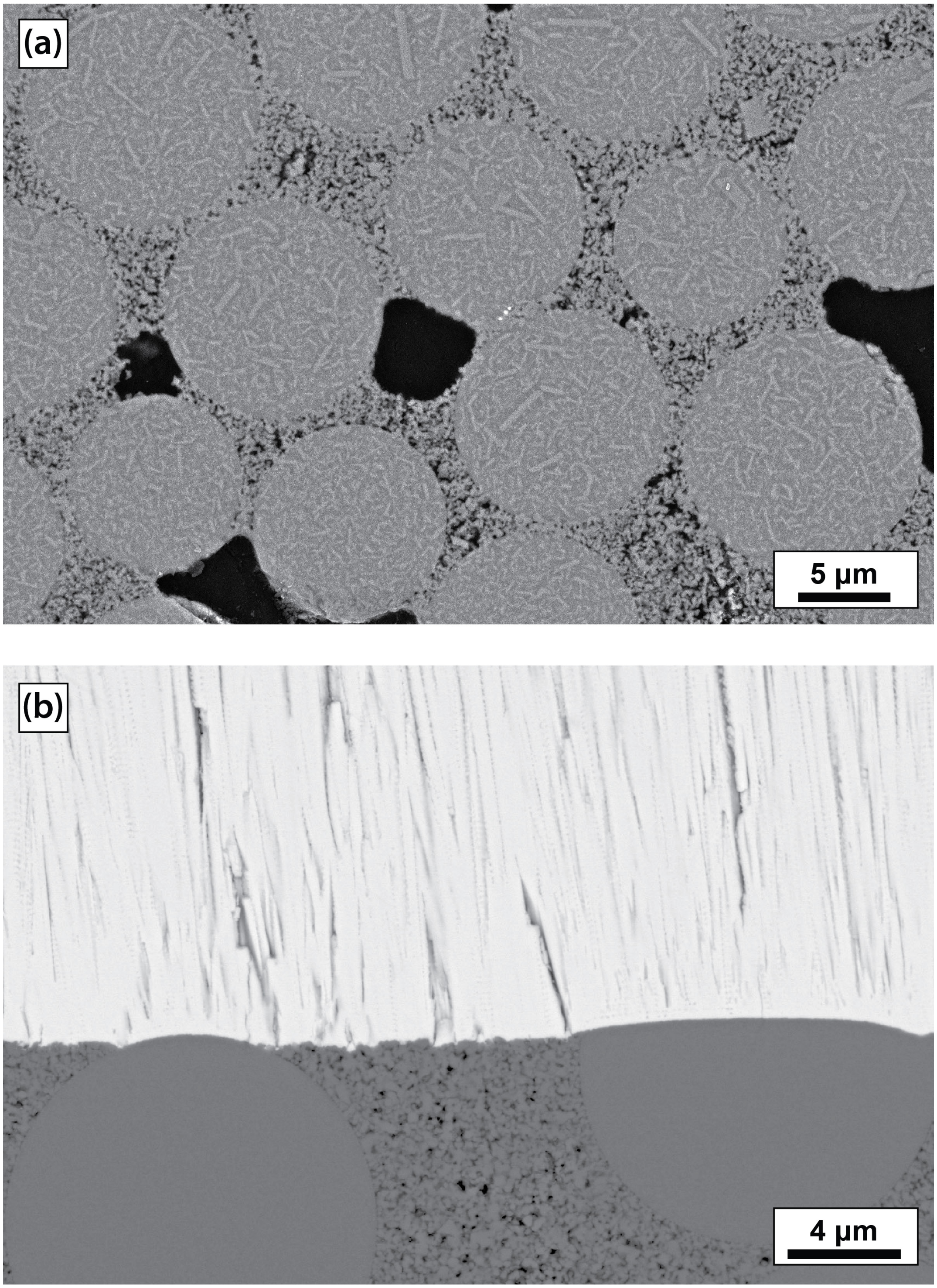

Figure 6.29: Cross-section images of (a) fibers near the backside surface of Y_2O_3-E, deposited at 1085°C, with extensive grain growth visible in the fibers, and (b) fibers near the coated surface of the same sample showing no visible grain growth.

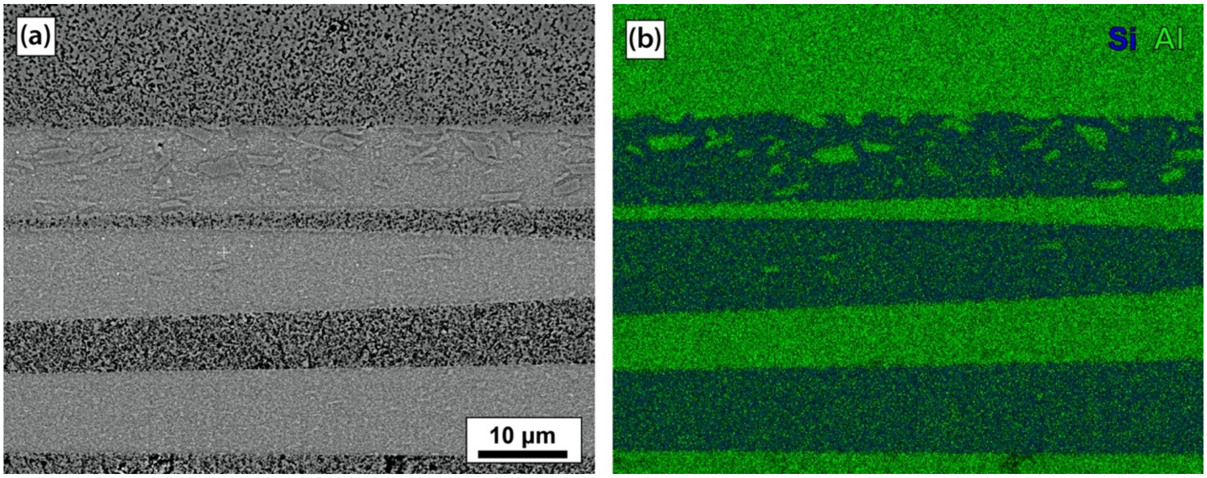

Figure 6.30: Cross-section image of fibers near the backside surface of Y_2O_3-E deposited at 1095°C, and (b) an SEM EDS elemental map showing the coarsened grains are alumina.

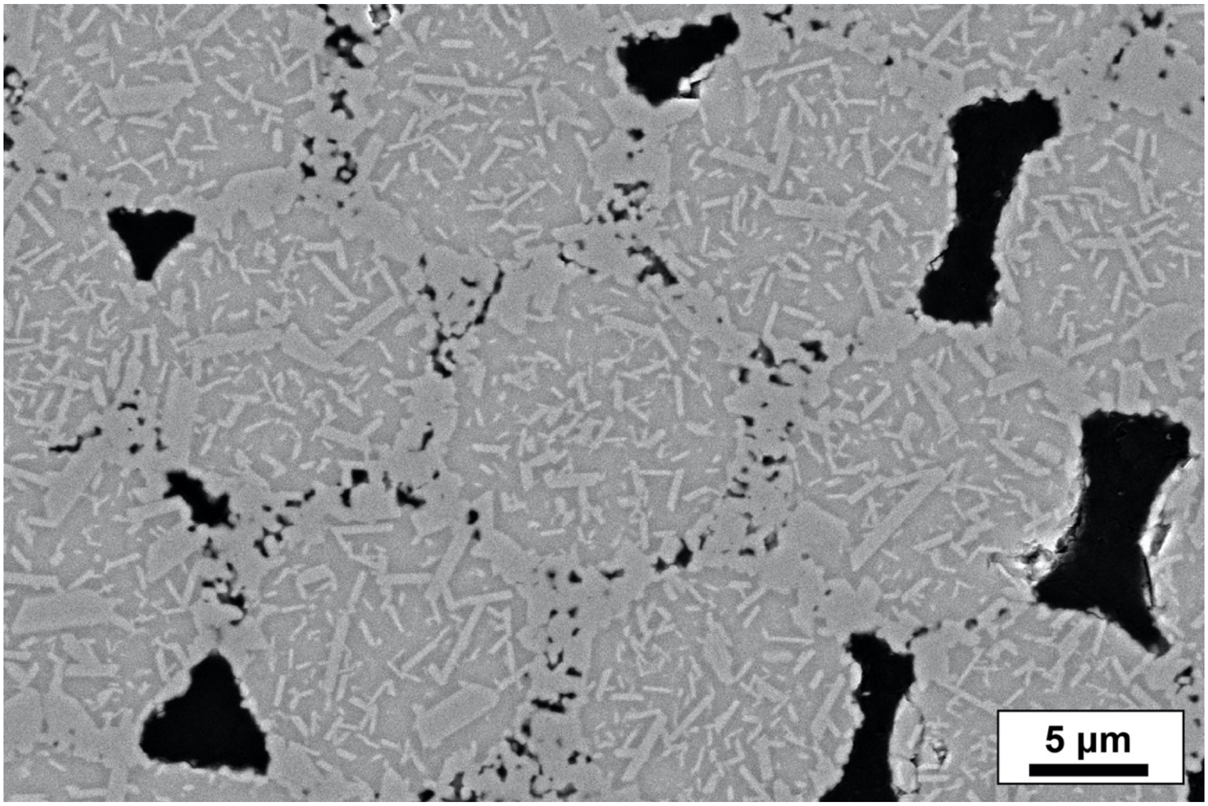

Figure 6.31: Visible grain growth in N720 fibers within an OFCC coupon annealed for 2h at 1600°C

Chapter 7: Degradation of EB-PVD Coated OFCCs in water vapor environments

This chapter is a culmination of the work of the previous chapters of this dissertation. The multilayer design of the coated OFCC barrier systems developed throughout the earlier chapters includes the porous matrix OFCC, the selective strengthening of said porous matrix, EB-PVD bilayers of comprising a diffusion barrier, 7YSZ, and a top coat with lower coefficient of thermal expansion (CTE). This concept is tested in this chapter to assess the efficacy of the design in simulated combustion environments at ambient pressures.

Previous work in **Chapter 4** showed that EB-PVD coatings have improved adhesion to OFCC substrates after furnace cyclic testing (FCT) experiments, attributed to the compliant, columnar microstructure, and the elimination of surface structuring required for good adhesion of thermally sprayed TBCs. However, the segmented microstructure that is advantageous for strain tolerance during thermal cycling is a concern for gas ingress. At sufficiently high temperature the mullite in the Nextel 720 fibers might react with water vapor and decompose by the following reaction [58]:

$$\mathrm{Al_4SiO_8(s) + 2\,H_2O\,(g) \rightarrow 2\,Al_2O_3 + Si(OH)_4\,(g)} \qquad \textbf{7.1}$$

This reaction will leave behind porous alumina in the fibers as the $Si(OH)_4$ species volatilizes out of the system. The N720 fibers are ~15 wt.% SiO_2 [36], corresponding to ~70.5 vol% mullite and 29.5 vol% alumina. The Al_4SiO_8 formula is used for mullite here as it is the composition in equilibrium with alumina [61]. This chapter presents a study of the extent of the fiber degradation in coated OFCC samples, and how differences in the coating materials' CTE, morphology, and density will influence the amount of water vapor ingress.

The approach to modify the deposition parameters to create multilayer coating systems with denser interlayers for the purpose of mitigating some gas ingress is also outlined.

7.1 Additional experimental details

7.1.1 Multilayered EB-PVD depositions

An additional coating system was developed, utilizing a denser interlayer of 7YSZ for the intention of mitigating some gas ingress when undergoing FCT in high temperature water vapor. **Figure 7.1** is a schematic illustration of the intended multilayer T/EBC system, with the added layer of denser 7YSZ. This thin, denser layer of 7YSZ was deposited without substrate rotation. Removing substrate rotation will create a denser coating, as it will grow without much of the inter- and intra- columnar porosity due to reduced shadowing effects and increased surface diffusion [111].

Two coating systems were created with this design, one with YZO as the top coat, designated YZO-S and one with yttria as the top coat, designated Y_2O_3-S. These two systems were processed using the UCSB evaporator described in **Chapter 3.** For each composition, two substrates were loaded into the substrate heater apparatus as described in **Chapter 3**. Two substrates were loaded to have two coated OFCCs, one to analyze as deposited, and one to run with FCT. The initial layer of 7YSZ was deposited on the first stationary OFCC, with a targeted surface temperature of 1100°C to maximize density. The shutter was closed, and the substrate heater was rotated manually 180° to expose the other OFCC substrate. After the same time of stationary 7YSZ deposition for both substrates, automatic substrate rotation was initiated. After a short-time depositing 7YSZ with substrate rotation, the shutter was closed, the e-beam powered down, and the source ingots switched while maintaining the backside heating, identical to the bilayer deposition method described in **Chapter 3**. The top layer was then deposited, with the target surface temperature for the topcoat being 1000°C in both depositions. The targeted total thicknesses were to be comparable to the 7YSZ/YZO and 7YSZ/yttria bilayers. The thicknesses of the layers and process parameters for all cycled coatings are presented in **Table 7.1**.

7.1.2 Vapor rig cycling details

FCT of the coatings in the vapor rig was performed in accordance with the method described in **Chapter 3**, with all coatings cycled 100 times with a 30 minute dwell, for a total of 50 h of water vapor exposure at temperature. Six coated OFCCs in total were cycled. 7YSZ-E, YZO-A, Y_2O_3-A, and Y_2O_3-E, these 4 coatings were previously described in **Chapter 6**. As well as the two coatings with the stationary deposition 7YSZ layer, designated YZO-S and Y_2O_3-S.

7.2 Results

7.2.1 7YSZ monolayer

Figure 7.2 (a,b) shows the surface of the 7YSZ-E coating before and after the FCT water vapor exposure. The coatings surface showed signs of morphological change. Especially the surface of the roughened, elongated pyramids showed an increase in pore size. The surface also lost visible, distinct facets, with the column tips appearing more rounded.

There was no visible delamination along the width of the cross-section, shown in **Figure 7.3 (a,b)**, or any significant increase in channel cracks from the as-deposited condition. A closer look at fibers near the coating / composite interface in **Figure 7.4 (a,b)** showed a layer of porosity around the edge of the fibers that ranged in thickness from about 0.25 μm to 1 μm. The region of the fibers that was in direct contact with the 7YSZ coating did not appear to show a different level of porosity than the regions of the fibers in contact with the porous alumina matrix.

7.2.2 YZO bilayer

The surface of the YZO-A coating after cycling in **Figure 7.2 (c,d)** showed minimal evidence of morphological changes. There was very little evidence of morphological change on the pyramidal column tips of the YZO, with the facetted sides of the pyramidal tips and the crystallographic steps on those facets still distinctly visible.

Once again, there was no sign of delamination when viewing the cross-section of the sample after exposure, seen in **Figure 7.3 (c,d)**. Nor was there any indication of increased channel cracks than in the as-deposited condition. A closer look at fibers near the coating / composite interface in **Figure 7.4 (c,d)** showed porosity around the outer edges of the fibers, extending 1-2 μm into the fiber. The damage appears to be more significant on the region of the fiber closer to, or in contact with the 7YSZ interlayer of the EB-PVD coating, creating a crescent shape of the porosity in the damaged fibers.

7.2.3 Fiber degradation

Figure 7.5 presents an EDS Si elemental map of some damaged fibers near the coating interface in the YZO-A sample. The map illustrates that the porous regions of the fibers have reduced silicon compared to the bulk of the fiber. The porous regions of the fibers are essentially alumina, suggesting the silica in the N720 fibers (nominally ~15% by weight, equivalent to ~70% mullite volume content [36]) reacts selectively with water vapor that has penetrated the porous EB-PVD coating and matrix of the OFCC, forming the gaseous $Si(OH)_4$ species leaving only the alumina constituent. The volatilization of SiO_2 yields an estimated pore content of ~25% assuming no sintering of the residual alumina product.

7.2.4 Yttria bilayers

The two cycled yttria bilayered coatings, Y_2O_3-A, the columnar structure, and Y_2O_3-E the branched structure, both maintained good adhesion along the cross-section, as seen in **Figure 7.6**. Surface images after cycling in **Figure 7.7** showed a scaly appearance in both samples. The scales also appeared to cover the column tips as well as seal the gaps between them. When examining fibers near the coating/OFCC interface in **Figure 7.8**, the branched coating of Y_2O_3-E showed little to no evidence of degradation, and the columnar yttria showed some evidence of damage, with ~500 nm of damage seen on the fiber edges. A closer look at the bilayer coating itself in cross-section shown in **Figure 7.9** revealed another phase, visible with intermediate contrast in BSE imaging both at the 7YSZ/yttria interface, and at the yttria surface. The phase also appeared along the edges of channel cracks in the coatings, shown in **Figure 7.10 (a,c)**. EDS elemental maps in **Figure 7.10 (b,d)** reveal this phase contains silicon, forming as a rection product of the volatilized $Si(OH)_4$ from the mullite-containing N720 fibers. Visible in **Figure 7.10**, the Si-containing reaction phase grows up the channel cracks from the bilayer interface towards the coating surface. The reaction phase is likely the monosilicate, Y_2SiO_5 (YMS), as it is in contact with Y_2O_3 [112].

7.2.5 Multilayers with denser 7YSZ layer near the interface with OFCC

Cross-sections of the as-deposited multilayer of YZO-S are presented in **Figure 7.11**. Due to a complication with sample rotation, there was not a Y_2O_3-S sample to dissect for as-deposited imaging. Only one sample existed with a stationary 7YSZ layer, and it was used for FCT.   It is expected, however, that the as-deposited microstructure for YZO-S would be similar to that deposited for other YZO coatings of comparable thickness.

Many channel cracks are observed when examining the as-deposited cross-sections of YZO-S, seemingly more numerous than in the as-deposited cross-sections of YZO-A. The stationary 7YSZ layer appears denser, with less visible columnar porosity, than the rotated layer.

The surface of YZO-S, both before and after exposure, are presented in **Figure 7.12**. Before cycling, the surface morphology is very similar to that of YZO-A, with sharp facets on elongated square pyramidal-type column tips. After cycling was also very similar to YZO-A in **Figure 7.2 (d)**, with only small deviations from the as-deposited microstructure; slight pore coarsening near the tips of the columns, but with distinct facets and crystallographic steps still visible.

The surface of Y_2O_3-S before and after cycling is presented in **Figure 7.13**. Like the YZO-S and YZO-A, the surface morphology before and after cycling of Y_2O_3-S are nearly identical to Y_2O_3-A. The as-deposited exhibiting very sharply facetted square pyramidal column tips, and after exposure, the surface appears scaly, although the general shapes of the square pyramids are still visible. The scaly surface appears to seal-off some of the intercolumnar porosity.

Cross-sections post-cycling of YZO-S in **Figure 7.14** show good adhesion along the entirety. Many channel cracks are visible, but there is no indication there are more than in the as-deposited coating. A closer look does show a small amount of fiber damage (porosity) ranging from 0.25 to 1 μm, with more damage localized around channel cracks, labelled in **Figure 7.15 (b)** and **(d)**. This is less prevalent damage than observed in YZO-A, and especially less damage on fibers in direct contact with the denser 7YSZ layer. Overall, the observed fiber damage in YZO-S is less than YZO-A, but the damage is especially localized around coating defects, like channel cracks or growth defects from surface perturbations, with fibers away from these defects being less attacked.

Cross-section images of Y_2O_3-S after cycling in **Figure 7.16** also show no sign of adhesion loss across the whole section. Higher magnification in **Figure 7.17** reveals a similar (reaction) additional phase at both the surface of the yttria, and at the interface between the rotated 7YSZ interlayer and the yttria topcoat. The extent of fiber damage, shown in **Figure 7.18**, is similar to that observed with the columnar Y_2O_3-A, with the most observed damage near coating defects. The fiber damage is more prevalent than in Y_2O_3-E, comparable to Y_2O_3-A, but less than YZO-S, YZO-A, or 7YSZ-E.

7.3 Discussion

7.3.1 Mechanism of water vapor ingress and silica volatility

The proposed mechanism is presented schematically in **Figure 7.19**, and will be discussed in detail in this section. The configuration of the specimen in the vapor furnace (coupon surface is normal to the incident vapor flow) suggests there is a boundary layer of flowing gas over the surface of the coupon. The gas is able to diffuse down into the coating to the substrate via the intercolumnar gaps and the flow would be accelerated in the wider gaps created from channel cracks and coating growth defects. The water vapor that diffuses through to the OFCC substrate would interact with N720 fibers in contact with the coating and continue to diffuse through the porous alumina matrix and interact with N720 fibers near the coating interface.

The temperature at which this water vapor/N720 fiber interaction was taking place was constant at ~1200°C. SiO_2, wherein mullite readily reacts with water vapor [58] The interaction between the penetrating water vapor and the N720 fibers will be a reaction, forming $Si(OH)_4$ gas and leaving behind porous alumina. The $Si(OH)_4$ gas diffuses back up through the porous matrix, columnar porosity in the EB-PVD coating, or the larger gaps from coating defects or channel cracks, and then will diffuse out of the coating into the gas boundary layer and ultimately is carried over the surface of the coupon.

In the case of the 7YSZ monolayer and the YZO bilayer, the $Si(OH)_4$ gas diffuses out of the coated OFCC and does not interact further with any of the constituents along its path, namely the alumina matrix, the 7YSZ layer, or the YZO, or while in the boundary layer along the surface of the coating. The yttria bilayers, however, exhibit a different behavior. The outgoing $Si(OH)_4$ gas reacts with the yttria coating at the bilayer interface, along channel cracks and coating defects, and at the outer coating surface. Reaction is not significantly observed along the intercolumnar porosity. There also is enough $Si(OH)_4$ that escapes the coating to fill the boundary layer enough that it will react with the entirety of the surface of the yttria topcoat.

7.3.2 Differences in Si vapor interactions with Y_2O_3 , YZO, and 7YSZ

In the present work, the only topcoat material observed to react with the $Si(OH)_4$ vapor was Y_2O_3, forming YMS. No vapor interaction was observed in the YZO and 7YSZ coatings. Ternary equilibrium in the Zr-Y-Si-O system [112,113] suggests that $Y_2Si_2O_7$ (YDS) and $ZrSiO_4$ (zircon) as reaction products with ZrO_2 –$YO_{1.5}$ solid solutions and SiO_2. However, as the Y-activity decreases with decreased $YO_{1.5}$ content, the kinetics for the reactions may not be as favorable. While the conditions in the present work are different than the literature equilibrium studies, it is important to note that the Y- activity decreases with increasing ZrO_2 content. The ternary diagram does suggest YMS will form with YZO [112,113], but this reaction may not be as kinetically favorable due to the reduced Y- activity in the solid solution. Likewise with 7YSZ, zircon could be expected to form from interaction with silica, but the kinetics may not be favorable in the conditions of this work. Also worth consideration is the stability of the other silicates in water vapor. Both YDS and zircon have Si- activities (a_{SiO2} = 0.083 [61] and ~ 0.5 [114] , respectively) greater than that of YMS ($a_{SiO2} = 1.1 \times 10^{-4}$ [61]) and may decompose from SiO_2 volatilization.

7.3.3 Effects of morphology differences on yttria reaction

Y_2O_3-E generally exhibited minimal fiber damage There was extended fiber degradation near channel cracks, shown in **Figure 7.20**, coating defects, shown in **Figure 7.21**, and even more extensive damage near the coupon edges and below 'shadowed' areas of the coupons, seen in **Figure 7.22**. The 'shadowed' areas of the coatings were much thinner, and were created by the refractory wires needed to secure the OFCC to the substrate holder, and consequently did not receive much vapor flux. The increased fiber damage meant these locations on the samples were rich sources of $Si(OH)_4$ to quickly diffuse or flow out from the coating and into the boundary layer over the surface of the coupon.

There were notable differences between the yttria bilayers, the columnar Y_2O_3-A, and the branched Y_2O_3-E, in terms of the amount of silicate reaction phase observed at the yttria surface and at the 7YSZ/yttria interface, as well as the amount of visible fiber degradation detected. While the Y-silicate phase at the surface of each sample was comparable and ubiquitous, both the amount of Y-silicate at the 7YSZ/yttria interface and the extent of observed fiber degradation were less in the branched, Y_2O_3-E sample. This leads one to believe that the possible explanation could be the morphology of the coatings.

Y_2O_3-E was deposited at a greater surface temperature, which often leads to denser EB-PVD coatings [75,77,115], so it is reasonable to assume that this coating would be denser overall than Y_2O_3-A, or at least the 7YSZ interlayer in the bilayer systems. The increased density of the coating could reduce the speed of both water vapor ingress and $Si(OH)_4$ egress, which could explain the reduced fiber damage and Y-silicate reaction at the bilayer interface. However, Y_2O_3-S had a 25 μm thick layer of stationary deposited 7YSZ that would be denser than the 7YSZ interlayer in Y_2O_3-A or -E. However, Y_2O_3-S shows a similar amount of fiber degradation and reaction at the 7YSZ/yttria interface to that of Y_2O_3-A in spite of the denser interlayer. Y_2O_3-S and Y_2O_3-A also both had a columnar structure of the yttria topcoat. The branched microstructure of Y_2O_3-E has much finer features at its surface compared to the sharply faceted square pyramidal tips of the columnar structures. It might be assumed from these features that the Y_2O_3-E has a greater internal surface area than either Y_2O_3-A or Y_2O_3-S, and will therefore allow a faster reaction with the $Si(OH)_4$ gas in the 'boundary layer' that comes from the defects discussed earlier. Since the reaction happens faster in Y_2O_3-E, it sealed the surface to some extent to hinder the ingress of water vapor, which explains the reduced amount of observed fiber degradation in the Y_2O_3-E sample. The reaction at the 7YSZ/yttria interface does not happen as fast as the source of $Si(OH)_4$ is local, the fibers directly below the interface. The reaction at the surface happens faster as the $Si(OH)_4$ can come from a more plentiful source ,the large defects, elsewhere on the coupon and get distributed by the boundary layer of vapor flowing parallel to the coupon surface.

This also explains why reaction is not observed along the intercolumnar gaps in the yttria. The reaction at the surface and bilayer interface are two slightly different mechanisms. Given longer time exposure to water vapor, the reaction phase at the bilayer interface would be expected to grow up the columns.

7.3.4 Effects of topcoat CTE differences – YZO v 7YSZ

There is noticeably more fiber damage in the YZO-A than 7YSZ-E. The total thicknesses of the two coatings is comparable (160 vs 150 μm, respectively). One of the possible effects is the CTE differences between YZO [94](9-10 ppm/°C) and 7YSZ [51,92,95] (12-13 ppm/°C). Both of these materials have a greater CTE than the underlying OFCC, meaning that the intercolumnar gaps in the EB-PVD coating will close up on heating, as the coating material expands more than the substrate [116]. Additionally, since the temperature for the FCT vapor rig runs, 1200°C, was nearly 200°C greater than the deposition temperatures of these two coatings (1035°C), the intercolumnar gaps will become narrower than on deposition, reducing the pathways for water vapor ingress. This is shown schematically in **Figure 7.23**. As 7YSZ has a greater CTE than YZO, and therefore a greater difference to the OFCC substrate, the intercolumnar gaps will close further in the 7YSZ sample than the YZO coated sample at temperature. This further gap closure reducing could be the reason for the greater extent of fiber damage observed in the YZO bilayer coated specimen in **Figure 7.4**, however this is only one of the possible effects as due to limited samples, this difference in fiber damage cannot be definitively ascribed.

An additional difference between the two coatings was seen from the surface images after cycling. 7YSZ appeared to show a greater effect of diffusion, with the sharp facets of the column tips becoming rounded, as well as coarsened pores on the surface, seen in **Figure 7.2**. The surface of the YZO coating appeared less perturbed, with the sharp facetted features of the column tips still visible, and far less pore coarsening. These observations suggest that YZO is more resistant to morphological change in at 1200°C in water vapor. Despite the cubic phase having more vacancies than 7YSZ, it has been reported that high yttria contents, upwards of 50 mol.% $YO_{1.5}$, can drastically change the sintering behavior of yttria stabilized zirconias, being more resistant to densification. This is reported in other RE-zirconates as well, with $Gd_2Zr_2O_7$, $La_2Zr_2O_7$, and $Yb_2Zr_2O_7$ all being more resistant to densification than 7YSZ [64,117]. This could explain the morphological changes seen in the 7YSZ coating that are not seen in YZO coating. The RE- cation, Y in this case, is less mobile, so diffusion is slower in the higher RE-content zirconias. Despite the 7YSZ coating showing more resistance to water vapor ingress, the evidence of sintering could pose a challenge for long-term durability. The columns will be closer together at temperature and are at risk of sintering together, reducing or eliminating the compliance benefit of the columnar coating.

7.3.5 Effects of denser interlayer

When comparing YZO-A to YZO-S, there was a noticeable decrease in overall fiber damage in YZO-S. Especially when looking at fibers in direct contact with the 7YSZ interlayer; the fibers in contact with the stationary deposited 7YSZ in YZO-S exhibited minimal degradation, whereas the fibers at or near the 7YSZ interlayer in YZO-A had damage upwards of 2 μm into the fibers. Fiber damage was more extensive in localized areas near coating defects and channel cracks in YZO-S. The denser interlayer, therefore, noticeably mitigated some water vapor ingress, especially since the overall thickness of YZO-S, 115 μm, was less than YZO-A, 160 μm.

The addition of the denser interlayer in the yttria coatings had a more subtle effect. While overall, the fiber damage and extent of Y-silicate reaction was comparable between Y_2O_3-A and Y_2O_3-S, the regions of fibers in direct contact with stationary 7YSZ in Y_2O_3-S showed little to no evidence of degradation in **Figure 7.18**. This indicates, that at least locally, the denser interlayer helped mitigate some ingress. However, the Y-silicate reaction at the surface of the all yttria coatings was more effective in mitigating ingress than the denser 7YSZ interlayer, as evident by all of the yttria coatings showing less fiber damage than 7YSZ-E, YZO-A, or YZO-B. Similar to Y_2O_3-E, Y_2O_3-S showed more fiber damage near channel cracks, shown in **Figure 7.24**, and near shadowed regions and the coupon edge, shown in **Figure 7.25 (a)** and **(b)** respectively. Despite the denser interlayer, these regions provided enough $Si(OH)_4$ to cover the entire yttria surface in the reaction silicate and block the intercolumnar porosity.

While the denser 7YSZ did help prevent some ingress, it did not address a fundamental issue with applying coatings to an OFCC. Surface defects are inevitable from the processing of porous matrix OFCCs, and they lead to coating defects and large gaps in EB-PVD coatings, and the porous matrix, even if hardened with precursor, is still not strong enough to prevent all channel cracking from thermal stresses after deposition.

7.3.6 Assembling the entire multilayered system

Designing and implementing the multilayered system, from modified matrix to selectively strengthen the surface regions of the porous matrix – To EB-PVD coatings, bilayers, and bilayers with a denser interlayer – all were effective for improving T/EBC adhesion while mitigating gas ingress to the OFCC. The denser EB-PVD interlayer was not completely effective in this work. Even stationary deposition in EB-PVD will not produce a completely dense coating, and channel cracks from thermal stresses, as well as surface defects creating coating defects allow for gas ingress to the OFCC.

For improved efficacy, this denser deposition would need to be used in tandem with a surface treatment or coating to address these surface defects and, ideally, also create a hermetic layer. Reaction bonded aluminum oxide (RBAO) has been proven to do exactly this in literature [33,34]. Even with CTE mismatch between a 7YSZ coating and an alumina based OFCC, RBAO interlayers have shown to arrest thermally induced channel cracks preventing penetration of the porous matrix [34,35]. However, these channel cracks are also providing relief from thermal stresses on cycling for these coatings, especially the 7YSZ and YZO-based systems with a greater CTE mismatch. A denser layer, of RBAO, for example, would have fewer of these types of channel cracks, so an EB-PVD coating may not be as durable and show evidence of spalling.

There is a question of whether the coating will maintain adhesion and durability without the channel cracks present to relieve some thermal stresses. While the surface matrix region was hardened from precursor, it was not enough densification to prevent channel cracking, or to fill in the of the surface matrix cracks in the OFCC, existing from processing due to CTE difference between the alumina matrix and the N720 fibers.

7.3.7 Implications for other multilayered T/EBC systems

The results of this chapter have implications to other refractory ceramic systems containing silicon. Multilayered T/EBC systems are in development for SiC – based CFCC components. EB-PVD RE-Zirconates are targeted materials for a topcoat TBC, which is deposited on the hermetic EBC barrier of an RE-silicate [62]. While the RE-silicate has a reduced silica activity [58,61], it will still be at risk of volatilization in water vapor environments as target operation temperatures increase. Additionally, if any channel cracks form that penetrate to the SiC composite, (or TGO/bond coat), where ingress of water vapor would create an egress of $Si(OH)_4$ that would react with the RE-silicate EBC layers, or the RE-zirconate TBC topcoat. The reactions could damage the EBC layers by turning REmonosilicates into RE-disilicates, which are less resistant to volatility [62], and reaction with the TBC topcoat would be detrimental to the compliant, columnar microstructure.

7.4 Synopsis

EB-PVD coatings are well adherent after thermal cycling in high temperature water vapor, but fiber degradation is observed owing to volatilization of silica from the fibers through the porous matrix, porous coatings, and coating defects. Fiber damage is more severe in the YZO bilayer compared to the 7YSZ monolayer due to the greater CTE of 7YSZ, expanding to reduce the width of intercolumnar gaps and reducing gas ingress. In the experiments with the yttria coatings, the $Si(OH)_4$ gas from the water vapor reaction with the silica-containing N720 fibers reacts with the topcoat yttria at the bilayer interface, along channel cracks, and at the surface. The reaction at the surface happens readily from $Si(OH)_4$ from degraded fibers near coupon edges and 'shadowed' regions with low coating thickness, and from large coating defects and channel cracks. The reaction at the bilayer interface happens slower, and is from $Si(OH)_4$ forming locally from water vapor interaction with fibers directly below the interface, and diffusing back up the porous 7YSZ interlayer. The yttria coatings show less fiber damage overall because the reaction with yttria at the surface acts to mitigate further water vapor ingress. There is a threshold RE concentration for reaction to take place with the $Si(OH)_4$ gas, as no such reaction is observed in the 7YSZ or YZO layers or coatings.

EB-PVD coatings for EBC systems for porous matrix OFCCs would require a hermetic layer to prevent water vapor ingress and subsequent fiber damage. This layer could be a stationary EB-PVD layer which would be denser, or a reaction bonded aluminum oxide (RBAO) layer, which would have the added benefit of filling in surface cracks and defects on the OFCC surface. The outstanding question is how the EB-PVD coatings would withstand thermal stresses from CTE mismatch without the channel cracks present from the porous matrix.

7.5 Tables and Figures

Table 7.1: Table of parameters for the cycled coatings presented in this chapter

Coating designation	Stationary 7YSZ thickness (µm)	Rotated 7YSZ thickness (µm)	Topcoat thickness (µm)	Total thickness (µm)	Substrate temp. (°C)
7YSZ-E	-	150	-	150	1030
YZO-A	-	25	135	160	1050
Y_2O_3 -A	-	30	50	80	1035
Y_2O_3 -E	-	30	50	80	1095
YZO-S	16	8	90	114	7YSZ: 1060 YZO: 1020
Y_2O_3 -S	25	7	33	65	7YSZ: 1070 Y_2O_3: 1020

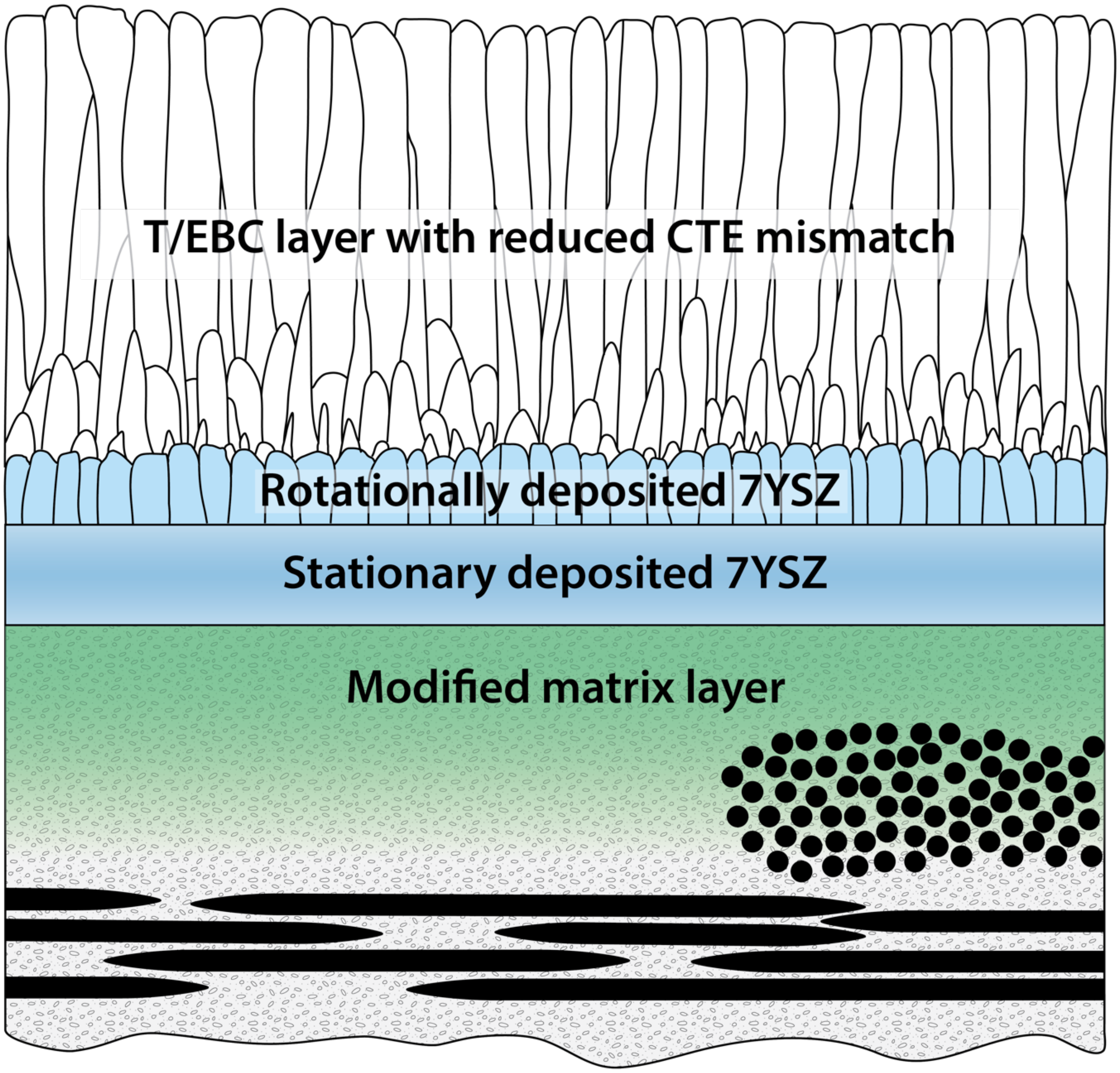

Figure 7.1: Schematic depiction of the proposed multilayer T/EBC system. From the bottom up, the porous matrix OFCC, the hardened matrix layers near the OFCC surface, a layer of 7YSZ deposited under stationary conditions (without rotation), a thin layer of 7YSZ deposited with substrate rotation, and then the topcoat of a CTE matched material, YZO or yttria in this case.

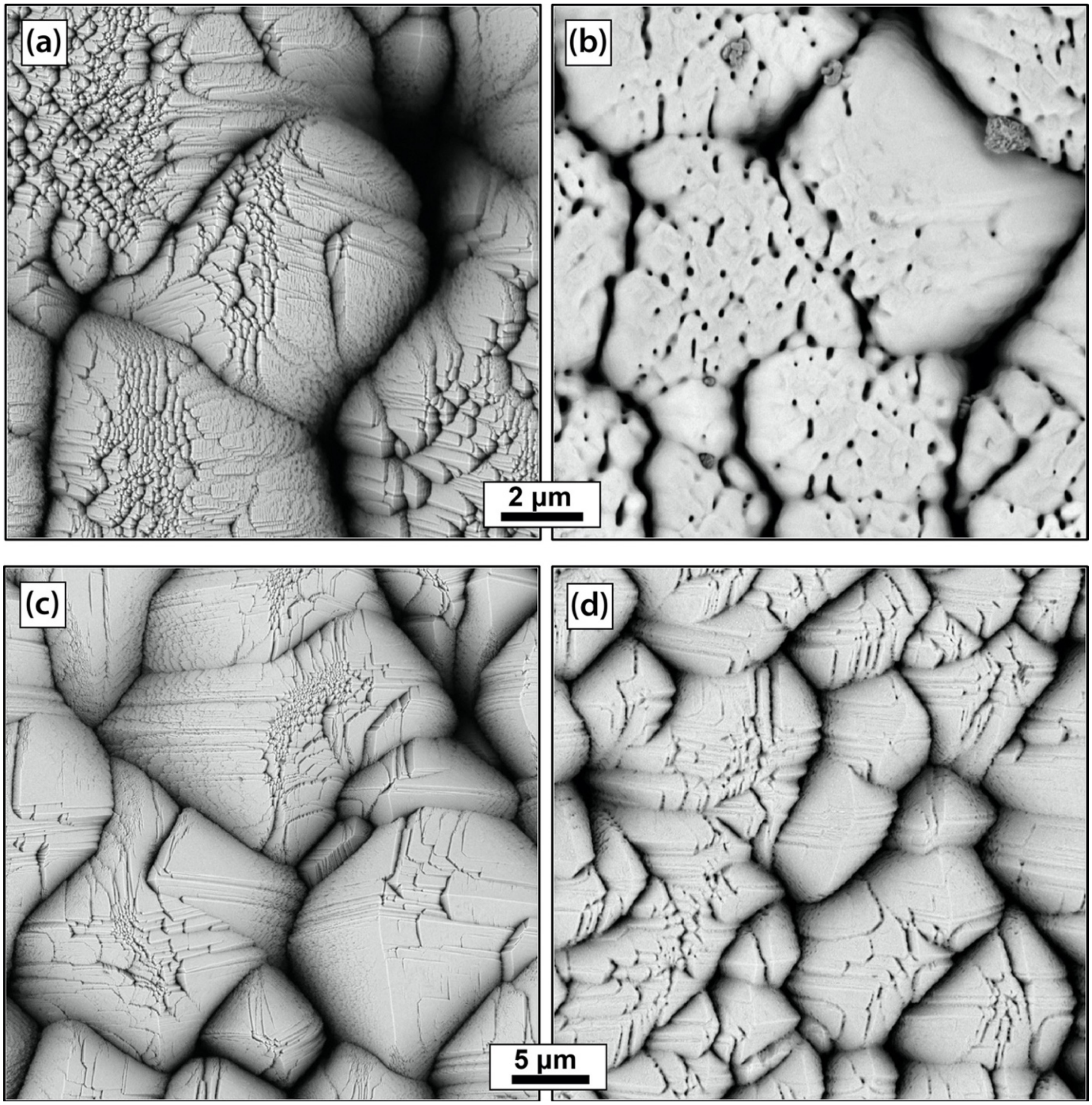

Figure 7.2: Surface images of column tips of samples 7YSZ-E (a,b) and YZO-A (c,d) in the as-deposited condition (a,c) and after 50h of water vapor exposure at 1200°C (b,d)

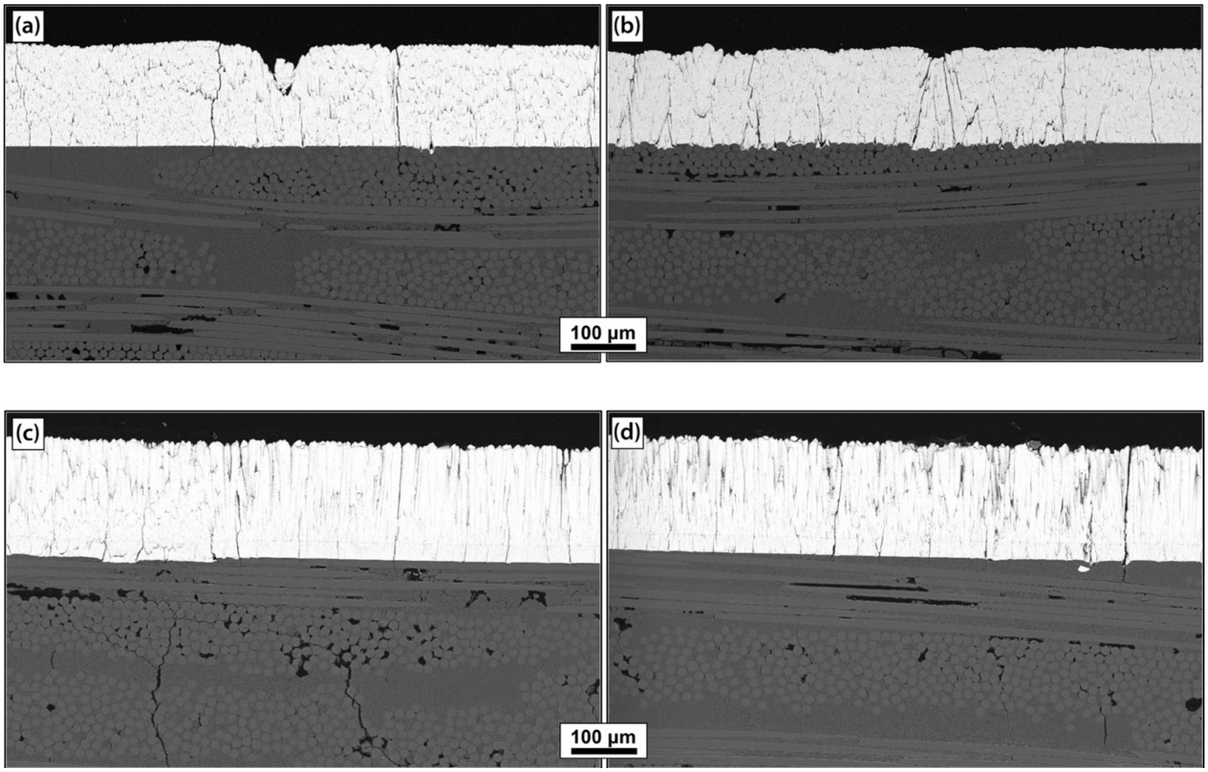

Figure 7.3: Post exposure cross-section images of (a) and (b) 7YSZ-E and (c) and (d) YZO-A corresponding to the coatings in Figure 2. Both coatings remained adhered to the substrate across the entirety of the sample even after the exposure to water vapor at 1200°C (b,d).

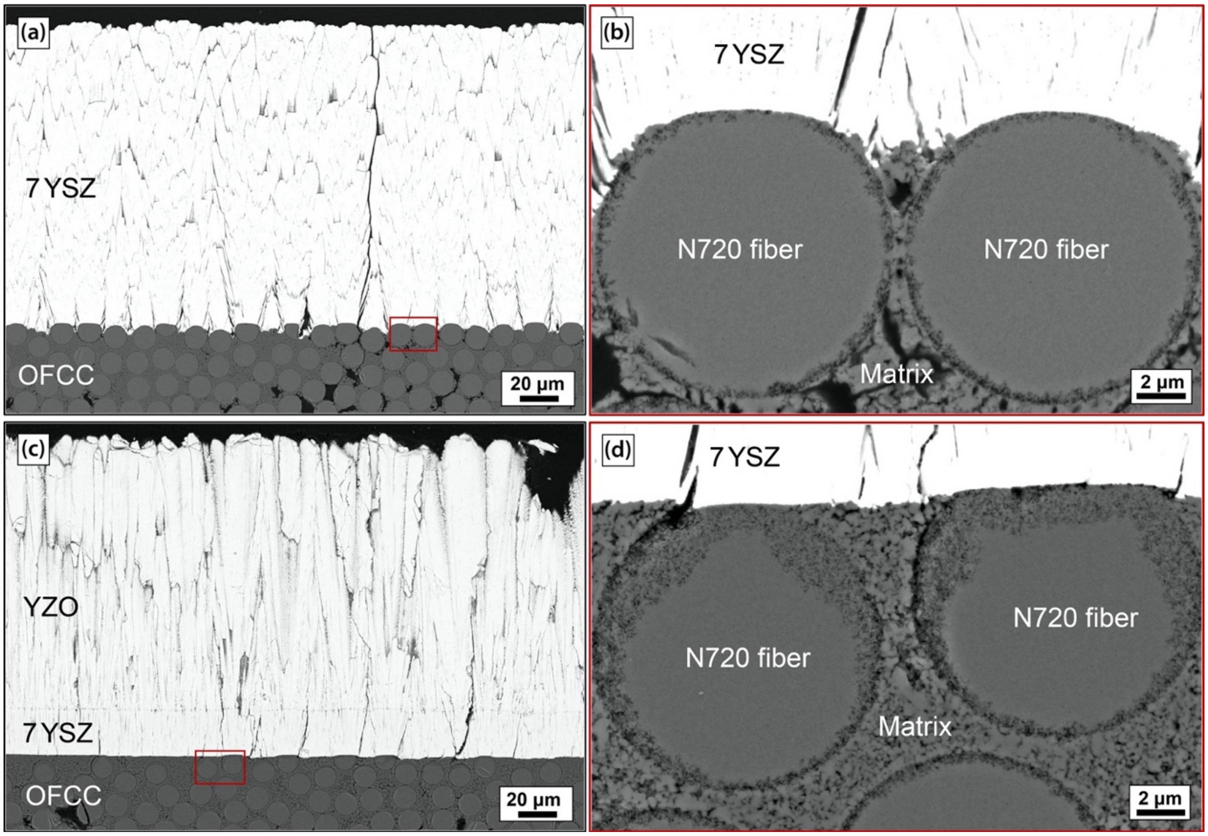

Figure 7.4: Higher magnification cross-section images of (a) 7YSZ-E after exposure, with the inset in (b) showing the consistent 0.5-1 μm of porosity around the outer edge of the fiber. The image of (c) YZO-A and the inset in (d) shows the greater extent of visible fiber damage compared to 7YSZ-E.

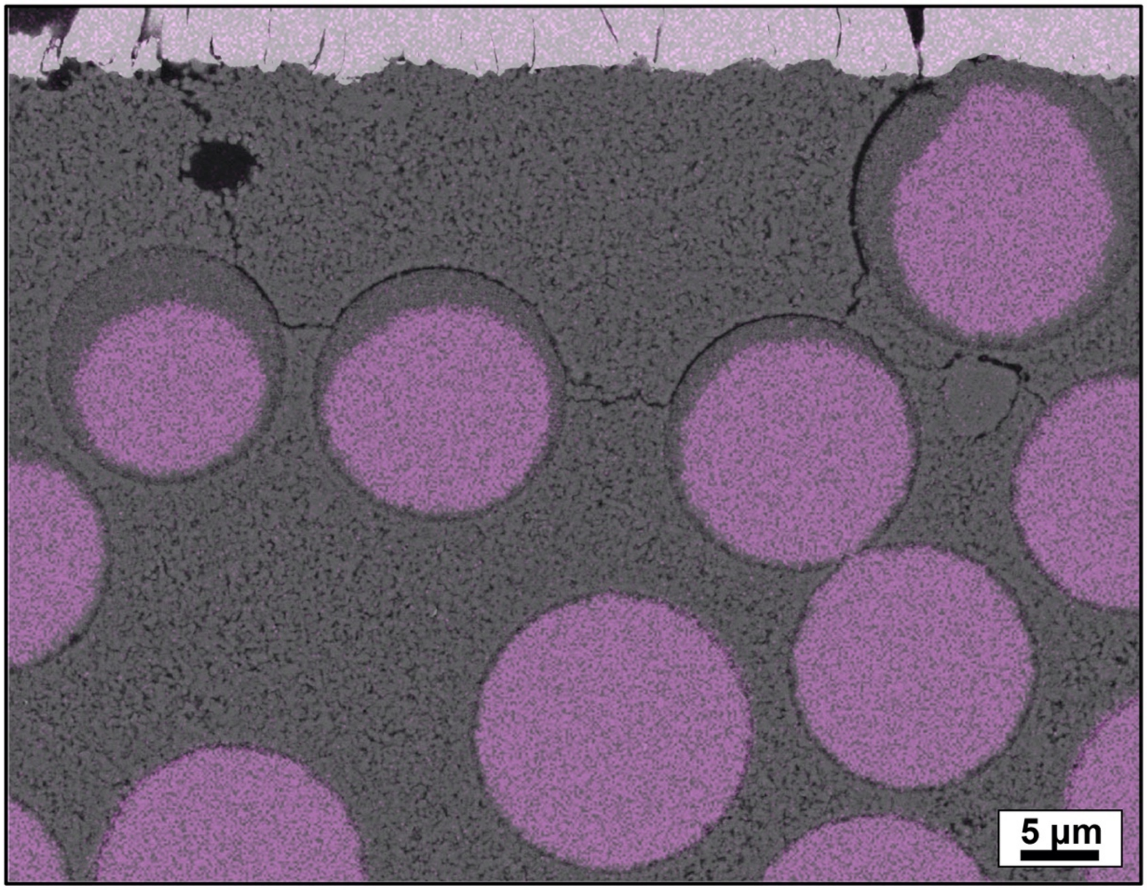

Figure 7.5: Cross-section image of some fibers near the surface of YZO-A with overlaid Si SEM-EDS map. The porous regions of the fibers are shown to be depleted of Si. Damage is limited to top 2 layers of fibers.

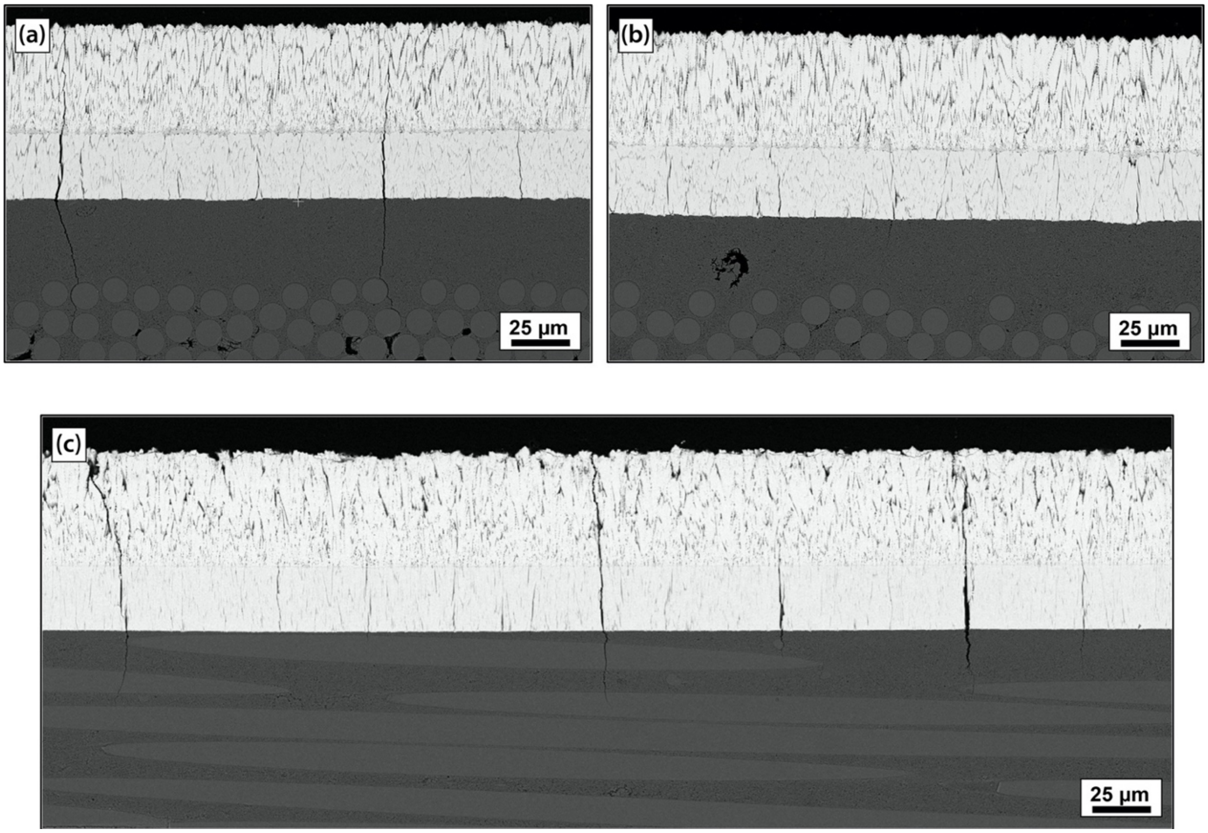

Figure 7.6: Post exposure cross-section images of (a,b) Y_2O_3-A and (c) Y_2O_3-E. Both coatings maintained adhesion across the entirety of the sample.

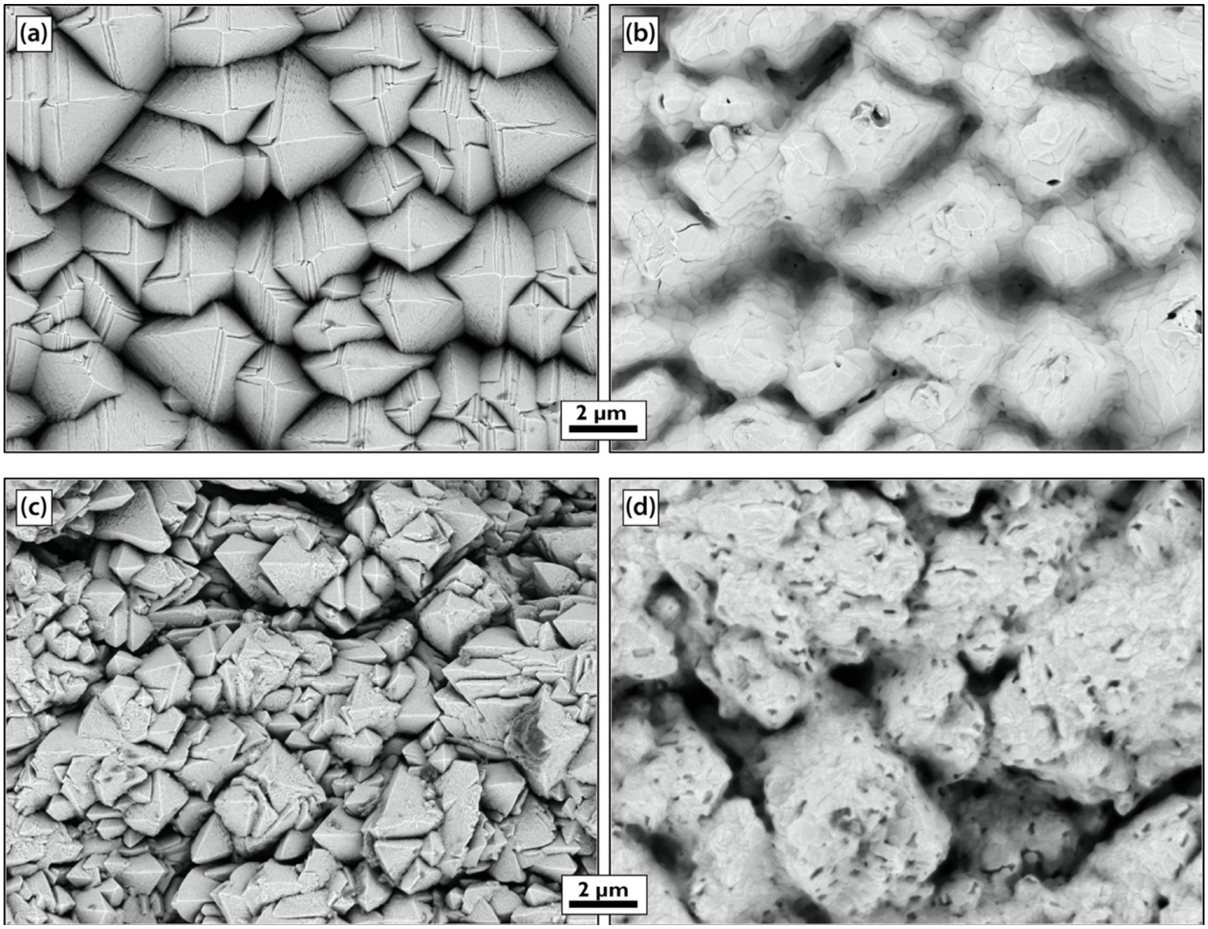

Figure 7.7: Surface SEM images of (a,b) Y_2O_3-A and (c,d) Y_2O_3-E, with (a,c) in the as-deposited condition and (b,d) after exposure to flowing water vapor at 1200°C. Both samples showed a “scaly” surface post exposure.

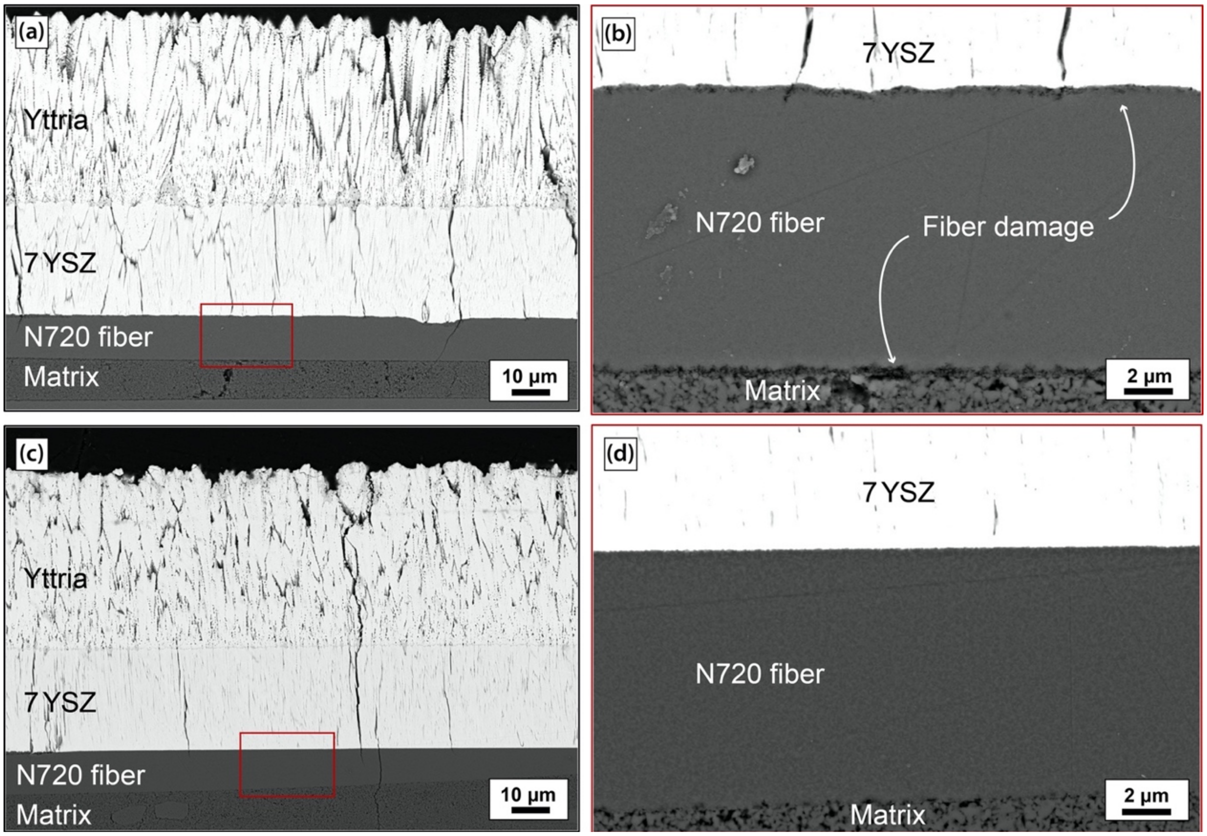

Figure 7.8: Higher magnification cross-section images of (a) Y_2O_3-A after exposure, with the inset in (b) showing the consistent 0.25 μm of porosity around the outer edge of the fibers. The image of (c) Y_2O_3-E and the inset in (d) shows minimal fiber damage.

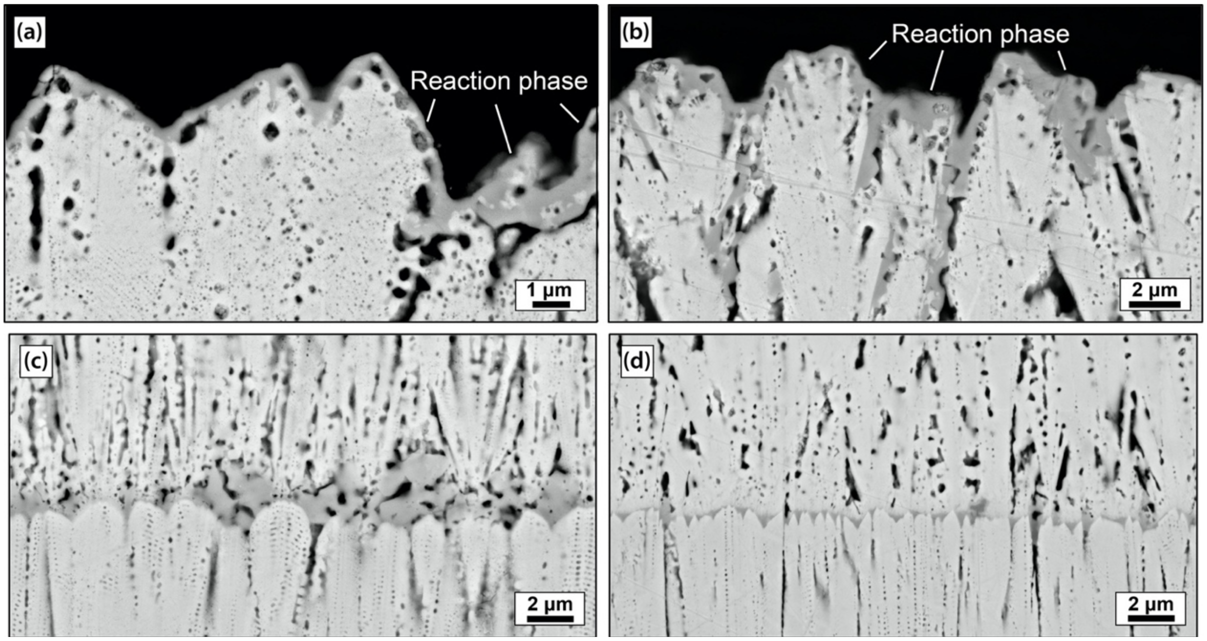

Figure 7.9: Post-exposure, higher magnification cross-section images of surfaces of (a) Y_2O_3-A and (b) Y_2O_3-E, both showing a contiguous "scale" of reaction phase at the surface above the intercolumnar porosity between column tips. There is also reaction phase observed at the bilayer interface of both (c) Y_2O_3-A and (d) Y_2O_3-E, with more reaction phase observed in Y_2O_3-A.

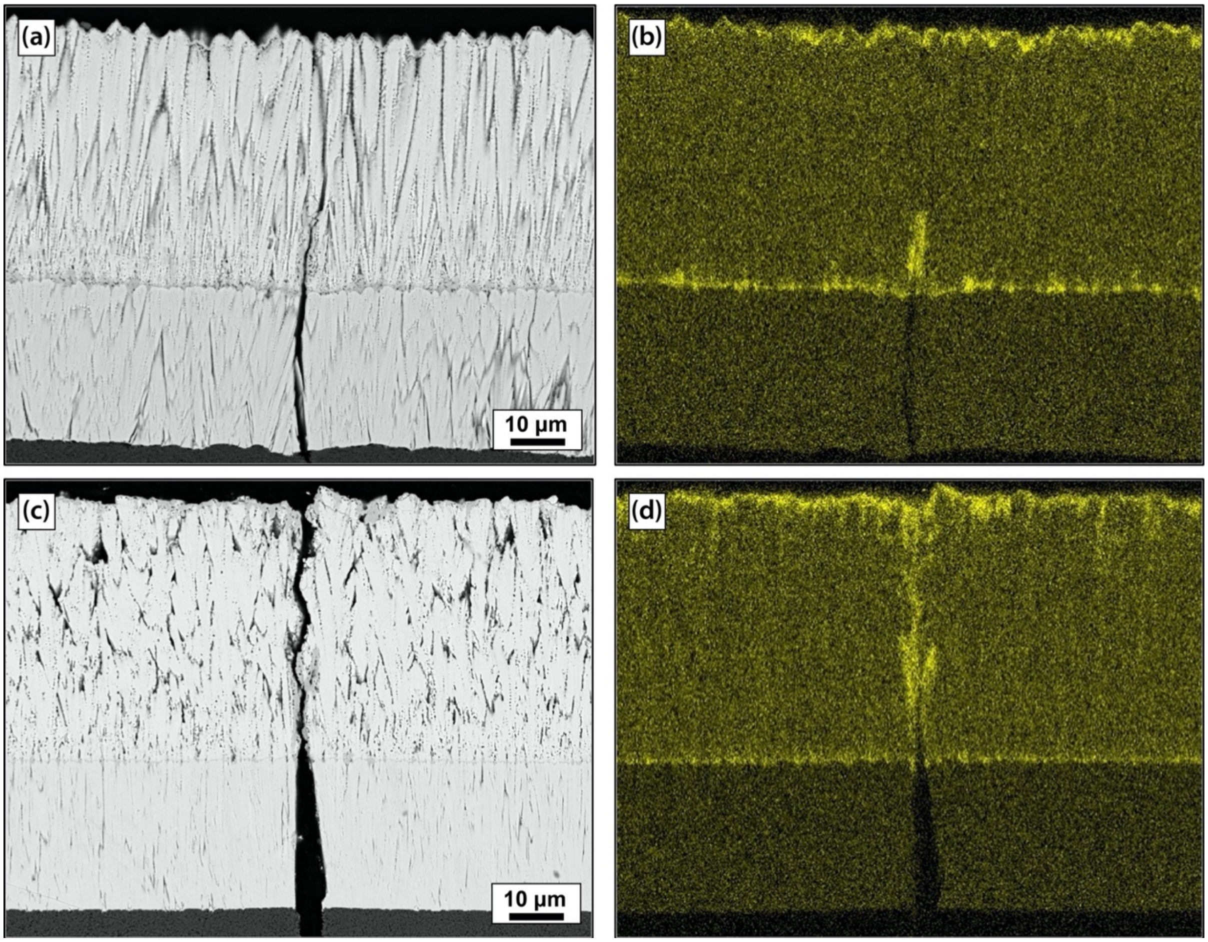

Figure 7.10: Post-exposure ross-section images of (a) a channel crack in Y_2O_3-A with (b) accompanying Si elemental SEM-EDS map, as well as (c) a channel crack in Y_2O_3-E with (d) accompanying Si elemental SEM-EDS map, with visible Si concentrated at the surface, bilayer interface, and along the channel cracks in both coatings.

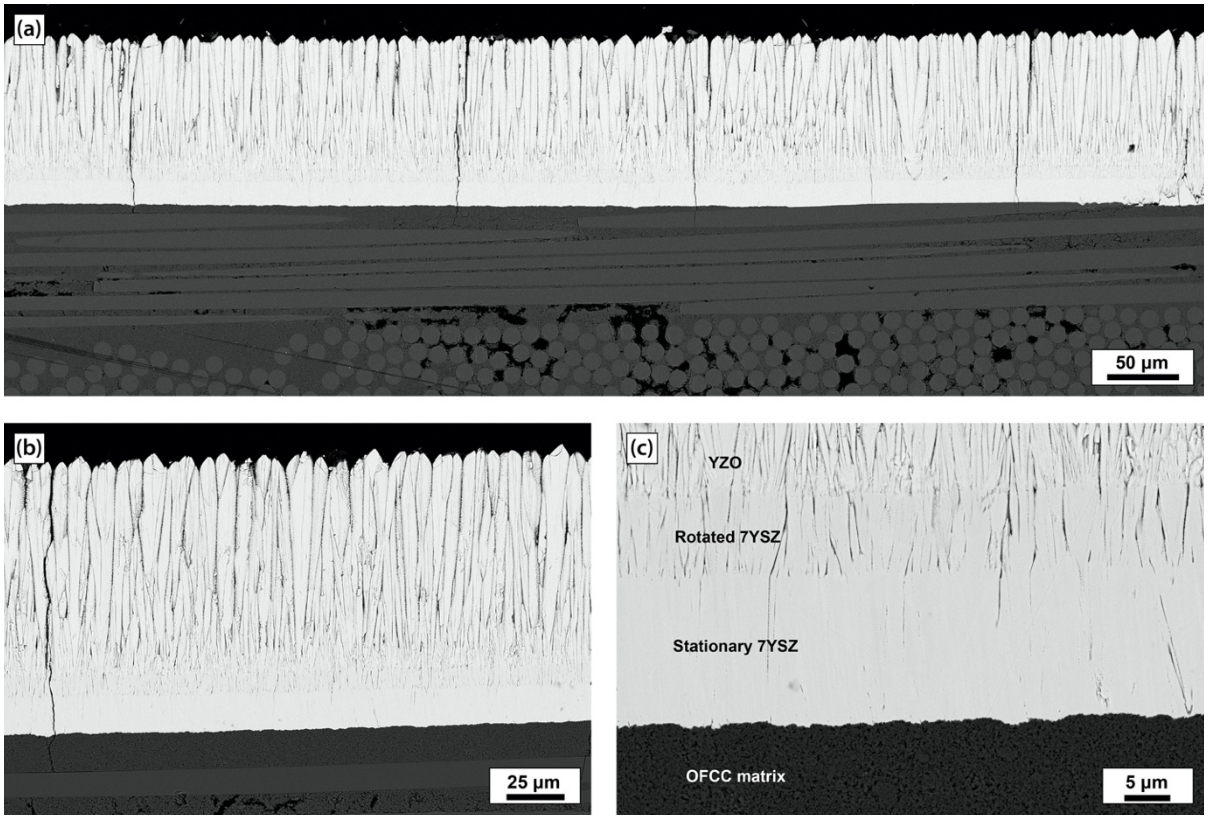

Figure 7.11: Cross-section images of YZO-S as-deposited.

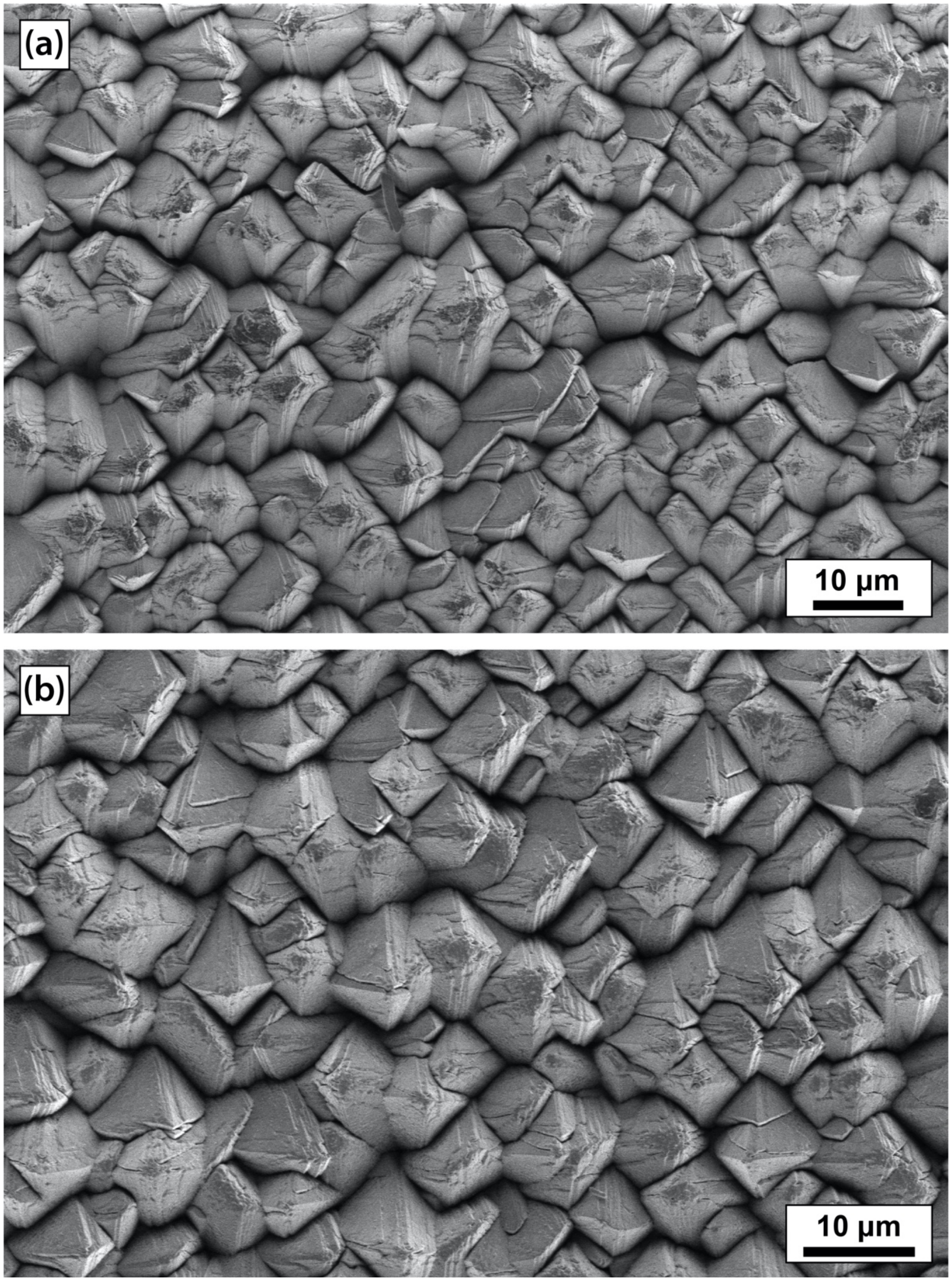

Figure 7.12: Surface images of column tips for YZO-S (a) before and (b) after exposure to water vapor for 50 h at 1200°C.

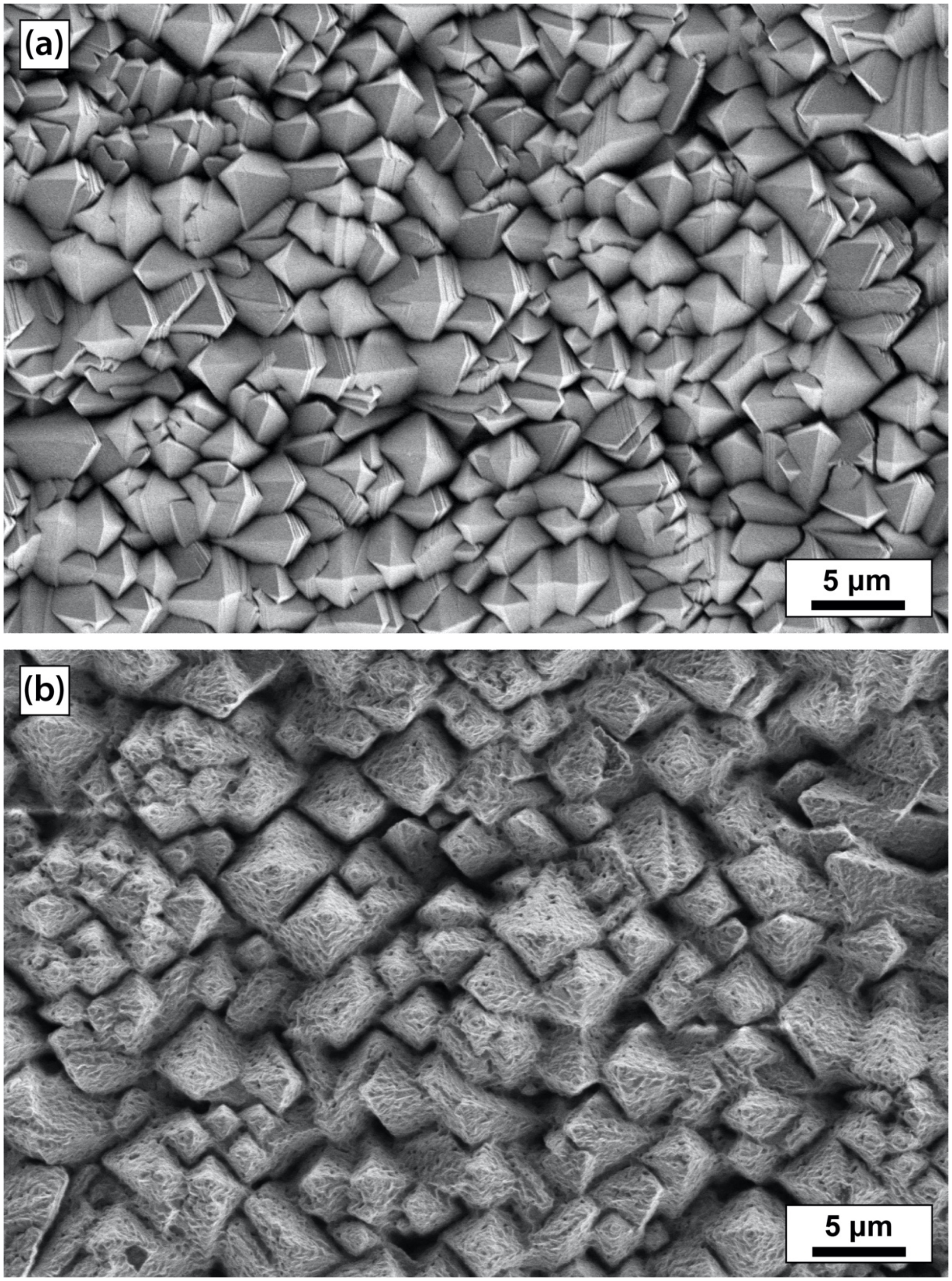

Figure 7.13: Surface images of Y_2O_3-S (a) before and (b) after exposure, with the similarly "scaly" appearance to Y_2O_3-A and Y_2O_3-E after exposure.

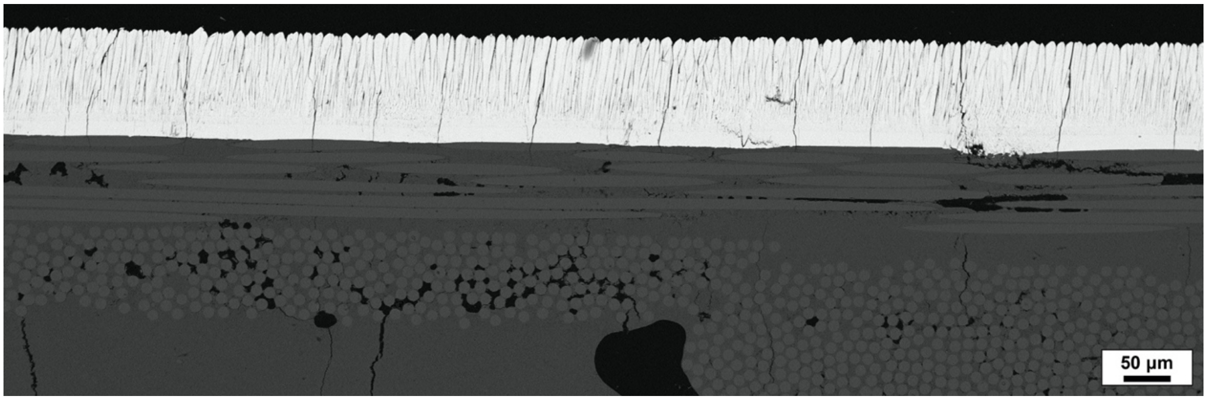

Figure 7.14: Post exposure cross-section image of YZO-S. The coating remained adhered to the substrate across the entirety of the sample even after exposure to water vapor at 1200°C.

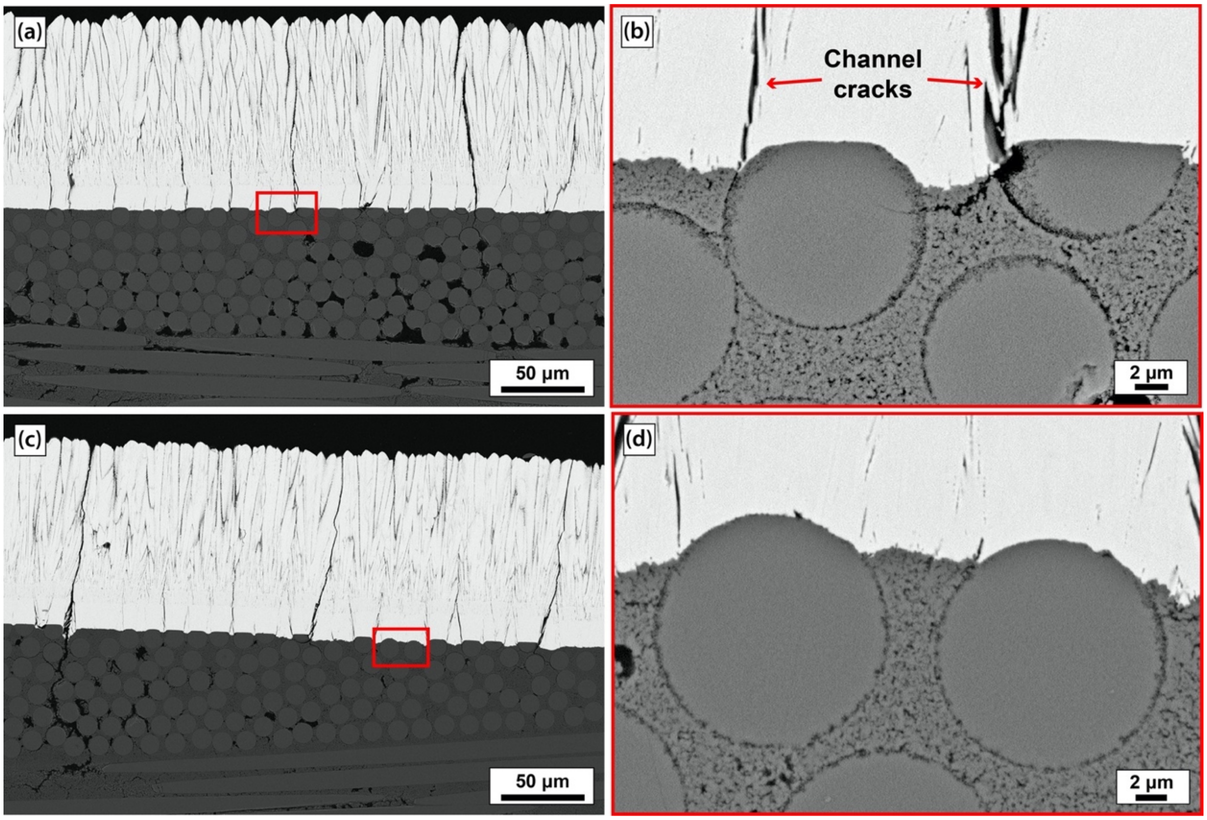

Figure 7.15: Higher magnification cross-section images of YZO-S after exposure. Insets in (b) and (d) show visible fiber damage, ranging from 0.25-1 μm into the fibers. Fibers near channel cracks in (b) exhibit more degradation.

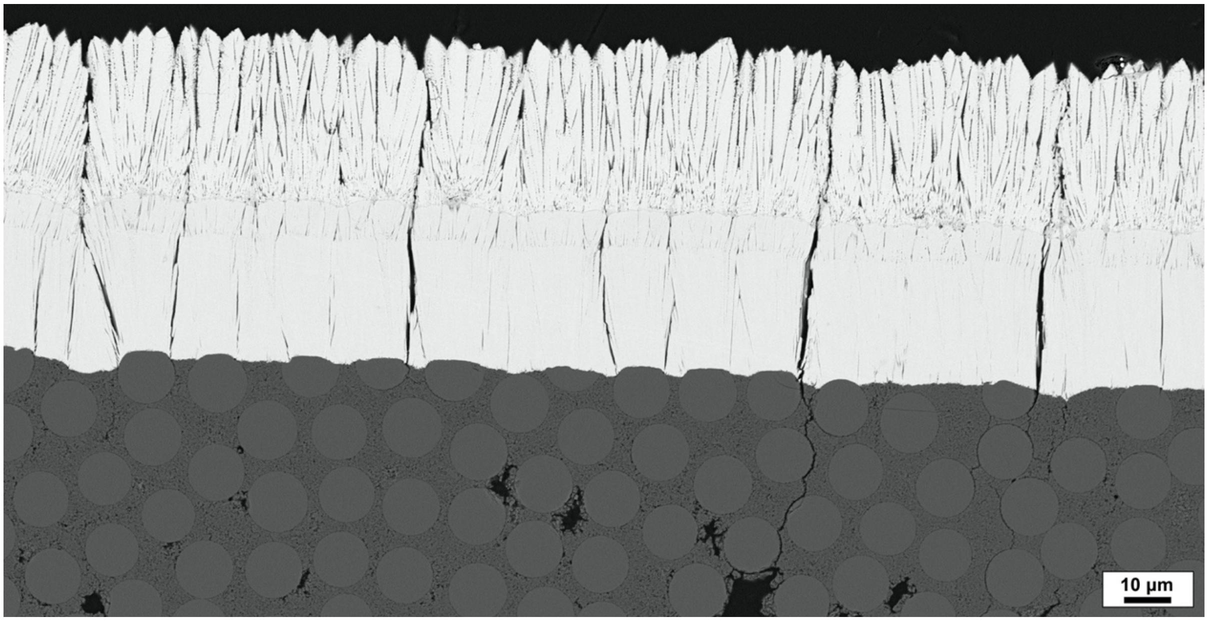

Figure 7.16: Cross-section image of Y_2O_3-S after exposure. While there are several visible channel cracks, there is still good adhesion across the entirety.

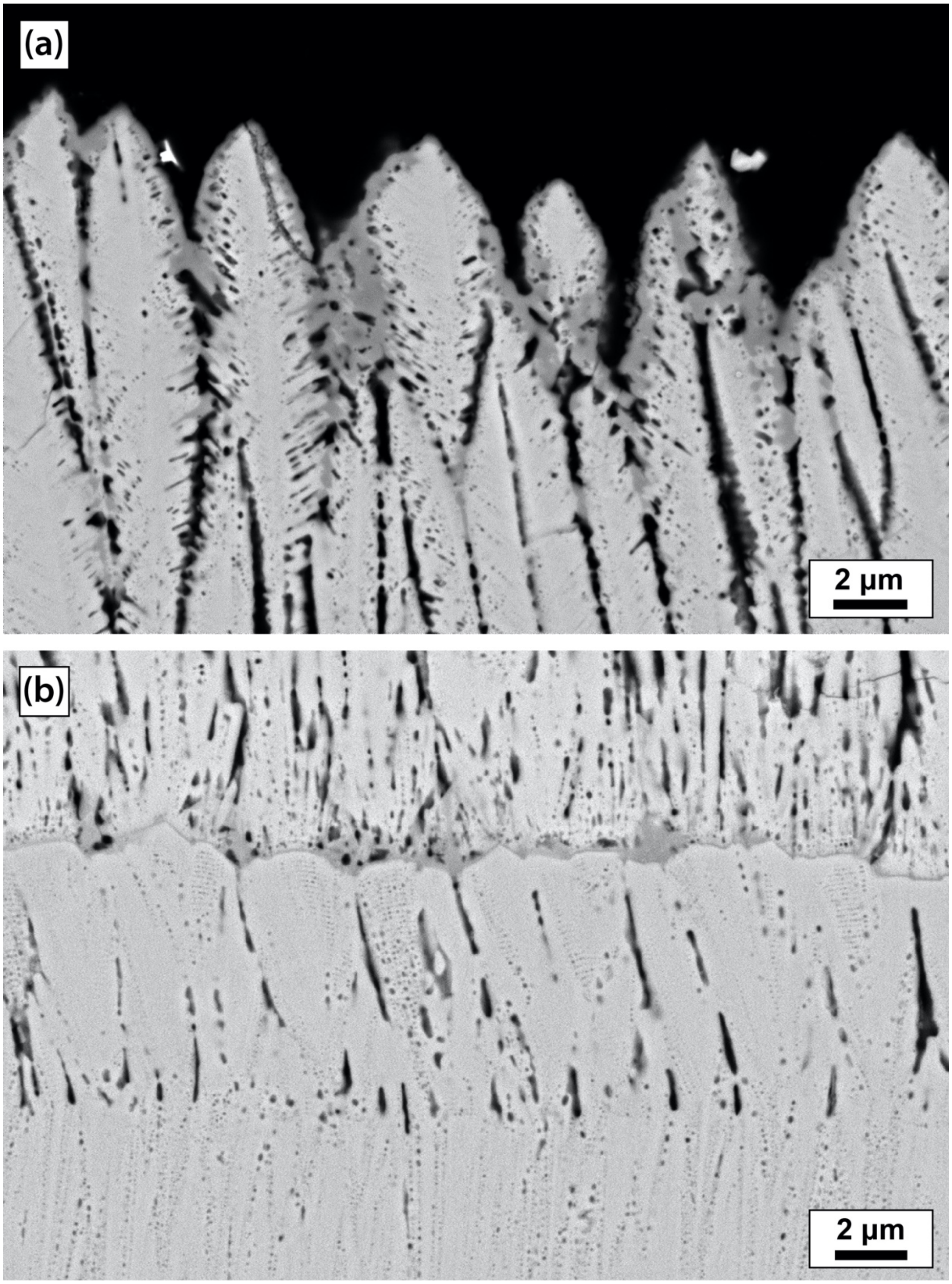

Figure 7.17: Images of the (a) surface and (b) 7YSZ/yttria interface of in Y_2O_3-S after exposure, with reaction phase visible in both.

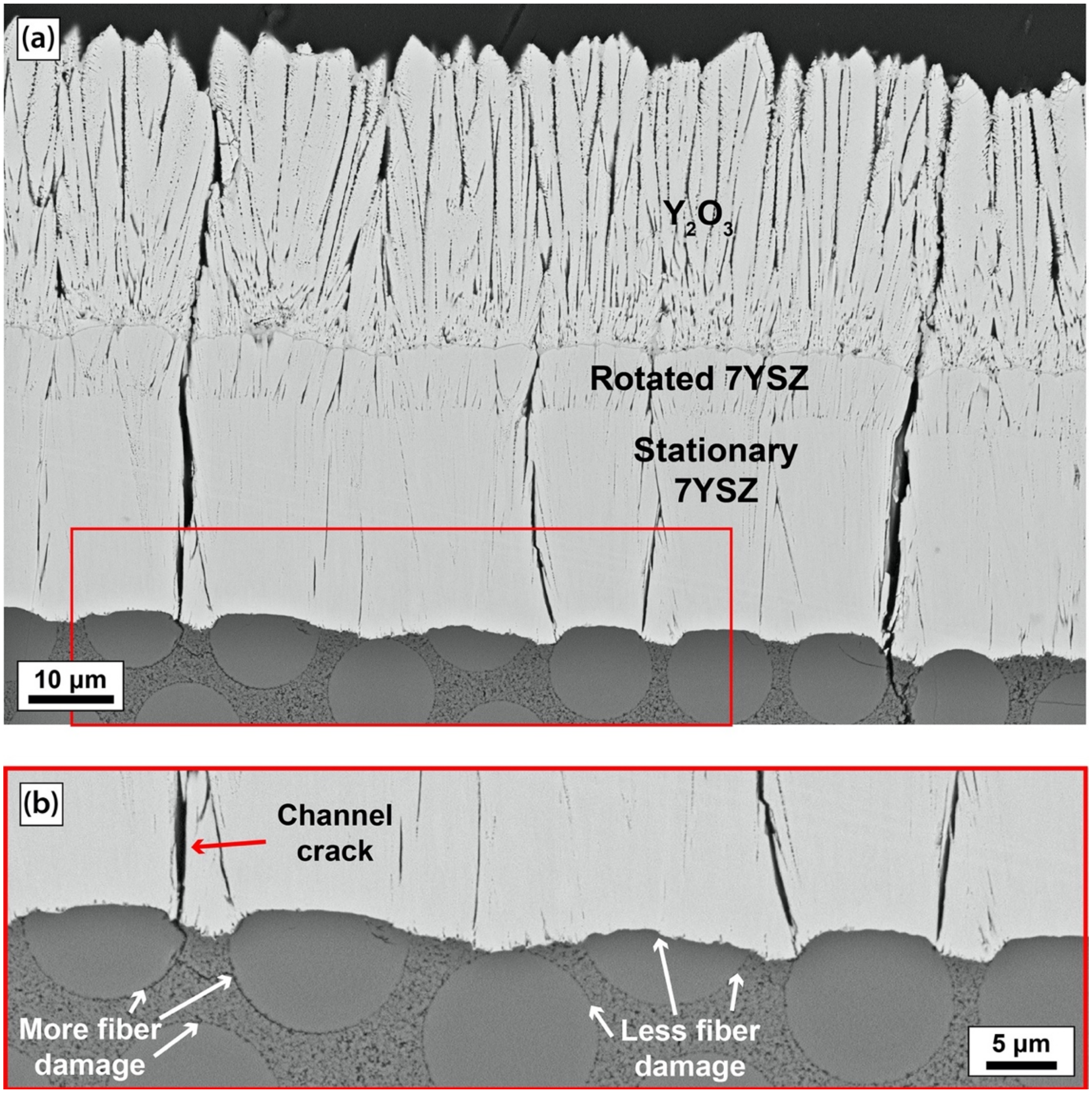

Figure 7.18: Cross-section image with inset (b) showing the general extent of fiber damage in in Y_2O_3-S after exposure.

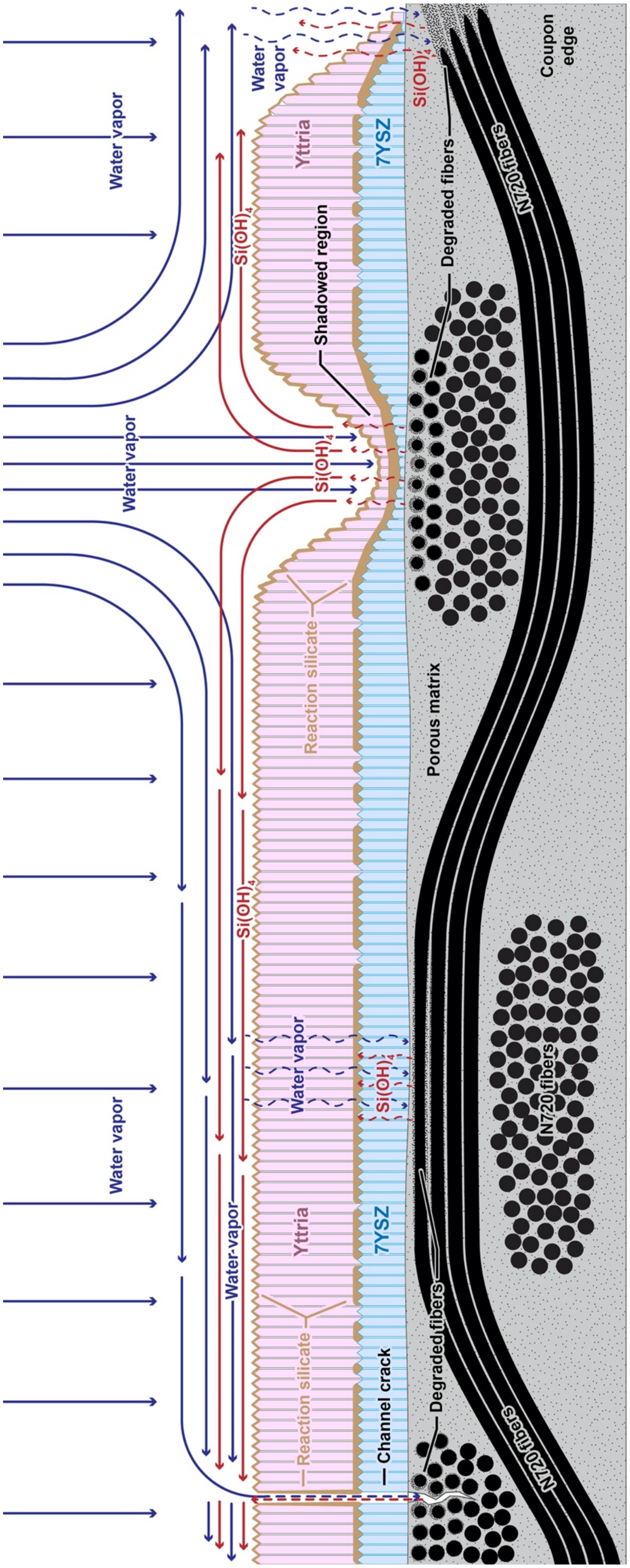
Water vapor
Water vapor
Water vapor
Water vapor
Water vapor
$Si(OH)_4$
$Si(OH)_4$
$Si(OH)_4$
$Si(OH)_4$
$Si(OH)_4$
Yttria
Yttria
7YSZ
7YSZ
Shadowed region
Reaction silicate
Reaction silicate
Degraded fibers
Degraded fibers
N720 fibers
N720 fibers
N720 fibers
Porous matrix
Coupon edge
Channel crack

Figure 7.19: (previous page) Schematic depiction of the mechanism of water vapor ingress, reaction with N720 fibers, and $Si(OH)_4$ egress and its reaction with yttria at the bilayer interface and coating surface. Shadowed regions and coupon edges have more damaged fibers, as well as regions around channel cracks. The reaction silicate at the yttria / 7YSZ interface is from ingress and egress through the columnar gaps in the EB-PVD coating. The schematic is depicting the structure of sample Y_2O_3-A.

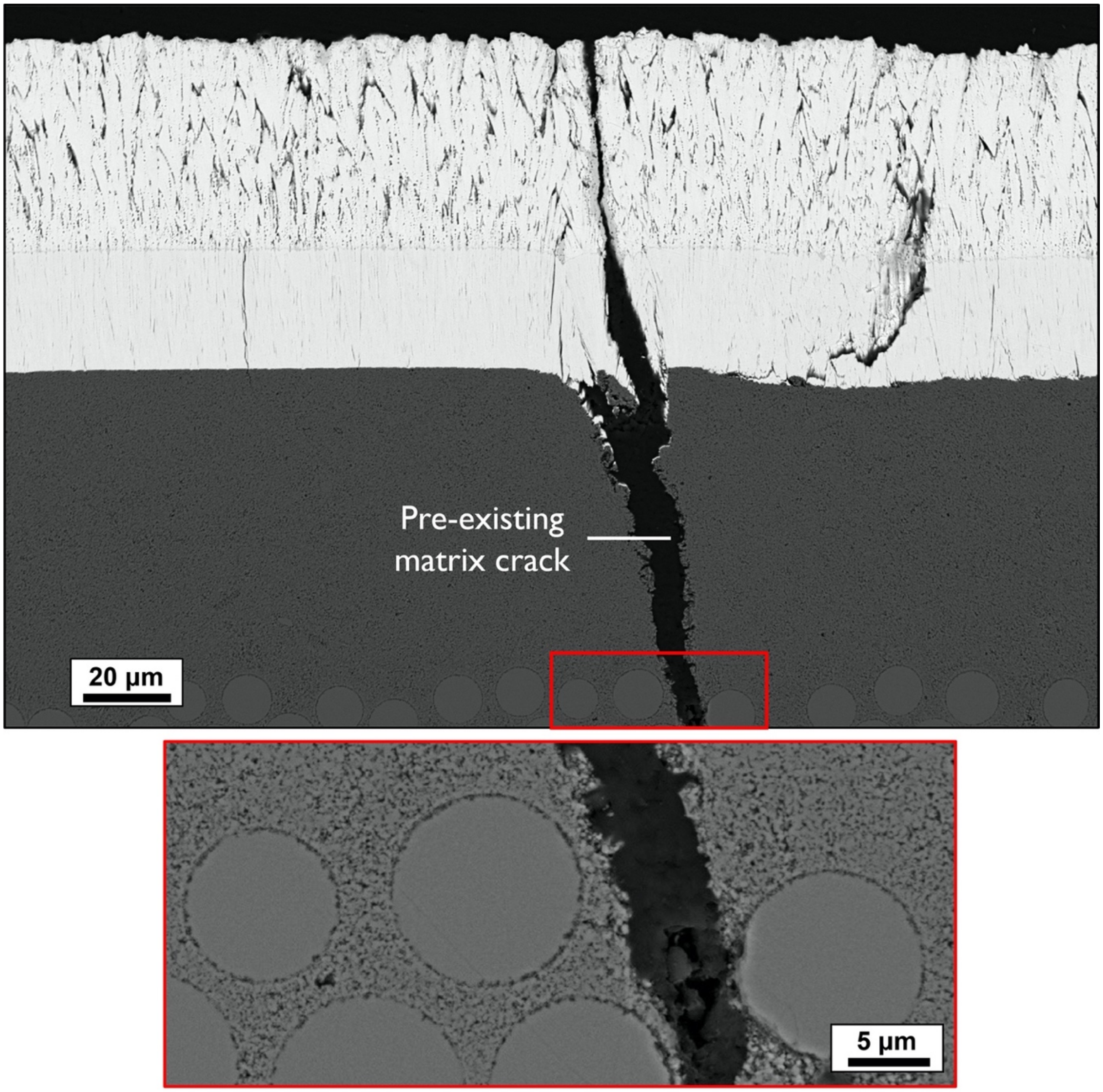

Figure 7.20: Image showing increased fiber damage near a channel crack in in Y_2O_3-E formed on a pre-existing surface crack in the porous matrix.

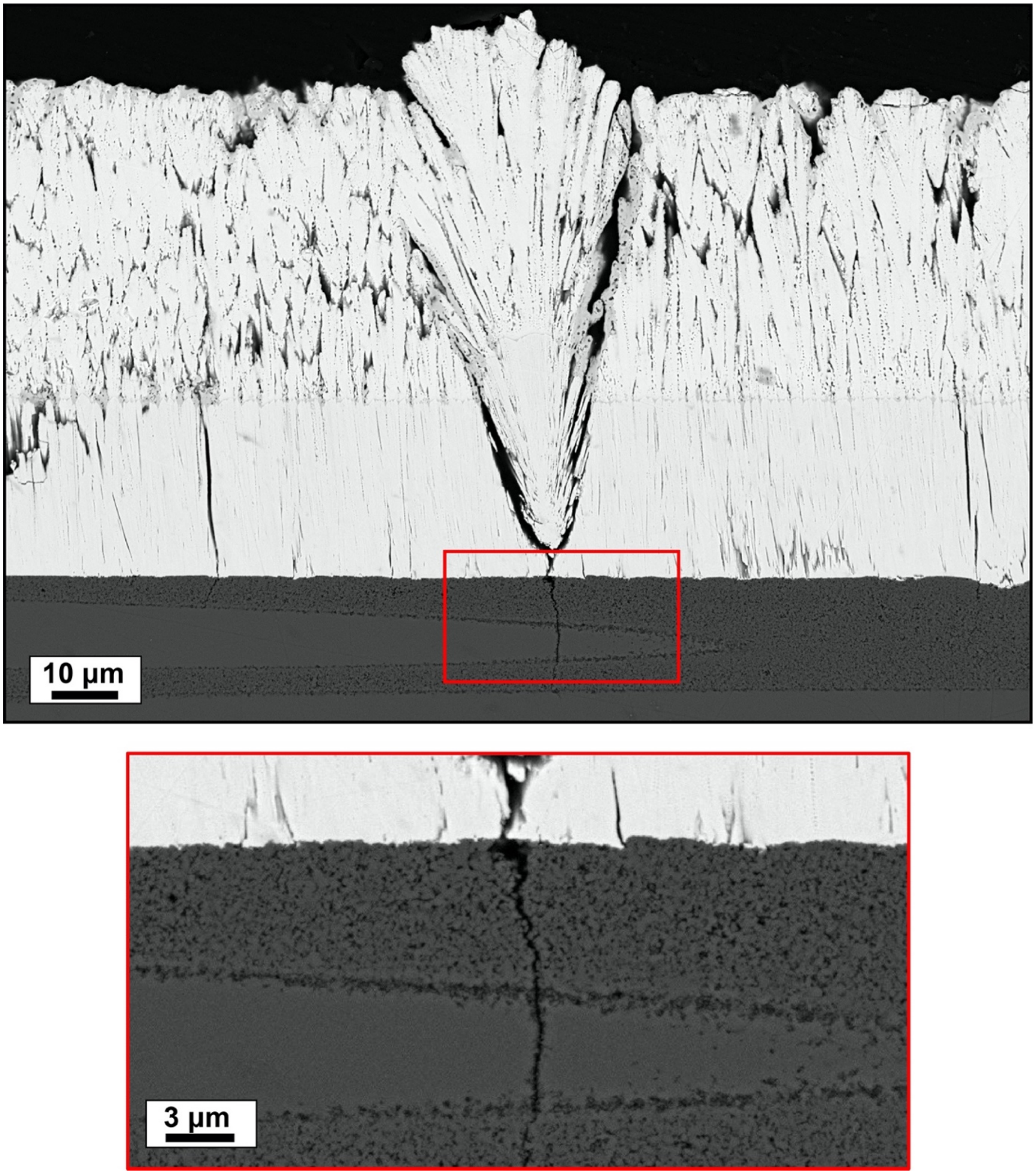

Figure 7.21: Cross-section image showing increased fiber damage in Y_2O_3-E near a conical defect in the coating.

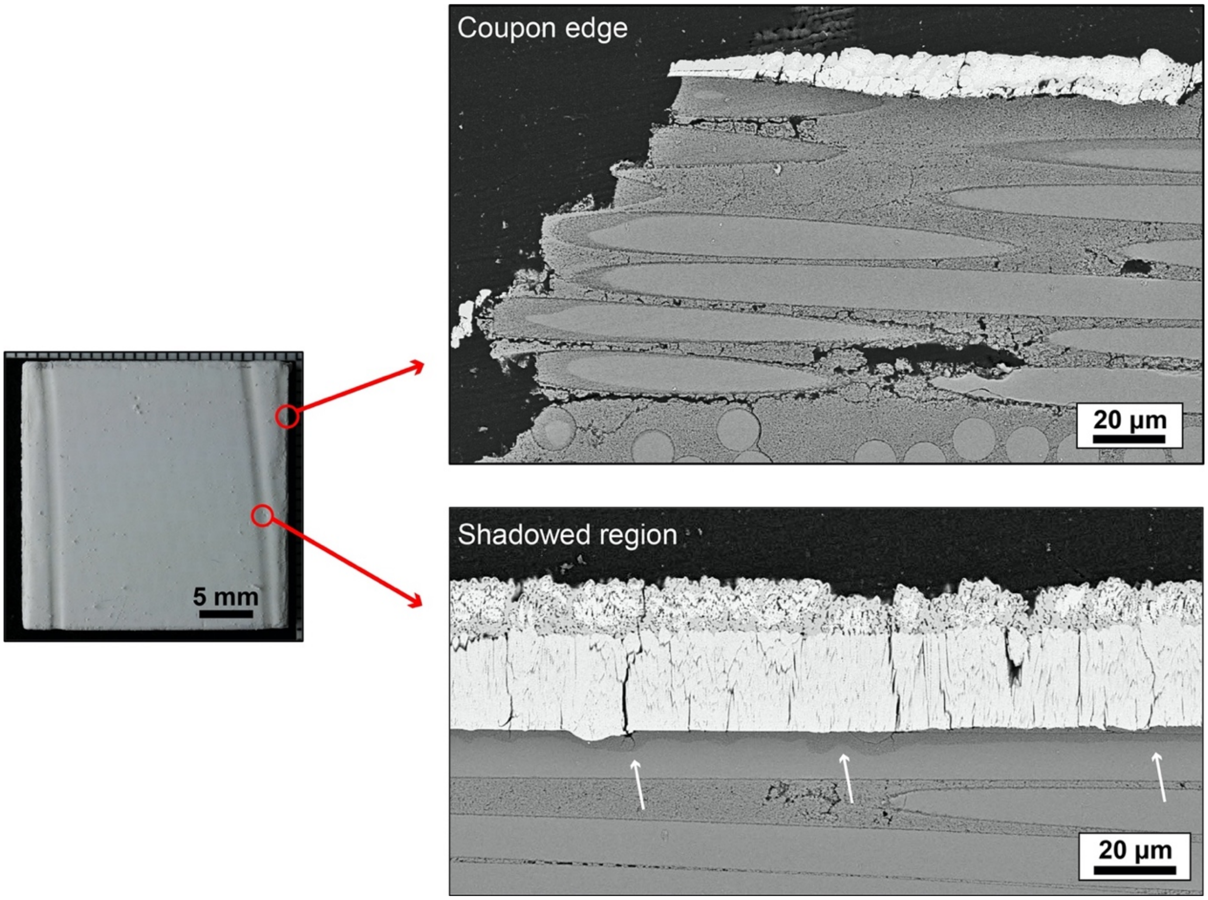

Figure 7.22: Macro image of the Y_2O_3-E coupon, and cross-section images of Y_2O_3-E after exposure showing increased fiber damage near the coupon edge and the shadowed regions where the deposited coating is thinner,

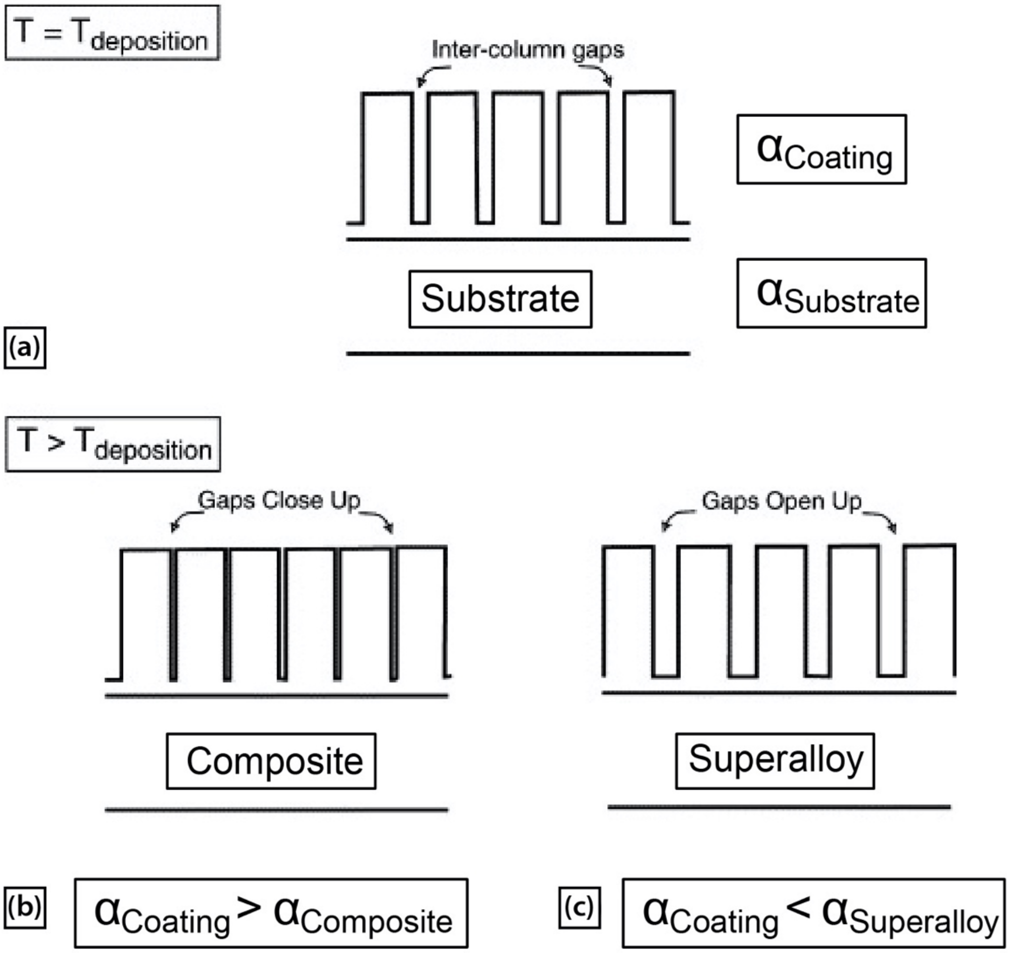

Figure 7.23: Schematic depiction of intercolumnar gaps (a) as-deposited, and how they (b) close up on heating when the coating CTE is greater than the substrate, the case of the 7YSZ and YZO coatings on an OFCC, and (c) how the gaps open up when the coating CTE is less than the substrate, the case with TBCs on superalloy substrates. Adapted from Lughi et al. [116]

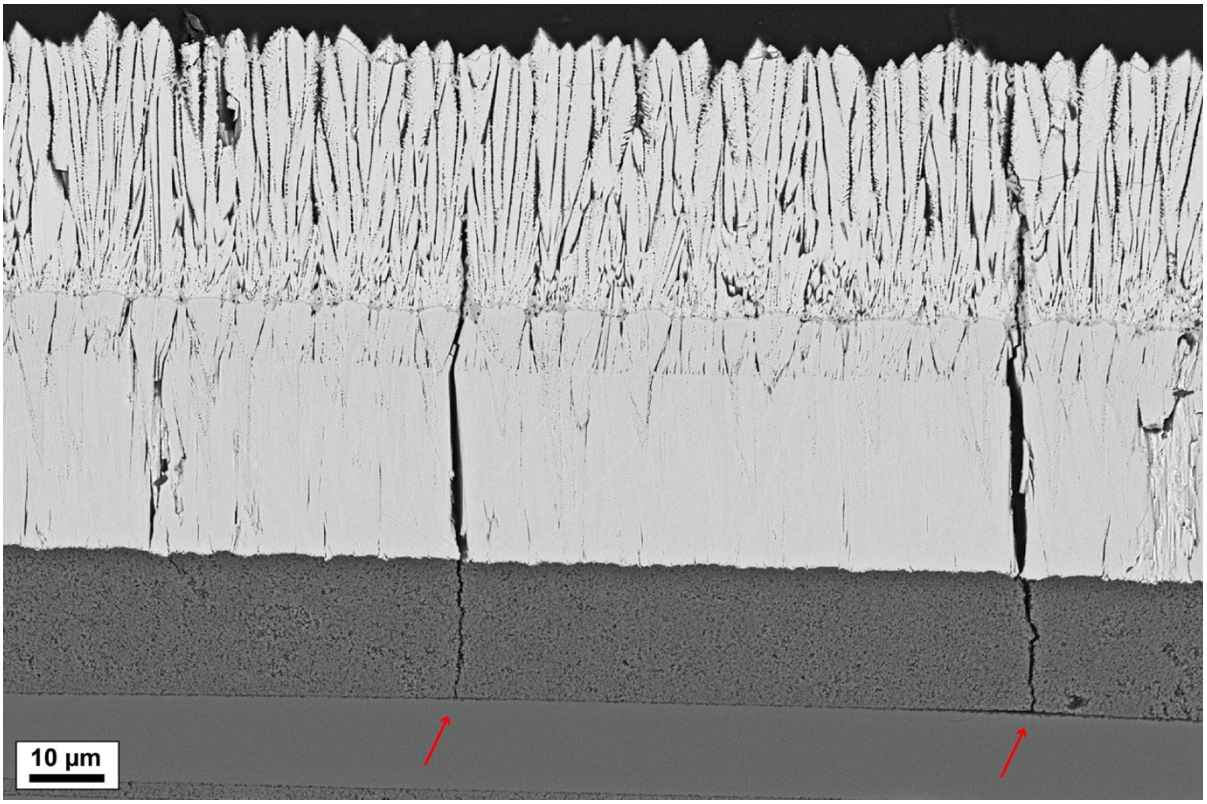

Figure 7.24: Cross-section images of Y2O3-S with arrows pointing to increased fiber damage around channel cracks.

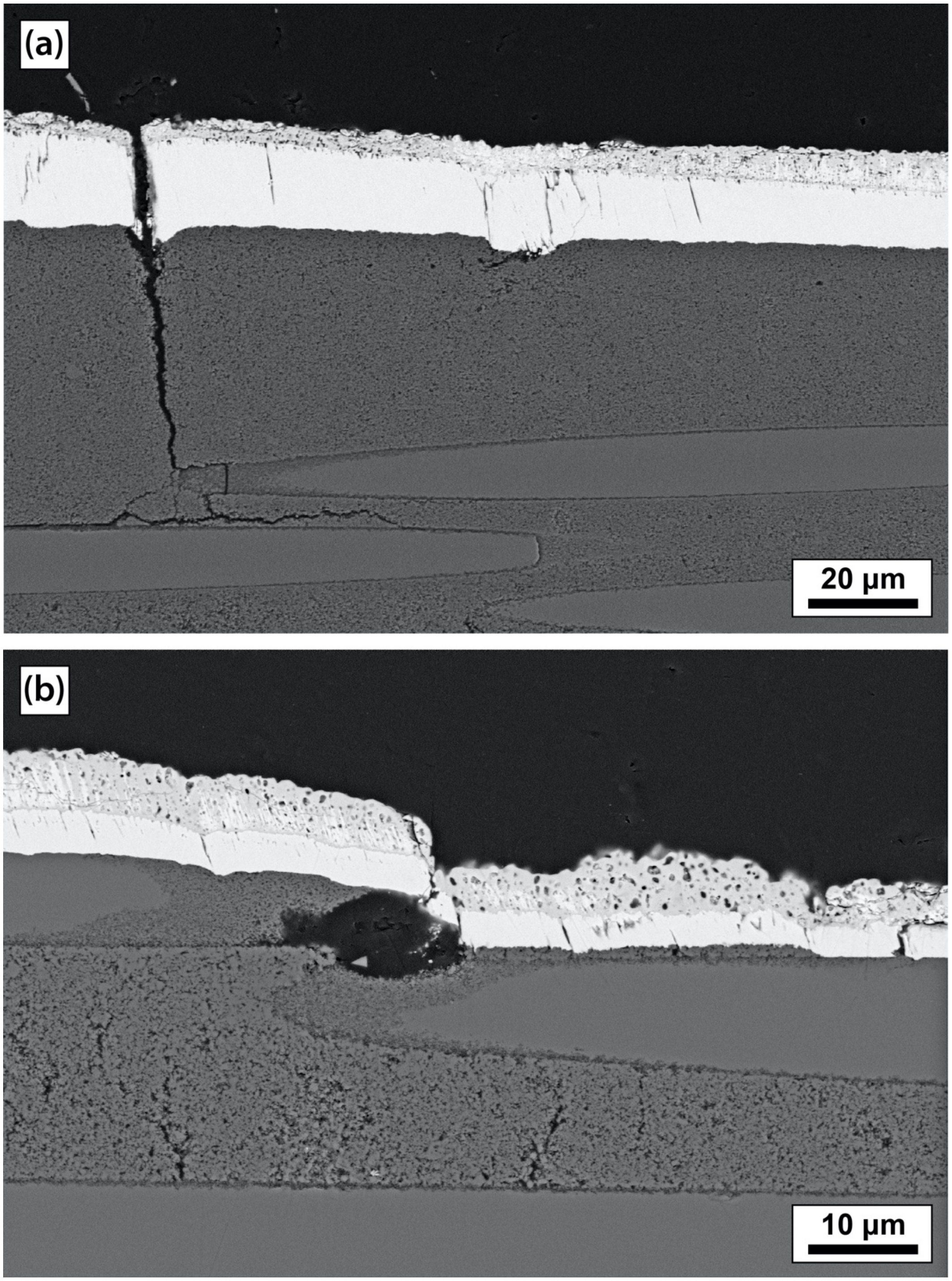

Figure 7.25: Cross-section images of Y2O3-S after exposure showing greater fiber damage (a) beneath the shadowed region of the coupon, and (b) the coupon edge.

Chapter 8: Conclusions

The primary goal of this dissertation was to investigate concepts for multilayer coating systems for porous matrix OFCCs and to assess their durability and efficacy in simulated combustion environments. The multilayer design is necessary to balance the material property requirements for effective OFCCs and coatings.

Furnace cyclic testing (FCT) was used to assess the durability of supplied air plasma sprayed (APS) coated OFCCs. The Gen1 samples, with a 48YSZ coating, fared better than the Gen2 samples with a 7YSZ coating. Both of these generations of APS coatings had a structured surface to provide mechanical interlocking with the coating and improved adhesion. Much of the delamination cracking observed in both samples after FCT was within the matrix, below the composite/coating interface. The laser ablation process used for the surface structuring damages fibers and locally sinters the porous matrix, leaving residual tensile stresses in the composite near the coating interface which caused the observed delamination cracking to initiate and propagate within the composite, below the interface. While the surface structuring is necessary for the adhesion of APS coatings to porous matrix OFCCs, the process can damage the composite, and does not address the poor interlaminar shear strength (ILSS) of porous matrix OFCCs which ‘allows’ for cracking within the composite below the coating interface.

48YSZ was shown to react with the alumina matrix and the N720 fibers, reacting with both the alumina and the silica in the alumina-mullite fibers. The 48YSZ was a desirable topcoat material, as the greater yttria content reduces the CTE compared to 7YSZ, however the observed reactions reinforce the need a compatibility layer in the coating system to provide a diffusion barrier between the better CTE matched topcoat and the OFCC.

Electron beam-physical vapor deposition (EB-PVD) was chosen to process the coatings for two main reasons. It creates a favorable microstructure with engineered columnar porosity, resulting in a compliant structure better able to accommodate thermal stresses from CTE mismatch. Moreover, the process creates adherent coatings without the need for surface structuring for mechanical interlocking. The initial FCT experiments showed EB-PVD 7YSZ coatings outperform APS 7YSZ coatings. No spallation or delamination cracking was observed, and no deleterious surface structuring was needed for adhesion, even on the porous matrix of the OFCC.

While the initial results from EB-PVD coatings were promising, further action was taken to selectively strengthen the porous OFCC matrix near the coating/composite interface to provide further resistance to delamination and channel cracking without sacrificing damage tolerance through the bulk of the composite. The porous matrix was strengthened by increasing its density by precursor impregnation and pyrolysis (PIP). Both full impregnation and surface application of precursor were methods attempted to produce the desired density gradient in the matrix. Full impregnation and "directional drying" adapted from previous work in the literature [41], was able to produce substantial hardening with a significant gradient due to the precursor solution segregation on drying. While the results of the full impregnation observed in this work did show substantial hardening near the surface, there was extensive hardening deep into the composite, as well as evidence of loss of crack deflection at the matrix/fiber interfaces. This was attributed to massive (up to 1 mm) voids in the OFCC matrix serving as reservoirs for the precursor solution, inhibiting the capillary forces driving the solution segregation to the surface. The surface application, or 'painting' method produced less hardening on the surface, but was able to realize a density gradient, with the infiltration of the precursor solution limited to the surface (top ~500 μm of the OFCC) and without evidence of matrix cracks penetrating fibers. There is certainly room for improvement, but the objective to create a stronger and denser surface region for improved EB-PVD coating growth and performance was shown to be feasible.

EB-PVD performed in this dissertation created barrier coatings with compliant microstructures thar are well-adherent without the need for surface structuring that can undermine coating durability. For bilayer depositions, in-situ ingot switching was performed to reduce potential cracking from CTE mismatch between the 7YSZ diffusional barrier and the OFCC before the better matched CTE layer is grown. Desired columnar microstructures were grown in all studied compositions, 7YSZ, YZO, and Y_2O_3 given the right surface temperature. Deposition rate did not appear to have significant effect on the resultant microstructures.

At higher surface temperatures, above 1070°C, less conventional morphologies were observed for 7YSZ and Y_2O_3, some inconsistent with literature. Notably, 7YSZ exhibited a columnar structure of $\langle 100 \rangle$ oriented columns with roof-top tips and the long edge of the tip being oriented ±60° off the substrate rotation axis, with one of the two orientations dominating with increased coating thickness. Y_2O_3's growth was particularly sensitive to surface temperature, growing with irregular morphologies and branched columns at the higher temperature depositions. YZO was grown with the desirable square-pyramidal-tipped columnar microstructure at the higher surface temperatures that perturbed the growth of both 7YSZ and Y_2O_3. Regardless of morphology, all coatings adhered well to the porous matrix OFCC and did not spall after cooling after deposition. The EB-PVD coatings presented in this dissertation provided insight into the sensitivity of grown microstructures on deposition surface temperature, while also highlighting the difficulty in accurately determining surface temperature during deposition with infrared pyrometry.

The multilayered barrier coating systems on OFCC, including the strengthened matrix, EB-PVD 7YSZ diffusion barrier, and EB-PVD topcoat with better matched CTE, were tested with FCT in simulated combustion environments containing flowing high temperature water vapor. All tested EB-PVD coatings were proven well adherent after FCT, but N720 fiber degradation from silica reaction with water vapor and subsequent volatilization was observed in all coatings. Gas ingress was expected, given the porosity of the coatings and OFCCs, but insight was provided into the mechanisms of ingress and egress, the influence of different topcoat morphologies and CTE's, and potential reactions with the top coat material.

The tested YZO bilayer saw more severe fiber damage compared to the 7YSZ monolayer. The greater CTE of the 7YSZ caused the topcoat to expand, and reduced the width of intercolumnar gaps and reducing gas ingress. Having a more closely matched CTE to the OFCC substrate, the intercolumnar gaps in YZO did not close as much as with 7YSZ, leaving larger pathways for gas ingress. In all coated samples fiber damage from gas ingress is most severe near channel cracks, coating defects, the coupon edges, and 'shadowed' regions with reduced coating thickness. In the case of the yttria coatings, the $Si(OH)_4$ produced from these regions readily reacted with the surface of the yttria coating, forming a 'scale' of Y-silicate that acted to partially 'seal' the coating preventing some ingress, which is consistent with the fiber damage being less in the yttria coatings than 7YSZ or YZO. The reduced Y- activity in the 7SYZ and YZO coatings, arguably coupled with differences in reaction kinetics, led to the absence of silicate reaction phases in the times investigated.

In some samples (YZO-S and Y_2O_3-S), a denser layer of 7YSZ deposited under stationary conditions (no substrate rotation), was added as part of the 7YSZ diffusional barrier layer of the multilayer system to provide additional protection from water vapor ingress. While this layer did appear to provide some protection, it did not address a fundamental issue with applying coatings to an OFCC. Surface defects are inevitable from the processing of porous matrix OFCCs, and they lead to coating defects and large gaps or cracks in EB-PVD coatings. Additionally, the porous matrix, even if hardened with precursor, is still not strong enough to prevent all channel cracking from thermal stresses after deposition or thermal excursion. However, these channel cracks resulting from surface defects and thermal stresses are likely contributing to the overall coating durability and lack of spallation. A denser or hermetic interlayer would be required to prevent ingress, and could have the added benefit of filling in the surface cracks and defects and potentially mitigating thermally induced channel cracking, but could challenge overall coating durability with other failure modes.

The findings of this research suggest some possible directions for future work in this area. Areas of interest include (i) further developing the precursor selective strengthening (ii) studying the unusual growth behavior observed in 7YSZ and yttria EB-PVD while developing consistent methods of temperature determination, and (iii) introducing a hermetic layer to the T/EBC multilayered system.

The precursor processing was shown to selectively harden the porous matrix, but additional research thrusts will be useful to bring knowledge to the extent to which of the property gradient can be tuned. Toughness was of primary concern, but the incongruities in the composite and the matrix pockets therein made accurate hardness, let alone toughness measurements inconsistent and not necessarily reliable. Experiments with partially sintered alumina powder compacts would provide a more controlled environment to probe the density gradient with precursor drying and segregation without the large voids or matrix cracks from processing the OFCC matrix with fibers. This simulated matrix will be able to better realize the precursor segregation from the capillary forces on drying. Creating a consistent density gradient will make it easier to probe other associated properties such as strength, toughness, or composition, as well as making it easier to compare the effects of different precursor compositions, concentrations, and application methods.

The present work demonstrated the feasibility of EB-PVD barrier coatings on OFCCs as part of a multilayered system and provided insight into previously unobserved EB-PVD growth behavior in the Zr-Y-O system. However, continued efforts are needed to elucidate the mechanism of the branching in yttria coating growth and the origin of the ±60° oriented rooftop column tips in 7YSZ. Crystallographic studies including electron backscatter diffraction (EBSD) and TEM electron diffraction could be valuable to understand the growth behavior of these two materials. Growths on alumina plates will provide a defect-free surface for consistent growths that will be readily comparable to each other and to literature. Moreover, the temperature sensitivity of EB-PVD growth morphology demands developing better methods of surface temperature determination during deposition. Using more reliably calibrated pyrometry, especially if able to view the substrate surface facing the vapor cloud, and having a thermocouple in direct contact with the substrate surface, are possible routes for accomplishing more consistent surface temperature reading.

A hermetic layer is needed as part of the T/EBC system to completely mitigate gas ingress. For alumina-based OFCCs, a reaction bonded aluminum oxide (RBAO) coating has been shown to be a low permeability coating that is easily applied. In addition to preventing gas ingress, the RBAO coating will also provide a much more uniform and dense surface for EB-PVD, offering resistance to thermally-induced channel cracking, while also filling in the matrix surface cracks from OFCC processing. This layer would not be in lieu of the precursor strengthening, but in addition to it. These studies would bring effective barrier coatings for OFCCs closer to fruition.

Chapter 9: References

[1] Data & Statistics, IEA. (n.d.). https://www.iea.org/data-and-statistics (accessed April 21, 2021).

[2] IATA's Annual Review, (n.d.). https://www.iata.org/en/publications/annual-review/ (accessed April 21, 2021).

[3] Gas Turbines (DOE CHP Technology Fact Sheet Series) – Fact Sheet, 2016, Energy.Gov. (n.d.). https://www.energy.gov/eere/amo/downloads/gas-turbines-doe-chp-technology-fact-sheet-series-fact-sheet-2016 (accessed April 20, 2021).

[4] R.L. Bannister, N.S. Cheruvu, D.A. Little, G. McQuiggan, Development Requirements for an Advanced Gas Turbine System, in: Volume 4: Heat Transfer; Electric Power; Industrial and Cogeneration, American Society of Mechanical Engineers, The Hague, Netherlands, 1994: p. V004T10A013. https://doi.org/10.1115/94-GT-388.

[5] M. Halbig, M. Jaskowiak, J. Kiser, D. Zhu, Evaluation of Ceramic Matrix Composite Technology for Aircraft Turbine Engine Applications, in: 51st AIAA Aerospace Sciences Meeting Including the New Horizons Forum and Aerospace Exposition, American Institute of Aeronautics and Astronautics, Grapevine (Dallas/Ft. Worth Region), Texas, 2013. https://doi.org/10.2514/6.2013-539.

[6] F.W. Zok, Ceramic-matrix composites enable revolutionary gains in turbine engine efficiency, American Ceramic Society Bulletin. 95 (2016) 7.

[7] A.G. Evans, F.W. Zok, The physics and mechanics of fibre-reinforced brittle matrix composites, Journal of Materials Science. 29 (1994) 3857–3896. https://doi.org/10.1007/BF00355946.

[8] Commercialization of CMCs and developments for next-gen performance, (n.d.). https://www.compositesworld.com/articles/the-next-generation-of-ceramic-matrix-composites (accessed April 20, 2021).

[9] A.G. Evans, F.W. Zok, R.M. McMeeking, Z.Z. Du, Models of High-Temperature, Environmentally Assisted Embrittlement in Ceramic-Matrix Composites, J American Ceramic Society. 79 (1996) 2345–2352. https://doi.org/10.1111/j.1151-2916.1996.tb08982.x.

[10] R.C. Robinson, J.L. Smialek, SiC Recession Caused by SiO2 Scale Volatility under Combustion Conditions: I, Experimental Results and Empirical Model, Journal of the American Ceramic Society. 82 (1999) 1817–1825. https://doi.org/10.1111/j.1151-2916.1999.tb02004.x.

[11] E.J. Opila, J.L. Smialek, R.C. Robinson, D.S. Fox, N.S. Jacobson, SiC Recession Caused by SiO2 Scale Volatility under Combustion Conditions: II, Thermodynamics

and Gaseous-Diffusion Model, Journal of the American Ceramic Society. 82 (1999) 1826–1834. https://doi.org/10.1111/j.1151-2916.1999.tb02005.x.

[12] N.S. Jacobson, Corrosion of Silicon-Based Ceramics in Combustion Environments, Journal of the American Ceramic Society. 76 (1993) 3–28. https://doi.org/10.1111/j.1151-2916.1993.tb03684.x.

[13] F.W. Zok, Developments in Oxide Fiber Composites, Journal of the American Ceramic Society. 89 (2006) 3309–3324. https://doi.org/10.1111/j.1551-2916.2006.01342.x.

[14] D. Marshall, Ceramics for future power generation technology: fiber reinforced oxide composites, Current Opinion in Solid State and Materials Science. 5 (2001) 283–289. https://doi.org/10.1016/S1359-0286(01)00017-1.

[15] R.J. Kerans, R.S. Hay, T.A. Parthasarathy, Structural ceramic composites, Current Opinion in Solid State and Materials Science. 4 (1999) 445–451. https://doi.org/10.1016/S1359-0286(99)00046-7.

[16] F.W. Zok, C.G. Levi, Mechanical Properties of Porous-Matrix Ceramic Composites, Advanced Engineering Materials. 3 (2001) 15–23. https://doi.org/10.1002/1527-2648(200101)3:1/2<15::AID-ADEM15>3.0.CO;2-A.

[17] Ceramic matrix composites: Hot engine solution, (n.d.). https://www.compositesworld.com/articles/ceramic-matrix-composites-hot-engine-solution (accessed April 20, 2021).

[18] W. Pritzkow, A. Nöth, A. Rüdinger, Oxide ceramic matrix composites - manufacturing, machining, properties and industrial applications, Ceramic Applications. 3 (2015) 48–54.

[19] M. van Roode, A.K. Bhattacharya, Durability of Oxide/Oxide Ceramic Matrix Composites in Gas Turbine Combustors, Journal of Engineering for Gas Turbines and Power. 135 (2013) 051301. https://doi.org/10.1115/1.4007978.

[20] T. Behrendt, S. Hackemann, P. Mechnich, Y. Shi, S. Hönig, S. Hofmann, D. Koch, Development and Test of Oxide/Oxide Ceramic Matrix Composites Combustor Liner Demonstrators for Aero-engines, J. Eng. Gas Turbines Power. 139 (2017). https://doi.org/10.1115/1.4034515.

[21] C.G. Levi, J.Y. Yang, B.J. Dalgleish, F.W. Zok, A.G. Evans, Processing and Performance of an All-Oxide Ceramic Composite, Journal of the American Ceramic Society. 81 (1998) 2077–2086. https://doi.org/10.1111/j.1151-2916.1998.tb02590.x.

[22] N. Jacobson, D. Myers, E. Opila, E. Copland, Interactions of water vapor with oxides at elevated temperatures, Journal of Physics and Chemistry of Solids. 66 (2005) 471–478. https://doi.org/10.1016/j.jpcs.2004.06.044.

[23] A. Hashimoto, The effect of H2O gas on volatilities of planet-forming major elements: I. Experimental determination of thermodynamic properties of Ca-, Al-, and Si-hydroxide gas molecules and its application to the solar nebula, Geochimica et Cosmochimica Acta. 56 (1992) 511–532. https://doi.org/10.1016/0016-7037(92)90148-C.

[24] E.J. Opila, Thermodynamics and kinetics of gaseous metal hydroxide formation from oxides relevant to power and propulsion applications, Calphad. 55 (2016) 32–40. https://doi.org/10.1016/j.calphad.2016.06.007.

[25] I. Spitsberg, J. Steibel, Thermal and Environmental Barrier Coatings for SiC/SiC CMCs in Aircraft Engine Applications*, International Journal of Applied Ceramic Technology. 1 (2005) 291–301. https://doi.org/10.1111/j.1744-7402.2004.tb00181.x.

[26] P. Mechnich, W. Braue, Air plasma-sprayed Y2O3 coatings for Al2O3/Al2O3 ceramic matrix composites, Journal of the European Ceramic Society. 33 (2013) 2645–2653. https://doi.org/10.1016/j.jeurceramsoc.2013.03.034.

[27] M.A. Mattoni, J.Y. Yang, C.G. Levi, F.W. Zok, L.P. Zawada, Effects of Combustor Rig Exposure on a Porous-Matrix Oxide Composite, Int J Applied Ceramic Technology. 2 (2005) 133–140. https://doi.org/10.1111/j.1744-7402.2005.02015.x.

[28] E.Y. Lee, The Microstructural Characterization of Plasma Sprayed and Physical Vapor Deposited Partially Stabilized Zirconia Thermal Barrier Coatings, in: Plasma Surface Engineering, DGM Informationsgesellschaft, Oberursel, 1989: pp. 365–372.

[29] S. Sampath, U. Schulz, M.O. Jarligo, S. Kuroda, Processing science of advanced thermal-barrier systems, MRS Bulletin. 37 (2012) 903–910. https://doi.org/10.1557/mrs.2012.233.

[30] Rolls Royce, The Jet Engine, John Wiley & Sons, 2015.

[31] I. Spitsberg, J. Steibel, Thermal and Environmental Barrier Coatings for SiC/SiC CMCs in Aircraft Engine Applications*, International Journal of Applied Ceramic Technology. 1 (2004) 291–301. https://doi.org/10.1111/j.1744-7402.2004.tb00181.x.

[32] C. Gatzen, D.E. Mack, O. Guillon, R. Vaßen, YAlO3—A Novel Environmental Barrier Coating for Al2O3/Al2O3–Ceramic Matrix Composites, Coatings. 9 (2019) 609. https://doi.org/10.3390/coatings9100609.

[33] W. Braue, P. Mechnich, Tailoring protective coatings for all-oxide ceramic matrix composites in high temperature-/high heat flux environments and corrosive media, Materialwissenschaft Und Werkstofftechnik. 38 (2007) 690–697. https://doi.org/10.1002/mawe.200700184.

[34] P. Mechnich, W. Braue, H. Schneider, Multifunctional Reaction-Bonded Alumina Coatings for Porous Continuous Fiber-Reinforced Oxide Composites, International

Journal of Applied Ceramic Technology. 1 (2004) 343–350. https://doi.org/10.1111/j.1744-7402.2004.tb00185.x.

[35] P. Mechnich, W. Braue, ZrO2 Environmental Barrier Coatings for Oxide/Oxide Ceramic Matrix Composites fabricated by Electron-Beam Physical Vapor Depostion, Design, Development, and Applications of Engineering Ceramics and Composite Systems. 215 (2010) 285–293. https://elib.dlr.de/63946/ (accessed April 20, 2021).

[36] 3M^{TM} Nextel^{TM} Ceramic Fibers and Textiles: Technical Reference Guide, 3M Advanced Materials Division, St. Paul, MN, 2018.

[37] M.K. Cinibulk, K.A. Keller, T.-I. Mah, Effect of Yttrium Aluminum Garnet Additions on Alumina-Fiber-Reinforced Porous-Alumina-Matrix Composites, Journal of the American Ceramic Society. 87 (2004) 881–887. https://doi.org/10.1111/j.1551-2916.2004.00881.x.

[38] R.S. Hay, E.E. Boakye, Monazite Coatings on Fibers: I, Effect of Temperature and Alumina Doping on Coated-Fiber Tensile Strength, Journal of the American Ceramic Society. 84 (2001) 2783–2792. https://doi.org/10.1111/j.1151-2916.2001.tb01095.x.

[39] K.A. Keller, T.-I. Mah, T.A. Parthasarathy, C.M. Cooke, Fugitive Interfacial Carbon Coatings for Oxide/Oxide Composites, Journal of the American Ceramic Society. 83 (2000) 329–336. https://doi.org/10.1111/j.1151-2916.2000.tb01194.x.

[40] J.H. Weaver, J. Yang, F.W. Zok, Control of Interface Properties in Oxide Composites Via Fugitive Coatings, Journal of the American Ceramic Society. 91 (2008) 4003–4008. https://doi.org/10.1111/j.1551-2916.2008.02746.x.

[41] M.A. Mattoni, J.Y. Yang, C.G. Levi, F.W. Zok, Effects of Matrix Porosity on the Mechanical Properties of a Porous-Matrix, All-Oxide Ceramic Composite, Journal of the American Ceramic Society. 84 (2001) 2594–2602. https://doi.org/10.1111/j.1151-2916.2001.tb01059.x.

[42] J.A. Heathcote, X.-Y. Gong, J.Y. Yang, U. Ramamurty, F.W. Zok, In-Plane Mechanical Properties of an All-Oxide Ceramic Composite, Journal of the American Ceramic Society. 82 (1999) 2721–2730. https://doi.org/10.1111/j.1151-2916.1999.tb02148.x.

[43] J.H. Weaver, J. Yang, A.G. Evans, F.W. Zok, A modified test for measuring the interlaminar tensile strength of fiber-reinforced ceramic composites, Composites Science and Technology. 68 (2008) 10–16. https://doi.org/10.1016/j.compscitech.2007.06.002.

[44] J.Y. Yang, J.H. Weaver, F.W. Zok, J.J. Mack, Processing of Oxide Composites with Three-Dimensional Fiber Architectures, Journal of the American Ceramic Society. 92 (2009) 1087–1092. https://doi.org/10.1111/j.1551-2916.2009.03036.x.

[45] M.N. Rahaman, Ceramic Processing and Sintering, 2nd ed., 2003.

[46] W.-C. Tu, F.F. Lange, Liquid Precursor Infiltration Processing of Powder Compacts: I, Kinetic Studies and Microstructure Development, Journal of the American Ceramic Society. 78 (1995) 3277–3282. https://doi.org/10.1111/j.1151-2916.1995.tb07965.x.

[47] W.-C. Tu, F.F. Lange, Liquid Precursor Infiltration Processing of Powder Compacts: II, Fracture Toughness and Strength, Journal of the American Ceramic Society. 78 (1995) 3283–3289. https://doi.org/10.1111/j.1151-2916.1995.tb07966.x.

[48] C.G. Levi, F.W. Zok, Y. Jing-Yu, M. Mattoni, J.P.A. Loefvander, S.B. California Univ., Microstructural design of stable porous matrices for all-oxide ceramic composites, Zeitschrift Fuer Metallkunde. 90 (1999). https://www.osti.gov/etdeweb/biblio/20038426 (accessed September 8, 2021).

[49] H. Fujita, C.G. Levi, F.W. Zok, G. Jefferson, Controlling Mechanical Properties of Porous Mullite/Alumina Mixtures Via Precursor-Derived Alumina, Journal of the American Ceramic Society. 88 (2005) 367–375. https://doi.org/10.1111/j.1551-2916.2005.00061.x.

[50] C.G. Levi, Metastability and microstructure evolution in the synthesis of inorganics from precursors11Paper presented at Sympos. Synergistic Synthesis of Inorganic Materials, March 1996, Schloß Ringberg, Germany., Acta Materialia. 46 (1998) 787–800. https://doi.org/10.1016/S1359-6454(97)00260-7.

[51] M. Parlier, M.H. Ritti, A. Jankowiak, Potential and Perspectives for Oxide/Oxide Composites., AerospaceLab. (2011) 1–12.

[52] M.A. Mattoni, F.W. Zok, Strength and Notch Sensitivity of Porous-Matrix Oxide Composites, Journal of the American Ceramic Society. 88 (2005) 1504–1513. https://doi.org/10.1111/j.1551-2916.2005.00299.x.

[53] B.R. Marple, D.J. Green, Graded compositions and microstructures by infiltration processing, Journal of Materials Science. 28 (1993) 4637–4643. https://doi.org/10.1007/BF00414252.

[54] B. Kieback, A. Neubrand, H. Riedel, Processing techniques for functionally graded materials, Materials Science and Engineering: A. 362 (2003) 81–106. https://doi.org/10.1016/S0921-5093(03)00578-1.

[55] I.M. Low, R.D. Skala, D.S. Perera, Fracture properties of layered mullite/zirconia-toughened alumina composites, J Mater Sci Lett. 13 (1994) 1334–1336. https://doi.org/10.1007/BF00624487.

[56] S. Pratapa, I.M. Low, B.H. O'connor, Infiltration-processed, functionally graded aluminium titanate/zirconia–alumina compositePart I Microstructural characterization and physical properties, Journal of Materials Science. 33 (1998) 3037–3045. https://doi.org/10.1023/A:1004323201601.

[57] P. Honeyman-Colvin, F.F. Lange, Infiltration of porous alumina bodies with solution precursors: strengthening via compositional grading, grain size control, and transformation toughening, Journal of the American Ceramic Society. 79 (1996) 1810–1814.

[58] P.J. Meschter, E.J. Opila, N.S. Jacobson, Water Vapor–Mediated Volatilization of High-Temperature Materials, Annual Review of Materials Research. 43 (2013) 559–588. https://doi.org/10.1146/annurev-matsci-071312-121636.

[59] N.S.C. Jacobson, Thermodynamics and Kinetics of Silicate Vaporization, (2015). https://ntrs.nasa.gov/search.jsp?R=20150023065 (accessed March 25, 2020).

[60] N.S. Jacobson, E.J. Opila, D.L. Myers, E.H. Copland, Thermodynamics of gas phase species in the Si–O–H system, The Journal of Chemical Thermodynamics. 37 (2005) 1130–1137. https://doi.org/10.1016/j.jct.2005.02.001.

[61] H. Mao, M. Selleby, O. Fabrichnaya, Thermodynamic reassessment of the Y 2O3–Al2O3–SiO2 system and its subsystems, Calphad. 32 (2008) 399–412. https://doi.org/10.1016/j.calphad.2008.03.003.

[62] D.L. Poerschke, R.W. Jackson, C.G. Levi, Silicate Deposit Degradation of Engineered Coatings in Gas Turbines: Progress Toward Models and Materials Solutions, Annu. Rev. Mater. Res. 47 (2017) 297–330. https://doi.org/10.1146/annurev-matsci-010917-105000.

[63] R.M. Leckie, S. Krämer, M. Rühle, C.G. Levi, Thermochemical compatibility between alumina and ZrO2–GdO3/2 thermal barrier coatings, Acta Materialia. 53 (2005) 3281–3292. https://doi.org/10.1016/j.actamat.2005.03.035.

[64] R. Leckie, Fundamental Issues Regarding the Implementation of Gadolinium Zirconate in Thermal Barrier Systems, Ph.D. Dissertation, University of California, Santa Barbara, 2006.

[65] U. Schulz, A. Nowotnik, S. Kunkel, G. Reiter, Effect of processing and interface on the durability of single and bilayer 7YSZ / gadolinium zirconate EB-PVD thermal barrier coatings, Surface and Coatings Technology. 381 (2020) 125107. https://doi.org/10.1016/j.surfcoat.2019.125107.

[66] J. Gomez Chavez, Cmas/volcanic Ash Infiltration Performance Of Yttria Rich-Zirconia Thermal Barrier Coatings Produced By Electron Beam Physical Vapor Deposition, Open Access Theses & Dissertations. (2019). https://scholarworks.utep.edu/open_etd/75.

[67] S. Sampath, X.Y. Jiang, J. Matejicek, A.C. Leger, A. Vardelle, Substrate temperature effects on splat formation, microstructure development and properties of plasma sprayed coatings Part I: Case study for partially stabilized zirconia, Materials Science and Engineering: A. 272 (1999) 181–188. https://doi.org/10.1016/S0921-5093(99)00459-1.

[68] M. Mellali, A. Grimaud, A.C. Leger, P. Fauchais, J. Lu, Alumina grit blasting parameters for surface preparation in the plasma spraying operation, J Therm Spray Tech. 6 (1997) 217–227. https://doi.org/10.1007/s11666-997-0016-6.

[69] K.L. Mittal, W.-S. Lei, eds., Laser technology: applications in adhesion and related areas, John Wiley & Sons ; Scrivener Publishing, Hoboken, NJ : Beverly, MA, 2018.

[70] R. Kromer, S. Costil, J. Cormier, D. Courapied, L. Berthe, P. Peyre, M. Boustie, Laser surface patterning to enhance adhesion of plasma sprayed coatings, Surface and Coatings Technology. 278 (2015) 171–182. https://doi.org/10.1016/j.surfcoat.2015.07.022.

[71] C. Gatzen, D.E. Mack, O. Guillon, R. Vaßen, Improved Adhesion of Different Environmental Barrier Coatings on Al2O3/Al2O3-Ceramic Matrix Composites, Advanced Engineering Materials. n/a (n.d.) 2000087. https://doi.org/10.1002/adem.202000087.

[72] C. Gatzen, D.E. Mack, O. Guillon, R. Vaßen, Surface roughening of Al2O3/Al2O3-ceramic matrix composites by nanosecond laser ablation prior to thermal spraying, Journal of Laser Applications. 31 (2019) 022018. https://doi.org/10.2351/1.5080546.

[73] S.G. Terry, Evolution of Microstructure during the Growth of Thermal Barrier Coatings by Electron-Beam Physical Vapor Deposition, Ph.D. Dissertation, University of California, Santa Barbara, 2001.

[74] U. Schulz, B. Saruhan, K. Fritscher, C. Leyens, Review on Advanced EB-PVD Ceramic Topcoats for TBC Applications, International Journal of Applied Ceramic Technology. 1 (2004) 302–315. https://doi.org/10.1111/j.1744-7402.2004.tb00182.x.

[75] B.A. Movchan, A.V. Demchishin, Structure And Properties Of Thick Condensates Of Nickel, Titanium, Tungsten, Aluminum Oxides, And Zirconium Dioxide In Vacuum., Fiz. Metal. Metalloved. 28: 653-60 (Oct 1969). (1969). https://www.osti.gov/biblio/4181669 (accessed May 17, 2021).

[76] J.R. Anderson, Chemisorption and reactions on metallic films;, Academic Press, London; New York, 1971.

[77] J.A. Thornton, High Rate Thick Film Growth, Annual Review of Materials Science. 7 (1977) 239–260. https://doi.org/10.1146/annurev.ms.07.080177.001323.

[78] H.A. Beale, W. Grossklaus, Low pressure gas scattering of electron-beam- evaporated MCrAlY alloys, Thin Solid Films. 40 (1977) 281–289. https://doi.org/10.1016/0040-6090(77)90129-8.

[79] U. Schulz, K. Fritscher, C. Leyens, M. Peters, W.A. Kaysser, Thermocyclic Behavior of Differently Stabilized and structured EB-PVD thermal barrier coatings, Materialwissenschaft Und Werkstofftechnik. 28 (1997) 370–376. https://doi.org/10.1002/mawe.19970280811.

[80] A. Van der Drift, Evolutionary selection, a principle governing growth orientation in vapour-deposited layers, Philips Res. Rep. 22 (1967) 267.

[81] P. Hartman, W. Perdok, On the relations between structure and morphology of crystals. I, Acta Crystallographica. 8 (1955) 49–52.

[82] P. Hartman, On the crystal habit of fluorite, in: Materials Genesis, Publishing House of the Bulgarian Academy of Sciences, Sofia, 1974: pp. 111–116.

[83] B. Rashkova, Microstructural characterization of yttria-stabilized zirconia thermal barrier coatings grown on sapphire substrates, Charakterisierung der Mikrostruktur von Yttrium-stabiliziertem Zirconiumoxid Wärmedämmschichtsystemen gewachsen auf Saphire-Einkristallen. (2003). https://doi.org/10.18419/opus-6542.

[84] U. Schulz, S.G. Terry, C.G. Levi, Microstructure and texture of EB-PVD TBCs grown under different rotation modes, Materials Science and Engineering: A. 360 (2003) 319–329. https://doi.org/10.1016/S0921-5093(03)00470-2.

[85] S.G. Heinze, Phase Equilibria and Toughness of ZrO2-(Y/Yb)O 1.5-TaO2.5 Thermal Barrier Coatings, Ph.D., University of California, Santa Barbara, 2018. https://www.proquest.com/docview/2188322075/abstract/13FD9689ED334331PQ/7 (accessed May 17, 2021).

[86] Gas turbines, Siemens-Energy.Com Global Website. (n.d.). https://www.siemens-energy.com/global/en/offerings/power-generation/gas-turbines.html (accessed May 19, 2021).

[87] The GEnx Engine | GE Aviation, (n.d.). https://www.geaviation.com/commercial/engines/genx-engine (accessed May 19, 2021).

[88] Materials Characterization, ASM International, 2019. https://doi.org/10.31399/asm.hb.v10.9781627082136.

[89] Y.S. Touloukian, R.K. Kirby, E.R. Taylor, T.Y.R. Lee, Thermophysical Properties of Matter - the TPRC Data Series. Volume 13. Thermal Expansion - Nonmetallic Solids, Thermophysical and Electronic Properties Information Analysis Center, Lafayette, IN, 1977. https://apps.dtic.mil/sti/citations/ADA129116 (accessed October 28, 2021).

[90] J.A. DiCarlo, H.-M. Yun, G.N. Morscher, R.T. Bhatt, SiC/SiC Composites for 1200°C and Above, in: N.P. Bansal (Ed.), Handbook of Ceramic Composites, Springer US, Boston, MA, 2005: pp. 77–98. https://doi.org/10.1007/0-387-23986-3_4.

[91] J.A. Haynes, B.A. Pint, W.D. Porter, I.G. Wright, Comparison of thermal expansion and oxidation behavior of various high-temperature coating materials and superalloys, Materials at High Temperatures. 21 (2004) 87–94. https://doi.org/10.1179/mht.2004.012.

[92] R. Darolia, Thermal barrier coatings technology: critical review, progress update, remaining challenges and prospects, International Materials Reviews. 58 (2013) 315–348. https://doi.org/10.1179/1743280413Y.0000000019.

[93] U. Schulz, B. Saruhan, K. Fritscher, C. Leyens, Review on Advanced EB-PVD Ceramic Topcoats for TBC Applications, International Journal of Applied Ceramic Technology. 1 (2004) 302–315. https://doi.org/10.1111/j.1744-7402.2004.tb00182.x.

[94] K. Shimamura, T. Arima, K. Idemitsu, Y. Inagaki, Thermophysical Properties of Rare-Earth-Stabilized Zirconia and Zirconate Pyrochlores as Surrogates for Actinide-Doped Zirconia, Int J Thermophys. 28 (2007) 1074–1084. https://doi.org/10.1007/s10765-007-0232-9.

[95] R. John, L.P. Zawada, J.L. Kroupa, Stresses Due to Temperature Gradients in Ceramic-Matrix-Composite Aerospace Components, Journal of the American Ceramic Society. 82 (1999) 161–168. https://doi.org/10.1111/j.1151-2916.1999.tb01736.x.

[96] S. Lakiza, O. Fabrichnaya, M. Zinkevich, F. Aldinger, On the phase relations in the ZrO2–YO1.5–AlO1.5 system, Journal of Alloys and Compounds. 420 (2006) 237–245. https://doi.org/10.1016/j.jallcom.2005.09.079.

[97] R. Hay, E. Boakye, M. Petry, Y. Berta, K. Lehmden, J. Welch, Grain Growth and Tensile Strength of 3M Nextel 720^{TM} After Thermal Exposure, in: Ceram. Eng. Sci. Proc., 1999: pp. 153–163. https://doi.org/10.1002/9780470294567.ch19.

[98] U. Schulz, B. Saruhan, K. Fritscher, C. Leyens, Review on Advanced EB-PVD Ceramic Topcoats for TBC Applications, International Journal of Applied Ceramic Technology. 1 (2005) 302–315. https://doi.org/10.1111/j.1744-7402.2004.tb00182.x.

[99] T.H. Nielsen, M.H. Leipold, Thermal Expansion of Yttrium Oxide and of Magnesium Oxide with Yttrium Oxide, Journal of the American Ceramic Society. 47 (1964) 256–256. https://doi.org/10.1111/j.1151-2916.1964.tb14408.x.

[100] U. Schulz, M. Schmücker, Microstructure of ZrO2 thermal barrier coatings applied by EB-PVD, Materials Science and Engineering: A. 276 (2000) 1–8. https://doi.org/10.1016/S0921-5093(99)00576-6.

[101] H.G. Scott, The Yttria–Zirconia δ phase, Acta Cryst B. 33 (1977) 281–282. https://doi.org/10.1107/S0567740877003367.

[102] V. Jayaram, M. De Graef, C.G. Levi, Metastable extension of the fluorite phase field in Y2O3-ZrO2 and its effect on grain growth, Acta Metallurgica et Materialia. 42 (1994) 1829–1846. https://doi.org/10.1016/0956-7151(94)90009-4.

[103] U. Schulz, K. Fritscher, EB-PVD Y203 - and CeO2/Y203-stabilized zirconia thermal barrier coatings - crystal habit and phase composition, Surface and Coatings Technology. 82 (1996) 259–269.

[104] J.C. Vyas, G.P. Kothiyal, K.P. Muthe, D.P. Gandhi, A.K. Debnath, S.C. Sabharwal, M.K. Gupta, Growth of yttria and dysprosium thin films by molecular beam epitaxy and their characterization, Journal of Crystal Growth. 130 (1993) 59–66. https://doi.org/10.1016/0022-0248(93)90836-L.

[105] O. Rozenbaum, D. De Sousa Meneses, P. Echegut, Texture and Porosity Effects on the Thermal Radiative Behavior of Alumina Ceramics, Int J Thermophys. 30 (2009) 580–590. https://doi.org/10.1007/s10765-008-0510-1.

[106] B. Müller, U. Renz, Development of a fast fiber-optic two-color pyrometer for the temperature measurement of surfaces with varying emissivities, Review of Scientific Instruments. 72 (2001) 3366–3374. https://doi.org/10.1063/1.1384448.

[107] IMPAC Infrared GmbH, Pyrometer-Handbook, IMPAC Infrared GmbH, 2004.

[108] G. Yang, C.Y. Zhao, A Comparative Experimental Study on Radiative Properties of EB-PVD and Air Plasma Sprayed Thermal Barrier Coatings, Journal of Heat Transfer. 137 (2015). https://doi.org/10.1115/1.4030243.

[109] J. Manara, M. Arduini-Schuster, H.-J. Rätzer-Scheibe, U. Schulz, Infrared-optical properties and heat transfer coefficients of semitransparent thermal barrier coatings, Surface and Coatings Technology. 203 (2009) 1059–1068. https://doi.org/10.1016/j.surfcoat.2008.09.033.

[110] R.E. Juárez, D.G. Lamas, G.E. Lascalea, N.E. Walsöe de Reca, Synthesis of nanocrystalline zirconia powders for TZP ceramics by a nitrate–citrate combustion route, Journal of the European Ceramic Society. 20 (2000) 133–138. https://doi.org/10.1016/S0955-2219(99)00146-6.

[111] S.G. Terry, J.R. Litty, C.G. Levi, Evolution of Porosity And Texture in Thermal Barrier Coatings Grown by EB-PVD, in: Elevated Temperature Coatings: Science and Technology III, Warrendale, PA, 1999: pp. 13–26.

[112] N.M. Abdul-Jabbar, D.L. Poerschke, C. Gabbett, C.G. Levi, Phase equilibria in the zirconia–yttria/gadolinia–silica systems, Journal of the European Ceramic Society. 38 (2018) 3286–3296. https://doi.org/10.1016/j.jeurceramsoc.2018.03.020.

[113] F. Zhang, M. Chen, S. Zhang, P. Zhou, Y. Du, Thermodynamic modeling of ZrO2–Y2O3–SiO2 and ZrO2-Gd2O3–SiO2 systems, Calphad. 72 (2021) 102248. https://doi.org/10.1016/j.calphad.2020.102248.

[114] K. Nakano, N. Fukatsu, Y. Kanno, Thermodynamics of Zr/Hf-mixed silicates as a potential for environmental barrier coatings for Tyranno-hex materials, Surface and Coatings Technology. 203 (2009) 1997–2002. https://doi.org/10.1016/j.surfcoat.2009.01.035.

[115] U. Schulz, K. Fritscher, M. Peters, Thermocyclic Behavior of Variously Stabilized EB-PVD Thermal Barrier Coatings, J. Eng. Gas Turbines Power. 119 (1997) 917–921. https://doi.org/10.1115/1.2817074.

[116] V. Lughi, V.K. Tolpygo, D.R. Clarke, Microstructural aspects of the sintering of thermal barrier coatings, Materials Science and Engineering: A. 368 (2004) 212–221. https://doi.org/10.1016/j.msea.2003.11.018.

[117] J.M. Drexler, A.L. Ortiz, N.P. Padture, Composition effects of thermal barrier coating ceramics on their interaction with molten Ca–Mg–Al–silicate (CMAS) glass, Acta Materialia. 60 (2012) 5437–5447. https://doi.org/10.1016/j.actamat.2012.06.053.